



HAL
open science

Developement of an "all-in-one" approach for the synthesis of silica-based hybrid materials

Robert Winkler

► **To cite this version:**

Robert Winkler. Developement of an "all-in-one" approach for the synthesis of silica-based hybrid materials. Other. Université Montpellier, 2019. English. NNT : 2019MONTTS075 . tel-02479604

HAL Id: tel-02479604

<https://theses.hal.science/tel-02479604v1>

Submitted on 14 Feb 2020

HAL is a multi-disciplinary open access archive for the deposit and dissemination of scientific research documents, whether they are published or not. The documents may come from teaching and research institutions in France or abroad, or from public or private research centers.

L'archive ouverte pluridisciplinaire **HAL**, est destinée au dépôt et à la diffusion de documents scientifiques de niveau recherche, publiés ou non, émanant des établissements d'enseignement et de recherche français ou étrangers, des laboratoires publics ou privés.

THÈSE POUR OBTENIR LE GRADE DE DOCTEUR DE L'UNIVERSITÉ DE MONTPELLIER

En Chimie et Physico-Chimie de Matériaux

École doctorale Droit et Science politique

Unité de recherche : Institut de Chimie Séparative de Marcoule
(UMR 5257-ICSM)

**Development of an “all-in-one” approach for the
synthesis of silica-based hybrid materials**

Présentée par Robert WINKLER

Le 30 octobre 2019

Sous la direction de Stéphane PELLET-ROSTAING
et Guilhem ARRACHART

Devant le jury composé de

Rénal BACKOV, Pr, CRPP Université de Bordeaux

Cédric BOISSIERE, Dr, LCMCP Université Pierre et Marie Curie

Bénédicte LEBEAU, Dr, IS2M Université de Haute Alsace

Julian OBERDISSE, Dr, L2C Université de Montpellier

Guilhem ARRACHART, Dr, ICSM CEA Marcoule

Stéphane PELLET-ROSTAING, Dr, ICSM CEA Marcoule

Rapporteur

Rapporteur

Examinatrice

Examineur

Co-directeur

Directeur



UNIVERSITÉ
DE MONTPELLIER

In this work, we investigated the synthesis of new organosilane precursors and their polymerization to silica hybrid materials with REE extracting properties *via* an all-in-one approach.

To reach this goal, five organosilane precursors were synthesized in good yield. First, these new precursors were used to elaborate dense silica hybrid materials (SHM). The characterization of the local structure by FTIR and of the mesostructure by SAXS of the SHMs highlighted the link between the chemical and physical interactions between the headgroups of the precursors and the others species existing in the reaction mixture. These interactions drive the local connectivity of the siloxane network and the mesostructure of the obtained materials (lamellar and 2D hexagonal phases). Second, in order to improve the material properties, an innovative approach in two steps was proposed. The first step was based on the structuring of binary alcohol/water mixtures to influence the aggregation behavior of silica nanoparticles prepared from tetraethyl orthosilicate (TEOS). Here, a remarkable specific surface area of $2000 \text{ m}^2 \text{ g}^{-1}$ was achieved. In a second step, the reaction conditions that lead to materials with the highest specific surface area were used in combination with the synthesized organosilane precursors. The results show the potential of this approach to tailor the properties of the obtained materials. Finally, the SHMs synthesized from the pure organosilane precursors were successfully tested for the selective and efficient extraction of rare earth elements present in a simulated leachate of NdFeB magnets.

This work offers promising prospects for the "all-in-one" synthesis of SHMs with direct applications.

Ce travail de thèse porte sur la synthèse de nouveaux précurseurs d'organosilane et leur utilisation dans des matériaux hybrides à base de silice par une approche tout-en-un pour l'extraction de terres rares.

Pour atteindre cet objectif, cinq précurseurs d'organosilane ont été synthétisés avec un bon rendement. Premièrement, ces nouveaux précurseurs ont été utilisés pour élaborer des matériaux hybrides à base de silice dense (SHM). La caractérisation de la structure locale par FTIR et de la mésostructure par SAXS du SHM final a permis de mettre en évidence le lien entre les interactions chimiques et physiques entre les groupes fonctionnels des précurseurs et les autres espèces présentes dans le mélange réactionnel qui déterminent la connectivité locale du réseau siloxane et la mésostructure des matériaux obtenus (phases lamellaire et hexagonale 2D). Deuxièmement, afin d'améliorer les propriétés du matériau, une approche innovante en deux étapes a été proposée. La première étape est basée sur la structuration de mélanges binaires alcool/eau afin d'influencer le comportement à l'agrégation des nanoparticules de silice préparé à partir de tétraéthyl orthosilicate. Ainsi, une surface spécifique remarquable de $2000 \text{ m}^2 \text{ g}^{-1}$ a pu être obtenue. Dans une seconde étape, les conditions de réaction conduisant aux matériaux ayant la plus grande surface spécifique ont été utilisées avec l'addition d'un précurseur d'organosilane synthétisé ne présentant pas de groupe fonctionnel générant de forte interaction physico-chimique. Les résultats montrent le potentiel de cette approche pour adapter les propriétés des matériaux obtenus. Enfin, les SHM synthétisés à partir de précurseurs d'organosilane purs ont été testés avec succès pour l'extraction sélective et efficace d'éléments tel que des terres rares présents dans un lixiviat modèle d'aimant NdFeB.

Ces travaux offrent des perspectives prometteuses pour la synthèse « tout-en-un » de SHM à applications directes.

ACKNOWLEDGMENTS

I am grateful to the direction of the Institut de Chimie Séparative de Marcoule (ICSM) and the Commissariat à l'Energie Atomique et aux énergies alternatives (CEA) for the funding of this work and the access to their well-equipped facilities.

I would also like to thank my director Stéphane Pellet-Rostaing and my co-director Guilhem Arrachart for the opportunity to prepare this thesis under their supervision and their confidence, support and criticism during these three years.

Further, I would like to express my gratitude to all current and former co-workers of the ICSM and especially the LTSM and the LNER for all the supportive input and the helpful discussions. Notably, I would like to offer my special thanks to Cyrielle Rey for the help with TGA and the nitrogen sorption measurements, to Guilhem Arrachart, Fabrice Giusti, Nicolas Felines, Artur Larribau and Guillaume Mossand for their support with the organic synthesis, to Sandrine Dourdain, Pierre Bauduin, Jeremy Causse, Olivier Diat and Zijie Lu for the help with SAXS and several fruitful discussions, to Diane Rébiscoul for the help with infrared spectroscopy, to Sandra Maynadie for the help with NMR measurements, to Josef Lautru, Elisa Ré, Xavier Le Goff and Jingxian Wang for the assistance with microscopy, and to Béatrice Baus-Lagarde for the help and assistance at the ICP measurements.

Special thanks also go to Vainina Russello, Hélène Martin and Elisabeth Roussigné for their support with many administrative challenges.

My thanks are also extended to colleagues in other institutions. Thanks to Olivier Taché of the CEA Saclay for the help with USAXS measurements and Martiane Cabie for the help with TEM imagery.

My personal thanks go to Arthur Larribau, Nicolas Felines, Alexandre Artèse, Rémi Boubon, Markus Baum, Michael Bley, Max Hohenschütz, Regis Mastretta, Justine Benghozi, Zijie and Zijun Lu, Tanja Mehri for making my arrival in France and the past three years a very pleasant time.

Last but not least, my very special thanks go to my family in Germany and to my family in France. I'm very thankful for all their support during this adventurous and exciting period. Without the mind clearing weekends and vacations this work would not have been possible. Especially, I would like to thank my girlfriend for her never-ending moral support and for all the motivation she provided me with through her loving and understanding nature at all times.

TABLE OF CONTENTS

INTRODUCTION	1
I STATE OF THE ART	5
1 Silica hybrid materials.....	5
2 Sol-gel process	6
3 Fundamentals of self-assembly	17
3.1 The Gibbs free energy defines the thermodynamically stable state	17
3.2 Auto-assembled structures.....	20
4 Structured silica materials	24
4.1 The porosity of silica materials.....	24
4.2 Controlling the bulk structuring of SHMs	25
5 The scientific approach	29
II ORGANIC SYNTHESIS	31
1 Crucial synthetic methods	31
1.1 Synthesizing organosilanes.....	31
1.2 The multi-functional tool “click-chemistry”.....	33
2 Results and Discussion.....	37
2.1 Retrosynthesis approach.....	37
2.2 Azide synthesis.....	38
2.3 Click-Chemistry	40
3 Conclusion.....	44
III MATERIALS FROM ORGANOSILANES.....	45
1 Silsesquioxane synthesis	47
2 Silsesquioxane characterization.....	48
2.1 Propyl headgroup (H/T-MP2-A/B-C).....	48
2.2 Amine headgroup (H/T-MP1-A/B-C)	56
2.3 Methyl ester headgroup (H/T-MP3-A/B-C)	65
2.4 Carboxylic acid headgroup (H/T-MP3-A/B-C-H).....	72
2.5 Diglycolic acid amide headgroup (H-MP4-B-C and H/T-MP5-B-C).....	78
3 Conclusion.....	87
IV MATERIALS FROM TEOS IN MIXED SOLVENTS.....	91
1 Introduction	92
2 Sample preparation.....	93
3 Phase behavior of the ternary system	96
4 Impact of the TEOS addition on the sol structuring	97
5 Study of the sol-gel transition.....	100
6 Influence of the sol composition on the material structure.....	107
7 Discussion	113
8 Conclusion.....	115
9 Outlook.....	116
V MATERIALS FROM CO-CONDENSATION.....	119
1 The quaternary system – Co-condensation in structured media	119
2 Sample preparation.....	121
3 Organosilane incorporation in the material	122
4 Morphology of the co-condensed materials.	129
5 Discussion	140
6 Conclusion.....	141

VI	EXTRACTION CAPACITIES OF THE SILSESQUIOXANES	143
1	System selection	143
2	Extraction experiments.....	144
3	Metal separation using silsesquioxanes.....	146
1.1	Screening of the extraction properties at different pH.....	146
1.2	Mechanism of the Nd extraction by H-MP4-B-C.....	147
1.3	Competitive extraction in a simulated NdFeB magnet leachate	150
4	Conclusion and outlook.....	151
	CONCLUSION	153
VII	RÉSUMÉ EN FRANCAIS.....	155
VIII	REFERENCES	161
	List of Figures	186
IX	EXPERIMENTAL	191
1	Chemicals.....	191
2	Methods.....	192
1.1	Dynamic Light Scattering (DLS).....	192
1.2	Gas Chromatography-Mass Spectrometry (GC-MS).....	192
1.3	Electrospray Ionization Mass Spectrometry (ESI-MS).....	192
1.4	Fourier Transformed Infrared Spectroscopy/Attenuated Total Reflection (FTIR/ATR)	192
1.5	Nitrogen adsorption-desorption.....	193
1.6	Nuclear Magnetic Resonance spectroscopy (NMR).....	193
1.7	Small/Wide-Angle X-ray Scattering (SWAXS)	193
1.8	Scanning Electron Microscopy (SEM).....	193
1.9	Transmission electron microscopy (TEM)	194
1.10	Ternary phase diagrams.....	194
1.11	ThermoGravimetric Analysis (TGA).....	194
X	APPENDIX/NMR SPECTRA	195
1	Chapter II.....	195
2	Chapter III.....	225
3	Chapter IV	233
4	Chapter V	239

INTRODUCTION

Rare earth elements (REEs) are a group of 17 metals as defined by IUPAC.¹ They are critical for modern technologies like electric motors, information technology and lighting.² The conventional mining of REEs was found to have several economic and ecological drawbacks. Economically speaking, western countries are impacted by the market dominance of the Chinese REE industry.³ The Chinese monopole in combination with geopolitical factors was concluded to be a major challenge in the 2011 U.S. Department of Energy report.⁴ This is seen by their medium-term criticality matrix for the period of 2015 to 2025 is shown in **Figure 1**.

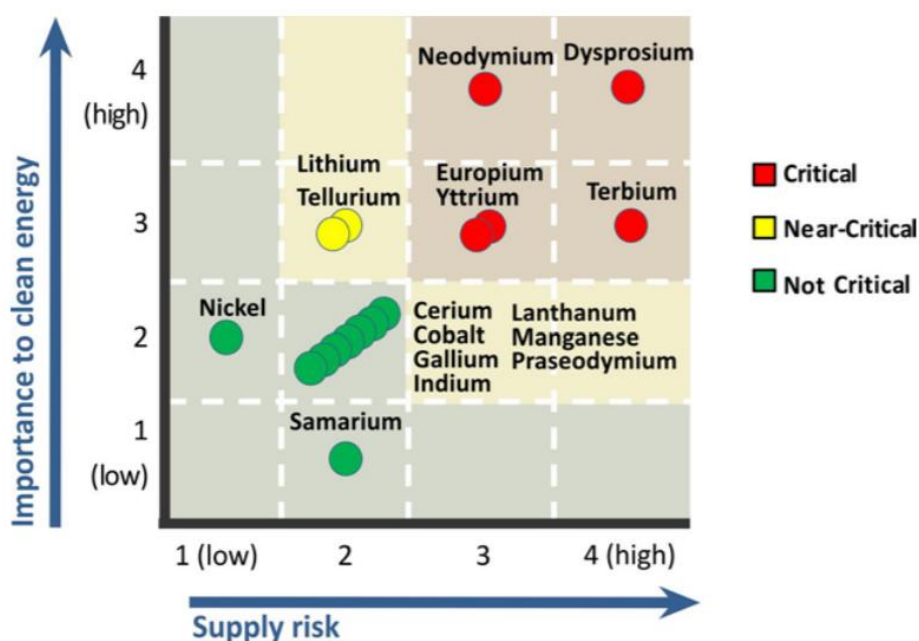


Figure 1. Medium-term (2015-2025) criticality matrix as developed in 2011.⁴

The most critical metals are typically the REEs used for clean energy production that are majorly mined in China. Ecologically speaking, REE mining is responsible for a large emission of toxic gasses⁵, the destruction of landscapes and agricultural land and ground water pollution.⁶ Furthermore, tremendous quantities of CO₂ are emitted during production. However, the demand of REEs is predicted to rise in the next decades mainly due to the production of permanent magnets.^{2,3,7} Therefore, mining is unavoidable unless alternative technologies are found.

To limit the quantity of newly mined REEs, an effective circular economy is necessary where recycling is a main feature with several advantages.⁸ First, the REEs are recycled in the countries that consume them. Therefore, the geopolitical implications lose

importance. Second, the REE recycling is less energy intensive than the production from primary resources and, amongst other things, less CO₂ emitting.⁹ Third, REEs are mined in their natural abundance. This means that the high need of naturally less abundant metals (*e.g.* Dy⁷) leads to the overproduction of more abundant metals with all disadvantages mentioned above. By recycling *e.g.* end of life (EOL) products, the REEs are recovered in proportions that are close to application.

For recycling, silica hybrid materials (SHM) with extracting functional groups are an interesting option. The synthesis of SHM is, conventionally, a multistep procedure. The first step is the formation of a siloxane network that constitutes the inorganic structure *via* the sol-gel process. By tuning a multitude of parameters and the addition of structuring additives, it is possible to tailor the obtained morphology. The second step corresponds to the removal of the solvent by *e.g.* freeze drying or supercritical (SC) CO₂. The chosen method influences the retention of the morphology of the formed siloxane network. In the final step, the resulting materials are functionalized with organic groups. This methodology leads to several disadvantages such as the necessity of the additive removal after the sol-gel process or the inhomogeneous grafting of the functional molecules on the material surface.

The all-in-one approach of SHM synthesis is capable of eliminating these drawbacks. By the modification of the employed siloxane precursor with an organic function and the ingenious choice of the reaction conditions, a material with the desired properties can be obtained directly after drying. In previous works^{10,11}, the potential of this approach has been explored. Using the same approach, in this study, new precursors and synthetic routes for the elaboration SHMs are proposed.

In the first chapter, a review of the existing SHM, their methods of elaboration and the underlying mechanisms is given. This includes the factors that influence the sol-gel process, the physical interactions that are important for soft matter and the combination of both to form structured materials. Based on these principles, a scientific approach is elaborated that is followed in the chapters of this work.

The second chapter is dedicated to the synthesis of the precursor molecules by click chemistry in order to provide multifunctional organosilanes.

In the third chapter, the material formation using only the synthesized organosilane precursors is investigated and discussed.

In order to improve material characteristics, an innovative approach using structured binary *tert*-butanol (TBA)/water mixtures as solvents for the polymerization of tetraethyl orthosilicate (TEOS) is presented in the fourth chapter.

In the fifth chapter, the novel approach using the system TEOS/TBA/water is extended by the addition of an organosilane precursor in order to elaborate functionalized materials.

Finally, in the sixth chapter, an outlook is proposed by applying the materials synthesized from the pure organosilane precursors for REE extraction.

Introduction

List of abbreviations

ATR	Attenuated Total Reflection
BET	Brunauer Emmett Teller
CS	Co-Solvent
CuAAC	Copper(I)-catalyzed Alkyne Azide Cycloaddition
DCM	DiChloroMethane
DE	Diethyl Ether
DLCA	Diffusion Limited Cluster-cluster Aggregation
DLS	Dynamic Light Scattering
DMF	DiMethyl Formamide
DMSO	DiMethyl SulfOxide
EDX	Energy-Dispersive X-ray spectroscopy
ESI-MS	ElectroSpray Ionization Mass Spectrometry
Et ₃ N	Triethyl amine
EtOH	Ethanol
FTIR	Fourier-Transform InfraRed spectroscopy
GC MS	Gas Chromatography-Mass Spectrometry
H-bond	Hydrogen bond
ICP/AES	Inductively Coupled Plasma/Atomic Emission Spectroscopy
ICP/MS	Inductively Coupled Plasma Mass Spectrometry
MOF	Metal-Organic Framework
MsCl	Methanesulfonyl chloride
NMR	Nuclear Magnetic Resonance
OP	Organosilane Precursor
OZ	Ornstein-Zernicke
REE	Rare Earth Element
RLCA	Reaction Limited Cluster-cluster Aggregation
SAXS	Small Angle X-ray Scattering
SC	SuperCritical
SEM	Scanning Electron Microscopy
SHM	Silica Hybrid Material
TBA	<i>tert</i> -butanol
TEM	Transmission Electron Microscopy
TEOS	TetraEthyl OrthoSilicate
TGA	ThermoGravimetric Analysis
THF	TetraHydroFuran
T-S	Teubner-Strey
vdW	van-der-Waals

10000 m²/g), high reactivity and controllable structure, they are highly suitable for catalytic and adsorption applications.²⁴ Still increasing the inorganic content, materials that are principally constituted of metal oxides are obtained. For example, mesoporous silica is used in chemical and pharmaceutical analytics²⁵ or as drug carriers.²⁶ The surface properties of SiO₂ glass are modified by thin films to achieve various properties.²⁷

P. Judeinstein and C. Sanchez classified organic-inorganic hybrid materials into two groups depending on the type of interactions between the organic and inorganic phases.²⁸ Class I describes materials where the phases are linked by weak interactions like van-der-Waals (vdW) forces, electrostatics or hydrogen bonds (H-bond). Materials in this category are organic dyes in metal oxide matrixes or nanoparticle doped organic polymers. At more equal mixtures between organic and inorganic phases, the material morphology rather consists of interpenetrating polymers. Class II contains materials where the organic and inorganic phases are connected by covalent or ionic-covalent bonds. They can be synthesized by chemically modified sol-gel precursors like functionalized alkoxysilanes. The organic phases can also be introduced by post-synthetic grafting of the inorganic phase. In any case, the interactions between organic and inorganic phases can induce a controllable structuring of the obtained material. This possibility will be discussed at a later point.

Following the principle of the bottom-up approach, the synthesis of the inorganic phase is usually done using the sol-gel route.

2 Sol-gel process

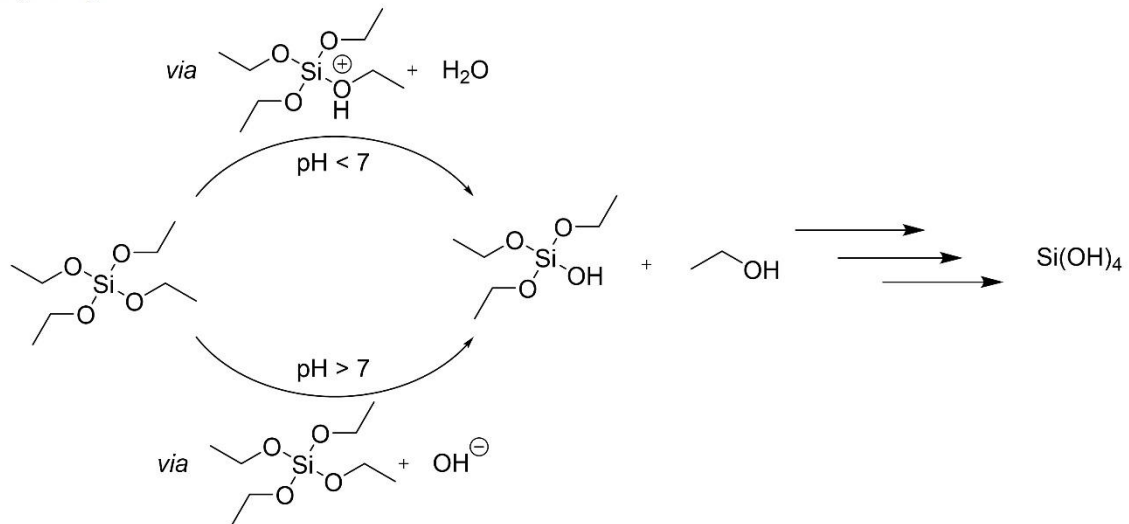
In the terminology of colloidal chemistry, a sol is a suspension of nanoscale (1 nm to 1 μm) solids in a liquid phase.²⁹ In this case, the sol is obtained by the polymerization reaction of a metal source to colloidal metal oxides using an acid and/or base catalyst in wet media. Depending on the applied procedure, this sol can be transformed to a gel, deposited as thin film or dried to obtain the isolated colloids. Typically, this is performed at mild (< 100 °C) temperatures. Silanes, which are discussed thoroughly in this work, represent a particular case of the materials synthesized from the sol-gel process. The chemistry of silicon leads to particular reaction properties compared to other, more metallic elements. A multitude of parameters influences the kinetics and the morphology of the obtained products. An exhaustive description of the sol-gel process of silanes is given in the two fundamental works by C. Brinker³⁰ and R. Ilter.³¹ In this section the parameters are categorized in three groups. The first group concerns the chemistry of silanes and their derivatives. It includes the effects of pH and catalysis conditions on the reactivity of the compounds with each other. The second group concerns the nature of the employed precursor, meaning its molecular structure. The third group concerns the parameters that influence the physical interactions of compounds in the sol-gel process.

Important parameters of the sol-gel process

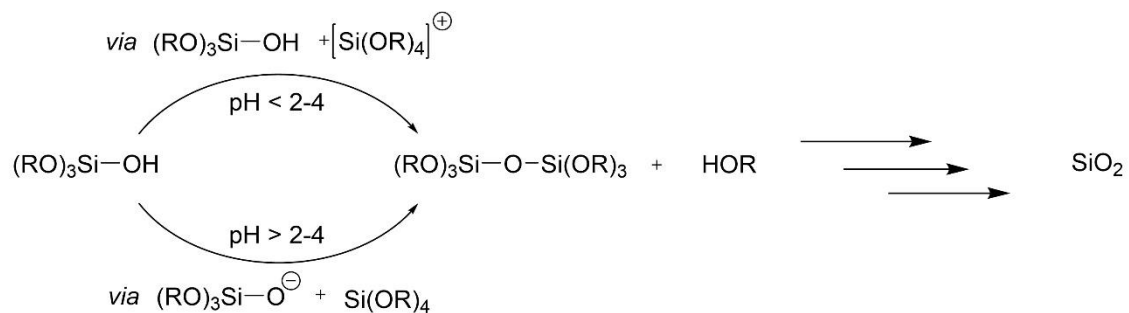
i. Chemistry

To illustrate the chemistry of the sol-gel process, tetraethyl orthosilicate is selected as an example since it is one of the most frequently employed precursors. The two chemical reactions that form the foundation of the sol-gel process are shown in **Figure 3**.

Hydrolysis



Condensation



Global reaction



Figure 3. Fundamental reactions of the sol-gel process using TEOS as example. Hydrolysis and condensation take place under acidic or basic conditions.

State of the art

The global reaction involves the reaction of one molecule of TEOS with two equivalents of water. The product, silica, which has the chemical formula SiO_2 in its fully condensed state, is formed together with four equivalents of ethanol. More generally, every cleavable alkoxy group in the precursor requires $\frac{1}{2}$ equivalent of water and will lead to $\frac{1}{2}$ oxygen in the chemical formula of the final product.

In most cases, the polymerization requires the hydrolysis of the alkoxy groups in TEOS. This can be done under acidic or basic conditions. The reacting species change depending on the pH. Below pH 7, water is the nucleophile which attacks the protonated alkoxy silane. Above pH 7, a hydroxide-ion attacks the alkoxy silane. In this process, silanol groups are generated. Then, the hydrolyzed species are available for the condensation reaction. The condensation can take place between two silanol groups forming water or between a silanol group and an alkoxy group forming the corresponding alcohol. Just as for the hydrolysis reaction, the condensation is pH dependent. However, the pH limit is linked to the pK_A of the silanol groups. As simulations show³², the pK_A depends on the neighboring silica groups and the degree exposure of the OH on the surface. Generally, at higher condensation degrees the pH limit lowers from 4 down to around 2. Above this pH, the surface OH groups are partially deprotonated and can act as nucleophiles. Below this pH, the OH groups are protonated which renders them a better leaving group. It is worth mentioning that non-hydrolytic methods are also possible when water is not available as oxygen source.^{33,34}

The varying reactivity of the evolving silica species leads to numerous colloidal morphologies. C. Brinker gave a general overview of the obtainable structures when modifying the reaction conditions³⁰ which has been reused by several authors.³⁵⁻³⁸ A representation is illustrated in **Figure 4**.

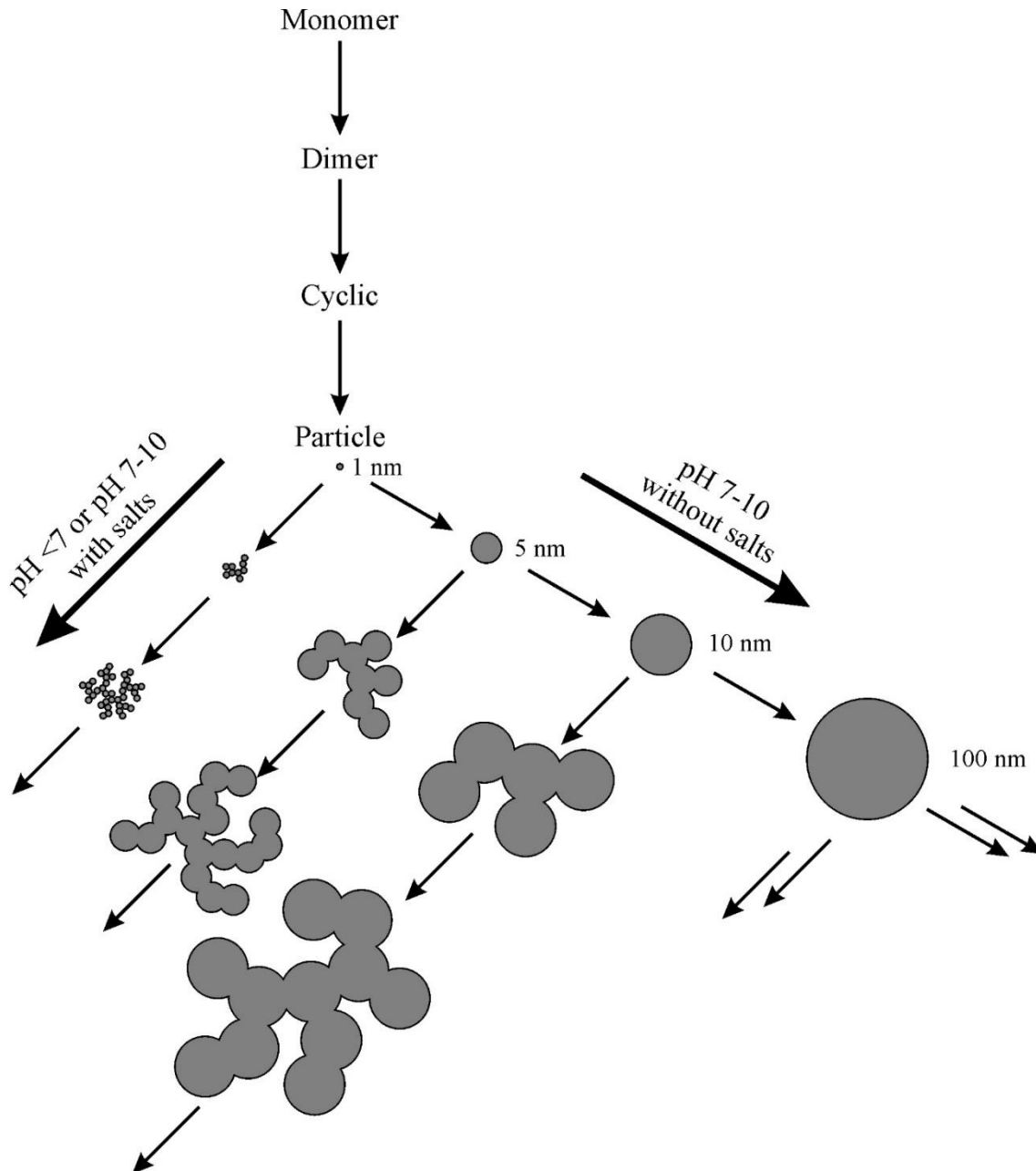


Figure 4. Influence of the sol pH and the ionic strength on the morphology of the obtained silica polymer. The Figure is redrawn from literature.³⁰

The catalysis conditions have the biggest influence on the growing polymer. Given an over-stoichiometric quantity of water in the system ($r = \frac{[H_2O]}{[Si]} \gg 4$), three pH-ranges have to be distinguished.

pH 7-10: In this pH range, the hydrolysis rate accelerates at higher numbers of silanol groups and siloxane bonds. The reason is the stronger electron withdrawing effect in the order -alkyl < -alkoxy < -hydroxy < siloxane. Therefore, the hydrolysis can be assumed complete when condensation takes place. The condensation behavior is controlled by electronic and steric effects. Sterically, all sites are silanol groups and, thus, active in condensation. Electronically, more siloxane bonds lead to higher charges

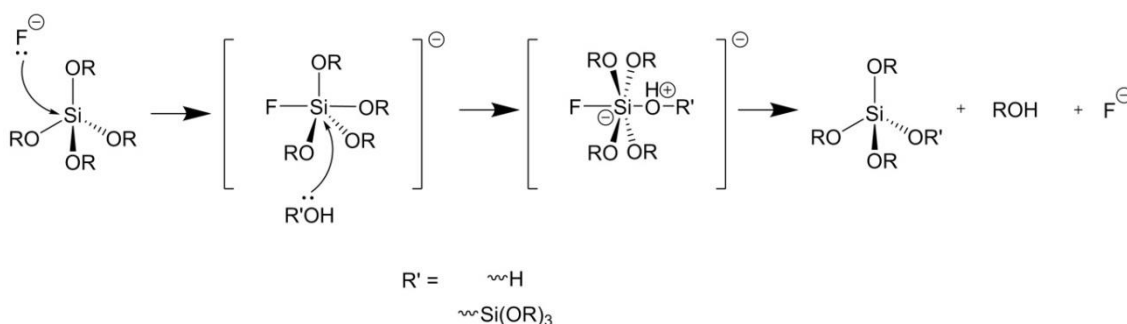
because of a lower pK_A . In other words, the more the condensation has advanced, the higher the surface charge of the growing polymer. A particular effect at this pH-range is the dissolution of already formed siloxane bonds leading to a release of monomers. The electronic effects favor the formation of large uniform particles *via* the preferential reaction of monomers with clusters. The increasing charge of clusters provides an electrostatic barrier that only less charged monomers can pass. The hydrolysis of siloxane bonds leads to the energetically favorable equilibrium state of silanes with four siloxane bonds. This drives unreacted or released monomers towards the inside of the growing particles. In **Figure 4**, the arrows to the right indicates the expected growth under these conditions. The most famous synthesis that makes use of this mechanism is the Stöber process.³⁹ Here, solid silica nanoparticles of controlled size are synthesized by the ammonia-catalyzed polymerization of TEOS in ethanol.

pH < 2: Highly acidic conditions that are sufficiently below the pK_A of silanol groups, strongly promote hydrolysis. In principle, hydrolysis of the alkoxy group slows down with increasing substitution at the remaining positions in the order -alkyl < -alkoxy < -hydroxy < siloxane. However, it has been shown^{40,41} that hydrolysis is completed after several minutes. Thus, monomers are available in their fully hydrolyzed form from the start. Contrarily to base catalyzed processes, condensation is irreversible. Therefore, the obtained structures are kinetically stabilized and not in equilibrium. Monomers tend to form small primary particles that connect to each other forming chains. Generally, the reaction occurs at the chain ends because of the easier accessibility compared to the interior of the branched structure, the statistical overweight of available bonds at chain ends and the increased presence of charged, more reactive species. In **Figure 4**, the arrow to the left indicates the expected growth under these conditions.

pH 2 to 4 -7: At intermediate pH, the obtained morphologies are between those mentioned earlier. Hydrolysis is acid catalyzed and its rate increases with decreasing pH. The hydrolysis rate of the alkoxy group is strongly affected by the remaining substituents and decreases in the order -alkyl < -alkoxy < -hydroxy < siloxane. Condensation and dissolution are base catalyzed and their rates decrease with decreasing pH. Therefore, deprotonated clusters preferentially react with positively charged monomers. At later stages, no monomers remain and the mechanism changes to a cluster-cluster aggregation. The dissolution of siloxane bonds is effective at pH > 4 at lower pH it stops to provide a continuous source of monomers that will drive the system towards equilibrium.

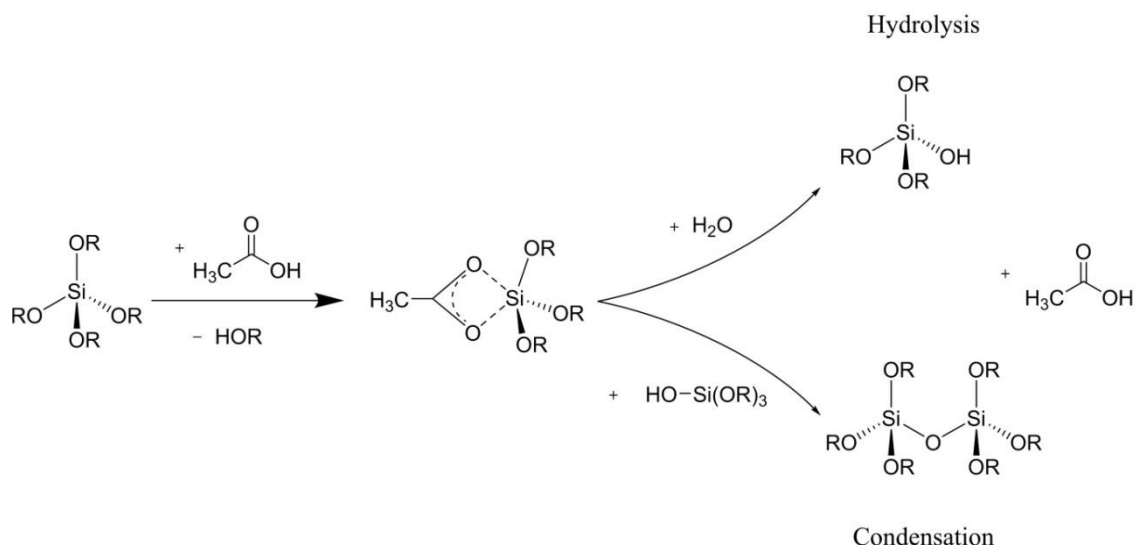
Especially under acidic conditions ($\text{pH} < 4$), re- and transesterification of alcohols influence the sol-gel kinetics. This effect is less pronounced under basic conditions. This is explained by the easier protonation of silanol and alkoxy silane groups under acidic conditions than the deprotonation of alcohols under basic conditions. The effects depend largely on the steric and electronic character of the alcohol in the system. Considering alkyl alcohols, the reactivity decreases with increasing steric hindrance. Transesterification will replace the alcohol that has been introduced by the alkoxy silane precursor by the smallest alcohol present in the system. In this case, sol-gel kinetics can be accelerated. Reesterification can modify the surface of the silica polymer after the distillation of water as azeotrope. Furthermore, given specific conditions, it may slow down the condensation rate (see **IV**).

Next to bases and acids, other sol-gel catalysts are known. Nucleophilic catalysis by fluoride (HF , KF , NH_4F ...) is an effective mean to accelerate the hydrolysis and condensation rates. Mechanistically, the fluoride ion which is similar in size to the hydroxyl ion, increases the coordination number of silicon from four to five or six. This promotes the intermediate state of the nucleophilic attack.^{30,42-44} The mechanism is displayed in **Scheme 1**.



Scheme 1. Mechanism of fluoride catalyzed hydrolysis or condensation reaction of silanes.

Carboxylic acids have been shown to catalyze the hydrolysis and condensation reaction to similar extents as strong acids. This behavior is explained by the formation of an ester between the carboxyl group and the silane.^{45,46} **Scheme 2** illustrates the mechanism. The ester has a strong electron withdrawing effect that increases the electrophilic character of the central silicon. The reaction proceeds only in presence of water or a stronger acid to condensation.^{47,48}



Scheme 2. Exemplary reactions of the proposed mechanism for the sol-gel catalysis by carboxylic acids.

Catalysis is the main parameter that influences the sol-gel process. By choosing the right catalyst the polymerization behavior can be tailored to obtain the desired material morphology and properties.

It should be noted that the stoichiometric ratio $r = \frac{[H_2O]}{[Si]}$ can have a significant impact when it is close to the minimum that is required for complete hydrolysis ($r = 4$). Below, the hydrolysis rate is decreased compared to the condensation rate. Below $r = 2$, the alcohol producing condensation is favored while at $r > 2$ the water producing condensation is favored. Large values of r promote the dissolution of siloxane bonds under basic conditions. The overall effects are difficult to predict. A further discussion would go beyond the scope of this work since none of the present studies are performed under these conditions.

ii. Precursor

Tetra-coordinated silanes can be described by the general chemical formula displayed in **Figure 5**.

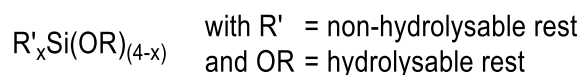


Figure 5. General chemical formula of silanes.

In any case of substitution, the steric effects dominate the electronic effects. The introduction of a larger hydrolysable rest -OR decreases the hydrolysis rate. The effect is even stronger when branching is introduced. This is explained by the steric hindrance

caused by -R group and the increasing positive inductive (+I) effect of larger alkyl chains that decreases the leaving group character of the corresponding alcohol. Replacing an alkoxy group by a non-hydrolysable rest leads to a higher electron density on the silicon atom caused by the +I effect. The hydrolysis rate at $\text{pH} > 7$ is decreased while it is accelerated at $\text{pH} < 7$. The condensation rate is slowed down at $\text{pH} > 2$ to 4 while it is accelerated at $\text{pH} < 2$ to 4. As mentioned before, the exact pH limit depends on the size and the structure of the silica polymer. However, when the non-hydrolysable rest causes steric hindrance, the hydrolysis and the condensation rate are decreased. This must be considered when trying to develop materials using two different precursors.

iii. Physics

Several experimental parameters influence the sol-gel process.

Temperature: Both, hydrolysis and condensation, are accelerated by higher temperature.

Solvent: Solvents can be classified by their polarity (dielectric constant, dipole moment) and their ability to be a hydrogen-bond donor and acceptor (protic) or only a hydrogen-bond acceptor (aprotic with heteroatom *e.g.* O, N, S...). **Figure 6** gives an overview of the possible combinations using frequently used examples.

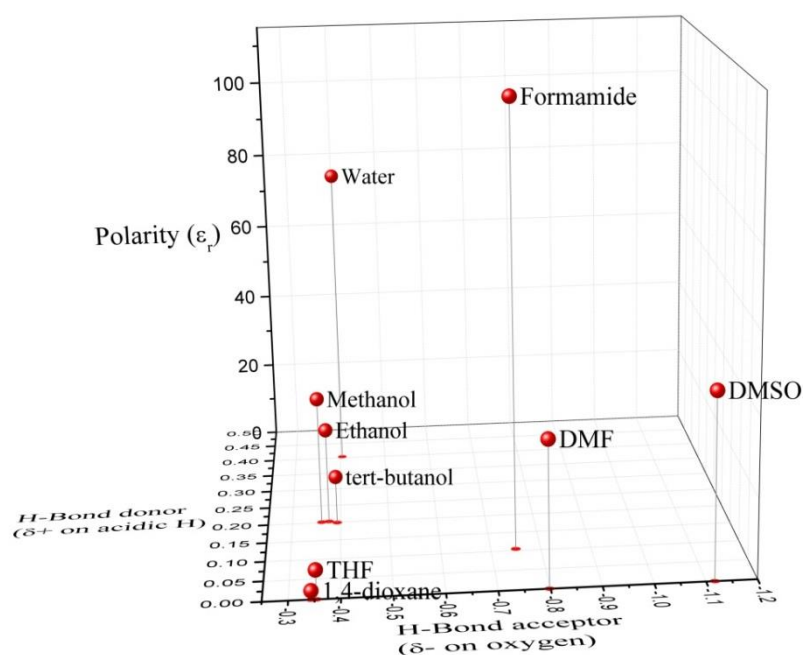


Figure 6. Classical sol-gel solvents plotted as a function of their relative dielectric constant and the relative charges on the oxygen atom and the labile proton (if present).

Solvent effects are mostly related to electronic effects. Here, polarity (displayed as the relative dielectric constant ϵ_r in **Figure 6**) is responsible for the stability and range of electric charges in solution. The characteristic distance of electrostatic forces in solution is given by the Debye screening length λ_D .²⁹

$$\lambda_D = \kappa^{-1} = \sqrt{\frac{\epsilon_r \epsilon_0 k_B T}{\sum_i (z_i e)^2 c_S}} \quad (1)$$

Here, ϵ_r denotes the relative dielectric constant, ϵ_0 the permittivity, k_B the Boltzmann constant, T the temperature, z_i the ion valence, e the elemental charge and c_S the salt concentration. The higher the dielectric constant, the longer is the distance over which charge influence each another. This impacts aggregation behavior of charged colloids that interact by electrostatic forces. On a molecular scale, the reaction rate of charged species is affected. By stabilizing separated electric charges, a higher dielectric constant favors charged transition states and ionic intermediate products.

Coming to the hydrogen bonding behavior, acid and base catalysis must be distinguished. At $\text{pH} > 7$, the hydrolysis rate depends largely on the hydroxyl ion activity. The activity is higher when no solvent with H-bond donor characteristics is present. Therefore, protic solvents (water, alcohols) slow hydrolysis at $\text{pH} > 7$ down. At $\text{pH} < 7$, the situation is inverted. The activity of oxonium ions is decreased with increasing H-bond acceptor properties of the solvent. Thus, solvents with strong H-bond acceptor characteristics (DMSO, DMF) slow the hydrolysis at $\text{pH} < 7$ down. Other solvents might have specific interactions with silica. For example, solvents with accessible carboxylic groups (*e.g.* formamide) can interact *via* complexation like mentioned earlier. This can degrade the solvent leading to pH modification during the reaction.

Salts: Inorganic salts influence the sol-gel process by the ionic strength I .⁴⁹

$$I = \frac{1}{2} \sum_{i=1}^n c_i z_i^2 \quad (2)$$

Here, c_i is the concentration of the ion i and z_i its valence. The higher the salt concentration, the higher the ionic strength becomes. Ion valence contributes proportionally to its squared value. Therefore, polyvalent ions have a stronger influence on the ionic strength. Comparing Eq. (2) with (1), it can be seen that an increasing ionic strength decreases the Debye length λ_D . Higher salt concentrations, especially of polyvalent ions, decrease the range of electrostatic forces between charges. Thus, colloidal solutions that are stabilized by repulsive charges aggregate more easily. **Figure**

4 illustrates this behavior. A study on the influence of salts on the pore size confirms this result.⁵⁰ The reported shrinking pore sizes at higher salt concentrations and valences can be related to the diminished electrostatic repulsions between primary particles. Furthermore, in the mentioned study, ion-specific effects can be suspected. Ion-specific effects were also reported when looking at different halide salts.⁵¹ However, no comprehensive study on specific ion effects was done to date.

Considering the multitude of parameters, the sol-gel process requires intensive anticipation of the occurring mechanisms to obtain the desired material. Chemical and structural factors combined with physical interactions play an important role during the sol evolution. By the addition of further molecules that have specific interactions with the silica polymer, highly ordered structures can be obtained.⁵²

3 Fundamentals of self-assembly

3.1 The Gibbs free energy defines the thermodynamically stable state

In order to explain the organization of silica structures by templating approaches, first an overview of the relevant physicochemical mechanisms of soft matter will be given. Soft matter is a subfield of condensed matter that can be deformed or structurally altered by thermal or mechanical stress that are in the order of magnitude of $k_B T$ (thermal fluctuations).⁵³ The reason is a subtle equilibrium between attractive and repulsive forces like illustrated in **Figure 7**. Generally, repulsive forces dominate at short distance while attractive forces dominate at long distances.

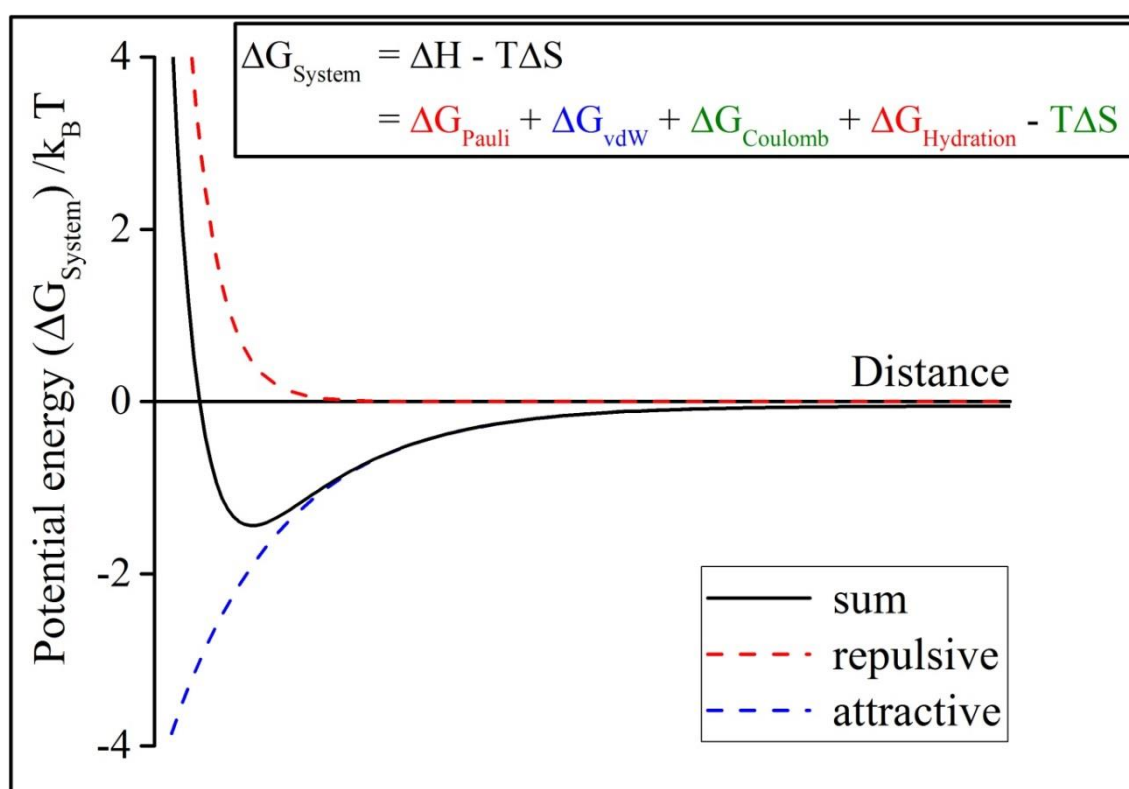


Figure 7. Decomposition of the Gibbs free energy of a typical colloidal system. The Gibbs free energy is given in units of $k_B T$ and plotted against the distance.

Depending on the physical properties of the components in the system, the potential energy can exhibit one or more minima. Like mentioned before, the energy to remove the system from this minimum is in the order of $k_B T$. This energetic equilibrium is expressed at the mesoscale. At smaller size scales, quantum effects will dominate the behavior whereas at bigger size scales macroscopic forces like gravity are more important. Thus, typical examples of this kind of systems include polymers, colloids, amphiphiles, liquid crystals and biological macromolecules. This concept was first introduced in the DLVO-theory to explain colloidal suspensions and their interacting forces, namely electrostatics and van-der-Waals forces.⁵⁴ Nowadays, the system has been refined to explain, for

example, surfactant-free microemulsions by the consideration of hydration and entropy.⁵⁵ **Table 1** lists several examples of repulsive and attractive interactions that can occur between mesoscale objects.

Table 1. Some examples of interactions that contribute to the Gibbs free energy, their direction and their distance dependence (r).

Name	Direction	Distance dependence of the energy
Electrostatic	Attractive (+/-) Repulsive (++, --)	$\exp(-r)$
Van-der-Waals	Attractive	r^{-6} (London) r^{-6} (Keesom) r^{-6} (Debye)
Pauli repulsion	Repulsive	r^{-12}
Hydration	Molecule/ surface dependent	$\exp(-r)$
Entropy	System dependent	

All the interactions contribute to the Gibbs free energy. Repulsive contributions (red in **Figure 7**) have a positive sign while attractive contributions (blue in **Figure 7**) have a negative sign. Some contributions (green in **Figure 7**) change direction depending on the system. In equilibrium, the system is at the state of minimal Gibbs free energy.

The Pauli repulsion and the attractive vdW-interactions are unidirectional. The Pauli principle excludes the presence of two objects at the same position. The interaction energy scale with r^{-12} and, thus, leads to a hard barrier compared to other interactions. The vdW interaction energy scales with r^{-6} . It includes London (induced dipole-induced dipole), Keesom (dipole-dipole) and Debye (dipole-induced dipole) interactions. Depending on the system, one or multiple of the contributions apply. The London forces always apply because they depend on the spontaneous dipoles that are formed by electron displacements around the atomic nucleus. Keesom and Debye interactions only apply when molecules with a permanent dipole are present. Consequently, both depend on the dipole moment. Additionally, Debye forces depend on the polarizability of the second molecule that will form the induced dipole. Next, electrostatic interaction energies decay exponentially with distance. Trivially, same charges are repulsive whereas opposite charges are attractive. This can be used to stabilize colloidal systems or to create strong interactions between different species. The dielectric constant of the surrounding solvent

($\epsilon_r \cdot e_0$) mentioned in Eq (1) has an influence on the decay length of the electrostatic interactions. When ϵ_r increases, the range of electrostatic interactions increases. The reason for the dielectric constant is the orientation of solvent molecules in the direction of the electric field. With increasing dipole moment, the dielectric constant increases. The charge is partially compensated with every layer of solvent surrounding it. In real systems, charges always occur in combinations with, at least, their counter-ions. Oftentimes, additional electrolytes are present in the solution. In any case, many factors (solvent, colloid surface charge density and polarity, counter-ion valence and charge density) are responsible for a high variability of ion-counter-ion interactions in colloid systems.^{56,57} Excluding ion-specific effects, a double-layer model describes the behavior of electrolytes close to charged interphases. the behavior of electrolytes close to charged interphases is described by a double-layer model. Here, oppositely charged ions will adsorb directly to the surface which will form the inner Helmholtz plane. Then, solvated ions will be closely attached to form the outer Helmholtz plane. Those ions are considered strongly bound to the interphase. The electric potential decreases linearly in the double layer. Afterwards, the system can be treated as a bulk phase and the classical exponential decay is observed.⁵⁸

Another repulsive force is hydration. It describes the energy needed to remove water from an interaction partner. Mathematically, it follows an exponential decay with distance.

$$\frac{\Delta G_{Hydration}}{V} = \Pi = \Pi_0 \exp\left(-\frac{r}{\lambda}\right) \quad (3)$$

Here, $\Delta G_{Hydration}$ is the Gibbs energy contribution from hydration, Π the hydration pressure, Π_0 the standard hydration pressure, r the distance and λ the decay length which for water is typically around 0.23 nm⁵⁹(layer thickness in the hydration shell). The standard hydration pressure depends on molecular characteristics. When the interactions between the hydrated species and water are strong (*e.g.* H-bonding), Π_0 takes a high value. Water has a considerable influence on the organization of mixtures on the molecular and mesoscale due to the strength of its interactions with other polar groups.

Lastly, entropy contributes to the Gibbs free energy. The entropy of a system state is a function of the number of possible combinations W by which the state can be realized.

$$S = k_B \ln(W) \quad (4)$$

Here S is the entropy and k_B the Boltzmann constant. At a molecular scale, it is highest in ideally mixed states where molecules have the highest degrees of freedom. However, entropy can be “bought” by enthalpic terms. In other words, interactions which are sufficiently strong counterbalance entropy. This relation is expressed using the Gibbs free energy G .

$$\Delta G_{system} = \Delta H_{system} - T\Delta S \quad (5)$$

Entropy can be attractive, for example, in the case of charged surfaces with counter-ions. Here, the merging of the charged surfaces expulses the counter-ions in the bulk because the ions have more degrees of freedom. In the case of neutral surfaces, entropy favors the dispersion of the system. This phenomenon is known as “depletion force”. In emulsions, entropy leads to the dispersion of the system and to smaller structures. The evaluation of the entropic term is never trivial and must be investigated case by case.

When surface active molecules (“surfactants” or “hydrotropes”) are present in the system, the Gibbs free energy minimum is oftentimes found in a structured state. This process is called self- or auto-assembly. In the following, the potential forms of organization will be presented.

3.2 Auto-assembled structures

Auto-assembled structures are obtained when a critical concentration of amphiphilic molecules in solution is reached. The amphiphilic molecules can be classified by the gain of free energy upon structure formation. Consequently, a higher gain of free energy leads to structures that are more stable on the time scale and structurally better organized. **Table 2** shows the different classes of amphiphilic molecules by descending free energy gain of structure formation in water.⁶⁰ The transition between classes is continuous.⁶¹

Table 2. Classes of amphiphilic molecules and self-assembly characteristics.

Class	Appearance	Free energy gain of structure formation per amphiphilic molecule	Particularities
Surfactants	Long chain amphiphilic molecules, highly hydrophilic headgroup (SDS)	Several $k_B T$	Structuring following packing parameters, liquid crystal phases
Hydrotropes	Short chain, bulky amphiphiles, highly hydrophilic headgroup (SXS)	1-2 $k_B T$	Structuring increases upon solute addition above the MHC
Co-solvent + solute	Short, uncharged amphiphiles (ethanol, <i>tert</i> -butanol) + hydrophobic solute	$\sim 1 k_B T^{55,62}$	Strongly fluctuating aggregates around a network of H-bonds ⁶² , stronger structuring near demixing conditions
Co-solvent	Short, uncharged amphiphiles (ethanol, <i>tert</i> -butanol)	$< 1 k_B T$	Unstructured to weakly structured fluctuating solutions ⁶³

The first example is the class of surfactants. Above a concentration called “critical micelle concentration” (cmc) they auto-assemble to defined aggregates. The object shape is directed by the packing parameter N_S .^{29,64} An overview is given in **Figure 8**.

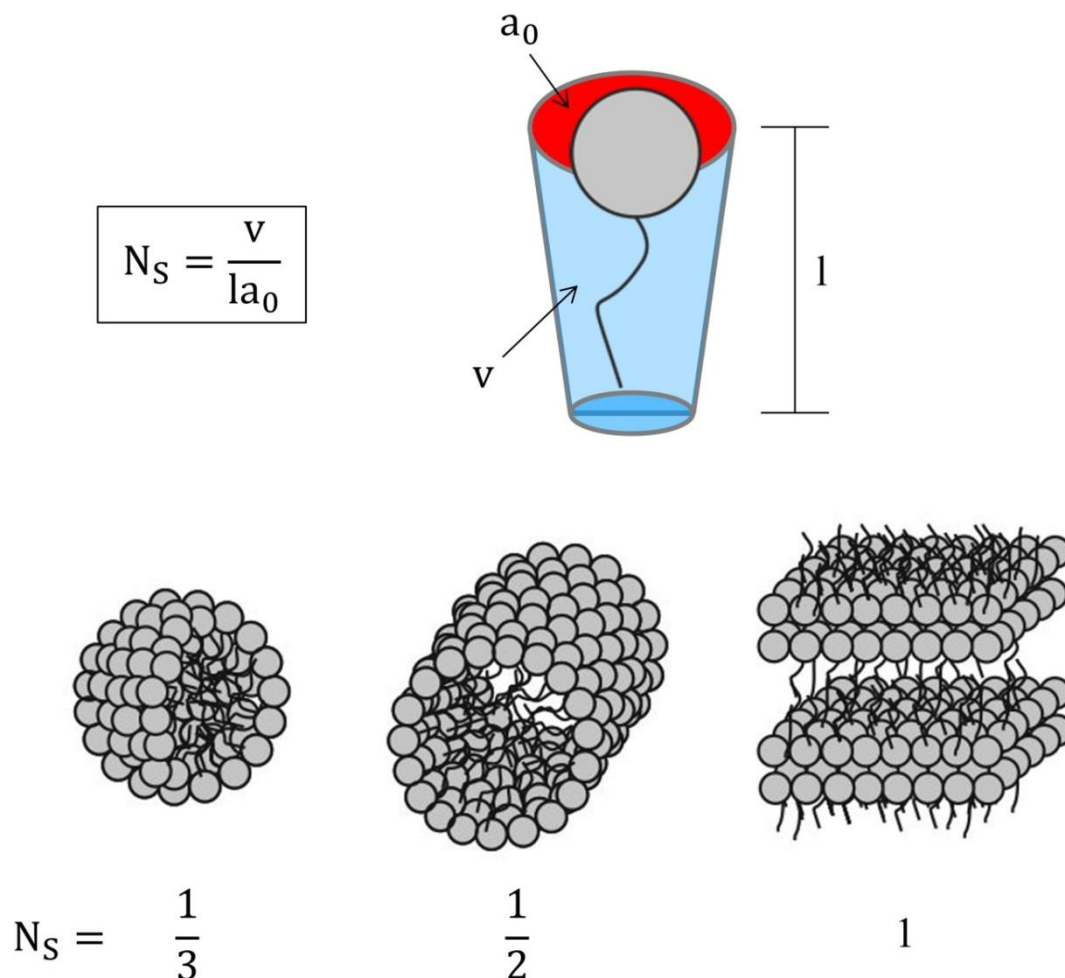


Figure 8. Packing parameter of surfactant molecules and the resulting morphologies of the self-assembled structures.

Approximating the shape of the aggregate forming molecules by a cone, N_S is defined as the volume v of the hydrophobic part divided by the length l of the hydrophobic chain and the apparent surface a_0 of the hydrophilic headgroup. The densest arrangement of those cones results in the obtained structure. Low packing parameters lead to spherical aggregates. As N_S increases, cylindrical and lamellar shapes are obtained. At high surfactant concentration or strong interactions between the aggregates, the formed structures organize on larger scales. These supramolecular structures are called liquid crystal phases.²⁹

Hydrotropes represent the second class of amphiphiles. They only aggregate in certain cases in binary mixtures with water. However, aggregation can be induced by the addition of a hydrophobic solute above the minimum hydrotrope concentration. The aggregates are without defined shapes.⁶⁰

Co-solvents are the third example of amphiphiles. Typically, they are fully miscible with water. The examples include the series of fully water-miscible alcohols: methanol, ethanol, *iso*- and *n*-propanol, and *tert*-butanol. The structuring in solutions that contain

co-solvents depends strongly on the other components of the system and the co-solvent itself. In the case of the classic co-solvent ethanol (EtOH), no structuring is observed in the binary mixture with water. Upon the addition of a hydrophobic solute, weak structuring can be observed. The structuring increases when approaching the demixing conditions.⁶² *Tert*-butanol, on the other hand, has strong hydrotrope-like characteristics. Structuring in binary aqueous mixtures is observed for certain compositions. Whatever the co-solvent, the addition of a hydrophobic solute increases the structuring.⁶³

By performing the sol-gel process in any of the mentioned structured media, the obtained silica morphology can be modified. The structures can function as micro reactors. This way, controlled release of a reactive species or confined growth inside the structures is possible.^{65,66} In particular, surfactants are used as templating agents for structured silica materials. The high free energy gain of the formed micellar and liquid crystal structures dominates the supramolecular structure of the system during the formation of the silica matrix. The next section details the application of these principles for the elaboration of organized silica materials.

4 Structured silica materials

4.1 The porosity of silica materials

One form of organization of SHMs is porosity. It is an omnipresent material property that can occur on one or more of the levels illustrated in **Figure 9**.⁶⁷

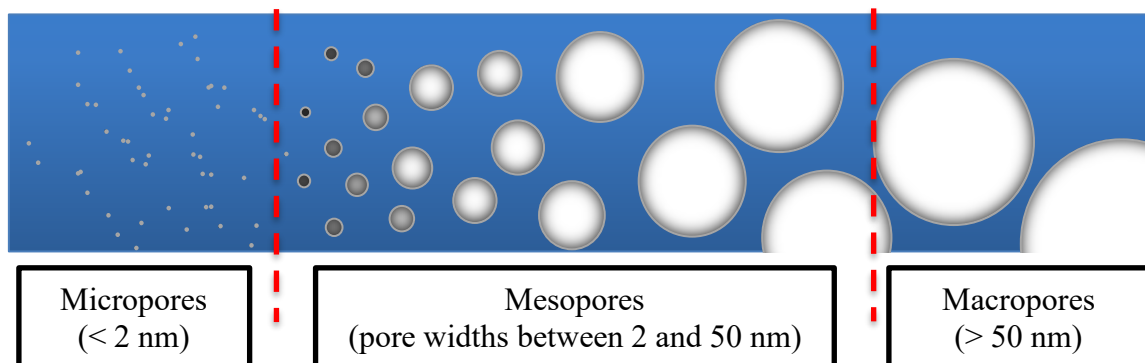


Figure 9: Porosity in different scales as recommended by IUPAC.⁶⁷

Depending on the functioning of the material, the size scale of porosity is important. For gas separation and storage or heterogeneous catalysis microporous materials like MOFs or Zeolites are of interest.^{68–70} Macroporous materials, on the other hand, have properties that are of interest for tissue engineering or microfluidics.^{71–73} For mesoporous SHMs that are treated in this work, applications are manifold. Polymers like tire rubber are reinforced using small amounts of mesoporous silica to augment physical properties. Stationary phases of high-pressure liquid chromatography make use of the high porosity of those materials to obtain good separations. For this application, the surface can be modified to create normal or reverse phases. Surface modification can also be used to graft catalysts or bioactive molecules on the material surface. For the latter, it is important to note that SiO_2 is inert in physiological conditions and non-toxic. This makes mesoporous silica nanoparticles attractive candidates for drug delivery systems.⁷⁴ Furthermore, mesoporous silica materials can serve as hard template for carbon materials. After templating, the silica matrix is leached by HF .⁷⁵ Another aspect is the separation of metal ions from liquid phases by adsorption at the material surface (solid-liquid extraction). The size of mesopores allows the incorporation of functional groups to achieve extraction selectivity.⁷⁶

The first reported synthesis of organized mesoporous silica was performed in 1969.⁷⁷ Since the effective commercialization of MCM-41^{78,79} by the Mobil Oil Company, silica materials with organized porosity have become an essential part in material research. They can be the object of study⁸⁰⁻⁸², synthesis tool for material production⁸³⁻⁸⁵ or model reaction media to study confinement effects.⁸⁶⁻⁹⁰ Ordering of the structure is achieved by the use of template molecules which are often self-assembling surfactants. The underlying mechanism is proposed to be initiated by a cooperative liquid crystal formation of surfactant structures with the growing silica matrix.^{52,76,91-93} The interactions between silica and the template structure can take place *via* electrostatic forces or hydrogen bonding.⁵² The synthesis of MCM-41, for example, requires the use of a cationic cetyl trimethylammonium bromide (CTAB) with a polymerization in alkaline conditions. This creates strong electrostatic attractions between the negatively charged silica matrix and the positively charged surfactant. The structure is tunable by the modification of the reactant stoichiometry⁹⁴, the surfactant geometry, reaction conditions and post-synthetic treatment.⁵²

Next to auto-assembled surfactant aggregates, alternative templating methods exist. Foams^{72,95}, pickering emulsions⁹⁶ and hard templates^{97,98} are effective to control structural organization. By the combination of different methods, even hierarchical porosity (i.e. combined macro- and mesoporosity) is obtainable.

4.2 Controlling the bulk structuring of SHMs

The second form of structural organization of SHMs are nanostructured organosilicas. They are solid phases that can be tailored by modifying the precursor molecules and their ratios.⁹⁹ Depending on the number of non-hydrolyzable groups on the tetra coordinated silicon, the synthesized materials are called silicates (SiO_2), silsesquioxanes ($\text{R-SiO}_{1.5}$) or siloxanes ($\text{R}_2\text{-SiO}$). Originally developed to incorporate organic functional groups into the walls of porous materials¹⁰⁰⁻¹⁰², the modification of the type of structuring and the periodicity has become a large field of interest.¹⁰³⁻¹⁰⁷

The most fundamental example is the self-assembly of long-chain alkyltrialkoxysilanes. The organization of single (α) and double (α, ω) silylated molecules was investigated.¹⁰⁸⁻¹¹⁰ After hydrolysis, these precursors become amphiphilic and are able to form lamellar or 2D hexagonal structures depending on the alkyl chain length. When conjugated, rigid precursor are used, the mesostructured is directed by vdW interactions.¹¹¹ However, no functional groups were present in these materials.

The introduction of functional groups has been widely investigated in literature.¹¹²⁻¹¹⁶ By the introduction of urea groups, H-bonding can be used to increase the long-range order.¹¹⁷ In a bioinspired approach¹¹⁸, the long-range order was improved by profiting

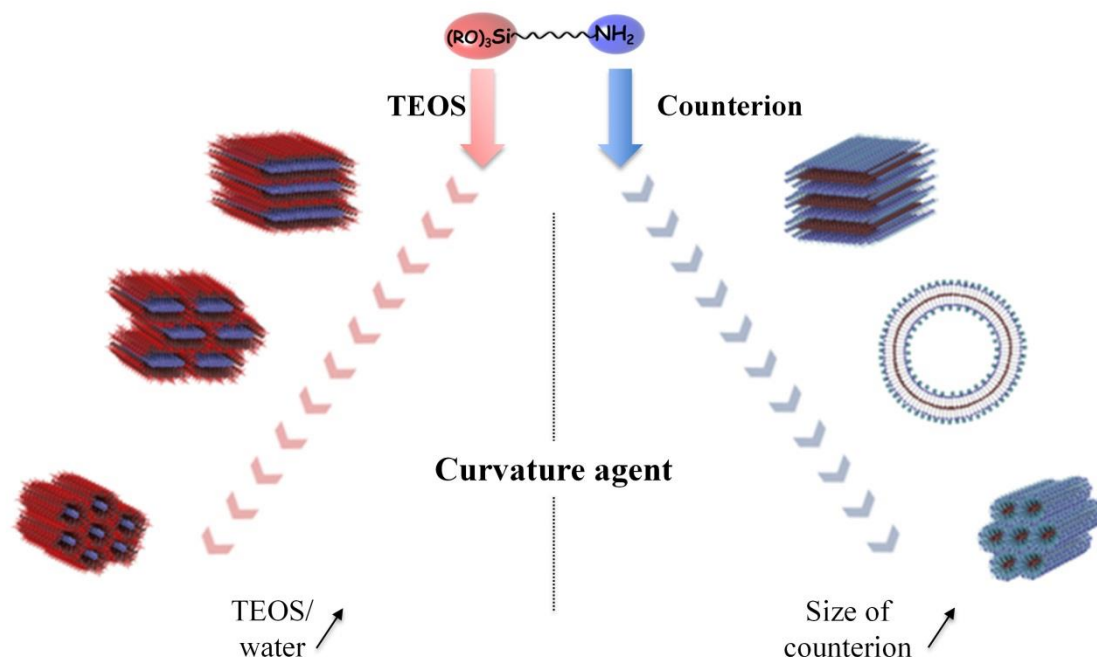


Figure 11. Material morphologies obtained by Romain Besnard *et al.* The curvature of the self-assemblies of the investigated molecule 11-aminoundecyltriethoxysilane was tailored using TEOS or counter-ions.¹⁰

First, the effect of pH and heat treatment on the morphology was investigated.¹¹⁹ In pure water, regardless of the pH, this organosilane precursor organizes to form lamellar structures with varying degrees of order. From HCl containing solutions, an ammonium chloride phase is formed upon drying between the amino headgroups. This ensures the lamellar structure upon annealing at 120 °C. From NH₄Cl containing solutions, a part of the amino groups will react with dissolved CO₂ to form a carbamate. The remaining, now protonated ammonium groups favor a pairing with the carbamate groups which leads to lamellar organization. Contrarily to the ammonium chloride phase formed under acidic conditions, this motive is not thermally stable. Its CO₂-releasing decomposition above 80 °C leads to an amorphisation of the overall material.

In a further study, the focus was on the effect of the counter-ion size under acidic conditions.¹²⁰ Like in the earlier study, under acidic conditions, an ion pair is formed by the protonated amino group and a deprotonated acid. Here, HCl was replaced by different organic acids of increasing size. Using sterically demanding organic acids, it was possible to increase the apparent headgroup size a_0 . This decreases the packing parameter N_S (see **Figure 8**) and modifies the curvature of the resulting aggregates. With bigger acids, 2D hexagonal structures were achieved. The results are in agreement with the calculated packing parameter of the ion paired organosilane precursor.

In another work, the effect of additional TEOS on the curvature was investigated.¹²¹ By increasing the TEOS/water ratio in the alkaline starting sol, the originally lamellar structure is swollen. Ultimately, this leads to reverse 2D hexagonal phases with the functional group on the interior of the structures.

In order to investigate the influence of the solvent and the catalysis on the morphology and the TEOS incorporation, the material syntheses using all previously examined curvature agents with different amounts of TEOS in water or THF were compared.¹²² It was found that the morphology of the materials synthesized in aqueous solution is strongly influenced by the emulsion formation in the system water/AUT/TEOS. When using THF, the material morphology is homogeneous and similar for all investigated conditions because all components are soluble. Concerning the chemical composition, under aqueous conditions, whatever the catalyst, the quantity of incorporated TEOS increased linearly with the TEOS/AUT ratio. For THF, under basic conditions, even at low TEOS/AUT ratios, unexpectedly high quantities of TEOS are incorporated. As the TEOS/AUT ratio increases the incorporation stagnates to reach the same quantity as under acidic conditions. This difference was attributed to varying reaction kinetics due to a changing catalytic activity in the two solvents.

Finally, since all of the produced materials are non-porous bulk phases, the accessibility of the functional groups was tested. To this end, palladium and platinum salts were introduced *via* dissolution in water into a freshly synthesized lamellar AUT material.¹²³ After reduction of the metal salts, homogeneously dispersed metal nanoparticles were found in the morphologically unaltered material. Furthermore, it was possible to quantitatively modify all amino groups in a freshly synthesized lamellar AUT material by ring-opening reactions in THF.¹²⁴ The material morphology remained after the modification. The obtained materials were successfully employed in solid-liquid extractions of REEs and iron. Both studies prove that all functional groups in the material are accessible in solution.

The present PhD thesis is based on the previously obtained results and will further develop the material synthesis while keeping the concept of an “all-in-one” approach in mind with the aim to provide SHMs with functional groups as easily accessible as possible to improve the application.

5 The scientific approach

While being easy in workup and upscaling, the previously reported SHM synthesis by polymerization of functionalized organosilanes has some disadvantages. First, they are dense solid phases. Therefore, they do not show any specific surface area. This disadvantage is negligible in solution because the functional groups are still accessible. However, when looking for different applications like i.e. CO₂-fixation by amines, the functional groups must be accessible by simple gas diffusion into the dry material. Second, the method of tuning the material morphology developed earlier only applies to amine functionalized precursors.¹²⁰ In order to tailor the morphology when using different functional groups, other methods need to be investigated. Third, the accessible structures are severely restricted because of the lack of inorganic matrix volume. In other words, structures with strong curvature are difficult to obtain because of the molecular geometry of the precursor.

To solve these problems, the scientific approach of the present work consists in three concepts:

- i. The incorporation of a manifold of functional groups into the organoprecursor to avoid post-grafting. The method of choice is Click-chemistry. This method is well described in literature and applicable to the restricted synthesis conditions due to the presence of the silane moiety. This is further developed in the chapter “Organic synthesis”
- ii. Without an amino headgroup the approach developed earlier fails. Another method has to be found to tailor the curvature of the silica material. **Figure 12** illustrates the proposed method.

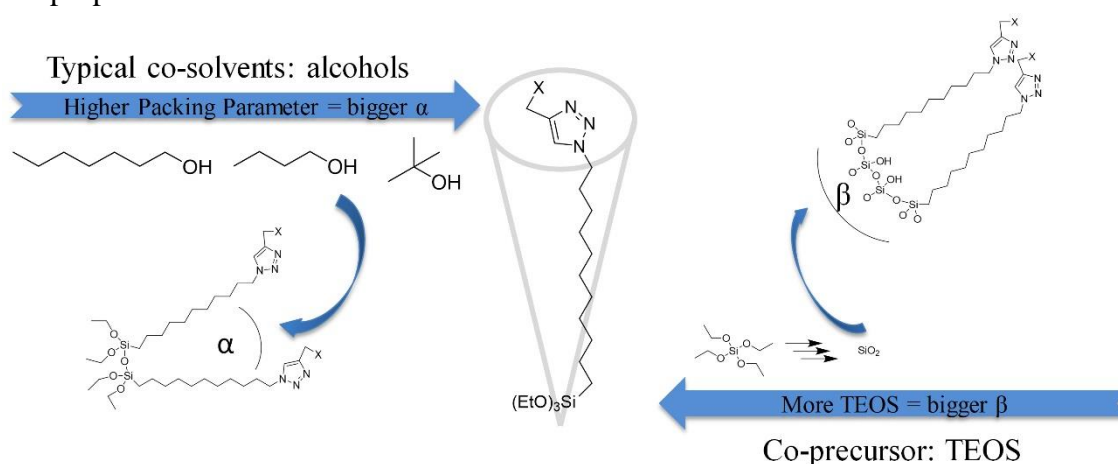


Figure 12. Impact of co-solvent or TEOS addition on the angle between two connected organosilane precursor molecules.

Relying on the theory of changing the shape of self-assembled objects developed for surfactants, a universal method to change the method is envisaged. Co-solvents can penetrate between alkyl chains and act as space holders. Bulky co-solvents lead to

stronger effects than long and linear co-solvents. TEOS has the inverse effect by reacting around the silane headgroup of the surfactant-like organosilane. In this way, it creates open spaces between the alkyl chains. Consequently, they will approach each other due to hydrophobic effects.

iii. In order to completely understand the interactions in systems with multiple components, it is necessary to understand the interactions between all of its components. Considering the concept ii., the starting solution contains four components: water, the organosilane precursor (OP), a co-solvent (CS) and TEOS. **Figure 13** depicts the four components (blue ellipses) and the systems that can be constructed with them. In this way the strategy followed in this thesis is outlined.

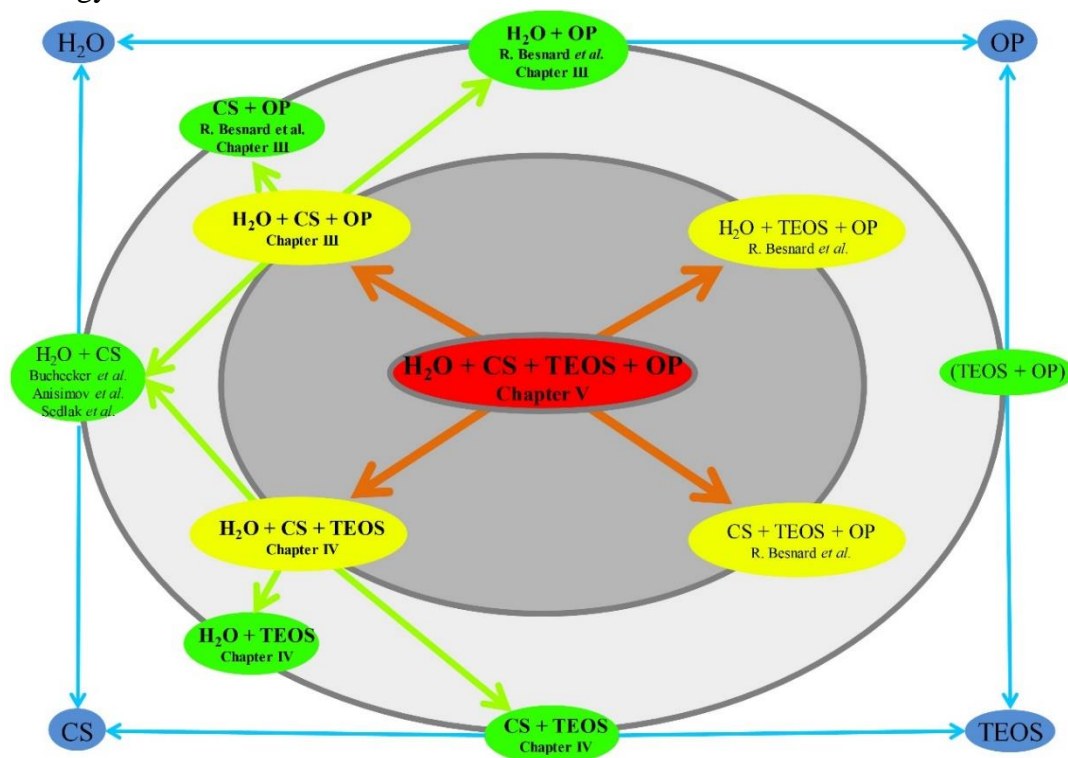


Figure 13. Splitting of the quaternary system water/co-solvent(CS)/TEOS/organosilane precursor(OP) into the ternary and binary subsystems. The relations are indicated by the arrows. The description of the ellipses indicates the literature or chapter number where the corresponding results can be found.

The strategy proposed in this work ultimately aims to understand the quaternary mixture of the four components (red ellipse). The quaternary mixture can be broken down into four ternary compositions (yellow ellipses). In turn, each of the ternary compositions can be broken down into three pairwise interactions (green ellipses). The ternary and binary systems can be divided into systems with or without OP. The systems containing the OP were already investigated by Romain Besnard *et al.*¹⁰ for AUT in water or THF. For comparability, in chapter III of this work, the polymerization of the newly synthesized OPs is studied in the same solvents. The ternary composition without the OP is based on the structuring observed in binary mixtures of water and *tert*-butanol. Considering the results from literature, the sol-gel process in these mixtures is evaluated in chapter IV. Finally, chapter V explores the materials synthesized from the quaternary mixture

II ORGANIC SYNTHESIS

1 Crucial synthetic methods

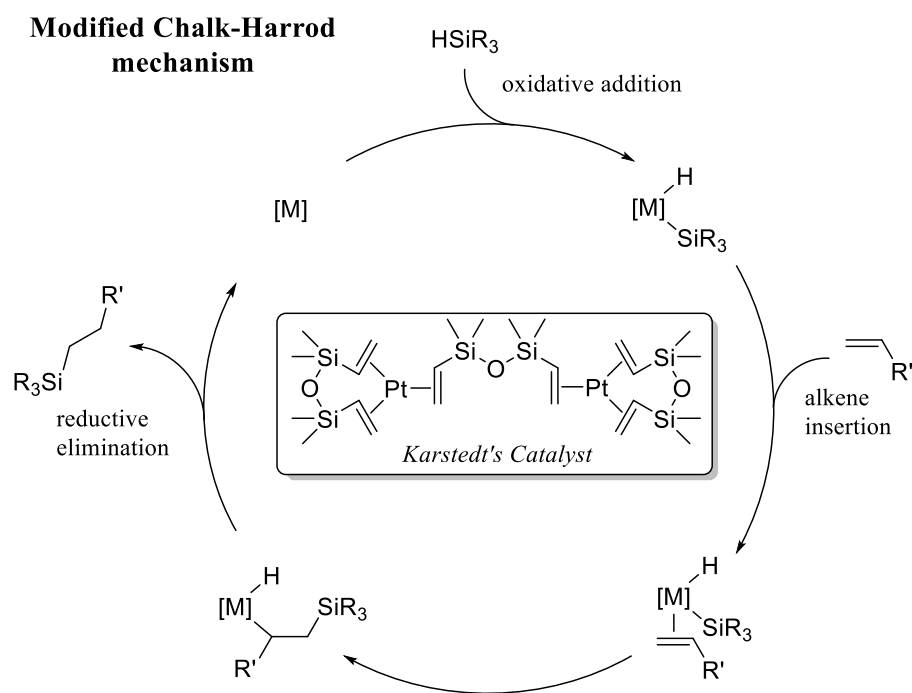
Organic synthesis lays the foundation for the “all-in-one”-approach used in this dissertation. This section will give an overview over the chemistry of the employed molecules.

1.1 Synthesizing organosilanes

The “all-in-one”-approach requires precursors that contain a polymerizable silane (i.e. alkoxy silane) and an organic moiety that offers the desired properties. Molecules where silicon and carbon are simultaneously present are called organosilanes.¹²⁵ The connection between silicon and carbon can be a direct bond or, for example, *via* a bridging oxygen atom. Organosilanes are unavailable from natural resources and must be synthesized. Important milestones towards the nowadays large abundance of synthetic methods are:

- 1823: Preparation of SiCl₄ by Berzelius¹²⁶
- 1863: Synthesis of Si(Et)₄ by Friedel and Crafts¹²⁷
- 1945: Discovery of the direct process synthesizing organosilanes using a copper catalyst from chlorosilanes¹²⁸
- 1946: Hydrosilylation by oxidative addition to C-C multiple bonds¹²⁹ and later (1957) by transition metal catalysis¹³⁰
- 1973: Development of the Karstedt’s catalyst¹³¹

Several methodologies are available to introduce the trialkoxysilyl groups: nucleophilic substitutions on halogenopropyltriethoxysilanes, the coupling of isocyanatopropyltriethoxysilane with amines, Heck cross coupling between an aryl halide and vinyltriethoxysilane, the rhodium-catalyzed silylation and the hydrosilylation of olefins are some of the most developed methods.¹³² Nonetheless, Karstedt’s catalyst remains to date one of the most important references for catalyzed hydrosilylation reactions.^{133,134} The catalyst complex and the catalytic cycle are displayed in **Scheme 3**.



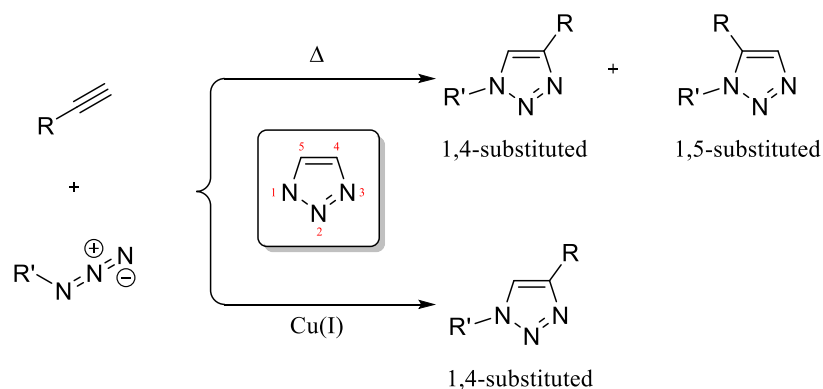
Scheme 3. Modified Chalk-Harrod mechanism (redrawn from literature¹³⁵)

The catalytic cycle starts with the oxidative addition of a trialkoxysilane to the catalyst. Then, the alkene is inserted into the complex. The insertion can be visualized by a four membered transition state consisting of the two carbon atoms of the alkene, the metal atom and one further ligand. In the present case, only the states leading to the desired product are drawn. It is possible that the insertion takes place at different positions and/or involving the added hydrogen atom. However, the reversible character of the reaction favors the insertion at the position leading to the *anti*-Markovnikov product. In the presented mechanism, the catalyst is recovered after the reductive elimination of the desired product. In reality, a multitude of side products are usually obtained including vinyl silanes (β -elimination), silane side products and combinations of the introduced alkene. Side product formation can be reduced and directed by the stoichiometry and ligand choice.¹³⁶

An exhaustive literature exists on this topic thanks to the large substrate scope and excellent performance.^{136,137} For the purposes of this work, it is sufficient to note that the reaction preferentially leads to the *anti*-Markovnikov product and that amines and alcohols should be avoided because they provoke side product formation.^{138,139} Taking this into consideration, the hydrosilylation using Karstedt's catalyst seems to be the ideal approach for the precursor synthesis. Considering the limitations of the reaction conditions related to the presence of the introduced silane group, we envisaged to use the Click-chemistry as synthetic tool to obtain the organosilane precursors.

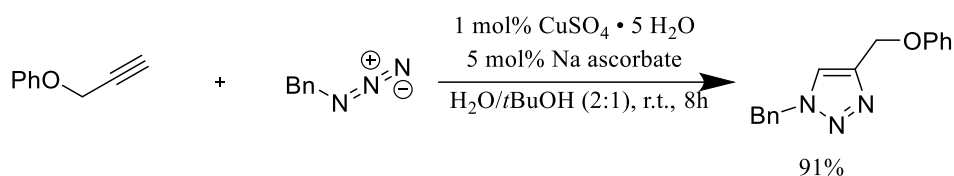
1.2 The multi-functional tool “click-chemistry”

The term “Click-chemistry” designates a class of reactions where two molecules are ideally coupled with a wide scope, few byproducts, stereospecificity to a single reaction product in high yield.¹⁴⁰ This definition by Sharpless *et al.* did not exist when Huisgen pioneered the 1,3-dipolar cycloaddition of alkynes and azides.¹⁴¹ His reaction produced a mixture of 1,4 and 1,5 substituted 1,2,3-triazols at harsh reaction conditions (toluene as solvent, high temperature).¹⁴² Since then, the reaction conditions have been refined¹⁴³ and new catalysts based on ruthenium^{144,145} (selective 1,5-product) or silver¹⁴⁶ were developed. Advances, especially in the field of biochemistry, lead to the discovery of copper(I) as a suitable catalyst for a selective synthesis of the 1,4-product (see **Scheme 4**).^{147–149}



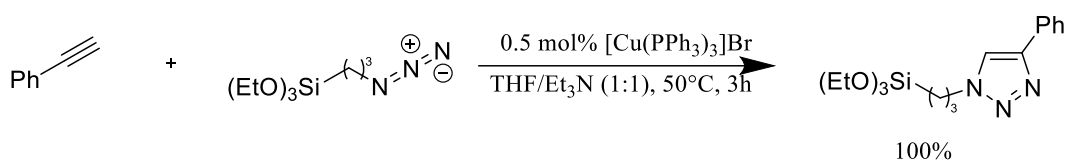
Scheme 4. Stereoselectivity of the 1,3-dipolar cycloaddition induced by heating or copper(I) catalysis.

This reaction, termed “Copper(I)-catalyzed Alkyne Azide Cycloaddition” (CuAAC) proceeds readily at room temperature and in benign solvents covering a seemingly unlimited scope of reactants.^{150,151} Its remarkable efficiency made it the exemplary model of Click-chemistry.



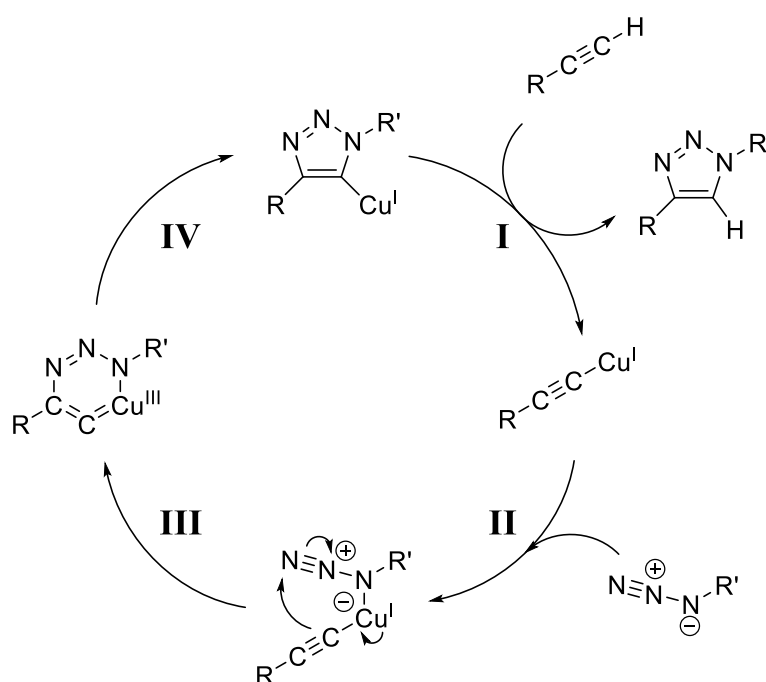
Scheme 5. Pioneering CuAAC as published by Vsevolod *et al.*¹⁴⁸

While the required Cu(I) species were first generated *in situ* by the addition of reducing agents. Adding these easily oxidizable compounds also stabilized the catalyst against oxidation by oxygen (see **Scheme 5**). The limited solubility of inorganic salts in organic solvents led to the development of more soluble copper(I)-complexes.^{152,153} The reaction was optimized further by using an amine source to increase the reactivity of the alkyne by deprotonation.¹⁵⁴ An example of such an improved reaction is shown in **Scheme 6**.



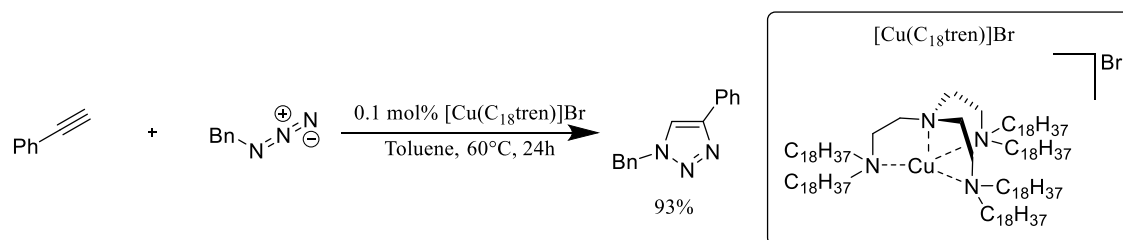
Scheme 6. Example of a water-sensitive CuAAC using a readily soluble Cu(I) catalyst published by Moitra *et al.*¹⁵³

Contrarily to the simplicity of the application, the catalytic mechanism, to date, remains subject of discussion.¹⁵⁵ Different mechanisms have been proposed and are supported by experimental evidence. First publications assumed a mononuclear catalysis by copper. Later, Worrel *et al.* proved that the σ -copper acetylide does not react with the azide in the absence of a supplementary copper source indicating a binuclear mechanism.¹⁵⁶ This was further supported by theoretical studies.¹⁵⁷ In more recent publications, however, a mononuclear mechanism with an activated copper-azide bond is proposed.¹⁵⁸ The initial mononuclear mechanism proposed by Sharpless *et al.* is shown in **Scheme 7**.¹⁵⁹



Scheme 7. Mononuclear mechanism of the CuAAC as initially proposed by Sharpless *et al.*¹⁵⁹

Studies on polydentate ligands like triaminoethylamine (tren) and its derivatives, which are unable to catalyze *via* polynuclear mechanisms due to steric hindrance, clearly support the sufficiency of a mononuclear mechanism (see **Scheme 8**).^{160–162} It should be noted that derivatives of copper-tren complexes possess the advantage of being easily recyclable.



Scheme 8. Exemplary CuAAC by $[Cu(C_{18}tren)]Br$ published by Candelon *et al.*¹⁶²

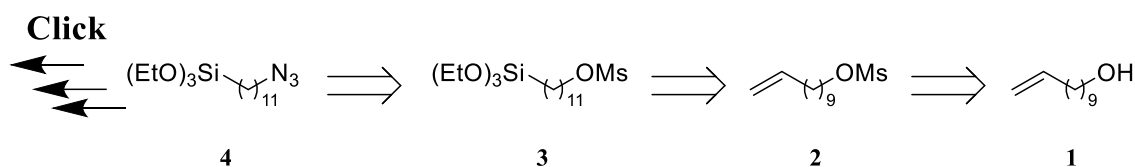
Regardless of the mechanistic details, CuAAC made its way into material and polymer chemistry. In these fields surface and properties modification are important to customize materials for various applications. Especially surface modified porous silica materials have gained tremendous importance because of their chemical inertia and biocompatibility.¹⁶³ Here, a combination of sol-gel processing and CuAAC can be the answer to many synthetic problems. The order of material formation by the sol-gel reactions and functionalization by CuAAC can be changed to adapt to individual needs. In other words, whether a pre-synthesized silica matrix is modified by CuAAC or the sol-gel process is performed using silica-precursors customized by CuAAC is up to choice.^{153,164,165} This is thanks to the high adaptability of the CuAAC click reaction to the sensitivity of alkoxysilanes to water (see **Scheme 6**). Copper catalyzed Click-chemistry, thus, is a perfectly suitable method for the purposes of this work.

2 Results and Discussion

The first part of the present work was entirely dedicated to the synthesis of the required organosilane precursors. In this section, the performed syntheses and their optimization are discussed.

2.1 Retrosynthesis approach

Based on previous work in our institute^{119–122} and the requirement of a readily “clickable” precursor, 11-azidoundecyl triethoxysilane (**4**) is the targeted molecule. The retrosynthesis of **4** is presented in **Scheme 9**.



Scheme 9. Retrosynthesis of 11-azidoundecyl triethoxysilane.

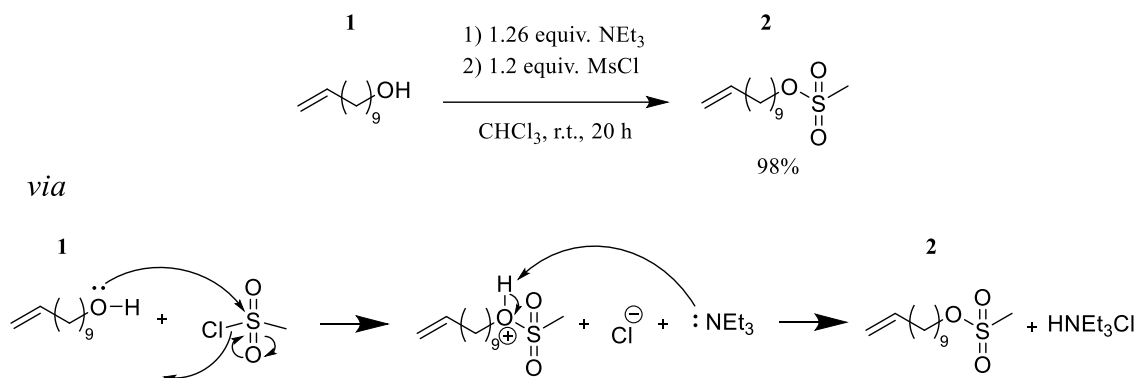
10-undecen-1-ol (**1**) was chosen as starting material for four reasons:

- i) The terminal alkene allows the regioselective introduction of an alkoxy silane group by hydrosilylation.
- ii) The alcohol on the other end of the chain can be changed to other groups by a manifold of different reactions
- iii) The chain length (11 carbons) permits the creation of possibly self-assembling molecules
- iv) The low cost of this molecule compared to its homologues with similar chain length such as 11-bromo-1-undecene

The retrosynthesis was inspired by earlier works and literature.¹⁶⁶ In earlier approaches¹⁰, the synthesis was done *via* the bromination of the alcohol using PBr_3 . This route was abandoned because of the toxicity of brominated compounds. The final functional groups should be introduced as late as possible because of side reactions. In this case, the azide group has priority over the alkoxy silane group and is introduced last because it is easily decomposed at higher temperature and may disturb the Karstedt’s catalyst activity by coordination. Conveniently, the azide formation can be performed under anhydrous conditions in order to avoid the degradation alkoxy silane group. To achieve good yield during hydrosilylation, the alcohol has to be protected *e.g.* by the addition of the methanesulfonyl group (mesylation). This has the additional advantage of creating a good leaving group for subsequent substitution by the azide.

2.2 Azide synthesis

The synthesis of the azide **4** starts with the mesylation of the alcohol present in **1**. The reaction is based on literature.¹⁶⁷ The reaction is shown in **Scheme 10**.

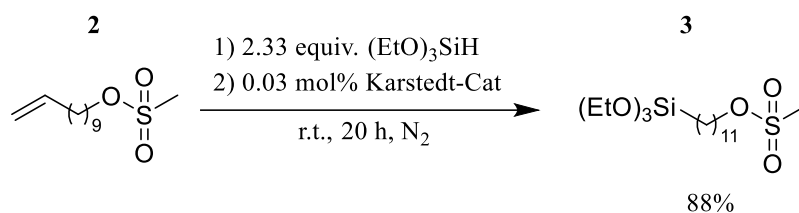


Scheme 10. Nucleophilic substitution of chloride by 10-undecen-1-ol by an addition-elimination mechanism on methanesulfonyl chloride.

Mesylation is a simple and straightforward chemical transformation that results in near-quantitative yields. It is generally conducted by adding methanesulfonyl chloride to a solution containing the alcohol and a non-nucleophilic base to catch the formed HCl. The mesylation has several advantages over the formerly used analogous approach by bromination *via* the Appel reaction.

- The reaction does not include highly toxic phosphorous or brominated compounds
- The yield is superior (74%¹⁰ vs 98%)
- Purification does not require column chromatography
- Only easily disposable waste is produced
- Methanesulfonyl is a better leaving group than the bromide in the follow-up reaction conditions¹⁶⁸

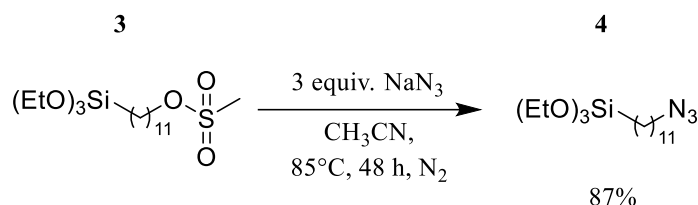
Methanesulfonic acid undec-10-enyl ester **2** is, then, hydrosilylated by a standard procedure using Karstedt's catalyst. The reaction proceeds like described in section II.1.1. (see **Scheme 11**)



Scheme 11. Hydrosilylation of methanesulfonic acid undec-10-enyl ester using Karstedt's catalyst.

Triethoxysilane was chosen as solvent to increase the formation of the desired product 11-methanesulfonic acid undecyl ester triethoxysilane **3**.

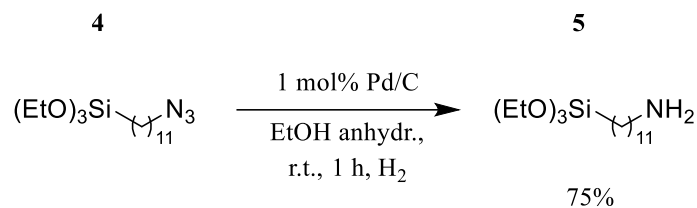
Afterwards, the corresponding azide **4** was obtained in a good yield of 87% *via* the nucleophilic substitution of the mesylate group. (see **Scheme 12**).



Scheme 12. Nucleophilic substitution of the methanesulfonyl group in methanesulfonic acid 11-triethoxysilyl undecyl ester by an azide.

The clickable product 11-azidoundecyl triethoxysilane **4** was obtained in a good yield and purity.

For completion purposes, the reduction to 11-aminoundecyl triethoxysilane **5** will be presented. (see **Scheme 13**) The reaction is inspired from literature.¹⁶⁶



Scheme 13. Reduction of 11-azidoundecyl triethoxysilane to 11-aminoundecyl triethoxysilane by palladium catalysis

Thanks to the replacement of the formerly used Appel reaction by a mesylation the global yield of **5** was doubled. (28%¹⁰ to 56% in four steps)

2.3 Click-Chemistry

The organosilane synthesis *via* CuAAC was optimized by, testing three different catalysts. Of the readily soluble tris-triphenylphosphane copper bromide ($[\text{Cu}(\text{PPh}_3)_3]\text{Br}$, **C1**), the very hydrophobic and recyclable catalyst tris(2-dioctadecylaminoethyl)amine copper bromide ($[\text{Cu}(\text{C}_{18}\text{tren})]\text{Br}$, **C2**) and $\text{CuSO}_4/\text{NaAscorbate}$ (see **Scheme 5**), the latter was immediately discarded because of the high amount of side product in aqueous conditions. The catalyst structures of **C1** and **C2** are drawn in **Figure 14**.

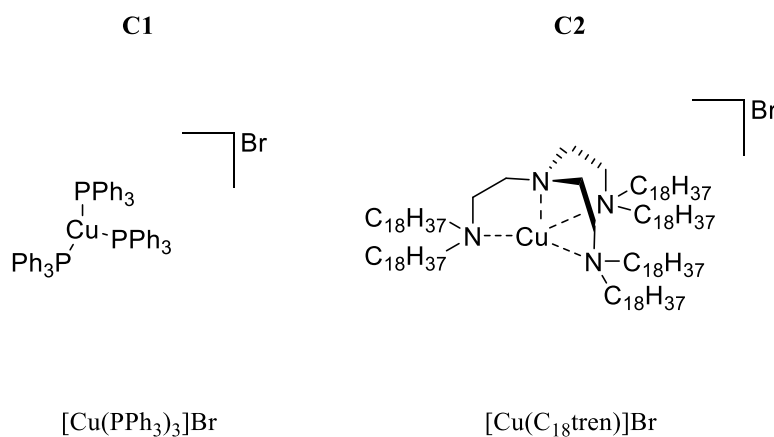


Figure 14: The two catalysts used for CuAAC: tris-triphenylphosphane copper bromide ($[\text{Cu}(\text{PPh}_3)_3]\text{Br}$, **C1**) and tris(2-dioctadecylaminoethyl)amine copper bromide ($[\text{Cu}(\text{C}_{18}\text{tren})]\text{Br}$, **C2**).

In literature, **C2** was demonstrated to be effective in CuAAC type reaction at catalyst loadings between 0.1 mol% and 0.5 mol%.¹⁶⁹ In order to determine the required catalyst loading in the present case, the CuAAC progress of **4** to **P1** was followed. The results are displayed in **Figure 15**.

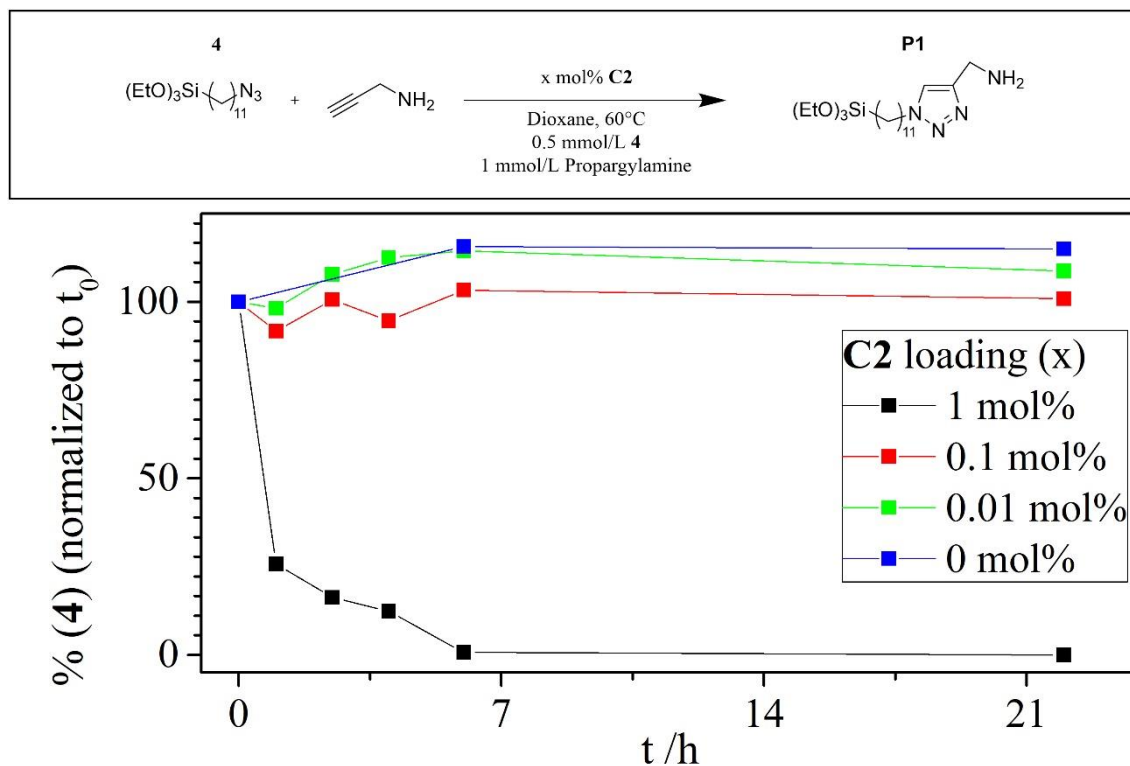
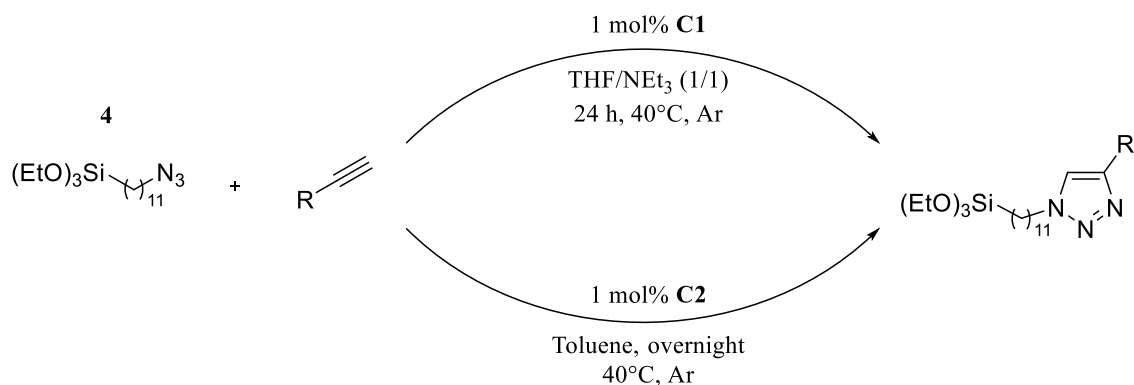


Figure 15: The monitoring of the normalized content of starting material **4** as determined by the internal standard method applied to GC-MS analysis. The inset shows the reaction conditions.

The presence of the starting material **4** was followed *via* GC-MS with dodecane as internal standard. The reaction was performed without catalyst and catalyst loadings of 0.01, 0.1 and 1 mol%. Under the observed conditions, the starting material is only consumed in presence of a catalyst loading of 1 mol%. Here, after 7 h no starting material was found. For all other samples, including the reference that contained no catalyst, no consumption of **4** was found. It is concluded that, for the present reaction, at least 1 mol% of catalyst has to be employed. In order to assure complete conversion, in the following, reactions are left overnight.

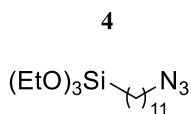
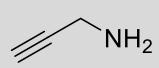
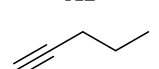
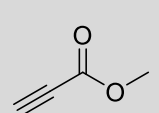
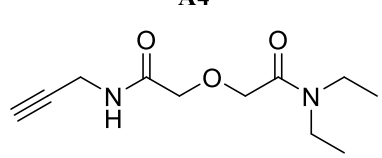
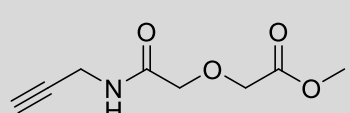
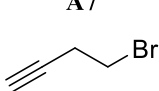
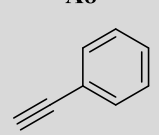
In order to compare the catalytic performance of **C2** to that of **C1**, a required catalyst loading of 1 mol% and a temperature of 40 °C were chosen. Toluene is chosen as solvent for **C2** because of the superior solubility of the catalyst at this temperature. An overview of the employed conditions is shown in **Scheme 14**.



Scheme 14. Reaction conditions of the investigated CuAAC.

C1 requires the addition of triethylamine to increase reactivity (see **II.1.2**). **Table 3** displays the results obtained for different alkynes. The synthesis of the alkynes **A4** and **A5** is described in the appendix.

Table 3: Substrate scope of the CuAAC using either [Cu(PPh₃)₃]Br (C1) or [Cu(C₁₈tren)]Br (C2). The synthesis of molecules A4 and A5 can be found in the appendix.

Azide	Alkyne	Yield	
		C1	C2
<p>4</p> 	<p>A1</p> 	81%	97%
	<p>A2</p> 	74%	89%
	<p>A3</p> 	/	90%
	<p>A4</p> 	50%	99%
	<p>A5</p> 	/	76
	<p>A7</p> 	66%	/
	<p>A8</p> 	31%	73%

The catalyst [Cu(C₁₈tren)]Br (**C2**) has shown superior yields in all cases. This can have several reasons. Toluene is less likely to contain higher amounts of trace water than THF or NEt₃. Traces of water can start the hydrolysis and condensation of the alkoxy silane which will be removed as precipitate with filtration. A temperature of 40 °C accelerates this process. Furthermore, the degradation of the catalyst by the oxidation of the phosphines¹⁷⁰ may reduce the activity. Finally, the work up of reactions using **C2** is easier and does not involve filtration using hygroscopic celite®. This minimizes the risk of introducing product degrading water. On another note, products synthesized with **C2** appear to contain less copper traces than those synthesized with **C1**. The products are generally of an almost colorless aspect while those synthesized with **C1** are slightly green. This is especially remarkable with products that have complexing properties (*e.g.* amine). The polydentate character of tren-ligands is the reason of this behavior. Generally, polydentate ligands form more stable complexes than their monodentate counterparts. The catalyst [Cu(C₁₈tren)]Br (**C2**), thus, is the better choice of catalyst for the synthesis of the required sol-gel precursors.

3 Conclusion

In this chapter, the synthetic route to organosilanes precursor molecules is described. The detailed protocols are given in the Appendix (see **1**). The synthesis of the “clickable” molecules was optimized and described. Here, a method to produce the azide **4** in a fairly good yield is elaborated and the synthesis of different alkynes that can contain potentially extracting moieties is described. The CuAAC between the two types of components is discussed. In a comparison between two catalysts in different reaction conditions, [Cu(C₁₈tren)]Br provided superior yields and purities of the products.

III MATERIALS FROM ORGANOSILANES

The sol-gel polymerization of organotrialkoxysilane precursors is well-known as an efficient route towards functionalized silica materials.¹⁷¹ The obtained materials are also known as silsesquioxanes or ormosils (**OR**ganically **MO**modified **SI**licas) with the chemical formula $\text{RSiO}_{1.5}$.¹⁷² By meticulous control of the reaction conditions, the local structure of the formed polymer is tunable. Next to randomly connected structures, cage- or ladder-like structures can be obtained.^{172–174} The structure formation is not necessarily exclusive.

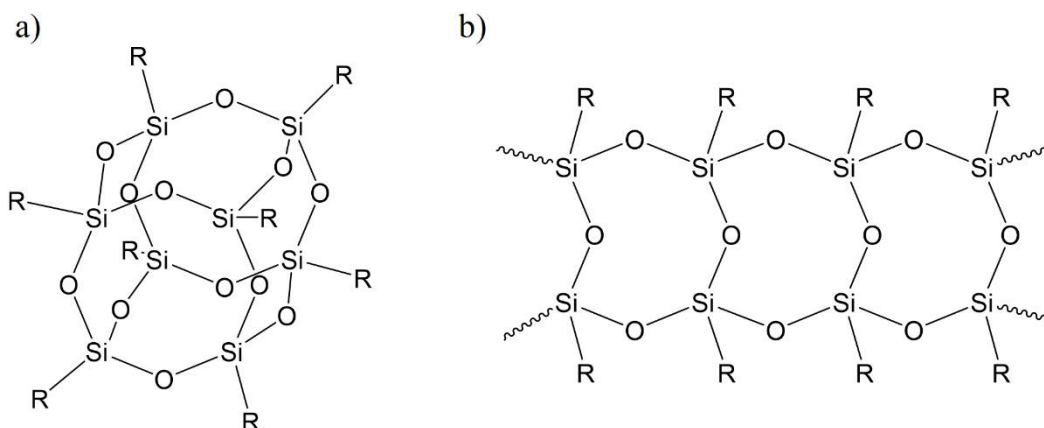


Figure 16. Typical structures of cage- (a) and ladder-like (b) silsesquioxanes.

Silsesquioxanes are used for catalytic studies, as precursors for porous materials, as co-polymer building blocks, in electronic devices, biomedicine, and for separation chemistry.¹⁷² In previous studies, the effectiveness and morphological versatility of amine-functionalized silsesquioxanes was thoroughly investigated.^{10,11} However, for the reasons mentioned earlier, the scope of accessible functional groups was widened by Click-chemistry. In the following, the self-assembly of the new precursors was investigated. **Figure 17** shows the situation of this chapter in the strategy outline proposed earlier (see **Figure 13**).

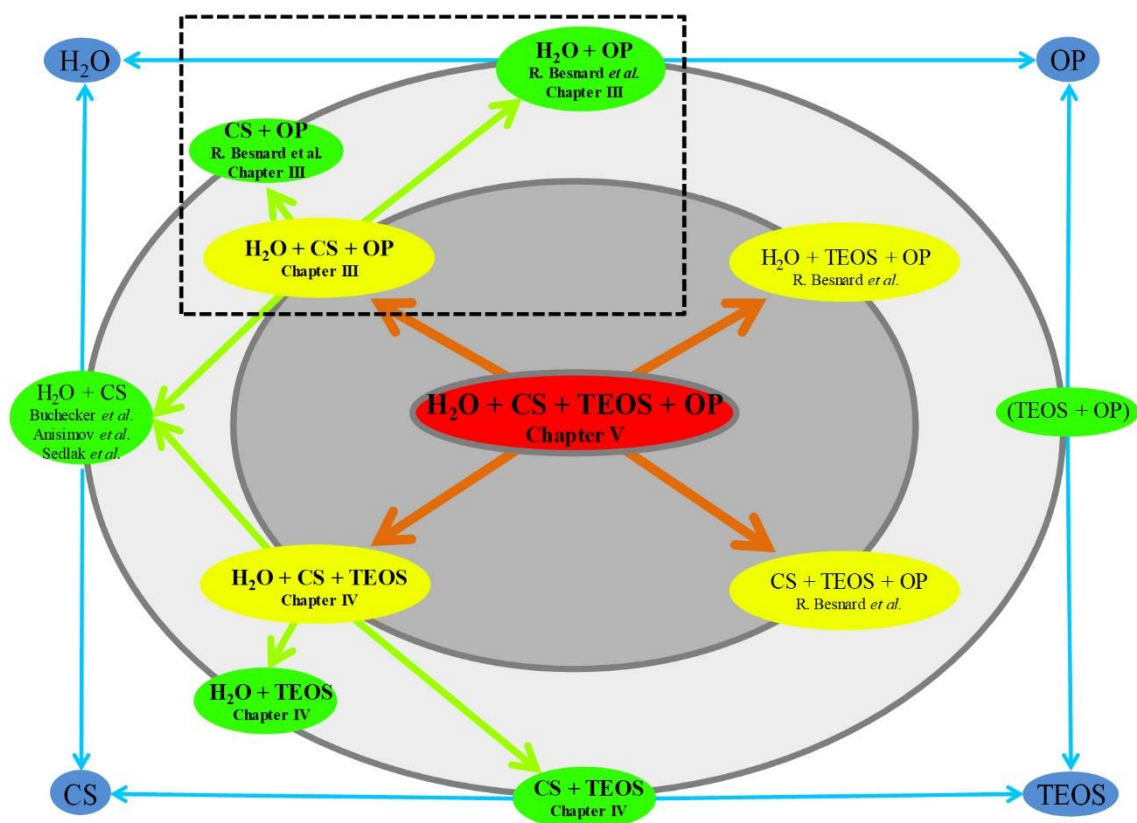


Figure 17. The strategy outline as developed earlier. The indicated area shows the systems that will be investigated in Chapter III.

For the study, five of the synthesized precursor molecules were polymerized using the sol-gel process. The employed precursor molecules are displayed in Figure 18.

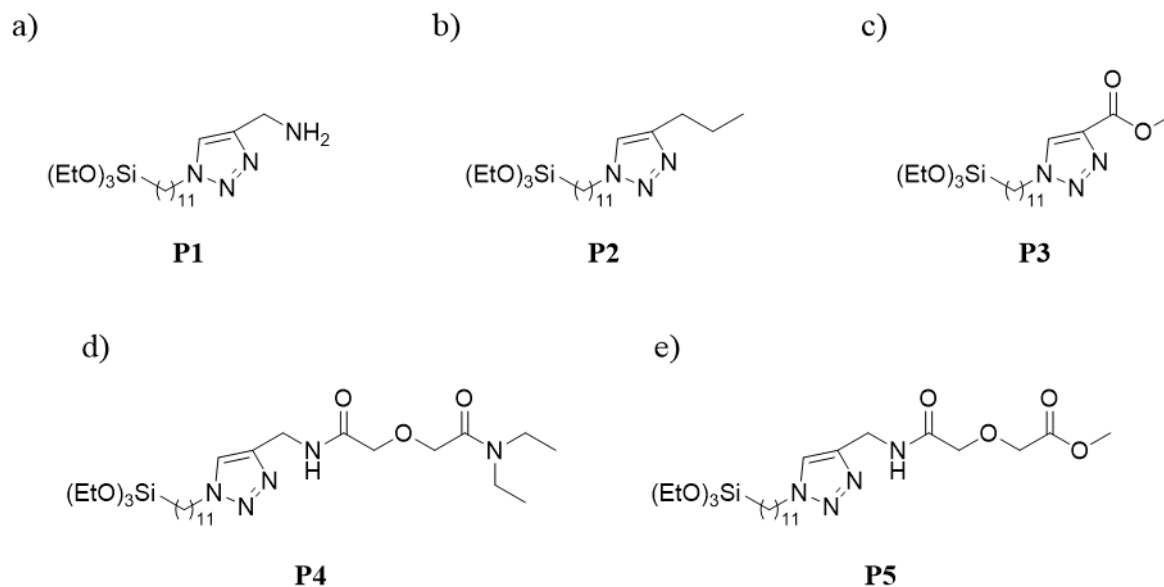


Figure 18. Structural formula of the organosilane precursors used for silsesquioxane synthesis.

1 Silsesquioxane synthesis

The material synthesis was performed in two different solvents for each precursor (see **Figure 19**).

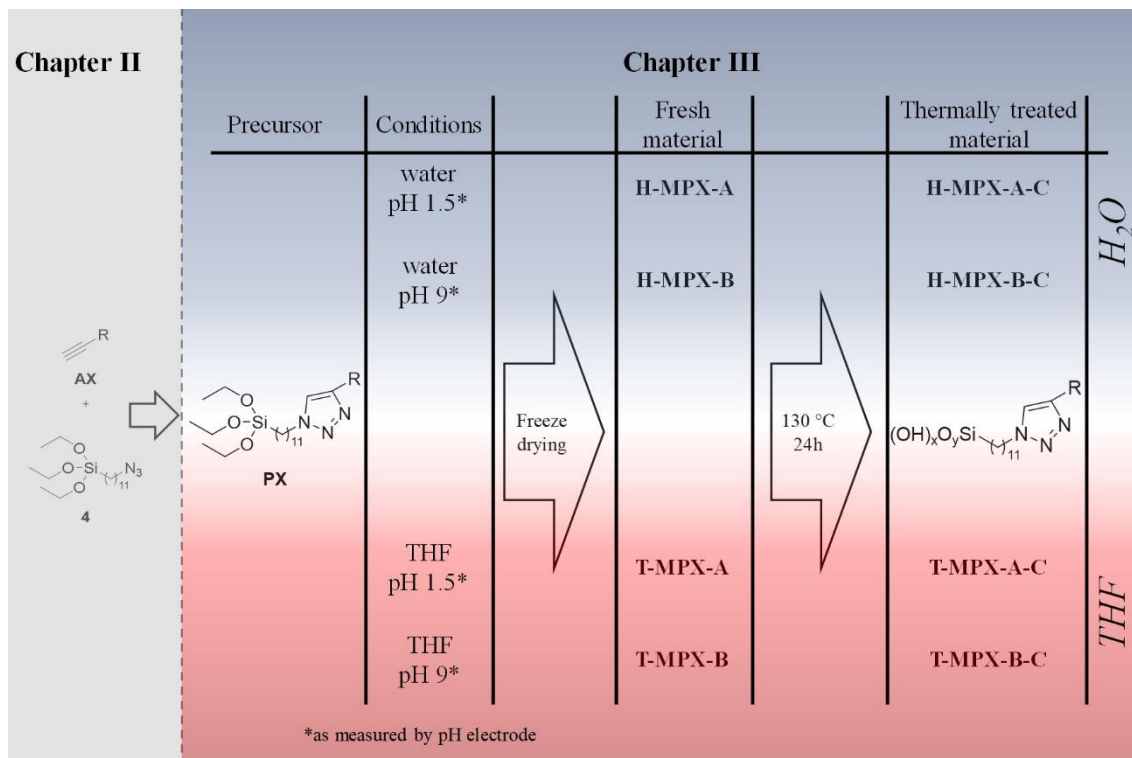


Figure 19. Overview of the experimental procedure for the synthesis of the SHMs from the precursor molecules (see II for details).

A one-step acidic (HCl, pH 1.5) or basic (NH₄OH), pH 9) catalysis was done for each solvent. Generally, 1.5 mmoles of organosilane precursor (**PX**, see **Figure 19**) were added to 50 mL of the solvent. Afterwards, the pH was adjusted and the solution was stirred for two weeks in a sealed flask. For the samples prepared in THF, the volume of added water was between 1 and 2 mL which corresponds to a water/SiO₂ ratio of ~50 to ~100. The obtained precipitate was freeze dried and washed using 60 mL (3x20 mL) EtOH/water (1:1), 60 mL (3x20 mL) EtOH to remove unpolymerized molecules and catalyst traces. After drying under vacuum, the fresh powders were characterized using various techniques including Fourier-transform infrared spectroscopy (FTIR), thermogravimetric analysis (TGA) and small angle x-ray scattering (SAXS) (**H/T-MPX-A/B**, see **Figure 19**). In a second step, the powders were heated to 130 °C during 24 h in order to promote the condensation of the siloxane network without degrading the organic part. The thermally treated materials were washed using 60 mL (3x20 mL) NEt₃/EtOH/water (8/60/32) to remove any eventual copper residues from organic synthesis, 60 mL (3x20 mL) EtOH/water (1:1), 60 mL (3x20 mL) EtOH, 60 mL (3x20 mL) EtOH/diethyl ether (DE) (1:1) and 60 mL (3x20 mL) DE to remove eventual degradation products.

The washed and vacuum dried powders (**H/T-MPX-A/B-C**, see **Figure 19**) were characterized using diverse techniques including FTIR, TGA and SAXS.

The ester hydrolysis was inspired from literature.¹⁷⁵ The materials synthesized from the precursor **P3** (**H-MP3-A-C**, **H-MP3-B-C**, **T-MP3-A-C**, **T-MP3-B-C**, 1 eq) were stirred in a solution containing LiBr (5 eq), NEt₃ (5 eq) in acetonitrile/water (94/6) for 3 days at 50 °C. The reaction scheme is displayed in **Scheme 16**. The obtained materials were washed using 60 mL (3x20 mL) acetonitrile, 60 mL (3x20 mL) EtOH/1 M HCl (1:1) to remove any base residues, 60 mL (3x20 mL) EtOH/water (1:1), 60 mL (3x20 mL) EtOH, 60 mL (3x20 mL) EtOH/diethyl ether (DE) (1:1) and 60 mL (3x20 mL) DE to progressively remove any salt or solvent residues. The washed and vacuum dried materials were characterized using FTIR, TGA and SAXS.

2 Silsesquioxane characterization

In order to investigate the effects of the solvent and the catalysis conditions on the composition, the local structure and the supramolecular organization of the silsesquioxanes, the characterization results are presented and discussed separately for each precursor. First, the material formation without potentially strongly interacting functional groups is examined. To this end, the materials elaborated from the precursor exhibiting a propyl chain instead of a functional group the (**P2**) are investigated. Second, the other silsesquioxanes synthesized from the precursors having functional groups (**P1**, **P3-P5**) are presented and discussed.

2.1 Propyl headgroup (**H/T-MP2-A/B-C**)

i. Composition and local structure motifs

The materials were synthesized using the precursor 4-propyl-1-(11-(triethoxysilyl)undecyl)-1H-1,2,3-triazole (**P2** in **Figure 18**). The chemical composition of the materials was investigated by FTIR. The obtained spectra are displayed in **Figure 20**.

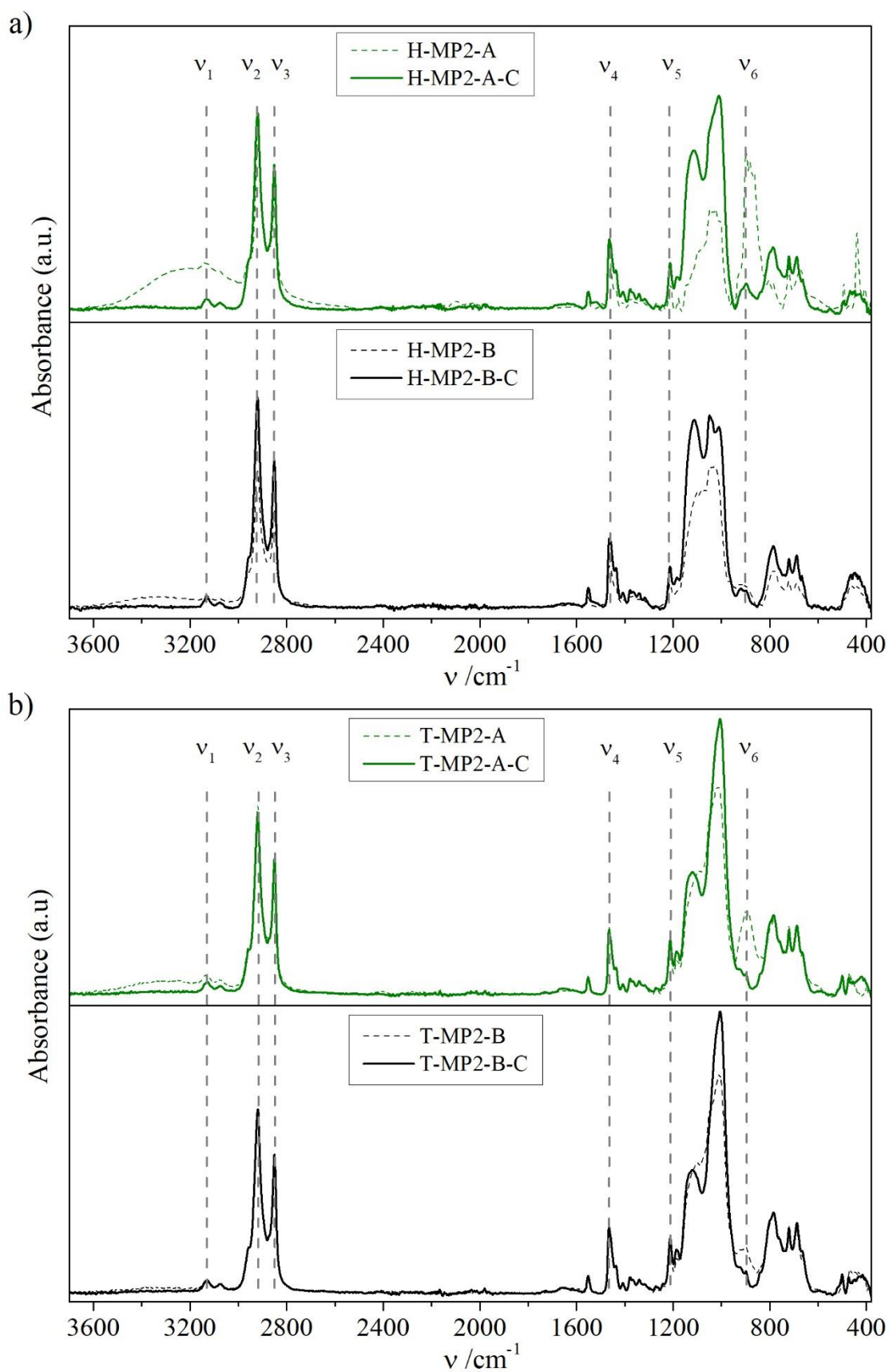


Figure 20. FTIR spectra of the fresh and thermally treated materials obtained from the precursor P2 using a) water or b) THF as solvent in the synthesis.

In the spectra, the typical signals of SHMs are found. All spectra show common peaks at 3130 cm^{-1} (ν_1) attributed to the C-H stretching modes in the triazole group, 2920 cm^{-1} (ν_2) and 2850 cm^{-1} (ν_3) attributed to the CH_2 asymmetric and symmetric stretching modes, 1460 cm^{-1} (ν_4) attributed to the C=C stretching in the triazole group, 1210 cm^{-1} (ν_5) attributed to the Si- CH_2 - stretching mode and $1020\text{-}930\text{ cm}^{-1}$ (ν_6) attributed to the Si-OH stretching modes.¹⁷⁶⁻¹⁷⁸ These peaks attest the presence of the triazole group and the retention of the Si-C bond. The broad peak in the region of $3600\text{ to }2800\text{ cm}^{-1}$ that is visible in all fresh materials, is assigned to the O-H stretching band which can be attributed to the presence of uncondensed Si-OH groups and residual water. The peak disappears after thermal treatment indicating the further polymerization of the siloxane network and the evaporation of the residual water.

In order to obtain information on the alkyl chain configuration and the silica connectivity, the C-H stretching modes and the Si-O-Si modes are investigated in the same way as in literature.¹⁷⁹⁻¹⁸² First, the position of the asymmetric C-H stretching mode and the ratio $R_{alkyl} = \frac{I(\nu_2)}{I(\nu_3)}$ reveal the conformation of the alkyl chains. Here, for all the materials, the peak positions are between $2919\text{-}2920\text{ cm}^{-1}$ and the ratios $R_{alkyl} = \frac{I(\nu_2)}{I(\nu_3)}$ are comprised between 1.40 and 1.34 which confirms the all-trans conformation. This result indicates that the alkyl chains are fully extended.

Second, the broad peaks in the range between $1200\text{ and }800\text{ cm}^{-1}$ are attributed to the siloxane bridges. In every spectrum, two broad peaks are identified that can be assigned to cage-like condensed motifs (P_T , $\sim 1110\text{ cm}^{-1}$) or open chain or ladder-like motifs (P_L , 1025 cm^{-1}).^{181,183} As apparent in **Figure 20**, the peak shapes depends on the catalysis conditions and the solvent. It is modified after thermal treatment. Moreover, the ratio $R_{silica} = \frac{I(P_T)}{I(P_L)}$ gives information on the predominant structure motif. It attests that the consolidated materials synthesized from aqueous solution show a higher content of cage-like motifs especially under basic conditions ($R_{silica} = 0.74$ for acid catalysis and 0.98 for base catalysis) than the materials synthesized from THF solutions. In the latter, both catalysis conditions show similar ratios ($R_{silica} = 0.44$ for acid catalysis and 0.43 for base catalysis). This behavior is attributed to experimental conditions and the precursor solubility. Albert S. Lee *et al.*^{173,184} identified the precursor and water concentrations as major determinants for the selective formation of structural motifs (ladder- or cage-like). When performing the reaction in THF, the precursor solubility and reasonable water concentration favor the formation of high molecular weight, ladder-like or open structures. In water, the precursor solubility is limited. Therefore, cage-like structures are favored. Additionally, the hydrolysis rate under basic conditions is slow.¹⁸⁵ This hinders the formation of more soluble hydrolyzed species before the onset of condensation. Another factor is the tendency towards condensation between already linked species under basic conditions. This further promotes the formation of cage-like motifs. After thermal treatment, the structure evolves as predetermined in the fresh materials.

In order to determine the molecular weight of the synthesized materials, TGA was performed. The results are shown in **Figure 21**.

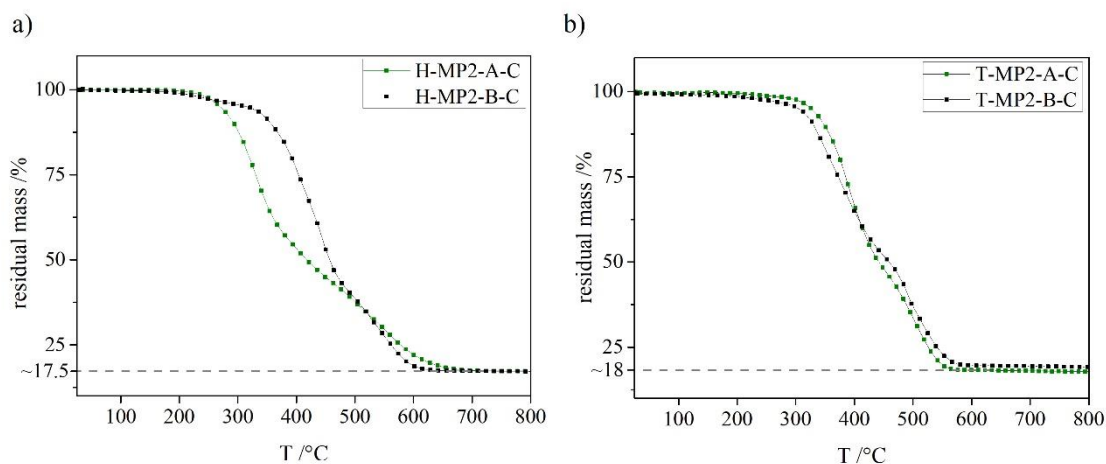


Figure 21. TGA weight loss curves in percent of the original mass during heating to 1000 °C. The dashed grey line indicates the residual mass percentage at 700 °C.

Figure 21 a) and **b)** show a continuous weight loss with increasing temperature. At 700 °C, the residual mass remains constant. The weight loss occurs in consecutive, overlapping stages. The first weight loss of ~55 w% occurs at different temperatures depending on the material. For the materials H-MP2-B-C, T-MP2-A-C and T-MP2-B-C, the onset is around 300 °C while it is around 200 °C for the material H-MP2-A-C. The second weight loss of ~36 w% has the onset around 450 °C for all materials. The first weight loss includes the decomposition of the triazole moiety¹⁸⁶ which theoretically accounts for a weight loss of ~27 w%. In the consecutive steps the rest of the carbon skeleton is decomposed. The constant mass until ~200 °C attests the successful silica consolidation and the water removal during the thermal treatment. For the calculation of the molecular weight, it was assumed that the residual mass at > 700 °C corresponds to fully condensed SiO₂. This is supported by the FTIR spectrum of the residual material (**Figure A.1**) where a mix of cristobalite and amorphous silica is found.¹⁷⁷

Thus, using

$$M_{TGA} = 100 * \frac{M_{SiO_2}}{w_{700^\circ C}} \quad (6)$$

where M_{TGA} is the molecular mass of the material as determined by TGA, M_{SiO_2} the molecular mass of silica (60.09 g mol⁻¹) and $w_{700^\circ C}$ the residual mass percentage at 700 °C, the molecular mass was calculated. The results are listed in **Table 4**.

Table 4. Residual masses at 700 °C and calculated molar masses M_{TGA} of the materials H/T-MP2-A/B-C.

Material	$w_{700^{\circ}\text{C}}$ (w%)	$M_{TGA}(\text{g}\cdot\text{mol}^{-1})$
H-MP2-A-C	17.5±1	343±20
H-MP2-B-C	17.5±1	343±20
T-MP2-A-C	18±1	334±20
T-MP2-B-C	19±1	317±17

The calculated values are in reasonable agreement with the theoretical molecular mass of the material (317 g mol⁻¹). Thus, as suggested by the FTIR spectra, the molecular structure was not degraded in the sol-gel process or during the thermal treatment.

A striking feature of the weight loss curves, however, is the differing onset temperature of the first weight loss for H-MP2-A-C. All other characteristics being similar, the difference can be correlated to the local structure. (see **Figure 20**). Seemingly, the difference of the supramolecular structure modifies the thermal stability of the organic function.

ii. Supramolecular organization

To investigate the supramolecular organization, SAXS was performed on the materials. The recorded scattering patterns are displayed in **Figure 22**.

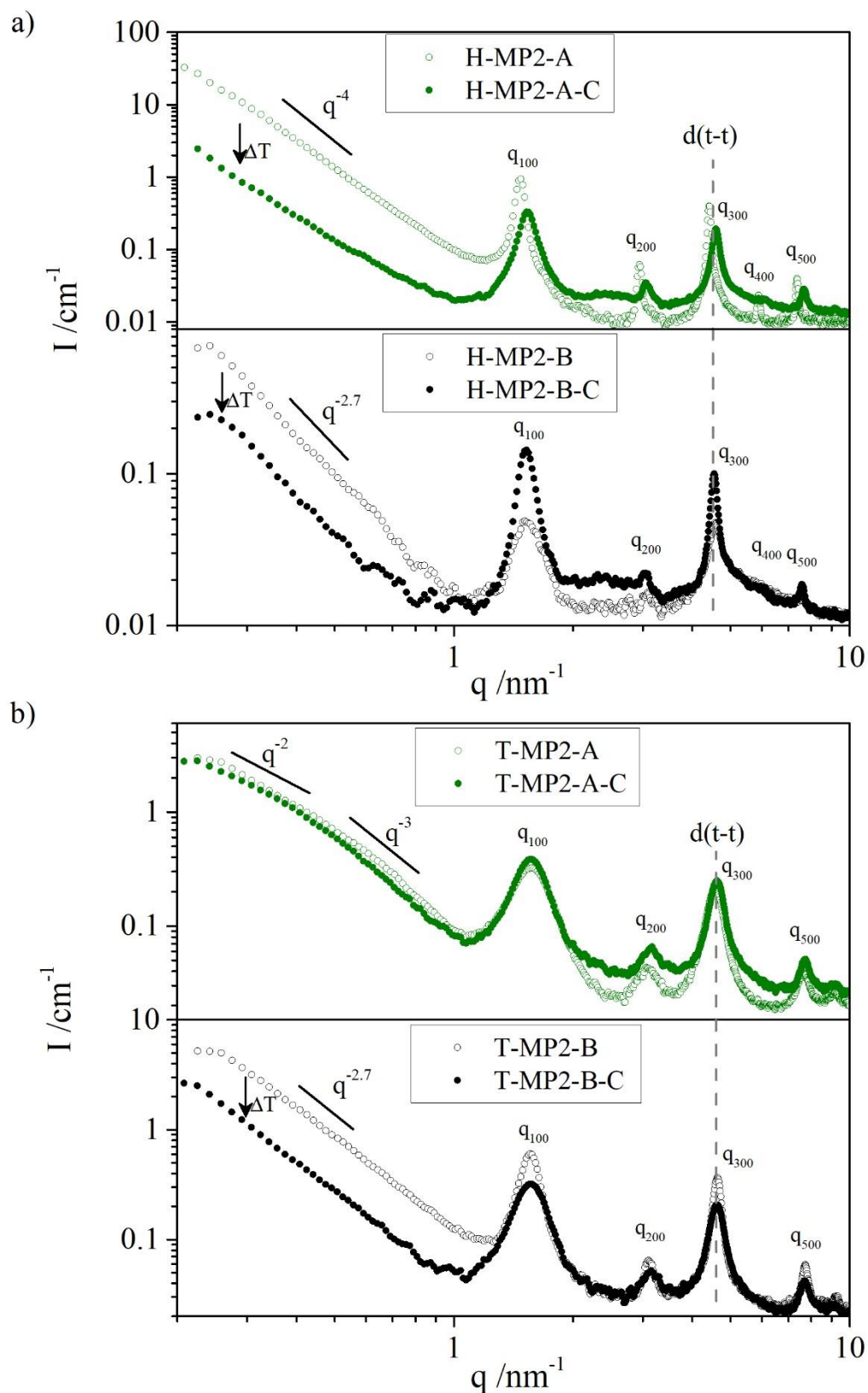


Figure 22. SAXS patterns of the silsesquioxanes elaborated from the precursor P2 in water (a) and THF (b). The indicated slopes serve as visual guide. The labels q_{n00} indicate the Bragg peak positions.

The SAXS patterns show several common features. For the following discussion, a visual aid is given in **Figure 23**. In all patterns, at $q > 1 \text{ nm}^{-1}$, Bragg peaks are observed at equidistant integer positions. This is characteristic for lamellar structures.¹⁸⁷ The peaks are denoted q_{n00} where n indicates the n -order peak. The peaks of even order show a decreased intensity compared to odd-order peaks. The first order peak (q_{100}) describes the average repeat unit length (d_r in **Figure 23 a**) while the higher order peaks (q_{n00} with $n = 2, 3, 4, \dots$) give information on the degree of long-range order. The repeat unit length is around 4.1 nm for all materials which corresponds to two extended **P2** molecules. Sharper peaks and the visibility of higher order peaks indicate a higher long-range order. This includes a higher number of stacked repeat units and less uneven sheets. The materials synthesized in aqueous solution reveal sharper peaks than the materials synthesized in THF. In the former, H-MP2-A shows sharper peaks than H-MP2-B. Thus, increasing lamellar characteristics are found in the order T-MP2-A \approx T-MP2-B < H-MP2-B \ll H-MP2-A. The thermal treatment leads to a slight smoothing of the Bragg peaks for all materials. It is concluded that some amount of long-range order is lost upon heating. An exception is peak q_{100} in H-MP2-B. This will be discussed later. It should be noted that the reason for the attenuation of the even-order Bragg peaks (q_{200} and q_{400}) is the similar thickness of the sheets in the lamellar structure. At close-to-equal thickness, even-order Bragg peaks are completely extinguished.^{188,189} Furthermore, the unexpectedly high intensity of peak q_{300} can be explained by an overlay with the triazole-triazole distance ($d(t-t)$ in **Figure 22** and **Figure 23**).

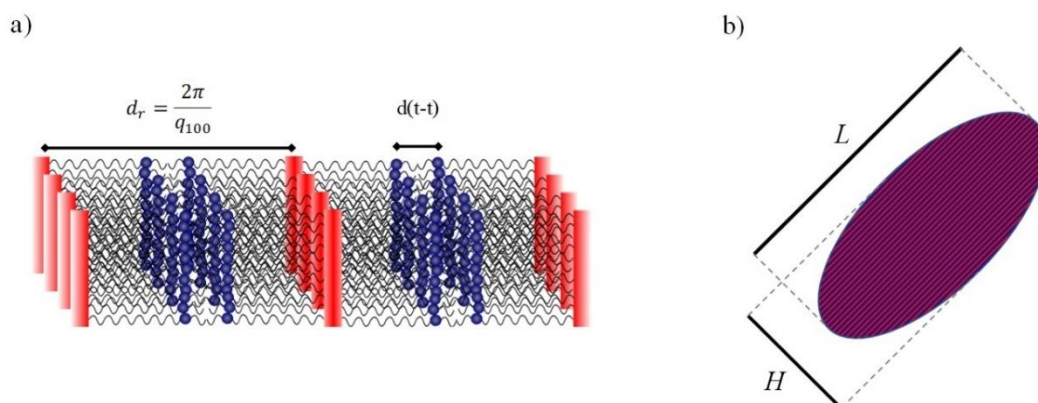


Figure 23. Scheme of the supramolecular arrangement of the MP2 materials when looking at two repeat units (a, Red = SiO_{1.5}, Blue = triazole) or a stack of several repeat units (b) with height H and length L .

At low q , a slope proportional to $q^{-\alpha}$ is observed. The value of α varies depending on the material from values around 2 (T-MP2-A) to 3.9 (H-MP2-A). Upon thermal treatment, α remains unchanged. However, the observed intensity at low q decreases. (ΔT in **Figure 22**). Fractal objects are excluded because earlier studies on similar materials showed no fractal properties.^{11,108,190} Therefore, these values are typical for intermediate objects between smooth disk-like ($\alpha = 2$) or spherical ($\alpha = 4$) objects. Knowing that all materials contain some share of lamellar structure, they are assumed to assemble to form

similar objects. Indeed, an object that can cause this variation of α is an oblate ellipsoid defined by the two diameters L and H (see **Figure 23 b**). H would, therefore, be proportional to the number of stacked repeat units. The two slopes observed for the material T-MP2-A ($\alpha \approx 2$ and 3) support this hypothesis because they are characteristic for oblate ellipsoids with a flat top (final lamellar sheet).¹⁹¹ Considering a high polydispersity, an ellipsoid can take any of the observed slopes by changing the ratio height/length (H/L). By approaching H/L to 1, the ellipsoid approaches a spherical shape and α becomes 4. At the same time, the number of repeat units increases and, thus, the long-range order increases. Both is observed for material H-MP2-A. With decreasing H/L , the flat (2D) character of the lamellar sheets becomes more important and α approaches 2. Simultaneously, the long-range order decreases. This is observed when comparing the materials H-MP2-B, T-MP2-A and T-MP2-B with H-MP2-A. Upon thermal treatment, the changing slope intensity can be related to a change of the ellipsoid size or number. However, α indicates a conservation of the object shape.

H-MP2-B is the only material that shows an increasing Bragg peak intensity after the thermal treatment. This is related to the particular supramolecular motifs that were observed in the FTIR spectra (see **Figure 20**). H-MP2-B-C exhibited the largest share of cage-like motifs. These motifs, contrarily to the ladder-like motifs, are unable to form extended structures. Hence, they produce defects in the lamellar structure. Nonetheless, they are at the same distance from each other as the lamellar layers. Therefore, the peak q_{100} and the $d(t-t)$ contribution are not influenced. On the contrary, the advancing polymerization reaction increases the SLD of the cages and, thus, their contrast with the organic part. Consequently, the intensity of peak q_{100} increases.

iii. Summary

To resume, the precursor **P2** was effectively polymerized and the obtained materials were consolidated without the degradation of any of the organic functions as revealed by FTIR and TGA. The materials polymerize to form a mixture of different supramolecular motifs depending on the synthesis conditions. The materials synthesized in THF polymerize mostly in a ladder-like fashion whereas the materials synthesized in water display a larger share of cage-like features. Generally, more cage-like motifs are formed under basic conditions. The supramolecular motifs, then, assemble in stacked layers as observed by SAXS. Depending on the dominant feature (cage- or ladder-like), the thermal treatment impacts the supramolecular organization differently. A striking difference is the temperature of decomposition found by TGA. The material H-MP2-A-C which also shows the largest share of cage-like structures, decomposes at lower temperatures than the others. Since the materials are chemically identical, it appears that this is due to the different supramolecular motifs.

2.2 Amine headgroup (H/T-MP1-A/B-C)

The materials were synthesized using the precursor (1-(11-(triethoxysilyl)undecyl)-1H-1,2,3-triazol-4-yl)methanamine (**P1** in **Figure 18**). Many studies have been conducted using organotrialkoxysilanes with amine headgroups.^{11,119,192} In this work, the structure formation in the presence of newly introduced, neighboring triazole group will be investigated.

i. Composition and local structure motifs

To examine the chemical composition of the materials, FTIR spectroscopy was performed. The results are displayed in **Figure 24**.

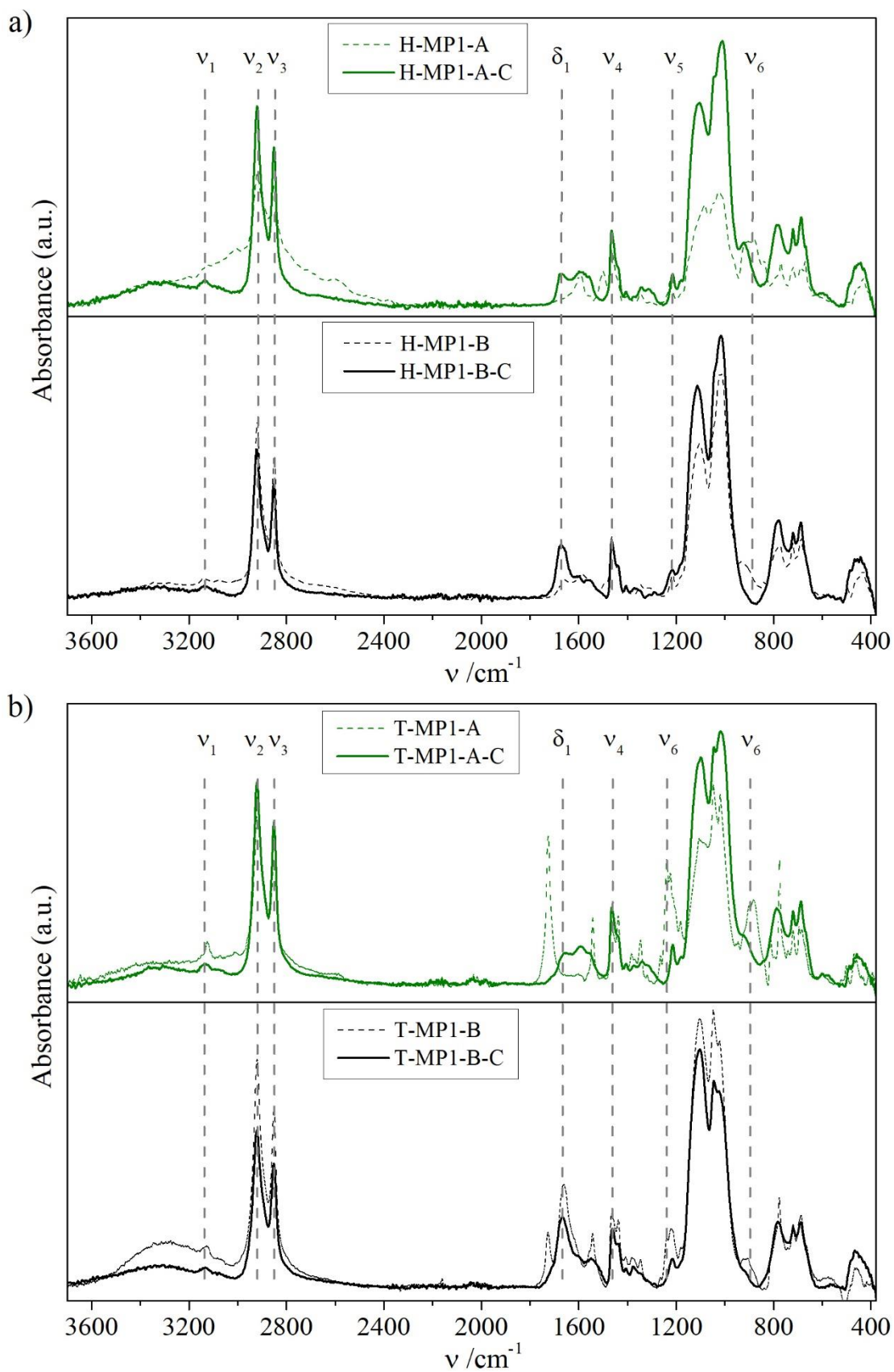


Figure 24 FTIR spectra of the fresh and thermally treated materials obtained from the precursor P1 using a) water or b) THF as solvent in the synthesis.

In the recorded spectra, the peak assignment is identical to that of the FTIR spectra of the **P2** materials (see **Figure 20**). Additionally, the signal at 1660 cm^{-1} (δ_1) is attributed to the N-H bending mode of the primary amine and the broad peak between 3600 and 2800 cm^{-1} is now assigned to X-H vibrations where X can be Si-O, H-O or N. Like explained earlier, the decreasing intensity of the large signal is, amongst other things, due to the reaction of the free silanol groups and the removal of residual water. The reaction is also indicated by the decrease of the Si-OH peak (ν_6). However, a residual broad peak remains. This may be caused by the presence of the amine group. For the materials H-MP1-A and T-MP1-A, a broad peak can be observed between 3000 and 2800 cm^{-1} . This signal is attributed to the primary ammonium group formed under acidic conditions. The simultaneous absence of peak δ_1 and the disappearance of the signal after washing with a basic solution support this attribution.

Next, the alkyl chain configuration and the supramolecular structures are examined. Like for the materials synthesized from **P2**, the asymmetric vibration mode of the alkyl chain (ν_2) is at typical wavenumbers (2919 - 2920 cm^{-1}) for an all-trans configuration. This is also confirmed by the ratio $R_{alkyl} = \frac{I_{(\nu_2)}}{I_{(\nu_3)}}$ of the all materials with values comprised between 1.27 and 1.30. Thus, for these materials, it can be also concluded that the alkyl chains are extended.

Following the earlier argumentation, the intensity of the signals at $\sim 1110\text{ cm}^{-1}$ and $\sim 1025\text{ cm}^{-1}$ is interpreted as a measure of the silica connectivity. At ratios >1 , cage-like motifs and at ratios <1 , ladder-like motifs are predominant. Contrarily to the **P2** materials, the share of cage-like motifs is higher when the materials are synthesized in THF ($R_{silica} = 0.9$ for T-MP1-A-C and 1.18 for T-MP1-B-C versus 0.77 for H-MP1-A-C and 0.81 for H-MP1-B-C). Here, basic conditions lead to a bigger share of cage-like motifs than acidic conditions. Compared to the materials synthesized from **P2**, overall higher shares of cage-like motifs are observed. The reasons are manifold. The higher solubility of **P1** in water compared to **P2** and/or the electrostatic interactions and H-bonding of the potentially protonated amine group can be responsible. Nevertheless, the preference for cage-like motifs under basic conditions is consistent. Here, it is pronounced for the materials synthesized in THF. It is reminded that this might be caused by the higher reactivity of already condensed silanol species with monomers under basic conditions.³⁰ This favors more compact structures.

To obtain further information on the silica matrix, ^{29}Si -NMR spectroscopy was performed. The results are shown in **Figure 25**.

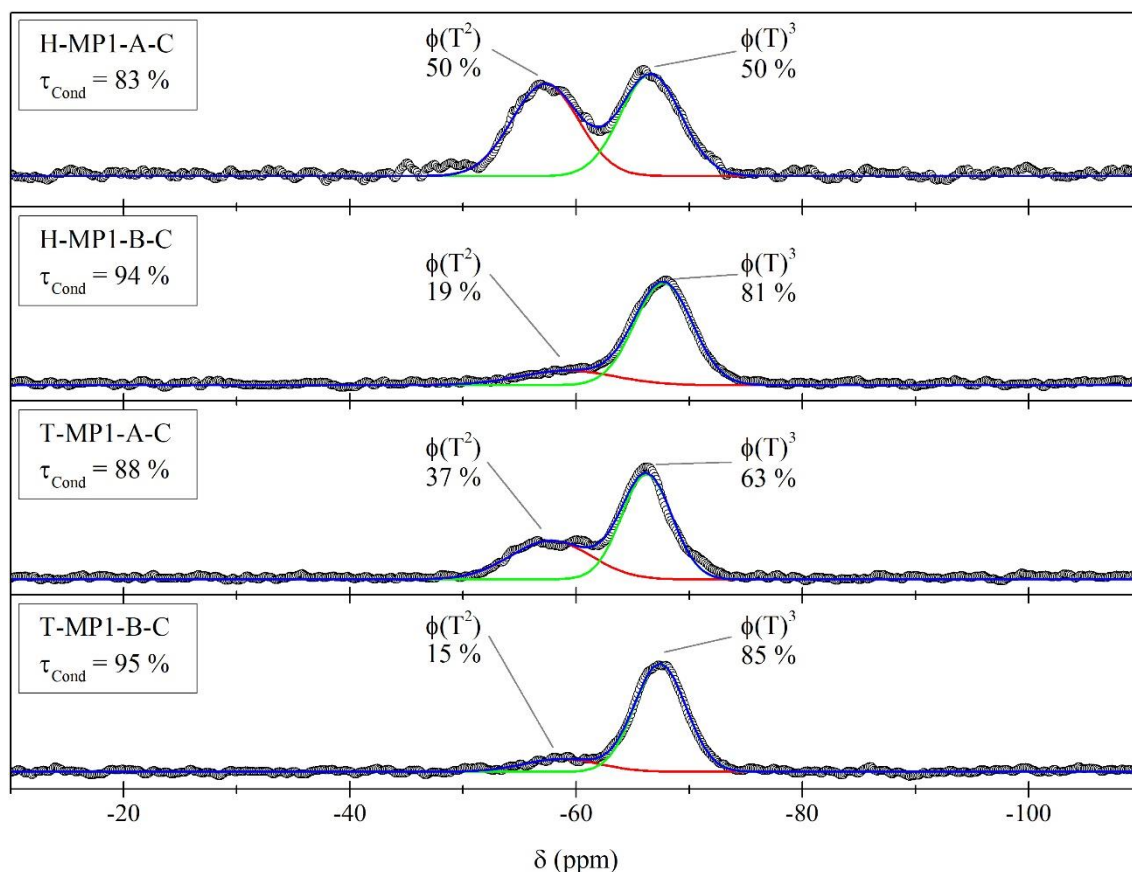


Figure 25. ^{29}Si (HPDEC)-NMR spectra of the materials H/T-MP1-A/B-C. The two contributions coming from different silanol species (T^2 and T^3) were fitted. Open circles represent the measured data. The blue line represents the cumulative fit obtained by the addition of the two contributions (red and green lines). The determined percentage of each contribution to the total area is indicated. It is used to calculate the degree of polycondensation (τ_{Cond}).

In the nuclear magnetic resonance (NMR) spectra, only signals from T units (T^x , $\text{R-Si}(\text{OH})_{(3-x)}\text{y}(\text{O})_{(x*0.5)}$ with $0 \leq x \leq 3$) were observed. This confirms the retention of the Si-C bond. All spectra contain a combination of T^2 and T^3 units indicating highly condensed materials. By peak decomposition, the individual contributions of T^2 ($\phi(\text{T}^2)$) and T^3 ($\phi(\text{T}^3)$) units to the global signal are obtained (red and green lines in **Figure 25**).

Defining T^3 as 100 % and T^2 as 66.7 % condensed, the overall degree of condensation of the material (τ_{Cond}) is calculated *via*

$$\tau_{\text{Cond}} = 100\% * \phi(\text{T}^3) + 66.7\% * \phi(\text{T}^2) \quad (7)$$

Generally, base catalysis leads to higher condensation degrees than acid catalysis. Comparing the solvents, a synthesis in THF leads to slightly higher degrees of condensation than in aqueous solution. The differences originate from the different local structure which, in turn, depends on the synthesis conditions like discussed for **Figure 20**

and **Figure 24**. Materials synthesized under basic conditions show denser networks due to the chemistry of the base catalyzed condensation.

In order to determine the molecular weight of the synthesized materials, TGA was performed. The results are shown in **Figure 26**.

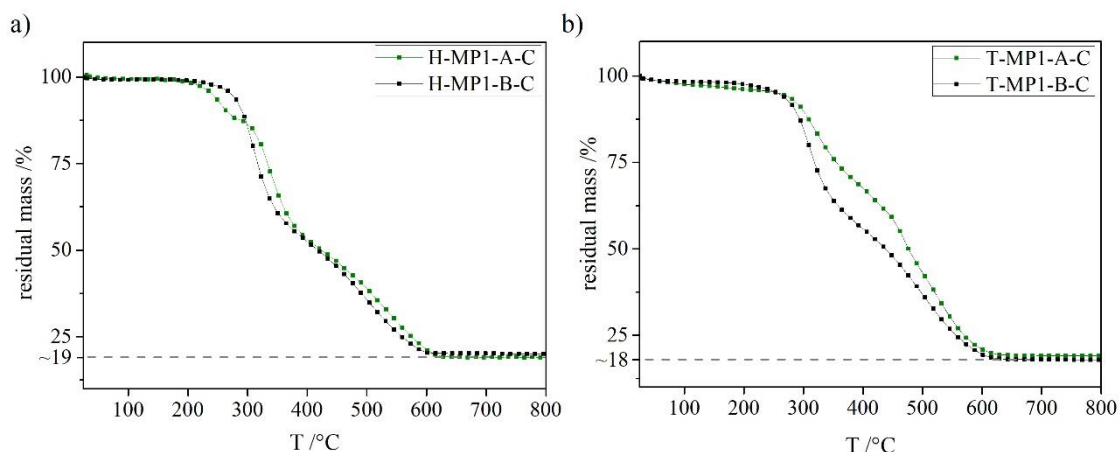


Figure 26. TGA weight loss curves of the P1 materials in percent of the original mass during heating to 1000 °C. The dashed grey line indicates the residual mass percentage at 700 °C.

The TGA curves show a continuous weight loss at increasing temperature. At 700 °C the residual mass remains constant. Like for the **P2** materials, the weight loss occurs in consecutive, overlapping stages. For all materials, the first weight loss of ~40 w% occurs at around 260 °C. The second weight loss of ~42 w% has the onset around 400 °C. During the two steps, the organic part is degraded. The residual mass is SiO₂. Using the residual mass, the molecular weight was calculated like explained earlier. The results are displayed in **Table 5**.

Table 5. Residual masses at 700 °C and calculated molar masses M_{TGA} of the materials H/T-MP1-A/B-C.

Material	$w_{700^{\circ}\text{C}}$ (w%)	M_{TGA} (g.mol ⁻¹)
H-MP1-A-C	19±1	316±20
H-MP1-B-C	20±1	300±20
T-MP1-A-C	19±1	316±20
T-MP1-B-C	18±1	333±20

The calculated values are in reasonable agreement with the theoretical molecular mass of the material (303 g mol⁻¹). Thus, like inferred from the FTIR spectra, the molecular structure of the precursor is conserved.

ii. Supramolecular organization

To investigate the mesoscale structuring of the materials, SAXS was performed. The patterns are shown in **Figure 27**.

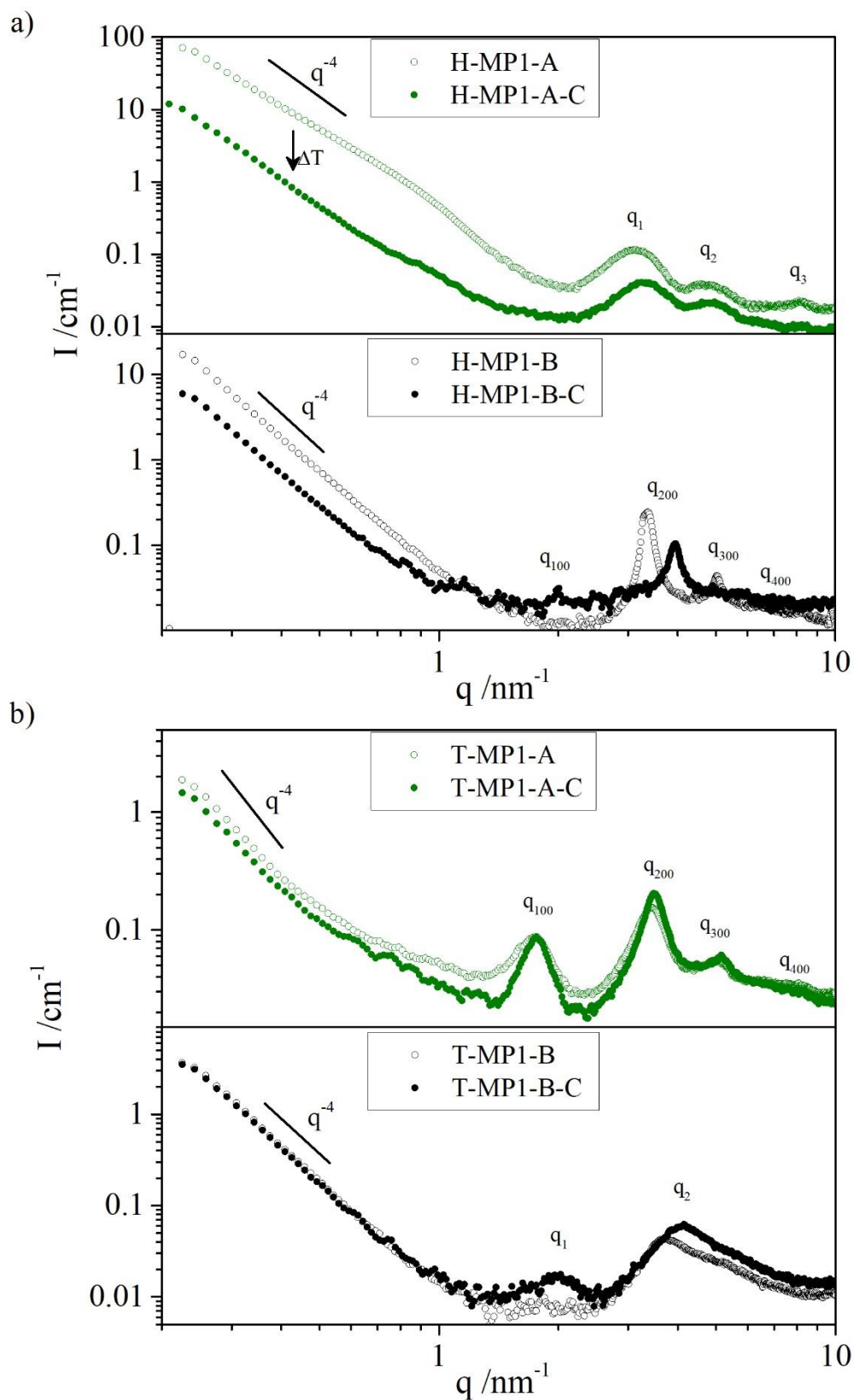


Figure 27. SAXS patterns of the materials produced from the precursor P1 in water (a) and THF (b). The indicated slopes serve as visual guide. The labels q indicate the Bragg peak positions.

At low q , the SAXS patterns, show a slope proportional to $\sim q^{-4}$ which indicates smooth surfaces. Complementary transmission electron microscopy (TEM) measurements confirm this observation for the materials T-MP1-A-C and T-MP1-B-C (see **Figure 28**). The Bragg peaks at $q > 1 \text{ nm}^{-1}$ reveal a lamellar structure for the materials H-MP1-B-C and T-MP1-A-C. Here, the labels q_{n00} (with $n = 1, 2, 3, 4$) designate the order. The determined repeat unit length of 3.6 nm corresponds to two extended precursor molecules.¹¹⁹ The lamellar structure is confirmed by the TEM image for T-MP1-A-C (see **Figure 28 a**)) with a repeat unit length of ~ 4 nm. The structure assignment for materials H-MP1-A-C and T-MP1-B-C is more ambiguous. The Bragg peaks are large indicating a rather disordered structure. For T-MP1-B-C, this is confirmed by TEM (see **Figure 28**) where no characteristic structure is identified. For material H-MP1-A-C the situation is similar. Lamellar characteristics can be suspected but the peak width and the absence of higher order peaks prevent a final conclusion. All materials show a shift of the Bragg peaks towards higher q after thermal treatment. This indicates the contraction of the structure due to the siloxane bridge formation. The effect is more pronounced for the materials synthesized under basic conditions. This might be caused by the loss of CO_2 as reported in earlier work.¹¹⁹

In aqueous solution, basic conditions appear to be more effective for the long-range structuring of the material. However, like reported earlier¹¹⁹, a considerable degree of amorphization is observed after thermal treatment. **P1** forms less organized structures under acidic conditions than **AUT**. This might be due to the steric demand of the triazole group or the increased molecular length. In THF, the effect of the catalysis conditions on the supramolecular organization is inverted. Here, basic conditions lead to a less structured material. Interestingly, a correlation with the high share of cage-like motifs can be noticed. Thus, basic conditions seemingly lead to compact cage-like motifs that aggregate in a disordered fashion. Under acidic conditions, the best structuration is observed. The reason might be the formation of a hydrophilic ammonium chloride pseudophase between the headgroups. This pseudophase would be insoluble in THF and could isolate itself by the formation of bilayers. Consequently, the polymerization would take place in this shape.

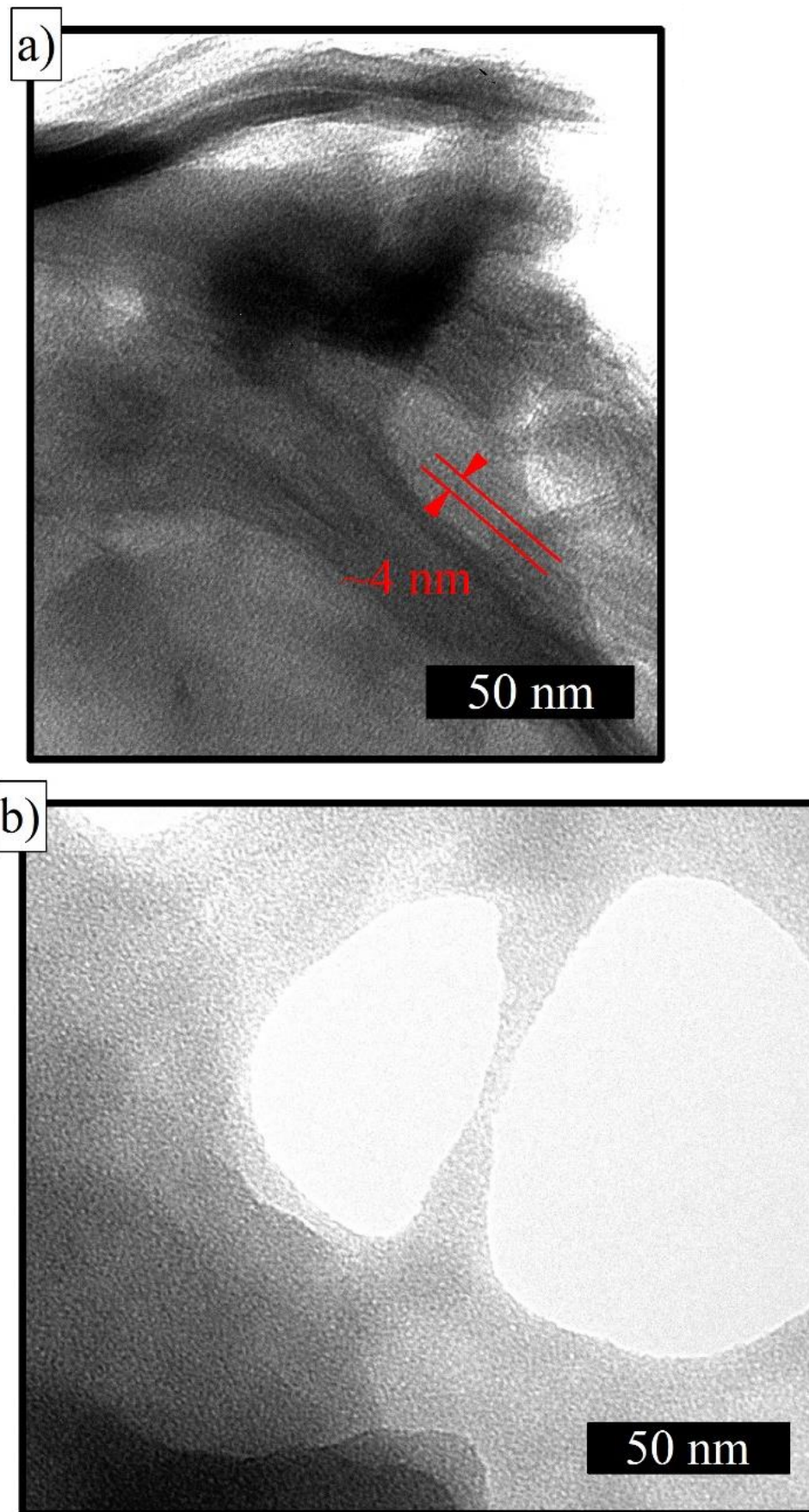


Figure 28. TEM images of the samples T-MP1-A-C (a) and T-MP1-B-C (b)

iii. Summary

To sum up, **P1** was effectively polymerized in all tested conditions without degradation. After the thermal treatment, all materials showed high degrees of condensation. The degrees of condensation were higher for the materials synthesized under basic conditions. At the same time, basic conditions lead to materials with a higher share of cage-like motifs. Both observations emerge from the nature of base catalysis. At a larger scale, the motifs then assemble to form bigger and occasionally lamellar structures. The most pronounced lamellar structure was observed for T-MP1-A-C. This is suspected to be driven by the formation a self-assembled structure involving the formation of a hydrophilic ammonium chloride pseudophase.

2.3 Methyl ester headgroup (H/T-MP3-A/B-C)

In this section, the materials synthesized from *methyl 1-(11-(triethoxysilyl)undecyl)-1H-1,2,3-triazole-4-carboxylate* (**P3** in **Figure 18**) are characterized.

i. Composition and local structure motifs

The local structure and chemical composition were investigated by FTIR. The spectra are shown in **Figure 29**.

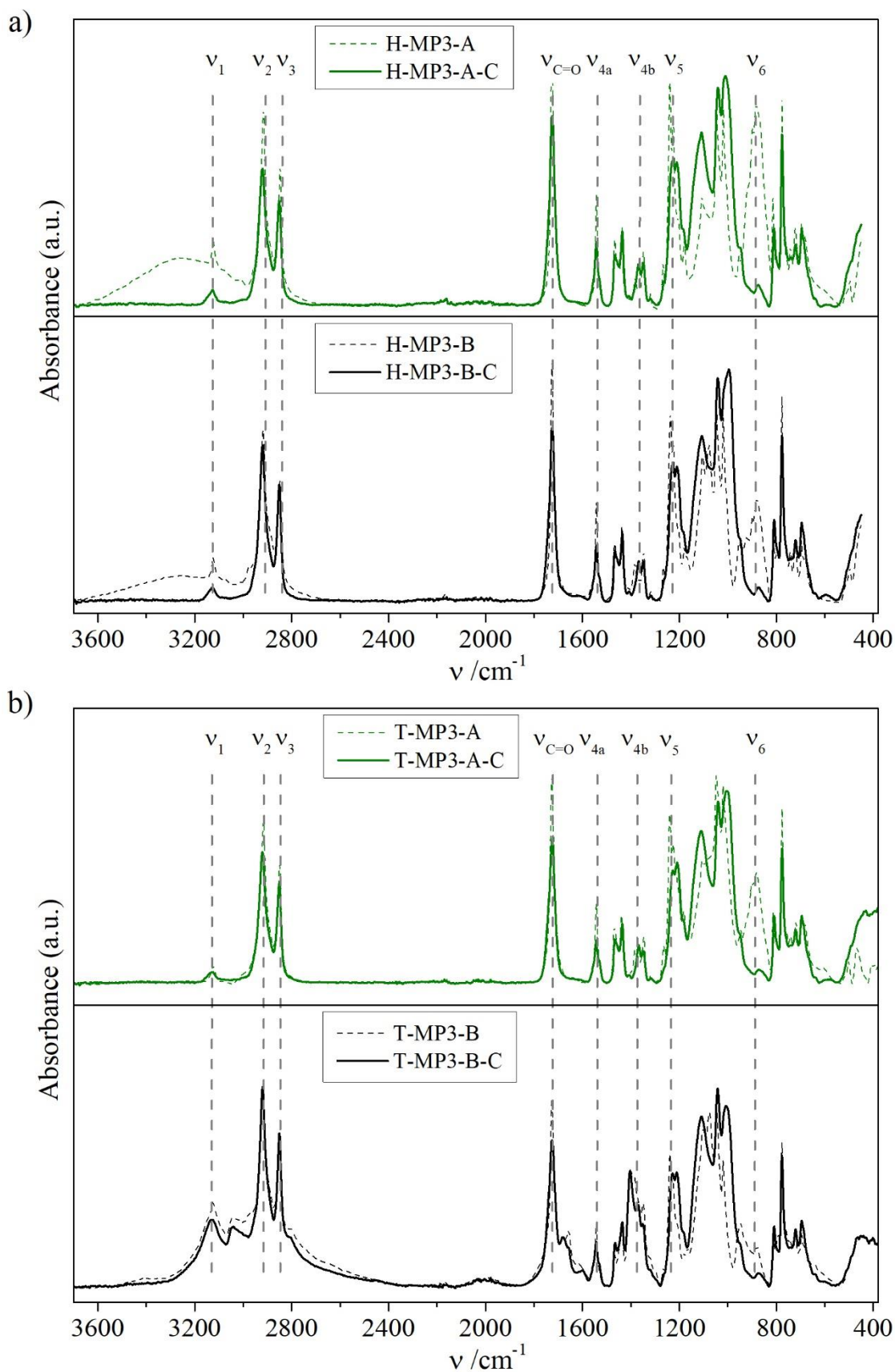


Figure 29. FTIR spectra of the fresh and thermally treated materials obtained from the precursor P3 using a) water or b) THF as solvent in the synthesis.

The conservation of the molecular structure is confirmed by the peaks indicated ν_1 - ν_6 . The assignment is identical to that for the materials produced from **P2** (see **Figure 20**). Peak ν_4 shows a particularity for this precursor. The C=C stretching modes are enhanced due to the presence of the conjugation with the carbonyl group. The peak at 1540 cm^{-1} is, therefore, enhanced and indicated with ν_{4a} . Another C=C mode is indicated by ν_{4b} . The C=O stretching mode is marked $\nu_{C=O}$. The peak is at the typical position for conjugated esters.¹⁹³ The spectra of materials T-MP3-B(-C) show an enlarging between 3400 and 2400 cm^{-1} , around the C=O mode and around 1400 cm^{-1} . This is due to residual NH_4Cl formed by the unplanned addition of HCl at the material work-up that was not properly removed after sample preparation. The enlarged regions correspond to the peaks found for NH_4Cl .¹⁹⁴ Because of the addition during work-up, the local structure (silica connectivity) formed during synthesis is considered unchanged. Upon thermal treatment, the materials show the same changes as observed earlier. The broad peak attributed to the O-H vibration modes and the peak attributed to the Si-OH mode (ν_6) disappear (see **Figure 20**).

Concerning the alkyl chain configuration, the peak position of the asymmetric C-H stretching mode (ν_2) between 2920 (H-MP3-A-C) and 2921 (T-MP3-A-C) indicates an all-trans configuration. This is confirmed by $R_{alkyl} = \frac{I(\nu_2)}{I(\nu_3)}$ between 1.31 (T-MP3-B-C) and 1.36 (H-MP3-B-C). Hence, the alkyl chains are extended.

The local structure motifs of the silica matrix are examined in the region between 1200 cm^{-1} and 800 cm^{-1} like explained earlier (see **Figure 20**). Similarly to the **P1** materials, synthesis in THF leads to a higher share of cage-like motifs than in aqueous solutions. In the latter, acid and base catalysis lead to similar values ($R_{silica} = 0.75$ for H-MP3-A-C and 0.71 for H-MP3-B-C). In THF, base catalysis leads to more cage-like motifs than acid catalysis ($R_{silica} = 0.79$ for T-MP3-A-C versus 0.94 for T-MP3-B-C). Like wise to the **P1** materials, the reason is the nature of base catalysis that leads to more compact structures. These results have to be treated carefully, because the C-O stretching mode of the ester is also found in this region.

In order to determine the molecular weight of the synthesized materials, TGA was performed. The results are shown in **Figure 30**.

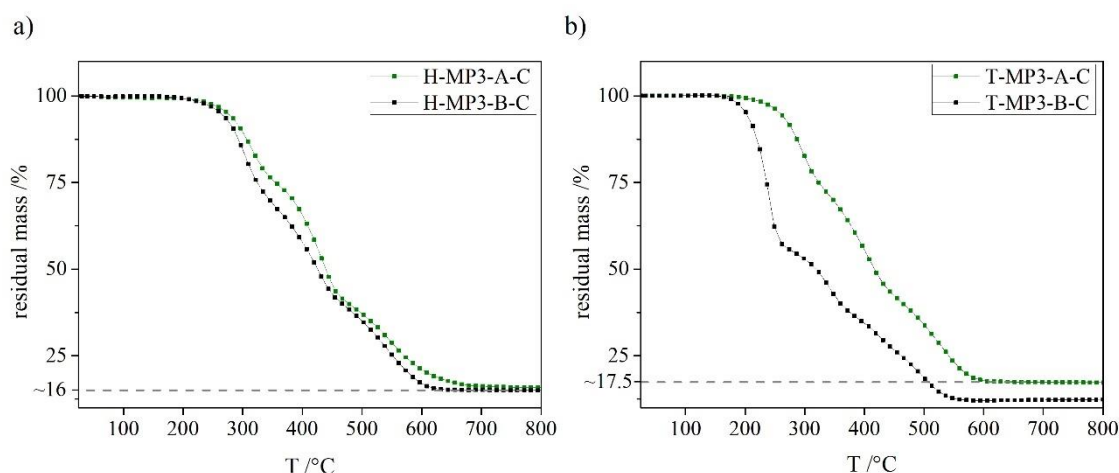


Figure 30. TGA weight loss curves of the P3 materials in percent of the original mass during heating to 1000 °C. The dashed grey line indicates the residual mass percentage at 700 °C.

The TGA curves show a continuous weight loss at increasing temperature. At 700 °C the residual mass remains constant. As observed for the P2 materials, the weight loss occurs in consecutive, overlapping stages. Like mentioned, NH₄Cl is present in material T-MP3-B-C. Therefore, the weight loss follows a different evolution. For the other materials, the first weight loss of ~25 w% occurs at ~200 °C. The second weight loss of ~35 w% has the onset at around 350 °C. The final weight loss of ~25 w% is observed at around 460 °C. Like before, the residue is pure SiO₂. For the material T-MP3-B-C, the same weight loss temperatures are found which indicates the presence of the material. However, a sharp weight loss at ~170 °C is observed that is assigned to the decomposition of NH₄Cl. Consequently, the weight losses attributed to the material are modified. Using the residual mass, the molecular weight was calculated, for all materials except T-MP3-B-C. The results are displayed in **Table 5**.

Table 6. Residual masses at 700 °C and calculated molar masses M_{TGA} of the materials H/T-MP3-A/B-C.

Material	$w_{700^{\circ}\text{C}}$ (w%)	$M_{TGA}(\text{g}\cdot\text{mol}^{-1})$
H-MP3-A-C	16±1	376±25
H-MP3-B-C	16±1	376±25
T-MP3-A-C	17.5±1	342±25

The calculated values are in reasonable agreement with the theoretical molecular mass of the material (332 g mol⁻¹). Thus, like inferred from the FTIR spectra, the molecular structure of the precursor is conserved.

ii. Supramolecular organization

To obtain information on the mesoscale structuring, SAXS was performed. The results are shown in **Figure 31**.

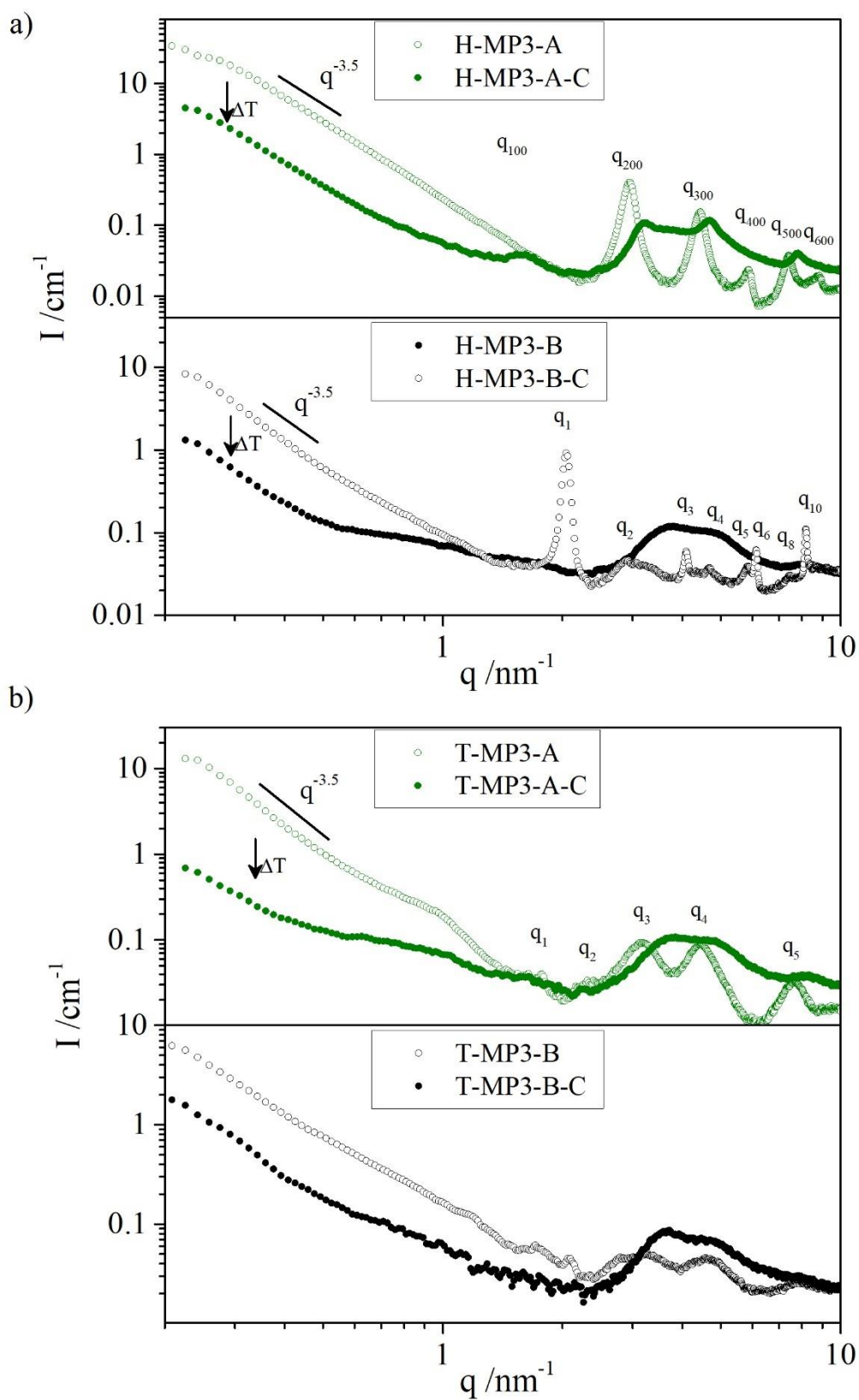


Figure 31. SAXS patterns of the materials produced from the precursor P3 in water (a) and THF (b). The indicated slopes serve as visual guide. The labels q indicate the Bragg peak positions.

The SAXS patterns of T-MP3-B(-C) are added for completeness and will not be discussed. The other patterns are separated into two regions. At $q > 1 \text{ nm}^{-1}$, excess scattering with a slope proportional to $q^{-\alpha}$ is observed. For all materials, α is close to 3.5. This indicates solid objects with a rough surface. Upon thermal treatment, α remains unchanged but the slope intensity decreases. At $q < 1 \text{ nm}^{-1}$, different arrangements of Bragg peaks are found. The peaks are well defined for the materials synthesized in aqueous solution. In H-MP3-A, a lamellar structure (q_{n00} with $n = 1, 2, 3, 4\dots$) is identified with corresponding Bragg peaks up to the eighth order. The repeat unit length corresponds well to two molecular lengths ($d = 4.3 \text{ nm}$). The first order peak (q_{100}) is extinguished due to the structure organization. This phenomenon is analogous to the extinction of the even ordered peaks explained for the materials synthesized from **P2**. An illustration of this is given in **Figure A.2**. After thermal treatment, the lamellar structure is conserved and contracted ($d = 4 \text{ nm}$ after thermal treatment). Thanks to this contraction, the first order peak is enhanced. However, the less sharp peaks indicate the loss of long-range order. The material H-MP3-B shows Bragg peaks that are assigned to a D-bicontinuous mesophase in a cubic lattice.¹⁸⁷ After thermal treatment, this structuring is not observed anymore. The Bragg peaks for T-MP3-A are large. This complicates the structural assignment. Using the highlighted peaks, a 2D hexagonal structuring can be identified. Nonetheless, a high degree of disorder is observed. After thermal treatment, the observed structure is further disordered. The absence of long-range order impedes the mesophase identification.

The deviation from lamellar structures in some of the materials synthesized from **P3** is explained by the molecular geometry. Indeed, different to the precursors discussed beforehand, **P3** has a branched headgroup with a rather stiff geometry due to the conjugation with the triazole group. This increases the packing parameter. Contrarily to the lamellar structures due to a packing parameter close to 1 observed earlier (see **Figure 22** and **Figure 27**), this ultimately leads to inversed structures (cubic bicontinuous, 2D hexagonal). They are energetically more favorable than a lamellar phase when the packing parameter becomes slightly higher than 1.²⁹ However, in the case of bicontinuous phases, the average curvature remains close to 0 like for lamellar phases.

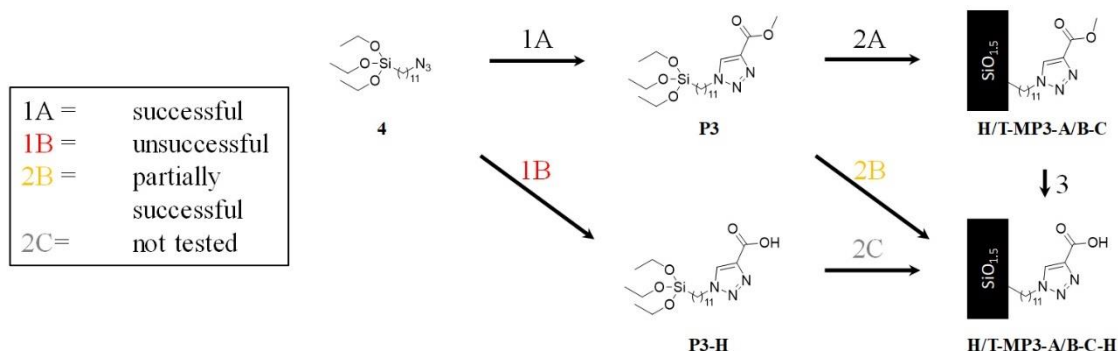
Concerning the discussed spectra, aqueous conditions appear to favor the long-range structuring of the materials compared to the synthesis in THF. In the fresh materials, the eighth order peaks of a lamellar (H-MP3-A) or cubic (H-MP3-B) phase are observed. However, only the lamellar structure is conserved after thermal treatment. Apparently, the consolidation of the silica matrix severely deforms the cubic structure. Only Bragg peaks that can be assigned to molecular dimensions remain. In the same way, the 2D hexagonal structuring observed for T-MP3-A is deformed.

iii. Summary

To resume, the precursor **P3** was successfully polymerized without degradation. The silica matrix of the synthesized materials appears to form more ladder-like motifs in aqueous synthesis conditions compared to THF. Similar to the materials investigated in previous sections, basic conditions lead to materials with higher shares of cage-like structures. This effect is more pronounced for the materials synthesized in THF. For the materials synthesized in water, the long-range order is well defined. The material T-MP3-A shows a less consistent long-range order. The formation of non-lamellar mesophases indicates a packing parameter of **P3** above 1. This is caused by the steric demand of the branched, conjugated headgroup. However, after thermal treatment the non-lamellar structures are degraded.

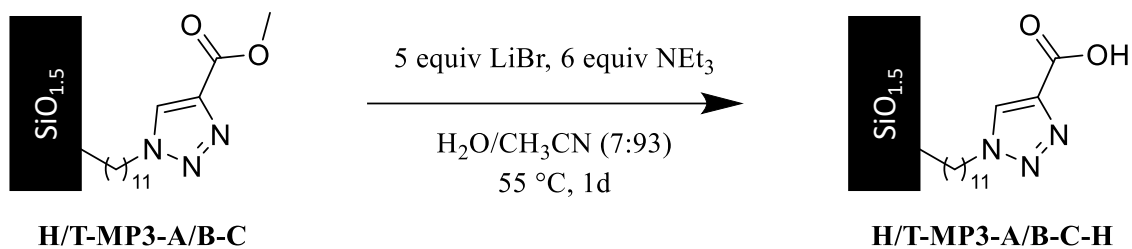
2.4 Carboxylic acid headgroup (H/T-MP3-A/B-C-H)

For applications *e.g.* extraction or post-synthetic modification, the conversion into a carboxylic acid is desirable. Keeping in mind the all-in-one concept of this thesis, several routes are possible. An overview is given in **Scheme 15**.



Scheme 15. Possible synthesis routes to the carboxylic acid containing material (H/T-MP3-A/B-C-H).

The upper horizontal arrows in **Scheme 15** labeled 1A and 2A show the synthesis that was described earlier (see **Figure 19**). From this synthesis, several derivations to the carboxylic acid species are conceivable. First, the synthesis of an alternative precursor (**P3-H**) *via* 1B using propiolic acid as a coupling reagent in the studied Click-chemistry conditions was tested. The reaction failed because the carboxylic acid group poisons the copper catalyst. Next, the simultaneous ester hydrolysis during the polymerization was examined (2B in **Scheme 15**). The hydrolyzed product was partially obtained in some conditions. The detailed results are described for **Figure A.3**. However, the conversion being far from completion in most conditions, this option was discarded. Finally, the post-synthetic hydrolysis of the materials H/T-MP3-A/B-C (3 in **Scheme 15**) was tested using the conditions displayed in **Scheme 16**.



Scheme 16. Hydrolysis reaction of the materials **H/T-MP3-A/B-C**.¹⁷⁵

i. Composition and local structure motifs

The completion of the reaction was verified by FTIR. The results are shown in **Figure 32**.

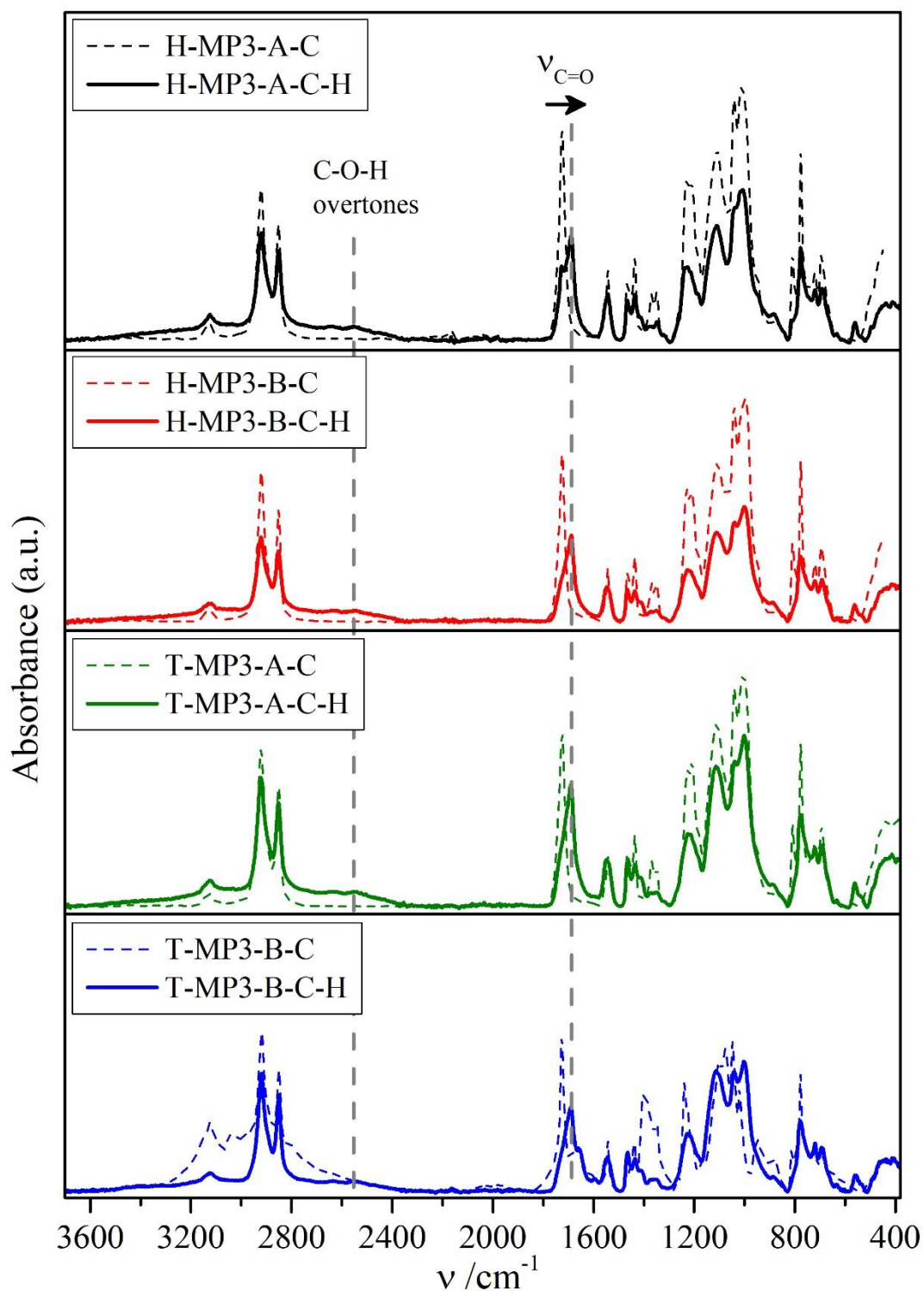


Figure 32. FTIR spectra of the P3 materials before (dashed lines) and after (solid lines) the hydrolysis reaction.

The reaction completion is confirmed by the shift of the C=O stretching mode from $\sim 1730\text{ cm}^{-1}$ to $\sim 1690\text{ cm}^{-1}$. Additionally, the presence of a broad peak between 3600 cm^{-1} and 2400 cm^{-1} attests the presence of the carboxylic acid O-H groups and residual water. Here, the broad peaks around 2600 cm^{-1} are typical for carboxylic acid overtones.

Concerning the local structure motifs, no change is observed. It is concluded that the silica matrix is unaffected by the hydrolysis reaction.

TGA measurements were performed to confirm the molecular weight of the hydrolyzed precursor. The results are shown in **Figure 33**.

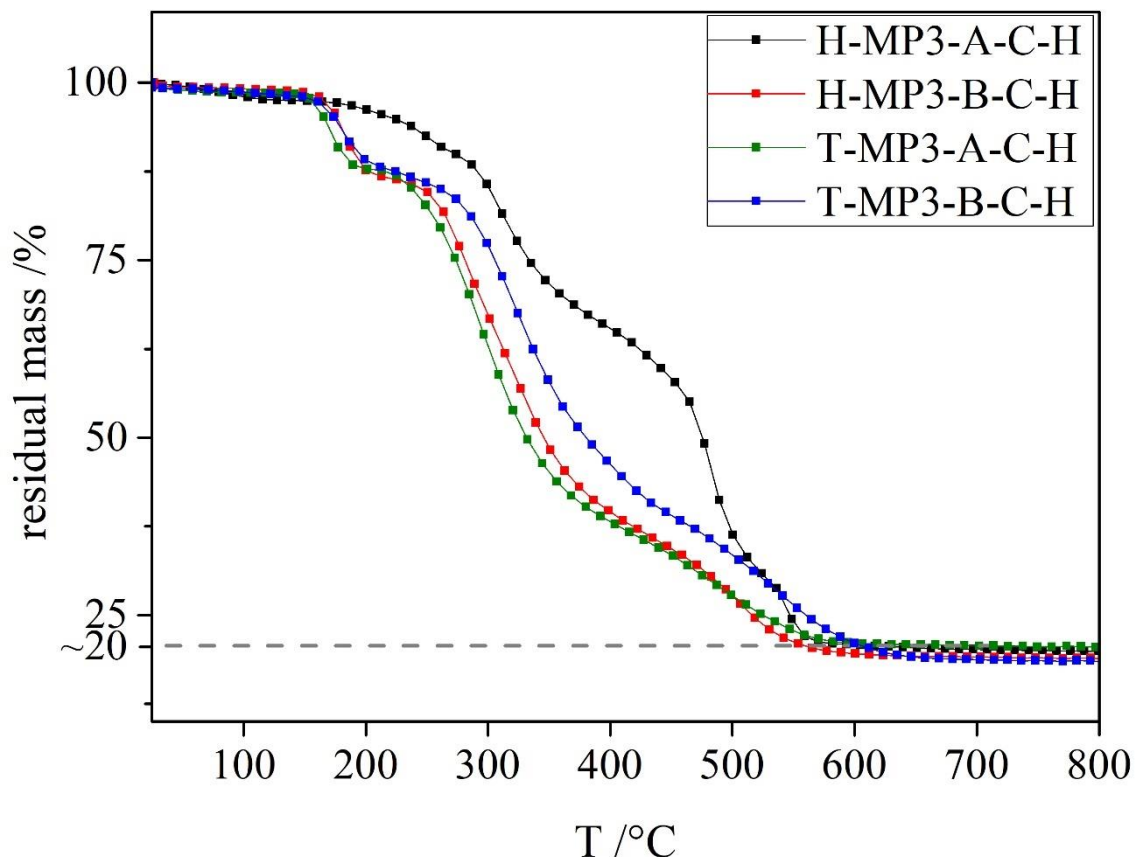


Figure 33. TGA weight loss curves of the hydrolyzed materials in percent of the original mass during heating to 1000 °C. The dashed grey line indicates the residual mass percentage at 700 °C.

For all materials, the weight loss curves show a weight loss in consecutive, partially overlapping stages. The first weight loss of ~15 w% occurs at 160 °C. For H-MP3-A-C-H the slope is less steep than for the others. Considering the theoretical molecular weight of the material (318 g mol^{-1}), a loss of 48 g mol^{-1} is inferred. This corresponds well to the loss of CO_2 by the degradation of the carboxylic acid. In two consecutive weight losses, the rest of the molecule is degraded until only SiO_2 remains. From the residual masses the molecular weight was calculated. The results are displayed in **Table 7**.

Table 7. Residual masses at 700 °C and calculated molar masses M_{TGA} of the materials H/T-MP3-A/B-C-H.

Material	$w_{700^{\circ}\text{C}}$ (w%)	$M_{TGA}(\text{g}\cdot\text{mol}^{-1})$
H-MP3-A-C-H	20±1	308±20
H-MP3-B-C-H	19.5±1	316±20
T-MP3-A-C-H	19±1	300±20
T-MP3-A-C-H	18.5±1	324±20

The obtained values are in good agreement with the theoretical molecular weight (318 g mol⁻¹). The hydrolysis is, thus, considered complete without the occurrence of side reactions.

ii. Supramolecular organization

Finally, the long-range order of the obtained materials was investigated using SAXS. The obtained scattering patterns are shown in **Figure 34**.

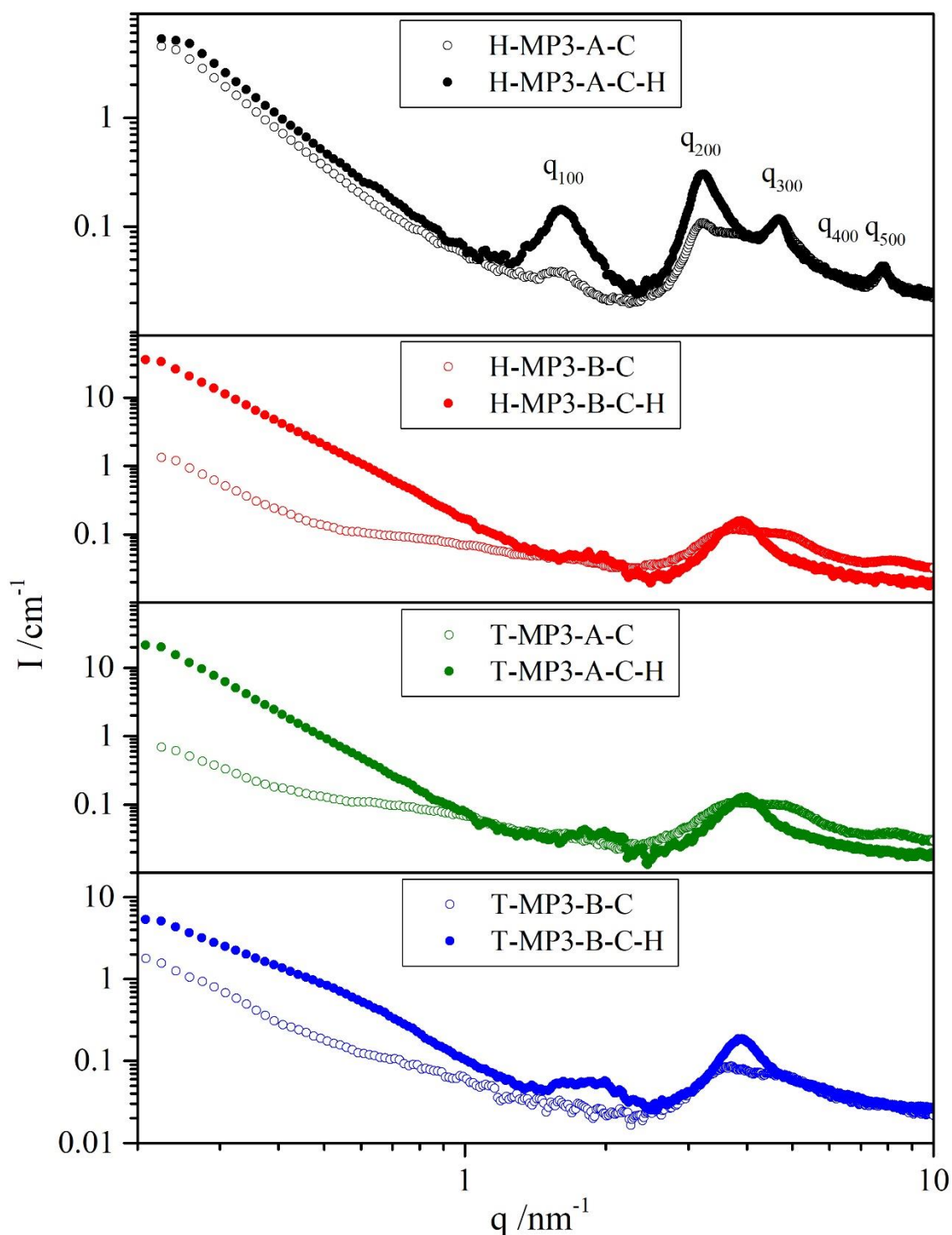


Figure 34. SAXS patterns of the hydrolyzed P3 materials. The labels q indicate the Bragg peak positions.

At $q > 1 \text{ nm}^{-1}$, Bragg peaks that correspond to a lamellar structure with a repeat unit length of $\sim 4 \text{ nm}$ are clearly identified for H-MP3-A-C-H. They are at similar positions as for H-MP3-A-C. The Bragg peaks for the other materials are significantly less sharp. The structure identification is impossible because of the absence of further peaks. Nonetheless, a peak corresponding approximately to two extended **P3-H** molecules is identified at $q = 1.8 \text{ nm}^{-1}$. At $q < 1 \text{ nm}^{-1}$, a slope proportional to $q^{-\alpha}$ is observed for all

materials. The values of α between 3.5 and 3.8 indicate the presence of rough mesoscale objects. For T-MP3-B-C-H, a slight decline of α to ~ 2.1 is found at $q < 0.6 \text{ nm}^{-1}$ (corresponding to $>10.5 \text{ nm}$ in real space). Excluding fractal objects, this probably originates from the presence of two-dimensional features of the mesoscale objects. However, the structure is severely disordered.

iii. Summary

Resuming, the hydrolysis of the **P3** materials was quantitatively achieved. The integrity of the silica matrix appears unchanged after the reaction. However, long-range order is absent for most of the materials except for H-MP3-A-C-H. Here, the retention of the lamellar structure after hydrolysis is identified.

2.5 Diglycolic acid amide headgroup (H-MP4-B-C and H/T-MP5-B-C)

Finally, the materials synthesized from *N,N*-diethyl-2-(2-oxo-2-(((1-(11-(triethoxysilyl)undecyl)-1H-1,2,3-triazol-4-yl)methyl)amino)ethoxy)acetamide (**P4** in **Figure 18**) and methyl 2-(2-oxo-2-(((1-(11-(triethoxysilyl)undecyl)-1H-1,2,3-triazol-4-yl)methyl)amino)ethoxy)acetate (**P5** in **Figure 18**) are investigated in this section. Synthesis was not performed under acidic conditions because the precursors were degraded. No solid was obtained for T-MP4-B even after three weeks of reaction at $50 \text{ }^\circ\text{C}$.

i. Composition and local structure motifs

To obtain information on the functional groups and the local structure, FTIR was performed. The results are displayed in **Figure 35**.

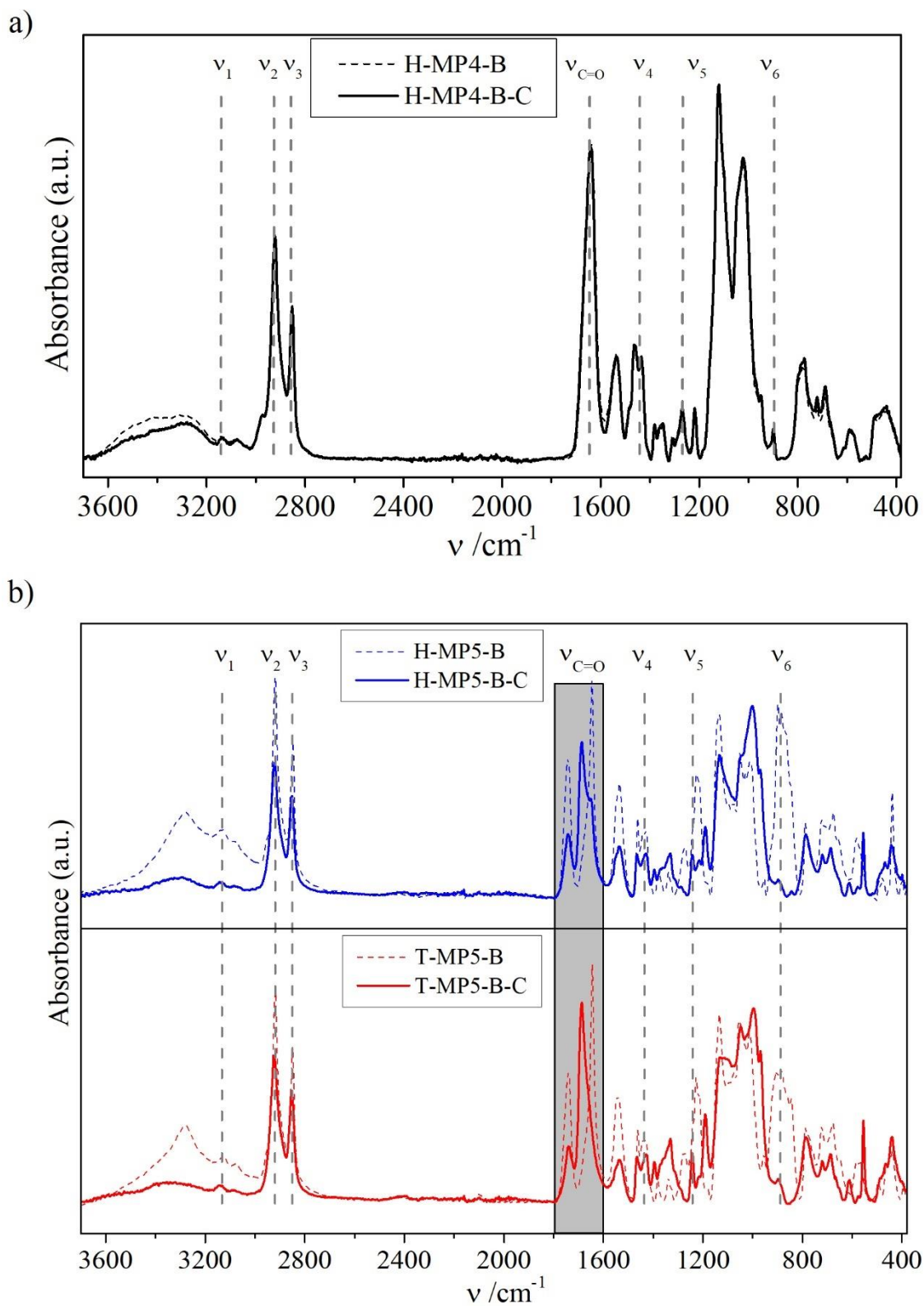


Figure 35. FTIR spectra of the fresh and thermally treated materials obtained from the precursors P4 (a) or P5 (b).

Not considering the diglycolic amide headgroup, the peaks highlighted ν_1 to ν_6 attest the retention of the molecular structure. The peak assignment is identical to the earlier FTIR spectra. Likewise, the broad peak between 3600 and 2800 cm^{-1} that is assigned to the X-H vibration modes, decreases after thermal treatment. The remarkable feature of this region is a sharp peak at 3280 cm^{-1} . This is indicative of a specific water H-bonding (see below).^{195–197} After thermal treatment, the residual broad peak at 3400 to 3200 cm^{-1} is attributed to the N-H vibration of the secondary (2°) amide. The decrease of the other modes is due to the reaction of the free silanol groups and the evaporation of the residual water. Additionally, the disappearance of ν_6 assigned to the Si-OH stretching mode, attests the advancement of the silane polymerization. The asymmetric position of the C-H stretching mode (ν_2) around 2920 cm^{-1} and the ratios $R_{alkyl} = \frac{I(\nu_2)}{I(\nu_3)}$ between 1.34 and 1.5 indicate an extended conformation of the alkyl chains.

Between 1800 and 1600 cm^{-1} , the C=O stretching modes and, here around 1640 cm^{-1} , the water bending modes are found. For H-MP4-B(-C) the peak at 1640 cm^{-1} is also assigned to the tertiary (3°) amide. The presence of the headgroup is, thus, confirmed. For the **P5** materials, a zoom of this region is shown in **Figure 36**.

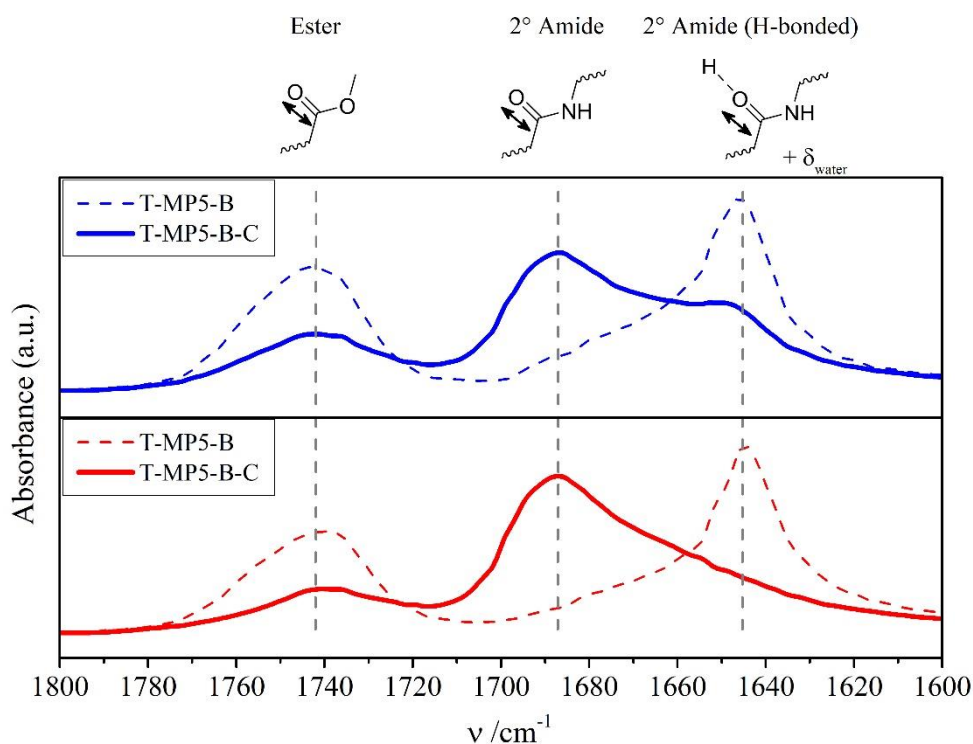


Figure 36. Zoom of the FTIR spectra of the **P5** materials. The assigned modes illustrated above.

Comparing the FTIR spectra of A4 and A5 (see **Figure A.6**) with the spectra displayed in **Figure 36**, three peaks are identified confirming the retention of the headgroup. The peak at $\sim 1740\text{ cm}^{-1}$ is attributed to the ester. After thermal treatment, its position remains unchanged but the intensity decreases. The other two peaks are attributed to the 2° amide. H-bonded carbonyls being typically red-shifted, the peak at $\sim 1650\text{ cm}^{-1}$ is assigned to the

H-bonded 2° amide and the peak at $\sim 1690\text{ cm}^{-1}$ is assigned to the free 2° amide.¹⁹⁸ The former is probably overlapped with the water bending mode. The attribution of the peak at $\sim 1650\text{ cm}^{-1}$ to the formation of an *e.g.* 3° amide or carboxylic acid during the sol-gel process is excluded because of the blue-shift after thermal treatment. In the investigated materials, the residual water, the uncondensed silanol groups or the 2° amide are potential H-bond donors that can be responsible for the red-shift of the 2° amide peak.

To determine the molecular weight of the synthesized materials and to verify the retention of the functional groups, TGA was performed. The results are plotted in **Figure 37**.

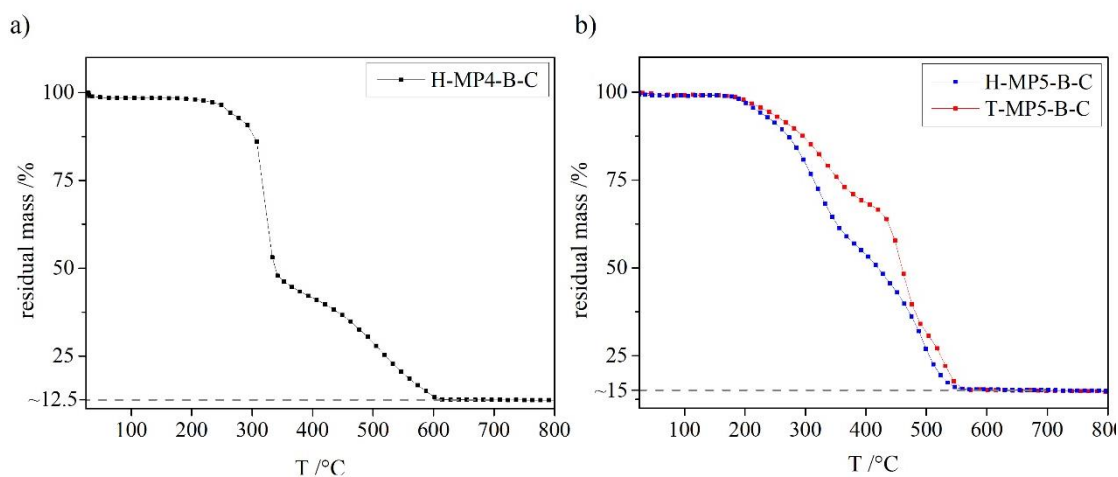


Figure 37. TGA weight loss curves of H-MP4-B-C (a) and H/T-MP5-B-C (b) in percent of the original mass during heating to 1000 °C. The dashed grey line indicates the residual mass percentage at 700 °C.

The weight loss curves show several consecutive weight losses corresponding to the degradation of the organic part of the materials. For H-MP4-B-C, a first weight loss of 60 w% takes place at $\sim 300\text{ °C}$. The second weight loss of 28 w% is observed at $\sim 460\text{ °C}$. For the materials produced from the precursor **P5**, the situation is similar. A first weight loss is observed at an onset temperature of $\sim 250\text{ °C}$. In this step, 40 w% (H-MP5-B-C) or 30 w% (T-MP5-B-C) are lost depending on the material. The final weight loss of 45 w% (H-MP5-B-C) or 55 w% (T-MP5-B-C) takes place at $\sim 450\text{ °C}$. Like explained earlier, only silica remains at $T > 600\text{ °C}$. Using these results, the molecular weight of the materials was calculated. The results are shown in **Table 8**.

Table 8. Residual masses at 700 °C and calculated molar masses M_{TGA} of the materials H-MP4-B-C and H/T-MP5-B-C.

Material	$w_{700^{\circ}\text{C}}$ (w%)	$M_{TGA}(\text{g}\cdot\text{mol}^{-1})$
H-MP4-B-C	12.5±1	481±30
H-MP5-B-C	15±1	401±30
T-MP5-B-C	15±1	401±30

The calculated molecular masses are in reasonable agreement with the theoretical values (475 g mol⁻¹ for H-MP4-B-C and 432 g mol⁻¹ for H/T-MP5-B-C). Hence, the functional groups are considered to be retained. Slight differences of the thermal stability are noticed between the materials H-MP5-B-C and T-MP5-B-C.

ii. Supramolecular organization

In order to obtain further structural information on the materials, SAXS was performed. The results are shown in **Figure 38**.

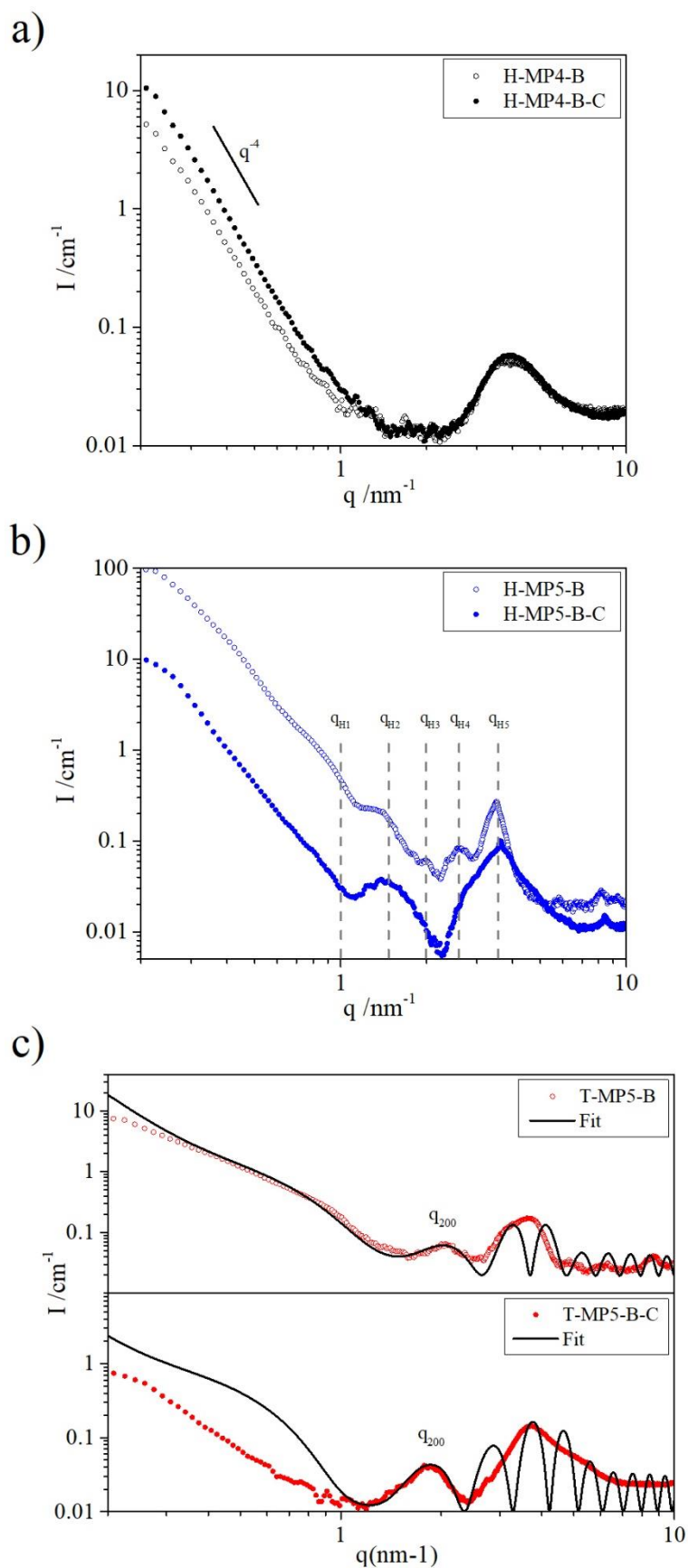


Figure 38. SAXS patterns of the materials synthesized from P4 (a), and P5 in water (b) or THF (c). The labels q indicate the Bragg peak positions.

All SAXS patterns show excess scattering at $q < 2 \text{ nm}^{-1}$ in the observation window with a slope proportional to q^{-4} . This indicates the presence of solid objects with a smooth surface. Furthermore, Bragg peaks are observable that allow the identification of the mesophases. In all patterns, a large peak at $\sim 4 \text{ nm}^{-1}$ is observed. For H-MP4-B(-C) (see **Figure 38 a**)), the absence of further peaks prevents the structure identification. For H-MP5-B(-C) (see **Figure 38 b**)), a 2D hexagonal structure can be identified using the Bragg peaks indicated q_{H1} to q_{H5} . Here, the first order peak q_{H1} at $\sim 1 \text{ nm}^{-1}$ (corresponding to a distance of 6-7 nm in real space) is barely visible because of its position on the slope. After thermal treatment, the enlarging of the peaks indicates the disordering of the structure. For T-MP5-B(-C) (**Figure 38 c**)), a lamellar structure is identified using a qualitative fit similar to that explained for **Figure 31**. It should be noted, that the fit was calculated without taking disorder into consideration. Nonetheless, the second order peak (q_{200} in **Figure 38 c**)) and some higher order peak positions for H-MP5-B are in good agreement with the fit. The lamellar structure shows an expansion from 6 nm to 6.7 nm^{-1} after thermal treatment. It is important to note that several Bragg peaks were identified in the WAXS part of the patterns of H-MP5-B and T-MP5-B (see **Figure A.7**). The peaks are more pronounced for T-MP5-B. For both materials, they disappear after the thermal treatment.

A proposition of material evolution after the thermal treatment is illustrated with the scheme in **Figure 39**.

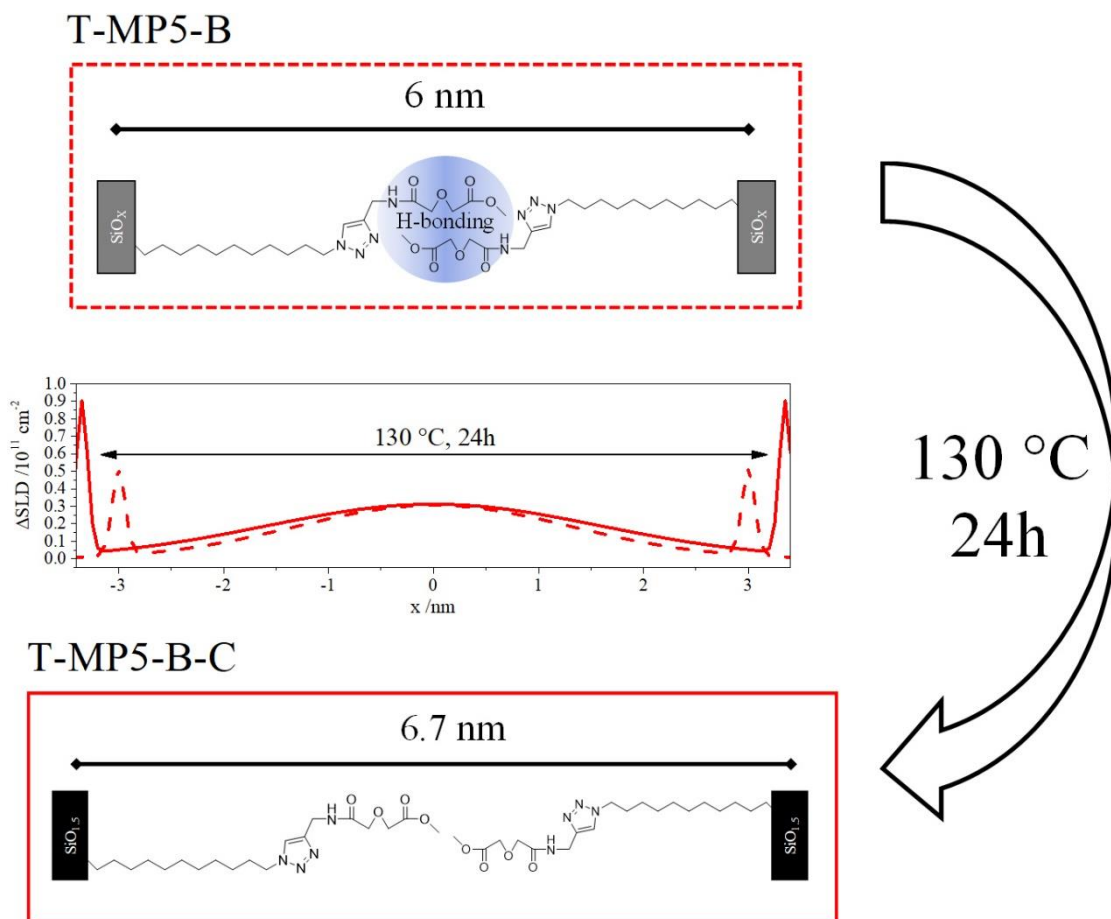


Figure 39. Scheme of the structural evolution of the material T-MP5-B during thermal treatment. The inset graph shows the SLD model used for the SAXS fits in Figure 38 c).

All results obtained so far for the material H-MP5-B indicate a lamellar structure with intercalated headgroups that are H-bonded to each other and with residual water (blue circle in **Figure 39**). After thermal treatment, the residual water is evaporated and the intercalation is broken. The H-bonding observed by FTIR (see **Figure 36**) and the Bragg peaks observed in the WAXS patterns (see **Figure A.7**) for the fresh materials that disappear after thermal treatment, support the hypothesis of an ordered intercalated phase. For the materials H-MP5-B(-C), the presence of similar features indicates that the situation is analogous but for cylindrical objects in a 2D hexagonal arrangement.

The different morphologies of the materials synthesized in water and THF may be explained by the formation of favorable H-bonds. Indeed, in organic solvents, H-bonds can persist up to high dilutions leading to the formation of agglomerates. Therefore, in THF, a H-bonded pseudophase can be supposed consisting of the headgroups and water. The silanols, then, would polymerize in a lamellar organization due to the geometric constraints of the precursor. In water, sufficient amounts of H-bond donors and acceptors are present and the headgroups can be hydrated. Consequently, the hydration of the headgroup would lead to an apparent increase of the packing parameter and this favors the formation of a 2D hexagonal phase.¹²⁰ After freeze drying, the formed structures

would remain thanks to the H-bonds through the means of the residual water. Once the water is removed, the driving force for the intercalation disappears and the structures dilate. None of this is observed for the precursor **P4**. The reason could be the steric demand of the diethyl amide group that prevents the close approach of the molecules.

iii. Summary

Resuming, the diglycolamic acid precursors **P4** and **P5** were readily polymerized under basic, aqueous conditions. In THF, a small yield was obtained for **P5** and no material was obtained for **P4**. Under acidic conditions, the degradation of the headgroup was observed. While no structure was determined for H-MP4-B(-C), two different mesophases were identified for H-MP5-B(-C) and T-MP5-B(-C). H-bonds between the headgroups and water presence are supposed to be at the origin of the formation of the different mesophases.

3 Conclusion

The investigation of the polymerization of the five newly synthesized precursors in water and THF under acidic and basic conditions allowed the identification of several methods to influence the mesoscale organization of silsesquioxanes. An overview of the results is given in **Figure 40**.

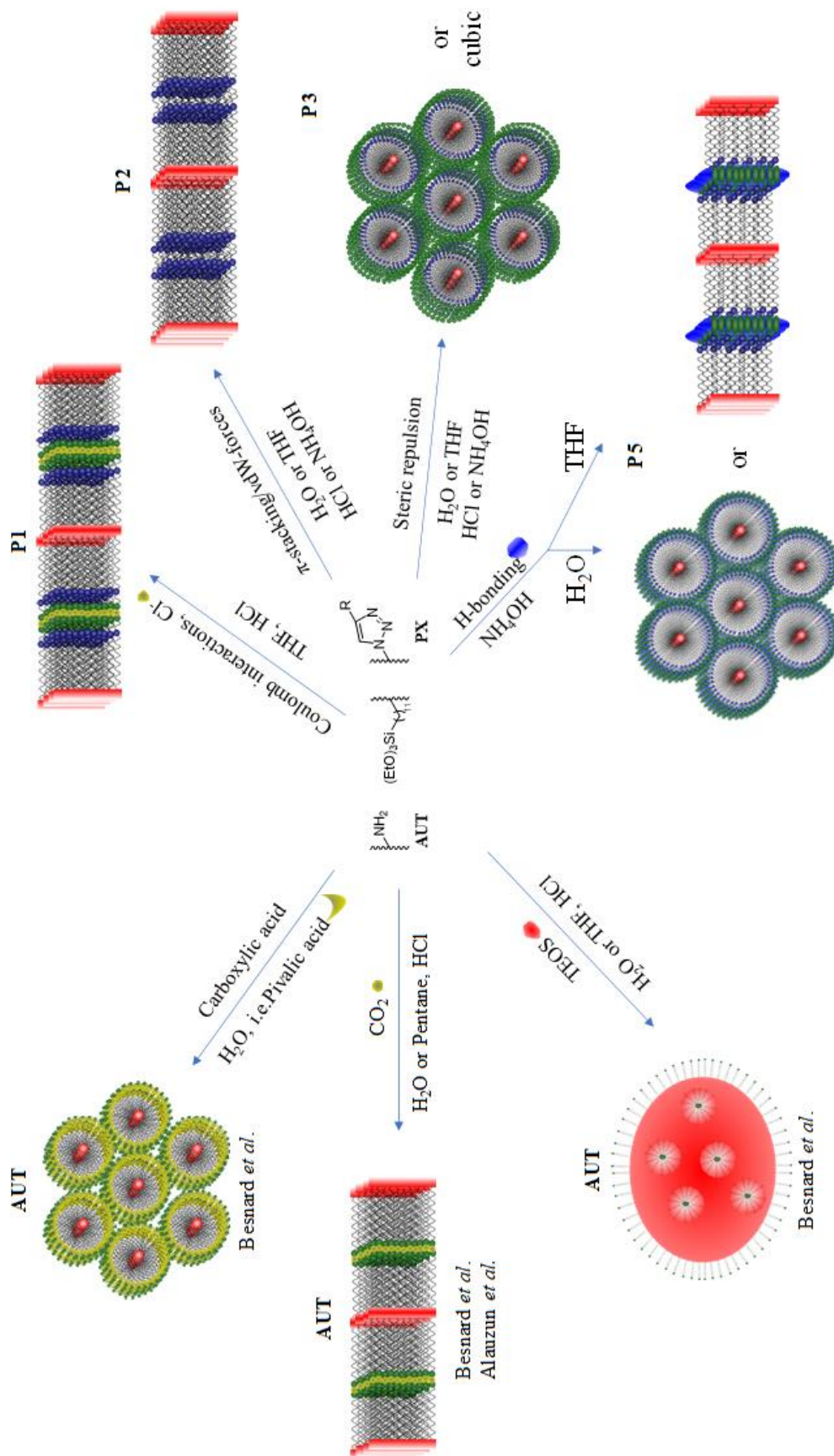


Figure 40. Overview of the identified methods to influence the mesoscale structure of the linear silsesquioxane precursors AUT¹⁰ and PX (this work).

The results of Besnard *et al.*¹⁰ and Alauzun *et al.*¹¹ were discussed earlier (see **I**). Their employed methods were not reinvestigated in this work. The polymerization of the newly synthesized precursors (**PX**) revealed the application of fundamental interactions to tailor the mesostructure of the fresh materials. Strong coulomb forces led to the formation of lamellar structures of T-MP1-A. A combination of vdW-interactions and π -stacking lead to highly ordered materials from **P2** regardless of the solvent or the catalyst. When using **P3**, the existence of structures with an overall curvature towards the silica matrix is correlated to the steric demand of the rigid, conjugated ester headgroup. Finally, for **P5**, the formation of a H-bond rich pseudophase between the head-groups is suspected to induce either a 2D hexagonal or a lamellar mesophase depending on the solvent. Moreover, in this study, it was shown that the specific headgroup interactions and the chemical affinity/reactivity between silanol groups drive the local connectivity of the siloxane network and the mesostructure in the final SHM. It is apparent that both are simultaneously responsible for the obtained morphology. In any case, the structures were found to be more defined before the thermal treatment. During the consolidation, the formation of new siloxane bonds severely twists non-lamellar mesophases leading to a loss of order. Lamellar structures, however, are found to be more resistant due to the one-dimensionality of the siloxane network contraction.

IV MATERIALS FROM TEOS

IN MIXED SOLVENTS

This chapter will investigate the impact of solvent structuring on the acid-catalyzed sol-gel process using TEOS. **Figure 41.** indicates the place of this chapter in the strategy outline.

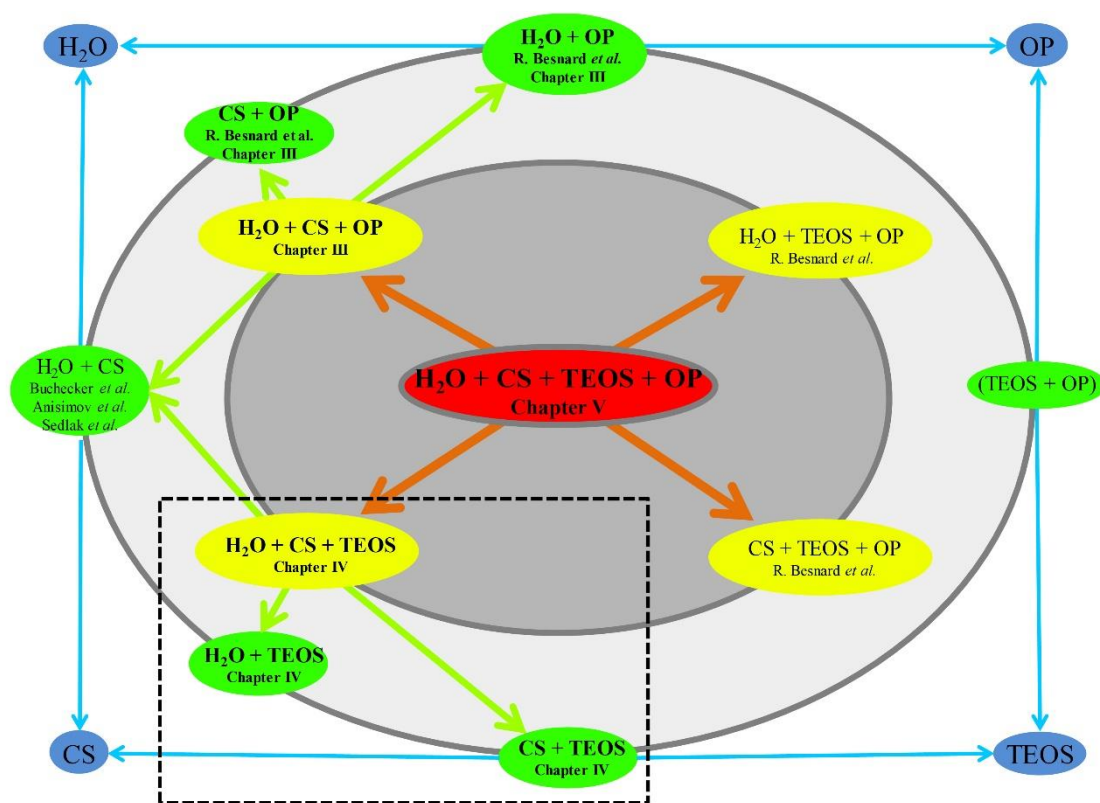


Figure 41. Illustration of the physical interaction hierarchy in systems containing water, co-solvent (CS), TEOS and a surfactant-like organosilane precursor (OP). A detailed explanation is given with Figure 13. The black circle marks the system discussed in Materials from TEOS in mixed solvents IV.

In the present conditions, aerogels are obtained.³⁰ A part of the results from this chapter was published.¹⁹⁹

1 Introduction

Silica aerogels are industrially widely applied materials^{200–203} due to their unique properties such as low thermal conductivity, low refractive index, optical transmission, low density, and high specific surface areas.²⁰⁴ Especially their high porosity and high specific surface area make them a useful choice for many applications like thermal insulation²⁰⁵, oil-water separation²⁰⁶, analytics²⁰⁷ and depollution.²⁰⁸ Furthermore, their production is nowadays easily scalable. The crucial factor of aerogel synthesis is the conservation of the wet gel structure during drying. To this end, the capillary forces must be minimized by using a low surface tension solvent during drying like supercritical CO₂.³⁰ To create wet gels that exhibit the desired properties, well-reported templating approaches can be used.^{78,209–212} Also, high internal phase emulsions can lead to foams exhibiting interesting properties.⁹⁶ Conventionally, large, self-assembling molecules known as surfactants are used because their free energy of structure formation is strongly favorable.²¹³ However, in a recent study⁶⁶, the effect of water/ethanol/dichloromethane microemulsion on the ammonia catalyzed silica polymerization was investigated. They found a connection between the type of microemulsion (W/O, bicontinuous or O/W)²¹⁴ and the obtained silica morphology, thus, proving the possibility of templating by surfactant-less microemulsions. In this paper, we investigate the fundamental aspects of using structured solvents in silica aerogel elaboration.

Such structures have been observed in mixtures of small amphiphilic molecules like EtOH or -most prominently- TBA and a hydrophilic solvent.^{215–220} The addition of hydrophobic molecules like 1-octanol amplifies this structuring.^{63,221–223} Here, subtle balances between hydration forces, entropy and curvature play important roles in the solvent structuring on the mesoscale.^{55,224,225} It is more reasonable to speak of fluctuating hydrophobic and hydrophilic domains instead of defined structures. In spite of their shapeless nature, such compartments show an influence on chemical reactivity.^{226–229}

Among the studies on chemical reactions in such structured solvents, very few deal with the synthesis of polymers²³⁰ or the sol-gel process.⁶⁶ Another recent study²³¹ showed that even the presence of binary mixtures of a deep-eutectic solvent and water is able to influence the silica morphology. A surprising result was reported by Wang *et al.*²³² where a small amount of a co-solvent is responsible for the formation of silica nanosheets.

In this study, the sol-gel process is performed in a system that contains only the essential components: TEOS as Si-source, water for hydrolysis, an alcohol to assure solubilization and HCl as catalyst. TEOS content and HCl/TEOS ratio are kept constant, in order to reduce experimental variables. To investigate the effect of structuring, like mentioned before, TBA is the ideal candidate.²¹⁸ For comparison, EtOH was chosen as non-structuring counterpart.

2 Sample preparation

From the ternary diagrams, several water/alcohol ratios were selected and are referred to as Acx to Gcx with $X=2$ for ethanol and $X=4$ for *tert*-butanol (**Table 9**). For the sample H_{REF} , no alcohol was added. The materials were prepared using an acid catalyzed sol-gel process. Ethanol or TBA, water and 37 w% HCl were mixed in the appropriate ratios indicated in **Table 9**. After stirring, TEOS was added and the container was closed. Biphasic samples were vortexed until complete mixing. The longest time required to obtain a monophasic sample was 3 min for H_{REF} (**Table 9**). Afterwards, the sols were kept in an oven at 50°C until two days after gelification. Then, the gels were transferred into 100 mL of ethanol and aged for one day at room temperature. Next, ethanol was decanted from the transparent gels and 100 mL of acetone were added. After ageing for 24h, the decanted gels were dried using SC CO₂ process. This was performed with a SEPAREX supercritical fluid extractor using a SC CO₂ flow of 30 g/min, at 100 bar and 60°C during 3 hours. The obtained white powders were kept in the glove box to prevent degradation. The sample references and compositions are presented in the **Table 9**.

Table 9. References, weight and molar fractions of alcohol and water in the samples containing 7.5 w% TEOS and 3.6 w% HCl ($n(\text{TEOS})/n(\text{HCl}) = 2.78$). Their localization in a ternary phase diagram is shown in Figure 42

Co-solvent	Reference	Weight fractions		Molar fractions	
		w_{water}	w_{alcohol}	x_{water}	x_{alcohol}
Ethanol	A_{C2}	0.1	0.79	0.24	0.71
	B_{C2}	0.15	0.74	0.32	0.63
	C_{C2}	0.24	0.65	0.47	0.49
	D_{C2}	0.33	0.56	0.58	0.38
	E_{C2}	0.43	0.46	0.68	0.29
	F_{C2}	0.61	0.28	0.82	0.15
	G_{C2}	0.8	0.09	0.93	0.04
Tert-butanol	A_{C4}	0.1	0.79	0.32	0.6
	B_{C4}	0.15	0.74	0.42	0.51
	C_{C4}	0.24	0.65	0.57	0.37
	D_{C4}	0.33	0.56	0.68	0.27
	E_{C4}	0.43	0.46	0.76	0.2
	F_{C4}	0.61	0.28	0.87	0.1
	G_{C4}	0.8	0.09	0.94	0.03
Ref. without alcohol	H_{REF}	0.89	0	0.97	0

Table 10. Samples used for the SAXS measurements (see Figure 43 b) and d)) All sample contain 7.5 w% TEOS.

Co-solvent	Reference	Weight fractions		Molar fractions	
		w_{water}	w_{alcohol}	x_{water}	x_{alcohol}
Ethanol (SAXS at t_0)	A_{C2}^*	0.14	0.79	0.28	0.71
	B_{C2}^*	0.19	0.74	0.36	0.63
	C_{C2}^*	0.28	0.65	0.50	0.49
	D_{C2}^*	0.37	0.56	0.61	0.38
	E_{C2}^*	0.46	0.46	0.70	0.29
<i>Tert</i> -butanol (SAXS at t_0)	A_{C4}^*	0.14	0.79	0.38	0.6
	B_{C4}^*	0.19	0.74	0.47	0.51
	C_{C4}^*	0.28	0.65	0.61	0.37
	D_{C4}^*	0.37	0.56	0.71	0.27
	E_{C4}^*	0.46	0.46	0.79	0.2

3 Phase behavior of the ternary system

In order to determine the solubility of TEOS in the binary mixtures of alcohol/water and to choose the most suitable sol compositions, first, the phase diagrams of the systems TEOS/alcohol/water were determined. Since TEOS hydrolyzes very fast at low pH, the phase diagram was prepared without catalyst addition. The phase diagrams are presented in **Figure 42**. The sample compositions are also displayed. “A” to “G” denote both A_{C2} and A_{C4} to G_{C2} and G_{C4} . For presentability in **Figure 42** the water and the HCl weight fraction in the prepared samples (see **Table 9** for compositions) were added to give “ w_{water} ” in the diagram.

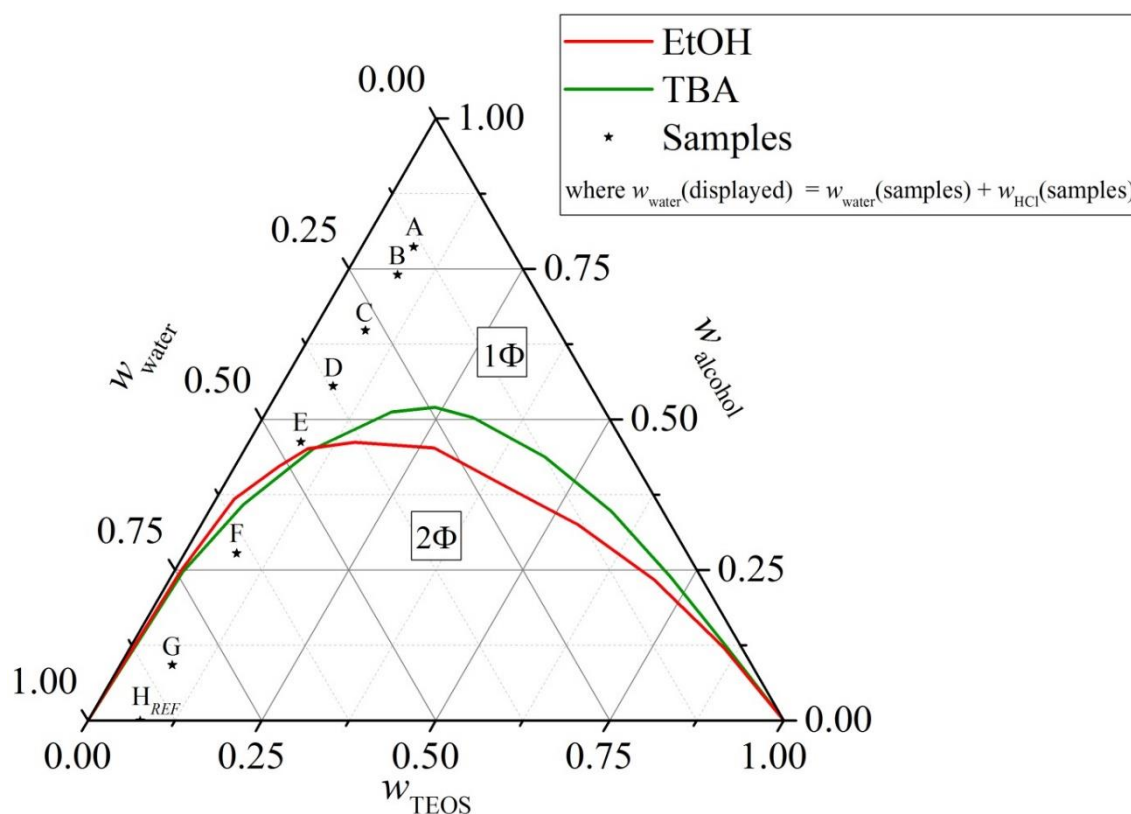


Figure 42. Ternary phase diagrams of the systems water/TBA/TEOS and water/EtOH/TEOS in weight fractions determined at $25 \pm 0.5^\circ\text{C}$. The mono- and biphasic regions are indicated in the respective areas. The selected sols are referred A to H (see Table 9 for compositions). “A” to “G” denote both A_{C2} and A_{C4} to G_{C2} and G_{C4} . For presentability, the water and the HCl weight fraction in the prepared samples (see Table 9 for compositions) were added to give “ w_{water} ” in the diagram.

Both phase diagrams show the classical behavior of systems containing two immiscible components, in this case water and TEOS, and a co-solvent, which is completely miscible with the other two. When adding a certain quantity of co-solvent (here: EtOH or TBA) the system can be mixed. The necessary amount to reach the monophasic region depends on the ratio of the immiscible components and the nature of the co-solvent. In addition, for considerations on the solubilization capacity of the co-solvent, a ternary phase diagram in molar fractions is illustrated in **Figure A.8**. The biphasic area is slightly smaller with TBA than with EtOH. Several reasons for this difference are identified: (i) the nature of the co-solvent, for example, its polarity or its molecular structure^{55,213,233}, and (ii) the co-solvent-co-solvent and co-solvent-solute interactions.^{63,234} According to earlier work⁶³, the high concentration of a solute with weak co-solvent-solute interactions favors solubilization by the integration of the solute in a hydrophobic pseudophase. In our case, the presence of a sufficient amount of TBA leads to a pre-structuring where the hydrophobic TEOS can be solubilized. In the case of EtOH, this pre-structuring does not exist and the solubilization of strongly hydrophobic compounds is less efficient.

4 Impact of the TEOS addition on the sol structuring

To gain further information on the samples, their structuring on the mesoscale was investigated by SWAXS at room temperature. The changes associated with the heating to 50 °C are considered to be not fundamentally important.²³⁵ The scattering patterns of the samples without HCl just after the addition of the 7.5 w% TEOS and of their associated binary mixtures are shown in **Figure 43**. The data in **Figure 43c**) were already published earlier.⁶³ The SAXS patterns of samples F_{CX} to H_{REF} are not displayed in **Figure 43** because they are biphasic and, therefore, not comparable to the systems without TEOS. The weight fractions of water of samples A_{CX} were adjusted to 0.1 in binary mixtures and 0.0925 in ternary mixtures to be compared with the data from the literature.

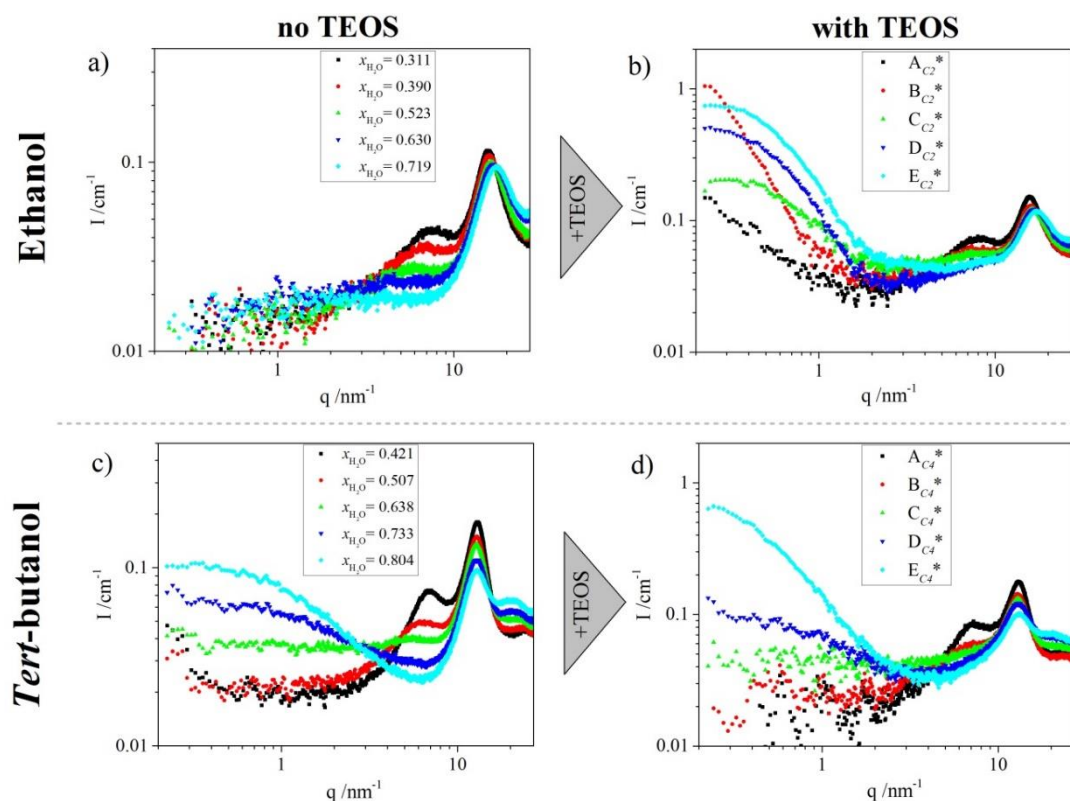


Figure 43. a) and c) SWAXS patterns of binary alcohol/water mixtures. b) and d) SWAXS spectra of ternary TEOS/alcohol/water mixtures at neutral pH just after the 7.5 w% TEOS addition. Data for c) was already published earlier.⁶³ Sample compositions of ternary mixtures are given in Table 10.

These SWAXS patterns display several results which depend on the solvent. First, at high q ($q > 3 \text{ nm}^{-1}$) several peaks attributed to the various pair correlations are visible. First, the peak at 20 nm^{-1} assigned to O-O pair correlations in the H-bonding network of water are visible in all patterns. It shifts slightly to smaller q with increasing alcohol contents. This corresponds to an increase of the distances in real space and may indicate the partial disruption of the H-bonded network.²³⁶ Second, the peaks at 15.5 nm^{-1} for the samples with EtOH and at 13 nm^{-1} for the samples with TBA corresponds to characteristics distances of approximately 0.4 nm and 0.5 nm respectively and are assigned to the pair correlations between the alkyl chains.²³⁷ Whereas their intensity depends on the alcohol content, their position does not shift significantly with the concentrations. The apparent shift of this peak to higher q in EtOH containing samples is due to the superposition with the peak assigned to O-O pair correlations. The apparent broadening upon addition of TEOS is due to the emergence of Si-Si pair correlations at 9 nm^{-1} and 16 nm^{-1} . In these mixtures, the peaks of TEOS are not clearly visible due to its low concentration. Thus, the positions of these peaks were determined using the SWAXS spectrum of pure TEOS. (see **Figure A.9**). Third, the peaks at 8 nm^{-1} (0.8 nm in real space) for EtOH and at 7 nm^{-1} (0.9 nm in real space) for TBA are attributed to the O-O correlation distance of the alcohol –OH groups.²³⁷ Accordingly, the peak intensity decreases with lower alcohol contents.

In the low q region of the pattern ($q < 3 \text{ nm}^{-1}$), significant differences between the two co-solvents can be noticed. In the samples with EtOH, the addition of TEOS, leads to a significant scattering increase presenting various slopes depending on the mixture: For the samples A_{C2} and B_{C2} a constant increase (q^{-1} for A_{C2} to $q^{-2.4}$ for B_{C2}) and no plateau are visible. For sample C_{C2} , D_{C2} and E_{C2} a plateau is reached. The plateau shifts to lower q values with increasing water contents. In the samples with TBA without TEOS, the scattering intensity increases with the water content from $x_{\text{water}} > 0.638$. A plateau is visible that shifts to lower q with increasing water content. After the TEOS addition, this scattering intensity increases noticeably whereas the shape remains the same (around one order of magnitude for sample E_{C4}) and the plateau shifts to lower q .

This intensity increase at low q indicates a structuring at the mesoscale.²³⁸ In the case of EtOH two different behaviors are observed. For lower water content (A_{C2} and B_{C2}), the maximum intensity is not inside the observation window indicating organization on a very large scale. The steeper slope for B_{C2} compared to A_{C2} indicates a structuring change. For C_{C2} and the samples with higher water contents, the intensity limit is in the observed q -range. This may be explained by the formation of large structures with trace amounts of highly hydrophobic compounds.²²³ In this case, the highly hydrophobic compounds may be the polycondensed oligomers of TEOS which are formed in the commercial product after the first opening due to air humidity.²³⁹ Thus, the excess scattering at low q for samples A_{C2} and B_{C2} is assumed to be caused by large shapeless aggregates. When adding more water, these aggregates get increasingly constrained by the H-bonding network of water formed around them (B_{C2}) until reaching objects of less than 30 nm in size (C_{C2} to E_{C2}).

In the binary system TBA/water, organization is due to rapidly fluctuating water- or TBA-rich aggregates.⁶³ This is typical for short chain alcohol/water mixtures.^{215–219} The visibility of these aggregates in SAXS patterns depends on their size and on their electronic density contrast to the rest of the solution. In EtOH/water mixtures, for example, the aggregates are too small and do not have a sufficiently high contrast to their surroundings to be visible.²¹⁷ When adding the hydrophobic TEOS a transition to a “pre-Ouzo” system is observed. Depending on the type and the weight percentage of co-solvent this leads to an enhanced structuring.^{55,63,240} In the case of TBA, the preformed structures are swollen by TEOS and this is visible in SAXS pattern by an increase of the intensity and the plateau shift to smaller q . This is due to a higher solubility of TEOS in the TBA-rich domains than in the water-rich domains. Samples which do not present any scattering intensity at low q in the binary mixtures remain unchanged upon addition of TEOS.

A size analysis of the aggregates in the structured systems gives insight on its morphology. Characteristic sizes were evaluated by the fitting of SAXS data. Classically, the SAXS patterns of surfactant-free microemulsions can be fitted using then Ornstein-Zernicke (OZ) function. The samples D_{C4} and E_{C4} and their corresponding binary mixtures show good agreement with the fit. In the samples without TEOS correlation

lengths of 0.65 nm for the binary mixture corresponding to D_{C4} and 0.77 nm for the binary mixture corresponding to E_{C4} are obtained. This is in agreement with literature.⁶³ In the samples with TEOS, correlation lengths of 0.88 nm for D_{C4} and 2.82 nm for E_{C4} have been found. Supposing spherical aggregates, the respective aggregate dimensions are 3.52 nm and 11.23 nm. The samples C_{C2} , D_{C2} and E_{C2} are fitted increasingly worse using the OZ function because the slopes at low q are too steep. However, approximatively, correlation lengths between 1.8 nm (C_{C2}) and 2.5 nm (E_{C2}) are obtained. The results are in agreement with an O/W microemulsion. The addition of TEOS enhances structuring by swelling the existing structure in the case of TBA or inciting the aggregation of the co-solvent around it in the case of EtOH. When decreasing the alcohol/water ratio (*e.g.* $D_{C4} \rightarrow E_{C4}$), the system minimizes the interphase formed by the alcohol. This is done by increasing the aggregate size. The results agree with the literature for similar systems. A swollen network of H-bonded groups is probably at the origin of the structuring.⁶² For ternary mixtures with low hydrophobic phase content close to the demixing line, structures resembling O/W aggregates were proposed.²⁴¹

To summarize, ternary mixture TEOS/alcohol/water (where “alcohol” can be EtOH or TBA) are typical surfactant-free microemulsions. The components take their roles as hydrophilic component (water), hydrophobic component (TEOS) and co-solvent or – more generally – hydrotrope (EtOH or TBA). The organization of components at the mesoscale increases when approaching the phase boundary.^{222,242,243} The type and the extend of structuring depends on the co-solvent. When using TBA, the aggregation is heavily influenced by structuring which is already present in the binary mixture TBA/water. They will allow the TEOS solubilization. With EtOH, structures which allow solubilization of TEOS are formed only in the ternary system.^{63,222}

5 Study of the sol-gel transition

After the addition of HCl used as a catalyst to initiate the TEOS hydrolysis, the durations until gelification at 50°C were determined by naked eye for both series. To confirm the results obtained by these observations for the TBA series and to reduce the error margins, gel time determination was also performed by dynamic light scattering (DLS).²⁴⁴ Upon TEOS addition, a slight heating was noticed that indicates the start of hydrolysis. The results are presented in **Figure 44**.

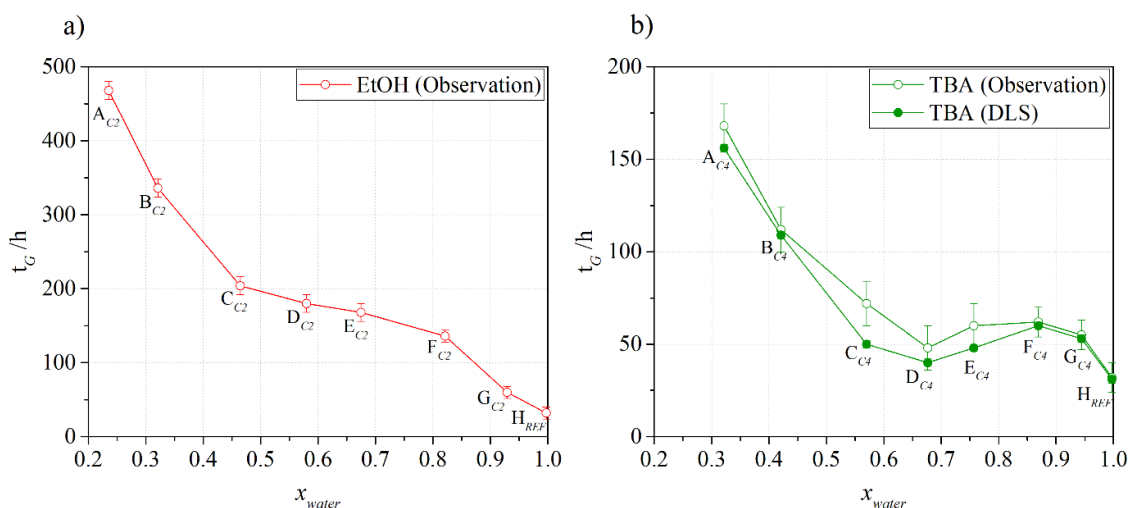


Figure 44. Gel times of the samples as a function of the molar fraction of water x_{water} as determined by observation and by DLS.

Comparing the results obtained by observation and DLS, overall shorter times were observed with the DLS method. However, all trends remain consistent. First, the gel times of the sols with EtOH at $x_{water} < 0.7$ are three times longer than the ones with TBA. This difference is reduced when the water content increases. Second, whatever the solvent, the gel time globally decreases with increasing water content. This evolution follows three stages. Up to $x_{water} = 0.5$, the gel time decreases almost linearly with the water content. For x_{water} higher than 0.5, the gel time decrease follows two different behaviors depending on the solvent. For sols containing EtOH, the gel time decreases linearly from $x_{water} = 0.5$ to $x_{water} = 0.8$ with a lower slope than at lower water contents. For sols containing TBA, the gel time evolution between $x_{water} = 0.5$ and $x_{water} = 0.8$ presents a minimum for the sample D_{C4} ($x_{water} = 0.677$). Finally, at high water contents ($x_{water} > 0.9$ for TBA and $x_{water} > 0.8$ for EtOH), a strong decrease of gel time is observed. Gel-time depends on the volume fraction occupied by the growing aggregate. Consequently, the aggregate structure has an important influence.

To investigate the morphology of the growing structures with the gel time, the structure evolution was followed by SAXS. The SAXS pattern evolution of the two sols C_{C4} and C_{C2} were chosen to illustrate the behavior and are presented in **Figure 45 a**).

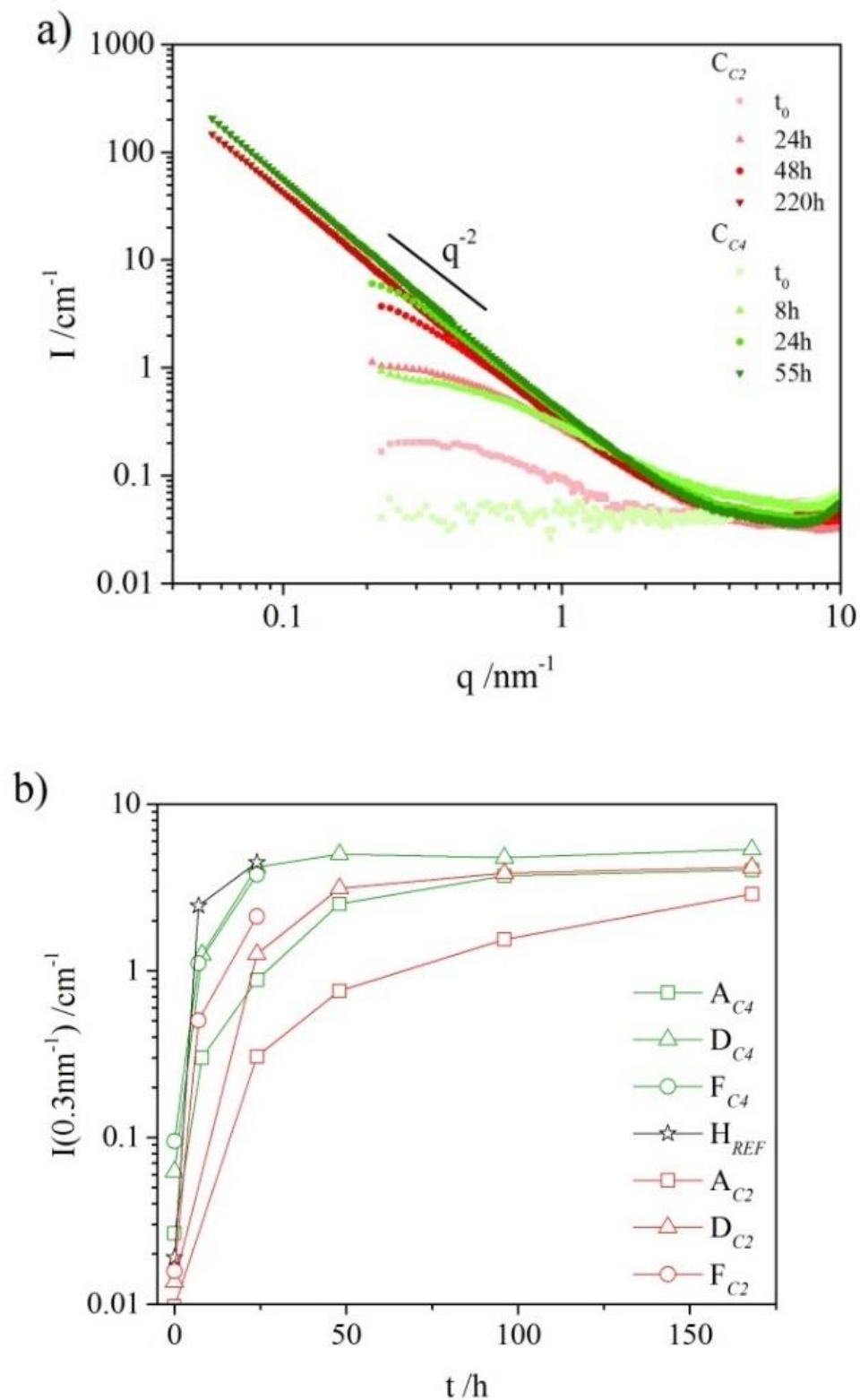


Figure 45. a) Evolution of the SAXS patterns of the sols C_{C4} and C_{C2} during the sol-gel transition. The symbol color intensifies with sample ageing. b) evolutions of the scattering intensity at $q=0.3 \text{ nm}^{-1}$ of the SAXS patterns as a function of time.

As discussed earlier, immediately after TEOS addition, the observed scattering originates from the mesoscale organization of unreacted components (t_0 in **Figure 45 a**). During the polymerization, the low q scattering develops the same way for all sols. Three aspects should be highlighted. First, all SAXS patterns present a slope proportional to $\sim q^{-2.1}$ (**Figure 45 a**). A plateau marks the end of this slope at low q . The intensity evolution rate of this plateau is proportional to the gel time as highlighted by the scattering patterns of C_{C4} 8 h and C_{C2} 24 h recorded at similar points during the polymerization ($\frac{t}{t_G} \approx 0.12$). During polymerization the plateau shifts to increasingly low q and higher intensities. Finally, after $\frac{t}{t_G} \approx 0.3$ no plateau is observable. Second, the slope is proportional to $\sim q^{-2.1}$ giving evidence of the nature of polymerization. Third, the initial organization of the water and the alcohol is not visible anymore after TEOS addition probably because its scattering is hidden under that of the developing silica polymer.

The evolution of the low q scattering pattern is characteristic for objects that primarily increase in size and not in number.³⁰ Logically, the disappearance of the plateau after $\frac{t}{t_G} \approx 0.3$ indicates that the correlation lengths become too large for the observation window. In **Figure 45 b**, the scattering intensities of selected samples at $q = 0.3 \text{ nm}^{-1}$ as a function of time are plotted. For all samples, like mentioned before, an increasing intensity is observed at longer times. The intensity increase is accelerated at higher water contents. The acceleration is directly correlated to the gel time of the samples. The shorter the gel times the faster the intensity increases. This is also observed for the development of Si-O-Si bonds as observed in the FTIR spectra (see **Figure A.10**).

The constant slope of $\sim q^{-2.1}$ is characteristic of the formation of fractal objects *via* a reaction limited cluster-cluster growth (RLCA) or a diffusion limited cluster-cluster growth (DLCA).^{30,31,245} Evidence has shown that rearrangements can lead to the same fractal dimensions.²⁴⁶ From the SAXS spectra we conclude that the polymerization rate is proportional to the gel time observed for the sols. Polymerization occurs *via* cluster-cluster aggregation of primary particles that are formed early in the process. The structural evolution is identical for all samples.

With the obtained structural information, the two different behaviors with EtOH and TBA in the region of samples A_{CX} to F_{CX} can be explained by several experimental factors. In order to simplify the explanation, it is assumed that hydrolysis was very advanced in all samples after several minutes and, thus, does not contribute to the gel time. This last assumption is reported in literature^{40,41} and supported by the fact that under acidic conditions, the hydrolysis is generally faster than condensation and the high $[\text{H}_2\text{O}]/[\text{TEOS}]$ ratio ($[\text{H}_2\text{O}]/[\text{TEOS}] = 15.7$ for samples A_{CX}) increases that effect.³⁰ This is also visible in the FTIR spectra of all samples which display a peak at 950 cm^{-1} corresponding to the $\equiv\text{Si-O}$ stretching of non-hydrolyzed TEOS only just after the TEOS addition. Moreover, the initially biphasic sample H_{REF} becomes monophasic after 3 min

of vortexing due to the increasing hydrophilicity of hydrolyzed species and the production of solubilizing EtOH during the reaction.

The first factor which affects the condensation rate is the concentration of catalytic species. A higher concentration increases the hydrolysis/condensation rate. Here, the catalysis occurs via the protonation of silica species and is proportional to the H_3O^+ concentration.³¹ The qualitative inspection of FTIR spectra (see **Figure A.11**) recorded along the polymerization showed that, indeed, the concentration of H_3O^+ increases with increasing water content. This is accordance with the observed trends.

Second, the re-esterification of hydrolyzed species may also impact the gel time. Indeed, partial re-esterification (RE) of hydrolyzed species is possible due to the reversibility of the hydrolysis reaction and can occur with reactive alkoxy species. Furthermore, RE is favored under acidic conditions.³⁰ TBA is too unreactive whereas EtOH is sufficiently reactive for this process to be considered.^{247,248} For our two systems, due to the high concentrations of EtOH compared to the strong dilution of silicate species, it is probable that RE leads to an overall decrease of silicate species reactivity. This effect is more pronounced at higher alcohol concentrations. In mixtures with high water content $x_{\text{water}} > 0.8$ this effect vanishes.

Third, the reaction rate is influenced by the repulsive forces between the charged primary particles and their diffusion. This is described by the aggregation rate constant k . The exact theoretical description of the aggregation rate constant k between two aggregates i and j is given by four terms.²⁴⁹

$$\begin{aligned}
 k_{ij} &= k_{ij}^{Diff} W^{-1} P_{ij} B_{ij} \\
 &= \frac{2k_B T}{3\eta} W^{-1} (ij)^\lambda \left(i^{\frac{1}{D_f}} + j^{\frac{1}{D_f}} \right) \left(i^{-\frac{1}{D_f}} + j^{-\frac{1}{D_f}} \right) \quad (8)
 \end{aligned}$$

Here, k_{ij}^{Diff} is the aggregation rate constant from Brownian diffusion, k_B the Boltzmann constant, T the temperature, η the dynamic viscosity, W the Fuchs stability ratio, λ the scaling constant ($\lambda = 0$ for DLCA and $\lambda = 0.5$ for RLCA) and D_f the fractal dimension of the aggregates. Evaluating the term $(ij)^\lambda$, the reaction between two identical aggregates has the highest rate and, therefore, determines the overall rate. With growing object sizes, the reaction rate increases. From scattering experiments (see **Figure 45**), it is known that the fractal dimension D_f of the objects remains constant with aggregate size. Therefore, it is sufficient to evaluate the reaction rate of two identical primary particles ($i = 1$ and $j = 1$) to analyze the aggregation behavior. This significantly reduces the complexity of **Eq (8)** to

$$\begin{aligned}
 k_{11} &= k_{11}^{Diff} W^{-1} = \\
 &= \frac{2k_B T}{3\eta} \left\{ 2r_0 \int_{2r_0}^{\infty} \frac{\exp\left(-\frac{V(h)}{k_B T}\right)}{h^2} dh \right\} \approx \frac{2k_B T}{3\eta} \left\{ \frac{2r_0}{\lambda_D} \exp\left(-\frac{V_{el}}{k_B T}\right) \right\} \quad (9)
 \end{aligned}$$

Here, h is the distance between particles, λ_D the Debye length, r_0 the primary particle radius, $V(h)$ the interaction potential at distance h and V_{el} the electric potential of two identical particles at contact.²⁵⁰ The last expression contains the approximation by Reerink and Overbeek.²⁵¹ This model only considers interaction potentials between surfaces from the classical DLVO theory. Nonetheless, the estimation of the electrostatic interactions gives indication about the behavior of the overall potential energies since the hydration of silica arises from surface charge.^{252,253} For the calculation of k the primary particle radii from the SAXS measurements (see **Table 11**), the viscosities^{254,255} (see **Figure A.12**) and the dielectric constants^{256,257} (see **Figure A.13**) were used. For the estimation of the electric potential, it is valid to approximate the primary particles to point charges. To determine the total charge of such a point charge, the surface charge density for silica determined at pH 0²⁵⁸ was applied on the spherical surface of the primary particles. The values of the surface potential are confirmed for the oppositely charged values at ~pH 9.^{258–260} A surface charge density of 1 charge/nm² was found valid. **Figure 46** shows the resulting reaction parameter k .

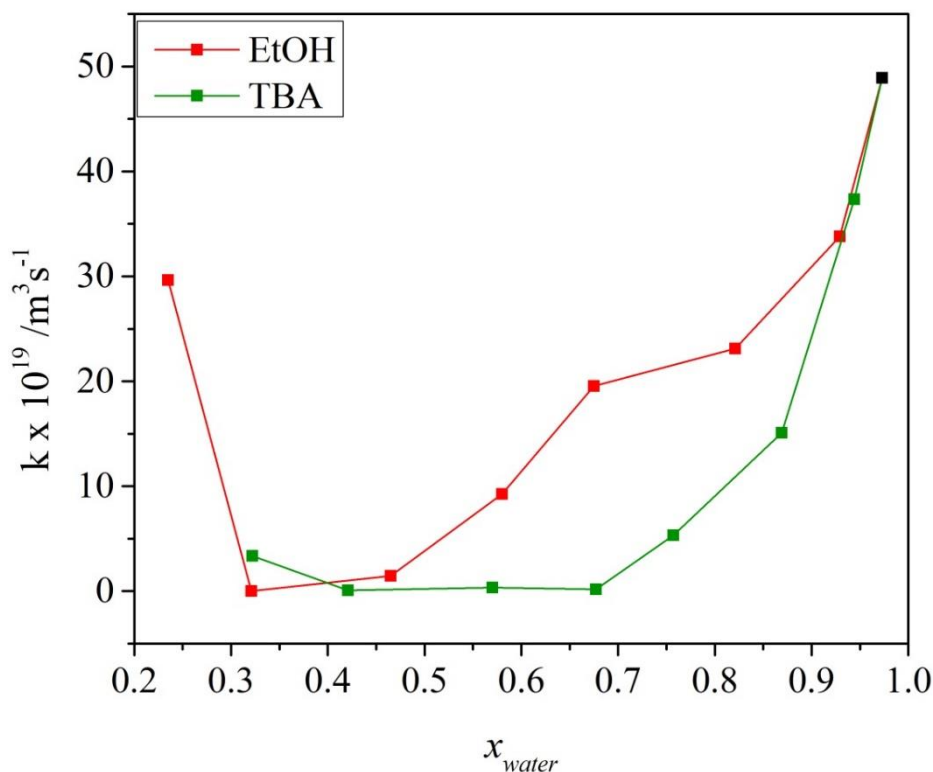


Figure 46. Reaction constants for the different sols estimated considering the electrostatic repulsion between primary particles.

Overall, the estimated reaction rate increases with increasing water concentration. For one, the viscosity decreases with increasing water concentration. Thus, the diffusion increases and objects potentially encounter each other more frequently. The encounters are moderated by repulsive forces between the objects. The increasing dielectric constant with increasing water concentrations attenuates the repulsive forces and the reaction rate accelerates.

While most of the gel time tendencies can be explained by these factors, the minimum of gel time for the sample D_{C4} cannot be explained by any of the mentioned factors because they describe continuous trends. A hypothesis allowing the explanation of this behavior is proposed in the discussion part.

6 Influence of the sol composition on the material structure

In order to obtain aerogels, first, a solvent exchange with EtOH was performed to induce the re-esterification of the materials surface making it more hydrophobic.^{261,262} This re-esterification reduces the capillary forces during solvent removal and, thus, minimizes the material modification during drying. Second, another solvent exchange with acetone and SC CO₂ was performed. Acetone was used for its high solubility in SC CO₂. The obtained materials were analyzed by nitrogen adsorption-desorption experiments. The specific surface areas S_{BET} obtained as a function of x_{water} are shown in **Figure 47**.

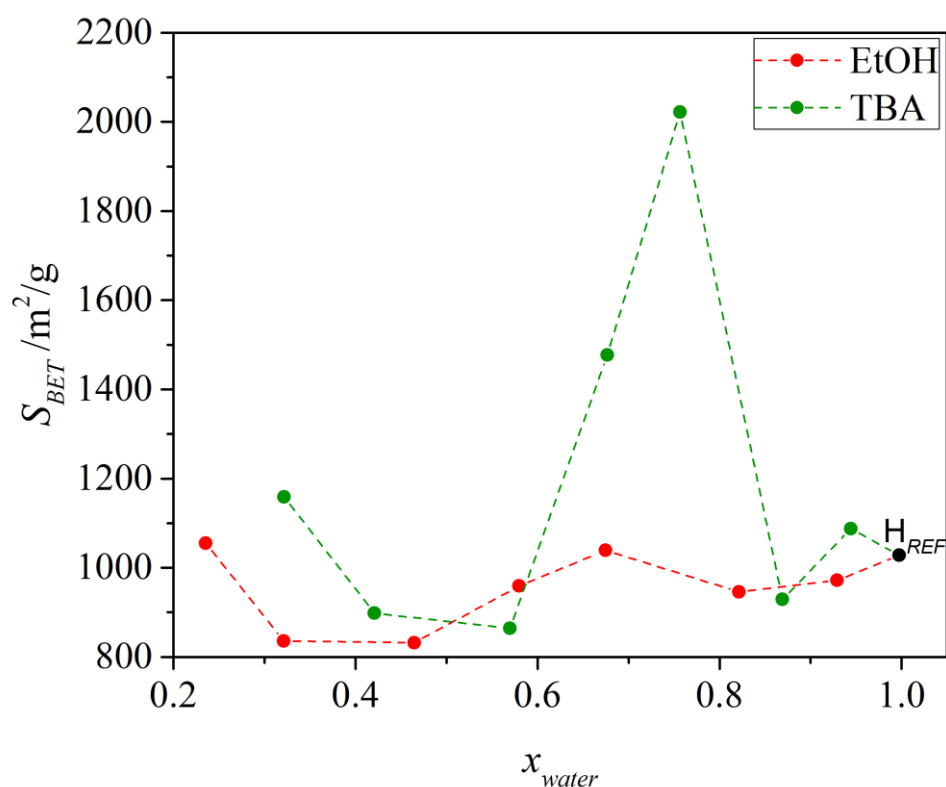


Figure 47. Specific surface areas (S_{BET}) of aerogels obtained by the BET method as a function of the molar fraction of water x_{water} in the corresponding sol.

Except for the samples D_{C4} and E_{C4} , whatever the solvent, aerogels have a similar S_{BET} of as around 1000 m²/g. For aerogels obtained from sols D_{C4} and E_{C4} S_{BET} of 1400 m²/g and 2100 m²/g are obtained respectively. This result can be related to the particular behavior in the sol-gel process already observed. The solvent of the samples D_{C4} and E_{C4} showed the most pronounced scattering.(see **Figure 43 c**) Furthermore, the samples D_{C4} and E_{C4} displayed unexpectedly low gel times.(see **Figure 44 b**)

To investigate the morphology at a scale of 1 to 30 nm SAXS was performed. The obtained scattering patterns are shown in **Figure 48**.

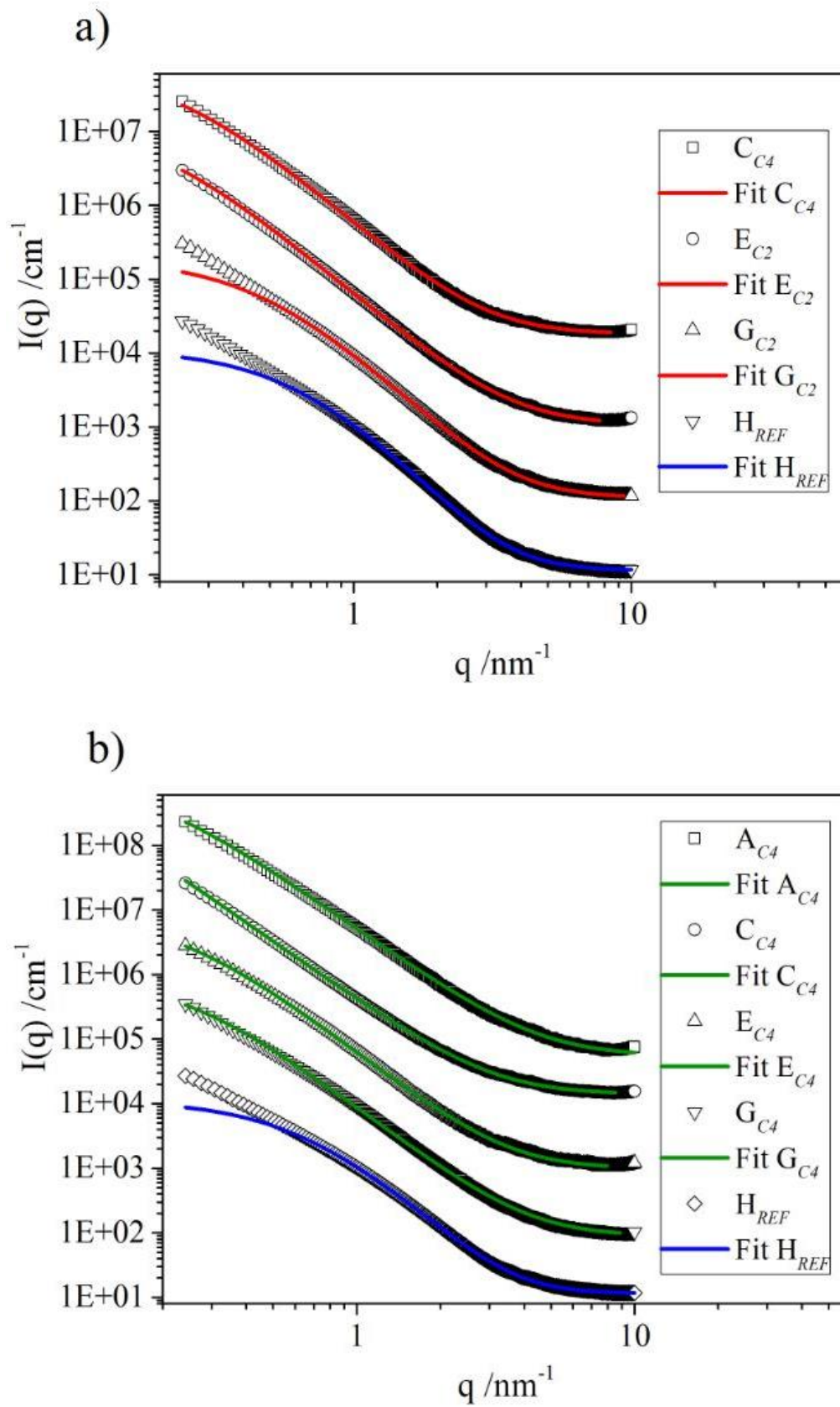


Figure 48. SAXS patterns of the aerogels with their corresponding fits. Data was multiplied by a factor of 10^x for better visibility. a) shows the SAXS patterns for aerogels obtained from ethanol containing samples and b) from TBA containing samples.

In all patterns, the same scattering evolution is observed. The data can be fitted using

$$S(q, \xi, D, r_0) = BG + \frac{D\Gamma(D-1)\sin([D-1]\arctan(q\xi))}{(qr_0)^D \left[1 + \frac{1}{q^2\xi^2}\right]^{(D-1)/2}} \quad (10)$$

where BG is the scattering intensity at high q ($> 10 \text{ nm}^{-1}$), q is the scattering vector, ζ the cut-off length of the fractal correlations, D the fractal dimension and r_0 the radius of the smallest scatterers. This function corresponds to a fractal structure with an exponential decay.²⁶³ This pattern is characteristic for aerogels produced from one-step acid catalysis.^{264,265} The scattering intensity starts to increase noticeably at $q < 8 \text{ nm}^{-1}$ indicating the formation of sub-nanometer sized particles. For the samples G_{C2} and H_{REF} and second contribution of fractal nature need to be added to achieve a good fit. The introduction of a second characteristic size is explained by the aggregation of primary particles into denser secondary particles. The complete fit results are given in **Table 11**. The values for D and ζ must be treated carefully because of the limited observation window in the present SAXS set-up.

Table 11. Results of the fits of the SAXS patterns of aerogels (see Figure 48). r_0 is the radius of the primary particles, D the fractal dimension and ζ the correlation length. The R-factor of the obtained fit is indicated in the last column. A good R-factor is below 0.1.

Co-solvent	Reference	r_0 /nm	D	ζ /nm	R-factor
Ethanol	C_{C2}	0.4 ± 0.1	2.75	4.2	0.04
	D_{C2}	0.3 ± 0.1	2.74	4.1	0.04
	E_{C2}	0.3 ± 0.1	2.74	5.0	0.042
	F_{C2}	0.3 ± 0.1	2.82	4.0	0.045
	G_{C2}	0.3 ± 0.1	2.85	2.0	0.019
Tert-butanol	A_{C4}	0.2 ± 0.1	2.70	5.4	0.033
	B_{C4}	0.3 ± 0.1	2.87	6.7	0.026
	C_{C4}	0.3 ± 0.1	2.73	12.3	0.034
	D_{C4}	0.4 ± 0.1	2.84	3.7	0.037
	E_{C4}	0.3 ± 0.1	2.81	4.1	0.046
	F_{C4}	0.3 ± 0.1	2.76	4.1	0.056
	G_{C4}	0.2 ± 0.1	2.78	3.9	0.067
Ref. without alcohol	H_{REF}	0.3	2.97	1.4	0.008

The samples were also characterized by TEM. A selection of the images is shown in Figure 49.

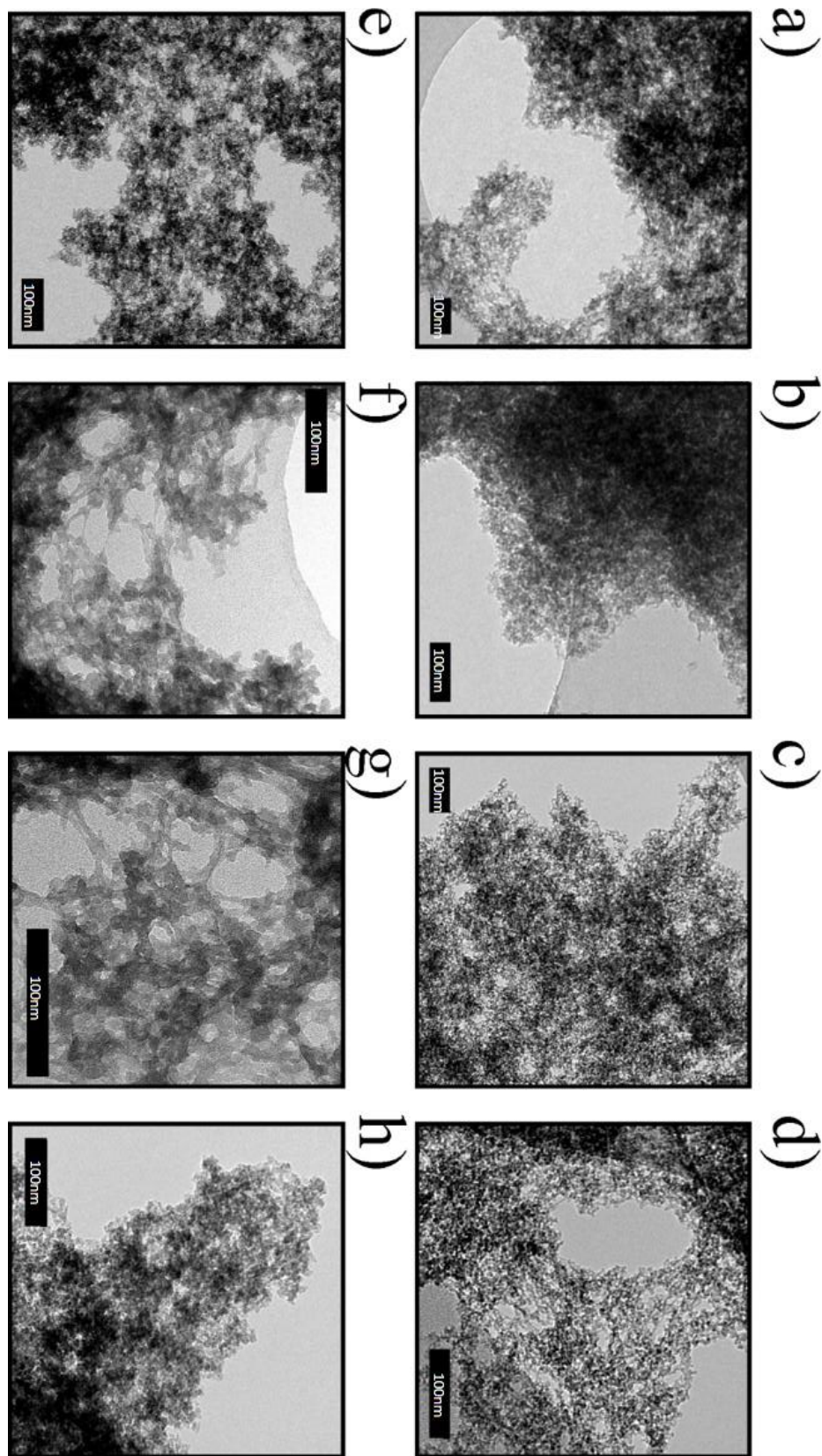


Figure 49. TEM images of aerogels produced from different sols: a) BC_2 , b) EC_2 , c) GC_2 , d) H_{REF} , e) AC_4 , f) DC_4 , g) EC_4 , h) FC_4 . Scale bar = 100 nm.

The TEM images show the typical granular structure of aerogels consisting in nanoparticles with radii of 0.2 to 0.8 nm. This agrees well with the sizes obtained by SAXS where radii from 0.23 to 0.36 nm were obtained. The structure at the scale of tens of nanometers varies between the samples. Samples where the solvent shows no excess scattering at low q are densely aggregated clusters (see **Figure 49 a) – e)** and **h)**). Aerogels that were produced in solvents where excess scattering at low q has been observed show an open network at the mesoscale (see **Figure 49 f)** and **g)**). This coincides with the samples that display increased specific surface areas. It is important to distinguish the porosity observed in samples D_{C4} and E_{C4} from the openings observable in the other samples. In D_{C4} and E_{C4} the surroundings of pores are like elongated bridges and flat surfaces. The openings observed in the other samples show the roughness at the size scale of primary particles and, therefore, merely represent holes due to sample preparation. Thus, TEM images indicate that the particular behavior observed for the sample D_{C4} and E_{C4} originates from structural differences.

7 Discussion

Binary mixtures of water and alcohol show interesting properties for the application as solvents in the sol-gel process. In the present comparison of EtOH and TBA, the typical formation of a surfactant-free microemulsion in the ternary mixture of water/alcohol/TEOS was observed. This mesoscale structuring, induced by the addition of hydrophobic TEOS, however, can be considered unimportant for the sol-gel process at low pH. The reason is the rapid hydrolysis of TEOS in the examined conditions which eradicates the induced structuring by the elimination of the hydrophobic compound. Then, the resulting hydrolyzed silicate species react to form sub-nanometer sized primary particles. By further Si-O-Si bond formation between the particles, an open silica network with fractal character is formed. The ratio of water/alcohol or the choice of alcohol does not change the mechanism of polymerization allowing the direct comparison. The network formation proceeds at different rates depending on the water/alcohol ratio which was observed by SAXS, FTIR and gel time measurements. As discussed, several experimental factors are responsible for the different rates. Investigations on the aerogels obtained after drying by SC CO₂, allow the conclusion that, indeed, a network of primary particles was formed during the sol-gel process. The aerogels displayed typical properties concerning specific surface areas and SAXS patterns and a typical morphology. However, two samples from the TBA-series display exceptional features that will be discussed in the following. The hypothesis on the mechanism is depicted in **Figure 50** in which the water content increases along the axis. The images illustrate the solvent behavior around the silica polymer. Light blue is water-rich phase, dark blue the hydration layer around silica and green the TBA-rich phase. In the picture illustrating pure water and the mixture 25 w% water in TBA (or TBA in water) the solution is considered as a homogeneous mixture. At the 50/50 mixture the solvent is considered heterogeneous. Here, it creates voids in the silica matrix after the sol-gel process.

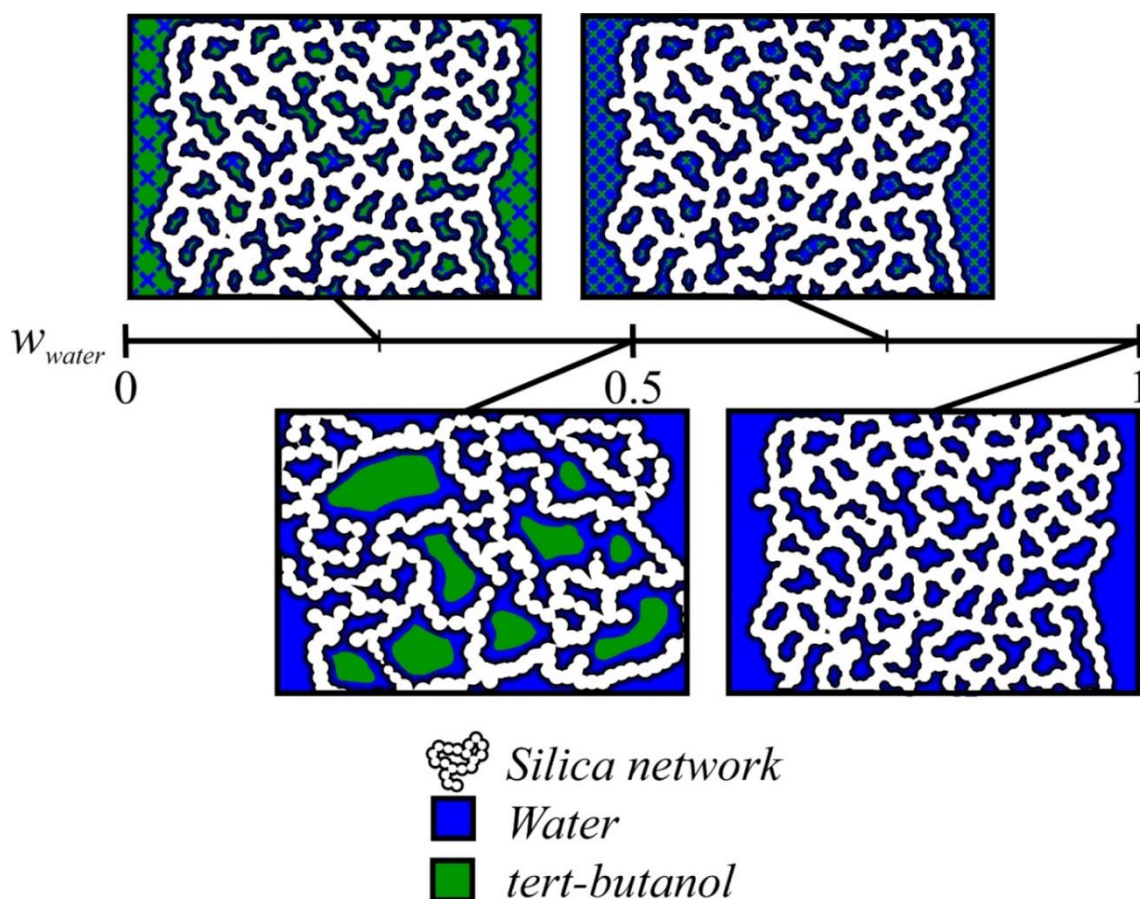


Figure 50. Simplified illustration of the structuring at the mesoscale during the sol-gel process according to the proposed mechanism.

Specific case of the C_{C4} and D_{C4} samples: impact of the solvent structuring

All the results obtained for the samples, $n(\text{TBA})/n(\text{water})$ of 0.404 (D_{C4}) and 0.264 (E_{C4}), suggest that compartmentation into water- and TBA-rich domains in mixed solvents is responsible for the gel time and the high specific surface area through the modification of the immediate environment of the growing silica polymer. Those ratios $n(\text{TBA})/n(\text{water})$ are similar to the ratios in the TBA/water binary mixtures for which structuring has been observed.^{220,227} However, this structuring is different from the classical templating the aggregation of large amphiphilic molecules. The free energy gain of structure formation in the present binary mixtures is very little. Therefore, the introduction of highly hydrophilic silica will influence the morphology of separated TBA-rich and water-rich domains instead of forming silica around existing domains. In this case, water-rich domains cover the surface of the growing silica polymer while TBA-rich domains are not in contact with silica. (see **Figure 50**) The reason is the positive surface charge on the silica surface that exists at the high acid concentrations ($\approx 1\text{ mol/L}$) in our experiments.²⁶⁶ The resulting counter-ion layer of solvated chloride ions supports the hydrophilicity. Thus, the immediate environment of the silica polymer can be considered as a bulk water phase above $x_{\text{water}} \approx 0.5$. As visible by the highest reaction rate observed for H_{REF} , a solution containing more water has an accelerating effect. The accelerating

effect is most pronounced at sample D_{C4} because the catalyst concentration in the water-rich domain is the highest. When adding more water, the catalyst in the water-rich domain gets diluted. This modification of the immediate environment appears to have an important effect on the specific surface area. The TBA-rich domains, although strongly fluctuating, are volumes that are excluded for the growing silica polymer. The excluded volumes will lead to pores in the aerogel (see **Figure 50**) which ultimately lead to unique structural features like observed in the TEM images. The size discrepancy between the solvent structuring in the binary case water/TBA and the observed morphological features is well documented in literature.^{267,268} These excluded volume pores connect the typical microporosity. In the case of unstructured solvents, the microporosity is inaccessible to N₂ for measurement. When mesoscale structuring is present, however, microporosity is accessible and leads to a significant increase of specific surface area.

8 Conclusion

In this study, the influence of a structured solvent on the kinetics and the resulting morphology of the sol-gel process was investigated. The results are promising for applications in several domains where high specific surface areas are important.^{205,206,269,270} For the investigation, binary mixtures of water/EtOH and water/*tert*-butanol were chosen as representatives of non-structured (EtOH containing) and structured (*tert*-butanol containing) solvents. Upon the addition of hydrophobic TEOS, enhanced structuring was observed for several samples, which agrees with literature.⁶³ After the rapid hydrolysis of TEOS (< 3 min) which was at the origin of the enhanced solvent structuration the solvents are assumed to return to their state in the binary mixtures. Here, the reaction conditions and structuring on the mesoscale determine the size of primary particles. Small silica particles (radii between 0.2 and 0.5 nm) then react with each other to form a fractal network. Discontinuity of the reaction rate between the samples was observed in sols containing the structured solvent (*tert*-butanol) by observation, DLS, FTIR and SAXS. Furthermore, the aerogels obtained by drying with SC CO₂ display noticeable morphological features and specific surface areas when resulting from structured solvents. These criteria lead to the conclusion that the solvent structuring in the immediate environment of the silica particles is responsible for the behavior observed. A hypothesis of the influence of the solvent structuring on the polymerization mechanism is proposed where the silica particles aggregate in a different manner depending on the solvent composition in their close surrounding. In structured solvents water-rich domains cover the silica particles. This leads to reaction conditions that are similar to those in pure water while *tert*-butanol-rich domains form regions where polymerization does not take place.

9 Outlook

It should be noted that current investigations lead to the proposal of another hypothesis. In that case, the increase of entropy by the release of solvent molecules bound to the silica nanoparticle surface upon aggregation plays a major role in the reaction kinetics. Consider the change of the mixing entropy when adding one molecule of alcohol to the binary mixture shown in **Figure 51**.

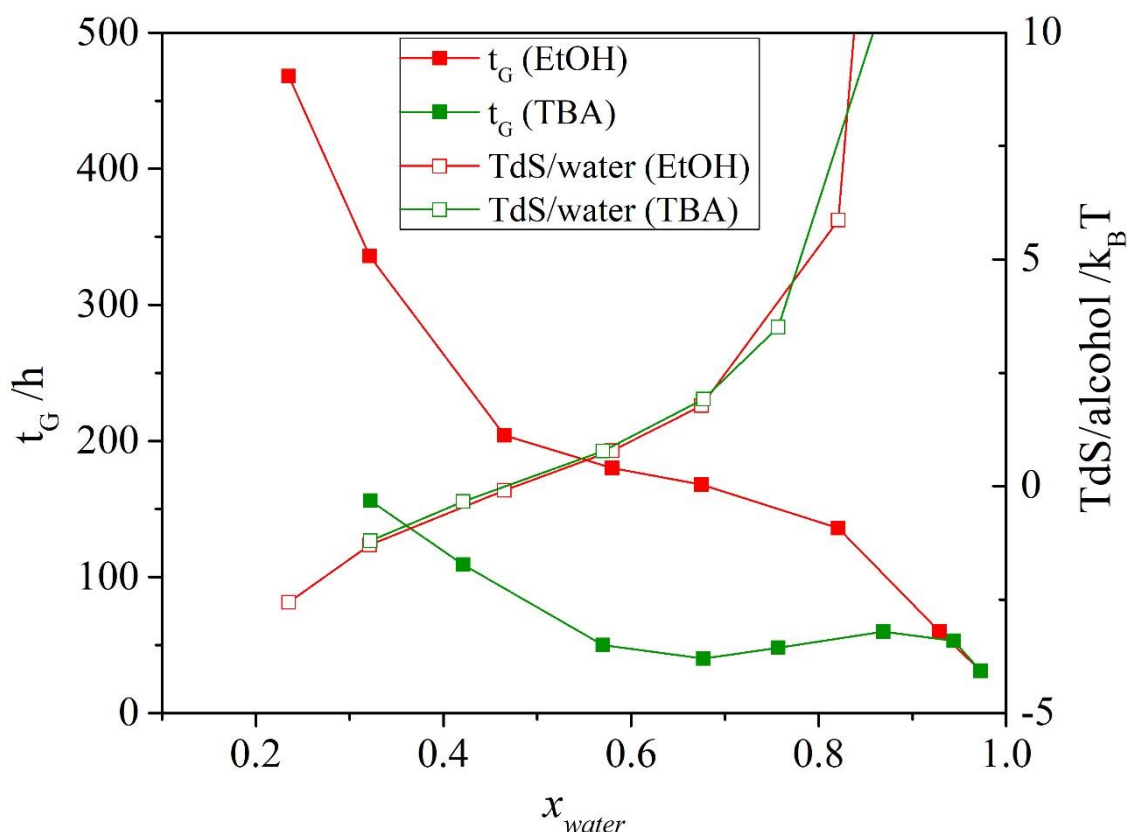


Figure 51. Mixing entropy gain per molecule alcohol when adding one molecule of alcohol into the solution.

Indeed, when supposing that the alcohol adsorbs preferentially on the nanoparticle surface, the release of physisorbed alcohol at low water contents decreases the entropy. This is unfavorable and the reaction is slowed down. At high water contents, the release of alcohol from the nanoparticle surface leads to an increase of the system entropy and the reaction accelerates. However, the calculations are far from complete and need further investigation.

This study offers promising perspectives in fundamental research and application. Concerning the fundamental research, the materials can be further investigated by Raman spectroscopy and ^{29}Si -NMR studies. This can help to understand the connectivity of the silica primary particles. By performing neutron scattering experiments with varying scattering contrast, the mechanism proposed in this chapter could be confirmed or refuted.

To generalize the results, it would be necessary to vary the parameters of sol-gel processing. This can, for example, be done by changing the type of co-solvent, the quantity of TEOS, the concentration or type of catalyst or salt addition. Concerning applications, the classic areas of interest of aerogels are concerned. The highly open structure of the aerogels developed herein can be of advantage. Another application is the incorporation of functionalized molecules into these aerogels. This will be investigated in the following chapter.

V MATERIALS FROM CO-CONDENSATION

1 The quaternary system – Co-condensation in structured media

With the interactions that govern the condensation in the ternary systems known, the aim is to understand the interplay of components in the quaternary system at the center of the strategy outline (see **Figure 52**). In the following chapter, the first exploratory results are presented and discussed.

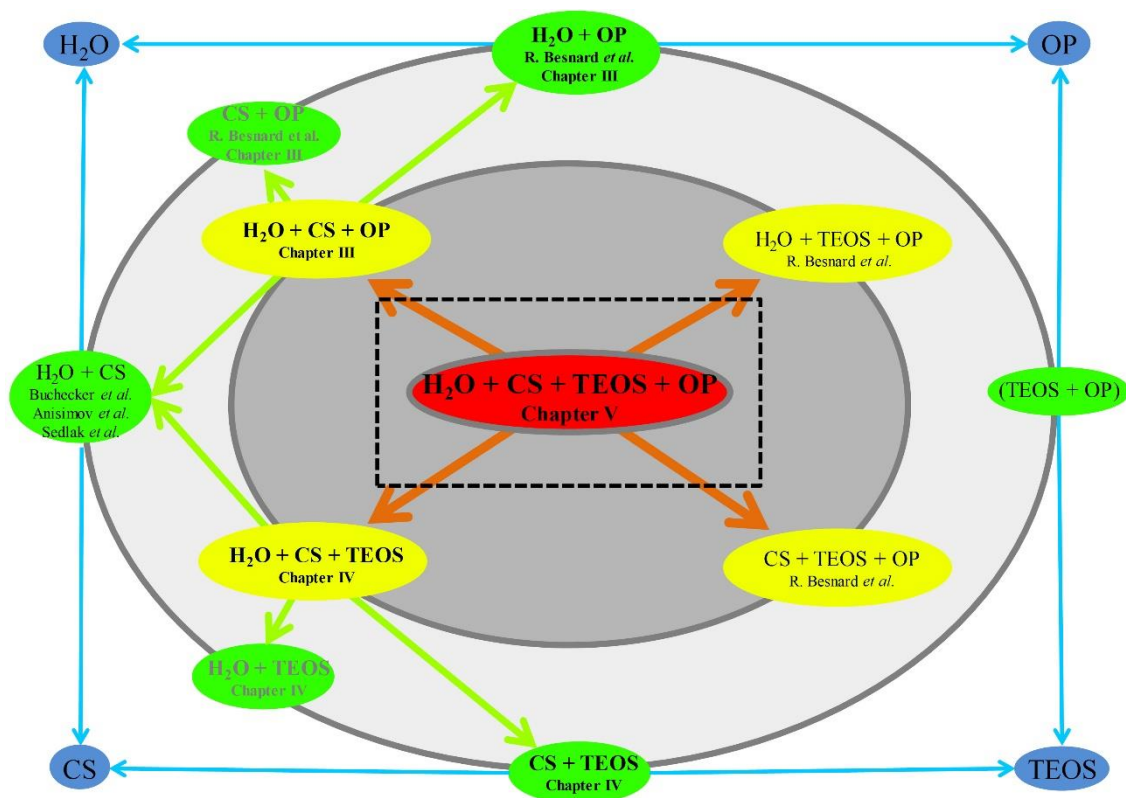


Figure 52. The strategy outline as developed in the introduction. The subject of the present chapter is highlighted by the black rectangle.

In this approach, two different kinds of silanes are used: the organosilane developed and synthesized in Chapter II and applied in Chapter III and TEOS. This essentially describes a co-condensation approach with well-known challenges. First, like mentioned in Chapter I, the chemical reactivity of silanes slows down upon substitution with alkyl groups.³⁰ Thus, the functionalized precursor may not be incorporated in the material in the quantity that was intended from the starting sol composition. The different reaction

rates of structurally different silanes lead to a tendency of homocondensation. Consequently, the different species of silanes may not cross-link uniformly. This can lead to a heterogeneous material composition.¹⁰⁶ Second, the orientation of the incorporated functional groups is an issue. Co-condensation approaches classically use sacrificial structuring agents. Depending on the polarity of the structuring agent and the functional group, the functionalization can be oriented towards the solid matrix.^{107,271} Third, the addition of a sacrificial structuring agent requires its elimination after synthesis. Classically, methods like washing with an organic solvent or SC CO₂, oxidation²⁷² or calcination are applied. However, care must be taken because some of these methods can damage the functional groups.¹⁰⁶ For the system chosen in this chapter, the mentioned risks must be evaluated. Here, the role of the structure-directing agent is played directly by the organosilane. Therefore, there is no need for an additional removal method. The problems resulting from polarity and reaction rate issues, however, persist. In order to evaluate the incorporation of the organoprecursor into the material and its direction, a kinetic study is conducted. The approach is based on the materials developed in Chapter IV. Consider again the sample with the biggest derivation from ideal behavior EC₄ which was synthesized from a solvent composition of water/TBA 1:1. Here, the solvent heterogeneities were most pronounced and a high specific surface area was measured for the obtained material. In the present chapter, to benefit from the solvent heterogeneities, the precursor **P2** was added with a molar ratio [P2]/[TEOS] = 0.1 at increasing delay times after the starting sol preparation. To limit strong physical interactions, the organosilane **P2** (see **Figure 53**) is selected to start the investigations of the quaternary system. In the following, the material morphology and the incorporation of the organosilane precursor are investigated.

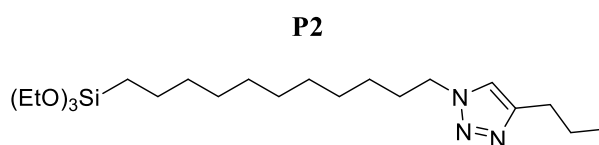


Figure 53. Molecular structure of 4-propyl-1-(11-(triethoxysilyl)undecyl)-1H-1,2,3-triazole (**P2**).

2 Sample preparation

The samples compositions are shown in **Table 12**. The order of addition is the same as the order of columns: 1) water 2) TBA 3) HCl (37w%) 4) TEOS 5) **P2** (optional, delayed). After the addition of **P2** the samples were vortexed. After 72 h the samples CoCo-1 to CoCo-4 and after 90 h the samples CoCo-5 and CoCo-Ref were freeze dried and washed with acetone. After the evaporation of acetone under vacuum, the analyses were performed on the freshly prepared materials.

Table 12. References, compositions in weight fractions and the time of P2 addition of the samples.

Reference	w_{water}	w_{TBA}	w_{HCl}	w_{TEOS}	w_{P2}	$t_{\text{Addition(P2)}} / \text{h}$	$T_{\text{freeze drying}} / \text{h}$
CoCo-1	0.42	0.45	0.035	0.074	0.015	0	72
CoCo-2	0.42	0.45	0.035	0.074	0.015	10	72
CoCo-3	0.42	0.45	0.035	0.074	0.015	24	72
CoCo-4	0.42	0.45	0.035	0.074	0.015	31	72
CoCo-5	0.42	0.45	0.035	0.074	0.015	48	90
CoCo-Ref	0.43	0.46	0.036	0.075	0	/	90

3 Organosilane incorporation in the material

To study the organosilane incorporation, six samples were prepared. The samples CoCo-1 to CoCo-5 contain the organosilane **P2** that was added at increasing delay after the TEOS addition (see **Table 12**). The sample CoCo-Ref was prepared without **P2**.

In order to verify the organic content in the materials thermogravimetric analysis was performed. The results are shown in **Figure 54**.

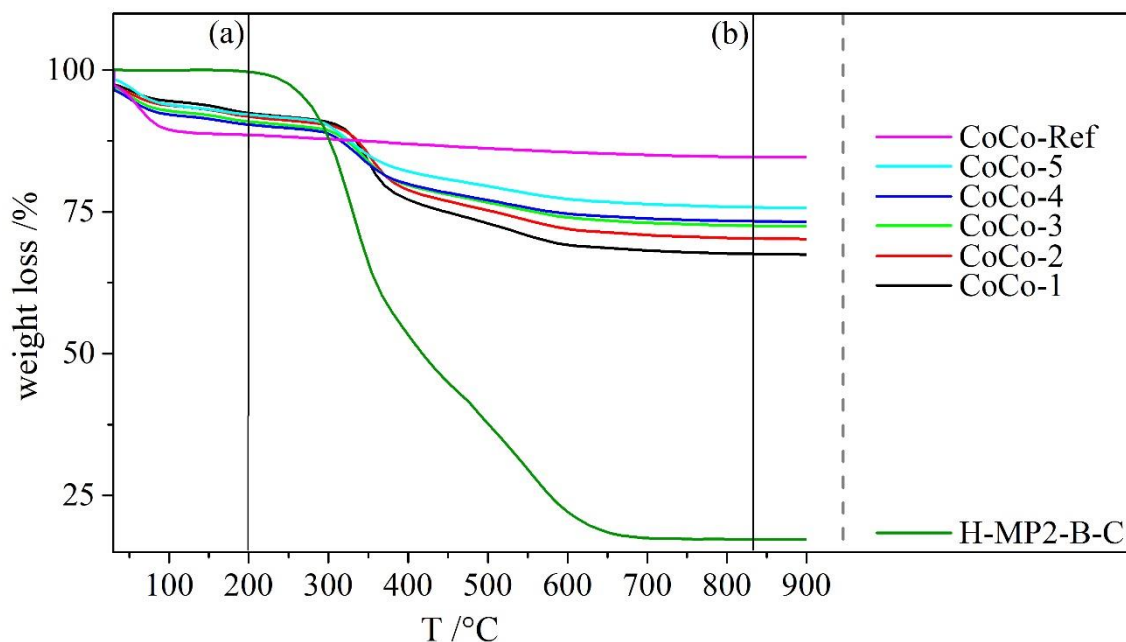


Figure 54. TGA weight loss curves for the different materials obtained by the co-condensation approach. The weight loss curve of sample H-MP2-B-C from chapter III is plotted for clarity. The lines (a) and (b) mark important features as discussed in the text.

The material H-MP2-B-C containing only **P2** was plotted for comparison. All samples show a constant weight loss with increasing temperature. The weight loss occurs in three steps. First, a weight loss of approximately 10 w% is observed until 200 °C (a). This weight loss is more pronounced in the order CoCo-Ref > ... > CoCo-1. The sample H-MP2-B-C shows no weight loss in this area. Then, from 200 °C to 800 °C (a to b), the samples CoCo-1 to CoCo-5 lose between 12 w% (CoCo-5) and 21 w% (CoCo-1). In this range, the sample CoCo-Ref shows a small weight loss of approximately 3 w%. The sample H-MP2-B-C loses 83 w% as mentioned in **III**. Finally, after (b) no weight loss is observed and the materials show an increasing residual mass in the order CoCo-1 < ... < CoCo-Ref. The first weight loss can be attributed to the release of water during the reaction of remaining free silanol groups. No weight loss is observed for H-MP2-B-C because the polymerization is already advanced thanks to a previous thermal treatment. The other samples show an increasing weight loss in the order CoCo-1 < ... < CoCo-Ref. This indicates that the share of SiO_x in the materials goes up with increasing **P2** addition delay. Accordingly, from (a) to (b), the increasing weight loss in the inversed order is due

to the increasing organic share. By comparison with H-MP2-B-C, it can be assigned to the thermal degradation of **P2**. The weight loss of CoCo-Ref in this temperature range is attributed to the calcination of the silica matrix. After point (b), the residue of all samples is purely inorganic SiO₂.

Assuming that the weight loss from (a) to (b) is caused by the thermal degradation of the fully condensed **MP2**, the organic content is quantified. The weight loss of sample CoCo-Ref in this temperature range is subtracted to eliminate the residual influence of the silica calcination.

$$w_{material}(\mathbf{P2}) = \frac{\Delta w}{m_f(org)} = \frac{w(a) - w(b) - \Delta w(CoCo - Ref)}{\left(1 - \frac{M(SiO_{1.5})}{M(MP2)}\right)} \quad (11)$$

Here $w_{material}(\mathbf{P2})$ is the weight percentage of incorporated **P2** in the material, $w(a)$ the residual mass percentage at (a), $w(b)$ the residual mass percentage at (b), $\Delta w(CoCo-Ref)$ the blank subtraction for the remaining silica consolidation, and $M(SiO_{1.5})$ and $M(MP2)$ the molar masses of SiO_{1.5} and the fully condensed organosilane **P2**. The results of this calculation are shown in **Figure 55**.

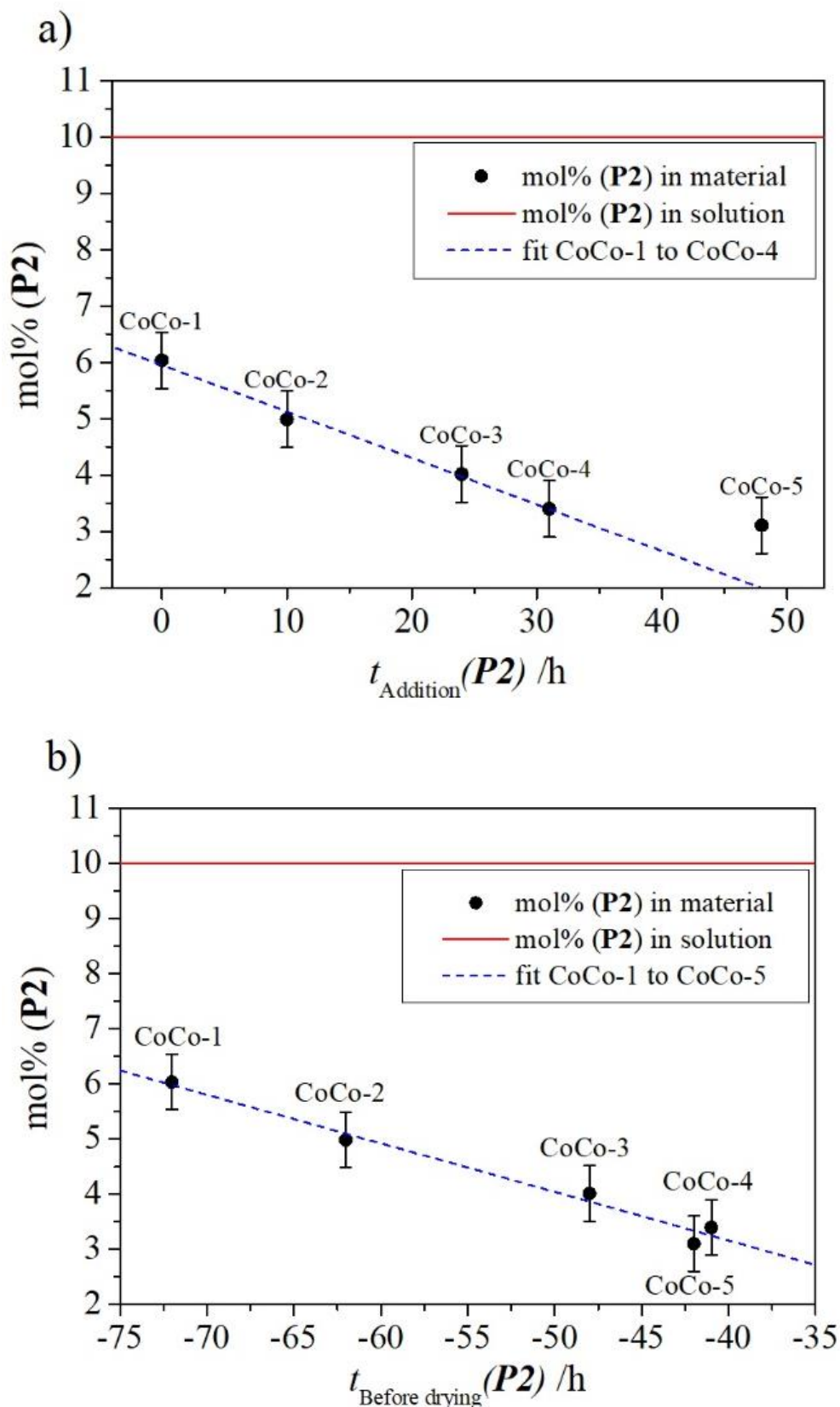


Figure 55. Molar percentage of the incorporated organosilane P2 in the material as a function of its time of addition a) after TEOS or b) before drying. The red line marks the initial percentage in the starting sol. The dashed blue line is a linear fit of the samples CoCo-1 to CoCo-4 (a) or CoCo-1 to CoCo-5 (b).

The molar percentage of the incorporated organosilane is displayed as a function of the time of addition of **P2** measured from (a) the moment of sample preparation or (b) the moment of drying. The incorporated share of **P2** is always lower than the initial molar ratio of 0.1 (red line in **Figure 55**) and decreases linearly (dashed blue line in **Figure 55**) with the addition delay. Arbitrarily, a lower share of **P2** than the initial ratio implies that the organoprecursor has a smaller reaction rate than TEOS. The decreasing share with increasing delay times has the same origin. The longer the reaction time the more the system approaches equilibrium (10 mol%). The sample CoCo-5 is particular due to its longer reaction time (see **Figure 55 a**). By performing the drying 18 hours after the other samples, a larger proportion of **P2** was incorporated than for sample CoCo-4. Plotted as a function of the moment of drying (see **Figure 55 b**), the sample CoCo-5 corresponds well to the linear decrease.

To obtain further information on the material composition, FTIR was performed. The recorded spectra are shown in **Figure 56**.

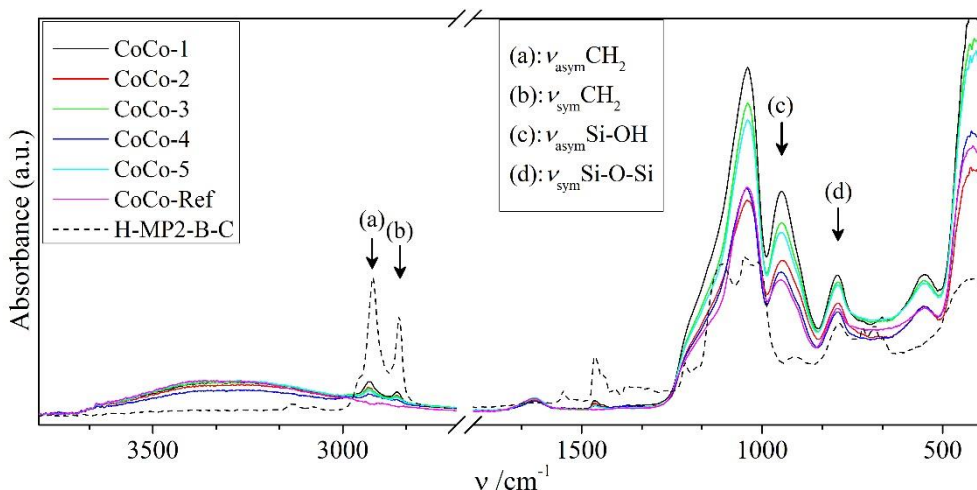


Figure 56. FTIR spectra of the materials obtained by the co-condensation approach. The spectrum of H-MP2-B-C from Chapter III is plotted for clarity. Points (a)-(d) designate important signals are discussed in the text.

The FTIR spectrum of sample H-MP2-B-C is added for clarity. The spectra display signals that are typical of SHMs. First, the signals assigned to the inorganic matrix are identified. The large peak in the region from 3800 to 3000 cm^{-1} is attributed to the O-H stretching modes. Here, the O-H groups are unreacted Si-O-H groups and residual water. The signal at 1600 cm^{-1} is attributed to the typical water bending mode. The signals at 1040 cm^{-1} and 790 cm^{-1} (d) are attributed to the asymmetric stretching modes of the Si-O-Si bonds while those at 950 cm^{-1} (c) and 550 cm^{-1} are attributed to the Si-OH stretching and rocking modes. Second, the signals from the organic part of the hybrid material are identified. The signals at 2930 cm^{-1} (a) and 2857 cm^{-1} (b) are attributed to the CH_2 asymmetric and symmetric vibration modes. The signal at 1460 cm^{-1} is attributed to the stretching modes of the 1,2,3-triazol group. Qualitatively, the FT IR spectra confirm the

Materials from Co-Condensation

incorporation of **P2** into the material. All sufficiently strong signals from H-MP2-B-C are found in the co-condensed materials indicating that the organic part was not degraded during synthesis. The water bending signal indicates the presence of residual water. The signals attributed to the silica matrix show an advanced condensation. For a quantitative analysis, the evolution of the signal intensities of the highlighted modes ((a)-(d) in **Figure 56**) was investigated. The results are shown in **Figure 57** and **Figure 58**.

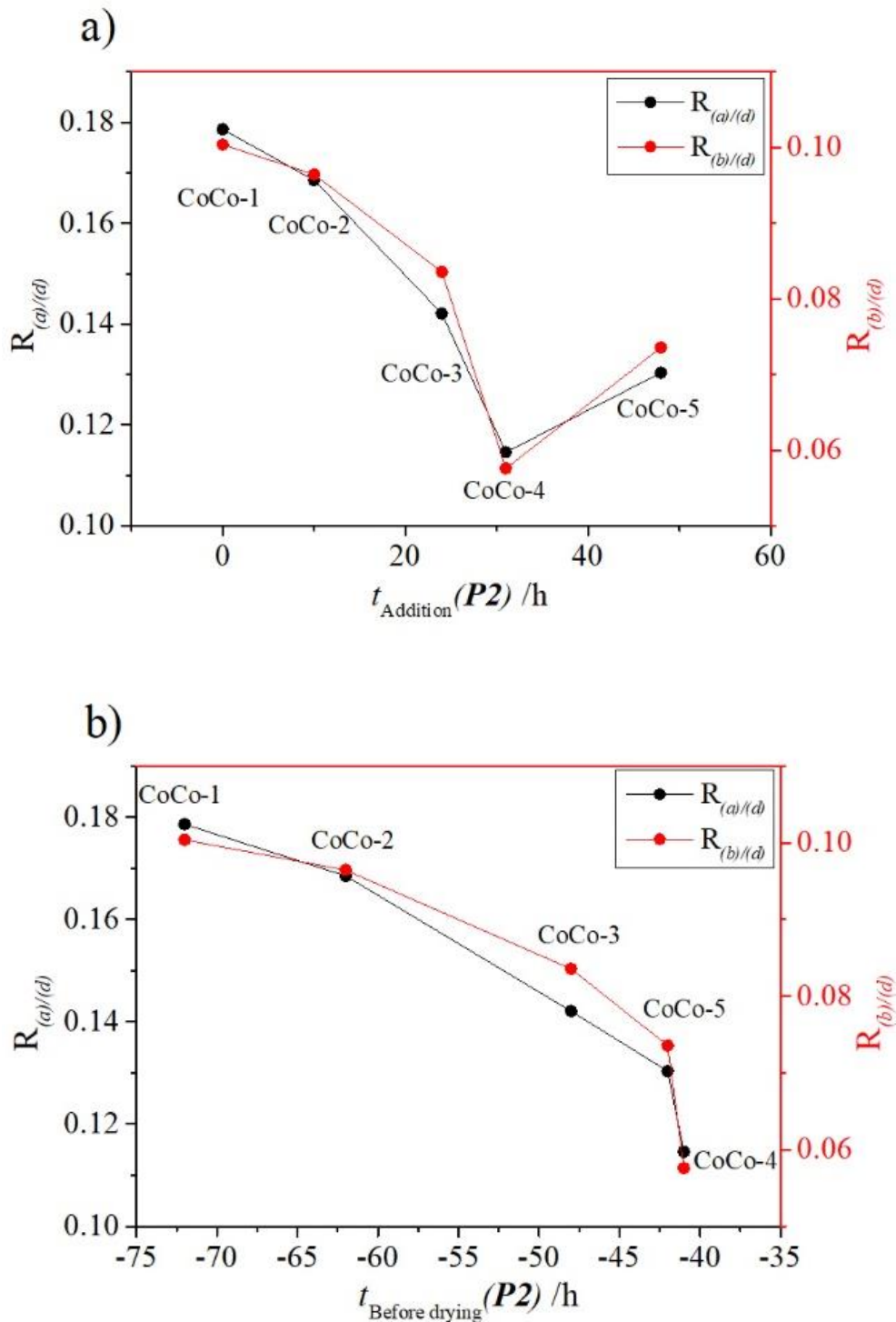


Figure 57. Intensity ratio ($R_{x/y}$) of the CH_2 signals to the silica matrix signal in Figure 56 as a function of the time of P2 addition a) after TEOS or b) before drying.

First, the incorporation of **P2** was investigated. To this end, the intensities of the two characteristic CH_2 signals ((a) and (b) in **Figure 56**) to the silica matrix signal ((d) in **Figure 56**) were investigated. The ratios of (a)/(d) and (b)/(d) become smaller in the order $\text{CoCo-1} > \dots > \text{CoCo-4} > \text{CoCo-5}$. Like explained concerning **Figure 55**, this inconsistency is due to the longer reaction time of CoCo-5 compared to CoCo-4. The plot

of the ratios as a function of the moment of drying (see **Figure 57 b**) reveals this issue. Here, the ratios follow a continuous decrease.

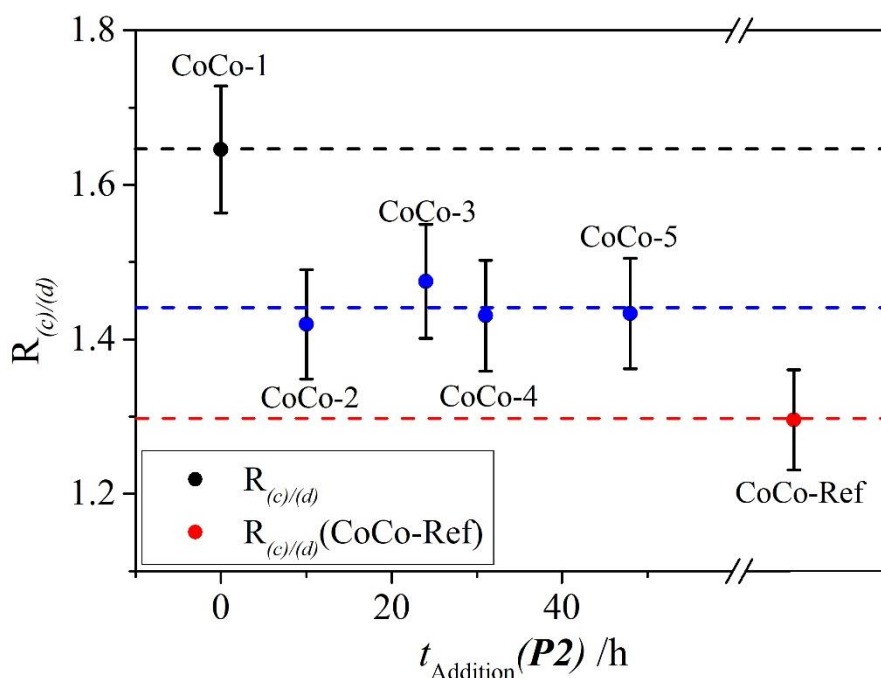


Figure 58. Intensity ratio ($R_{c/d}$) of the signals attributed to the free Si-OH and the siloxane bridges in the silica matrix in Figure 56 as a function of the time of P2 addition after TEOS for sample CoCo-1 to CoCo-5. The sample CoCo-Ref is plotted for comparison. The dashed lines indicate characteristic y-values as discussed in the text. Error bars of 5% are plotted.

Second, the effect of the **P2** incorporation on the condensation of the silica matrix is investigated. To this purpose, the intensity ratio of the signals attributed to the free Si-OH and the siloxane bridges was determined as a function of the time of **P2** addition. The sample CoCo-Ref was also plotted for comparison. The ratio shows an overall decrease going from CoCo-1 to CoCo-Ref. This indicates a decreasing number of free Si-OH bonds and, therefore, a more condensed silica network. Three characteristic degrees of condensation can be identified (dashed lines in **Figure 58**). CoCo-1 shows the lowest (dashed black line in **Figure 58**) and CoCo-Ref the highest (dashed red line in **Figure 58**) degree of condensation. The remaining samples show a comparable degree of condensation (dashed blue line in **Figure 58**). Considering the lowest value for CoCo-Ref, the addition of **P2** appears to decrease the degree of condensation found in the final material. Concerning the addition delay, the direct addition to the starting sol (CoCo-1) and the delayed addition (CoCo-2 to CoCo-5) must be distinguished. Considering that for the condensation reaction two free Si-OH bonds must come in contact, the conclusion is that **P2** hinders that contact by forming a steric barrier. In the case of CoCo-1, this barrier is most efficient. The barrier is equally efficient for samples CoCo-2 to CoCo-5 and, evidently, not present for CoCo-Ref. In any case, this difference is strongly related to the situation of **P2** in the material. Thus, from the three different condensation degrees, three different types of morphology can be inferred.

Resuming, **P2** is readily incorporated into the material. A maximum value of 6 mol% for the sample CoCo-1 reflects the naturally different reaction rates of the tetraethoxysilane (TEOS) and the alkyl triethoxysilane (**P2**). Using FTIR, this result was confirmed. Furthermore, the spectra indicated three different degrees of condensation which were ascribed to three different types of morphology. In the following the morphology is investigated.

4 Morphology of the co-condensed materials.

The porosity is a fundamental characteristic of the material morphology and important for applications. To investigate the porosity, nitrogen sorption experiments were performed. The adsorption isotherms are displayed in **Figure 59**.

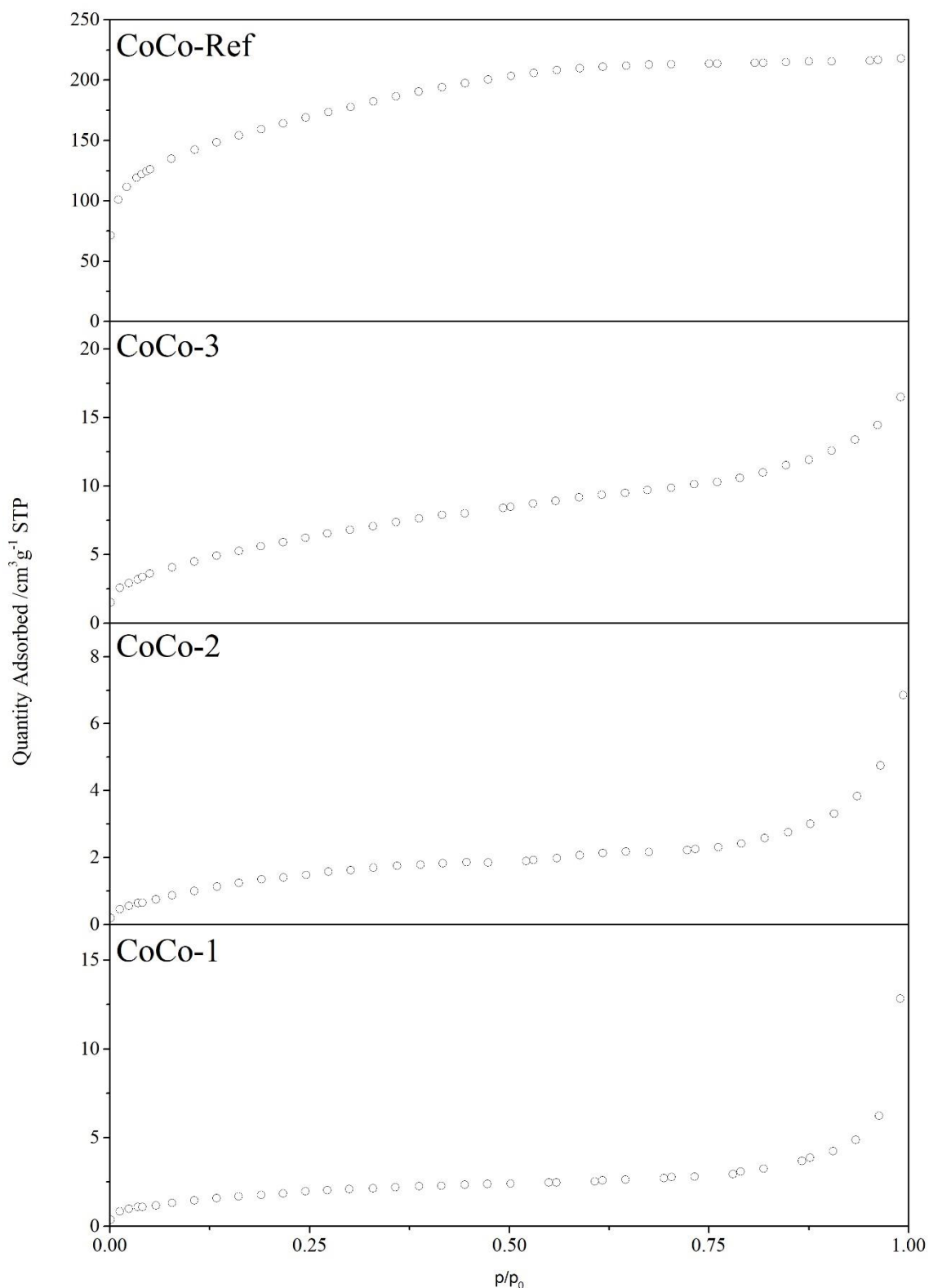


Figure 59. Nitrogen adsorption isotherms of the samples CoCo-1, CoCo-2, CoCo-3 and CoCo-Ref.

Gas adsorption isotherms are categorized into six types by IUPAC.²⁷³ An illustration of the different curves is given in the **Figure A.14**. In the present case, the samples CoCo-1 to CoCo-3 show a type II isotherm while the sample CoCo-Ref shows a type I(b) isotherm. Type II isotherms are observed for non-porous or macroporous samples. The

constant increase of adsorbed gas is due to the subsequent adsorption of N₂ layers. Type I(b) isotherms are characteristic for microporous materials. Here, the biggest part of adsorption occurs at low pressures and is due to pores with widths of several nm. Comparing the obtained isotherms, the slope between relative pressures of 0.1 and 0.7 increases in the order CoCo-1 to CoCo-Ref. Furthermore, the specific adsorbed quantity at relative pressures below 0.05 increases in the same order. This is evidence that the microporosity in the obtained materials increases. By fitting the obtained isotherms using the Brunauer Emmett Teller (BET) theory and the t-plot, the contribution of the microporosity to the specific surface area can be quantified. Using

$$\phi S_{external} = \frac{S_{t-plot}}{S_{BET}} \quad (12)$$

and

$$\phi V_{micropores} = \frac{V_{micropores}}{V_{porous,total}} \quad (13)$$

where $\phi S_{external}$ is the surface fraction of the non-porous surface to the total measured surface area, S_{t-plot} the non-porous surface area as determined by the t-plot, S_{BET} the surface area as determined by the BET method, $\phi V_{micropores}$ the volume fraction of the microporosity, $V_{micropores}$ the microporous volume as determined by the linear transformed BET equation and $V_{porous,total}$ the total pore volume as determined by the t-plot, the obtained results are put into relation. This is shown in more detail in the appendix (see **Figure A.15**) The results are displayed in **Figure 60**.

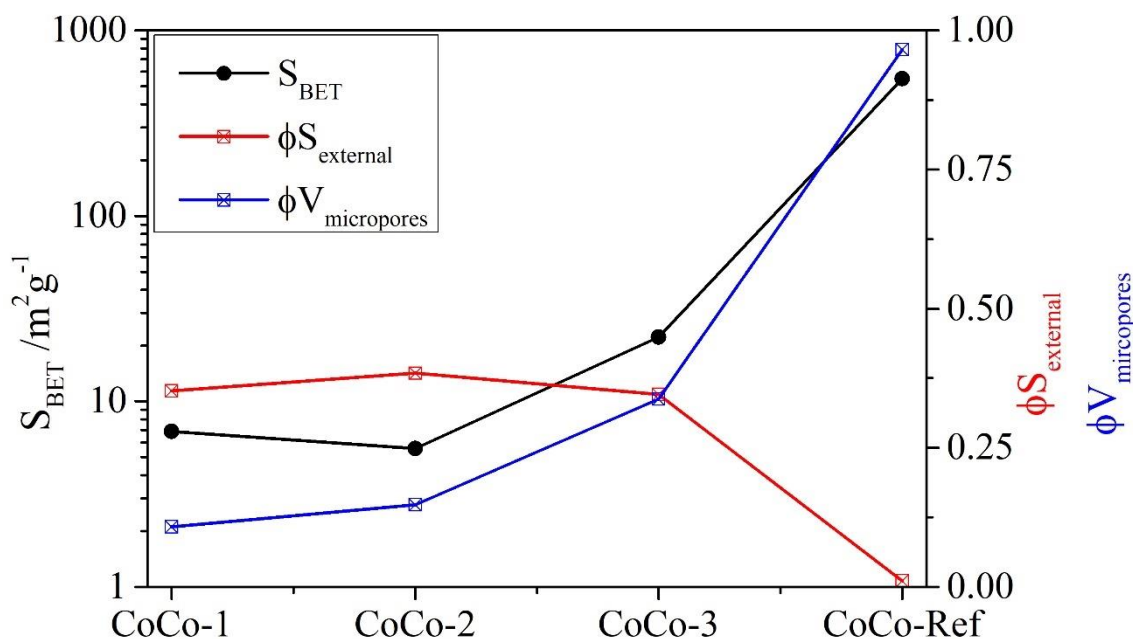


Figure 60. Results from N_2 sorption experiments for the materials obtained by co-condensation. The specific surface obtained by the BET method S_{BET} is plotted on a log-scale. The external specific surface area fraction of S_{BET} is obtained from the Harkins and Jura t-plot. The microporous volume fraction of the total pore volume is obtained from the linear transformed BET equation.

The specific surface area S_{BET} increase from Sample CoCo-1 to CoCo-Ref from 6.88 to $550 \text{ m}^2 \text{g}^{-1}$. At the same time, the porous volume fraction from micropores $\phi V_{\text{micropores}}$ increases from 0.11 to 0.97. On the other hand, the contribution of the non-porous surface ϕS_{external} decreases from 0.35 to 0.01. The observed trends indicate an increasing microporosity at more delayed additions of **P2**. The microporosity originates from the pre-condensation before the addition of the organosilane. Here, a fractal network is formed that classically results in a microporous material after drying.

To obtain further insight on the morphology, SAXS was performed on the materials. The resulting scattering patterns are displayed in **Figure 61**.

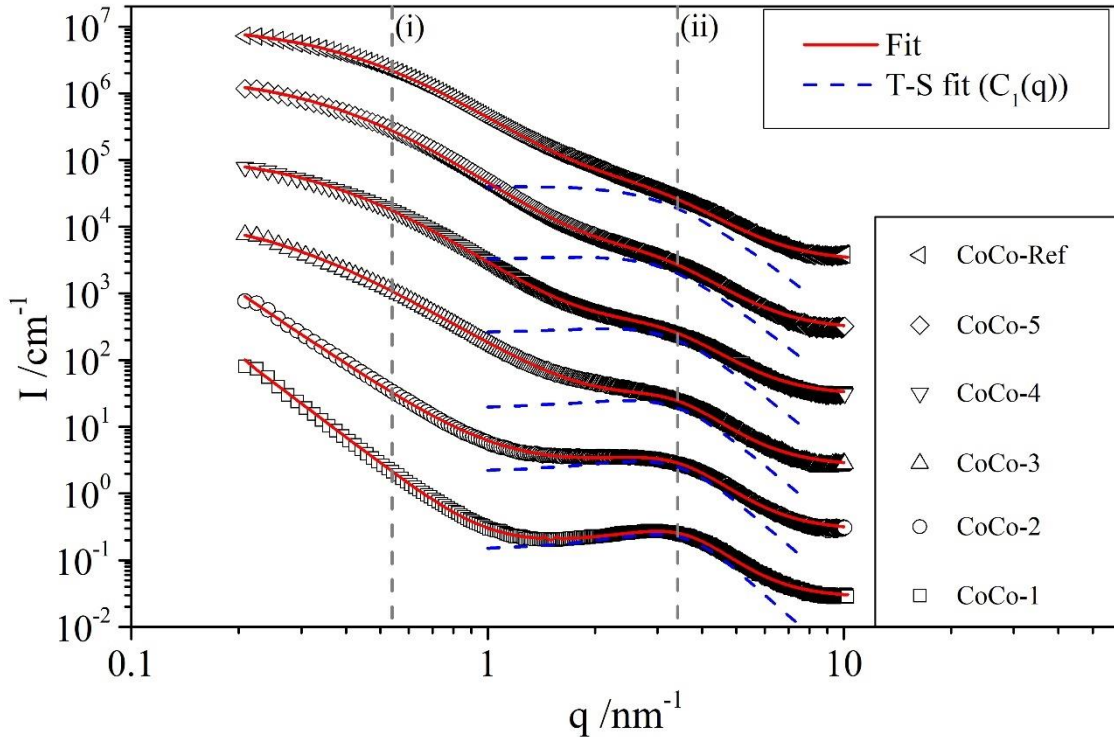


Figure 61. SAXS patterns of the materials produced by co-condensation. The measured patterns are represented by the open symbols. The corresponding fits are superimposed as red lines. The Teubner-Strey (T-S) contribution ($C_1(q)$) is added as a blue dashed line) For better presentability, the patterns were shifted by a factor of ten. Important features are indicated by (i) and (ii) and are described in the text.

All SAXS patterns show two features denoted (i) and (ii) in **Figure 61**. At lower q , (i) gives information on the mesoscale organization of the material. The primary objects that compose the material are described by (ii). For the latter, at $q \approx 3 \text{ nm}^{-1}$ (ii), a broad peak is observed. From CoCo-1 to CoCo-Ref, this peak decreases in intensity and appears to shift towards larger q . At $q < 2 \text{ nm}^{-1}$ (i), an increasing excess scattering is observed. Two shapes can be distinguished. The sample CoCo-1 shows a constant slope proportional to q^{-4} without a limit at very low q . The patterns from samples CoCo-2 to CoCo-Ref show decreasingly steep slopes where the limit can be suspected from sample CoCo-3. The observed limits exhibit a shift towards higher q from sample CoCo-3 to CoCo-Ref.

To obtain information on the scattering objects, microscopy was performed. A selection of the recorded SEM and TEM images is displayed in **Figure 62**.

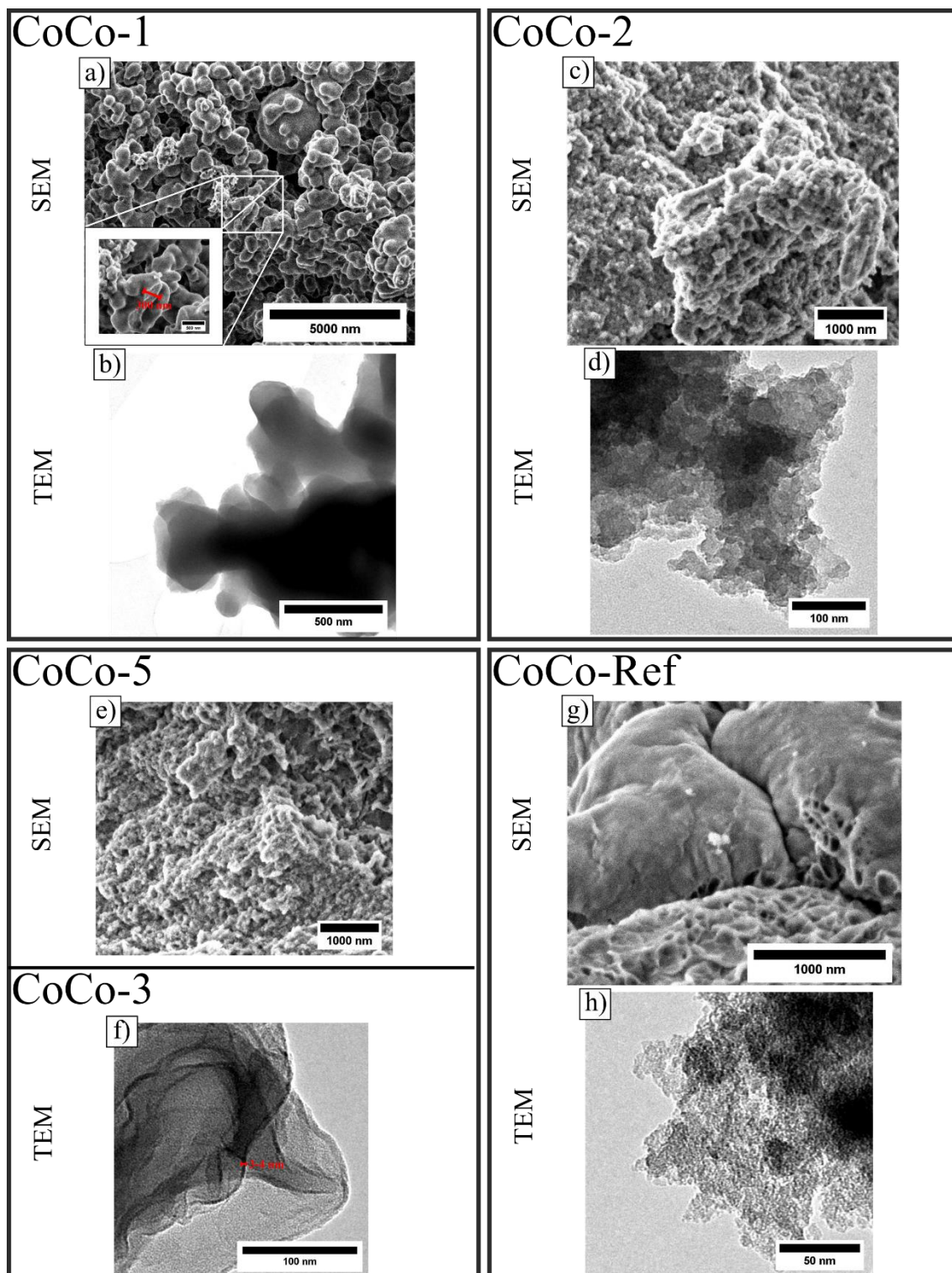


Figure 62. SEM and TEM images of the co-condensed materials: a) SEM CoCo-1 with zoomed inset, b) TEM CoCo-1, c) SEM CoCo-2, d) TEM CoCo-2, e) SEM CoCo-5, f) TEM CoCo-3, g) SEM CoCo-Ref, h) TEM CoCo-Ref. Scale bars are displayed in the images.

The microscopy images indicate characteristic sizes and give indications regarding the material morphology. Concerning the sample CoCo-1 where **P2** was added to the starting mixture, the SEM (a) and TEM (b) images show similar structures. The material is formed by sphere shaped, coagulated objects with smooth surfaces. The cross section of

these objects varies between 100 and 500 nm. The SEM (**c**) and TEM (**d**) images of sample CoCo-2 where **P2** was added after 10 h, show an aggregated structure of mesoscale particles with a rough surface. The particle diameter distinguishable in the TEM image (**d**) is around 10-50 nm. When going to more delayed **P2** addition times, the SEM images ((**e**) for CoCo-5) show a similar structure for the samples CoCo-2 to CoCo-5. When investigating the TEM images of the samples CoCo-3 to CoCo-5, solid materials with sheet-like structures can be observed. This is illustrated with TEM image of sample CoCo-3 (**f**). For this sample, sheets of 3-4 nm thickness were found that were strongly folded. For the samples CoCo-4 and CoCo-5 (not displayed), the structure observed by TEM bears resemblances with CoCo-3. However, the sheets are thicker (13 nm found for CoCo-5) and less folded. The SEM image of sample CoCo-Ref (**g**) without **P2** shows flat surfaces with patches of craters. At bigger zoom, in the TEM image for sample CoCo-Ref (**h**), the aggregation of nanoscale primary particles is seen.

Using this information, it is possible to effectively fit the SAXS patterns (see **Figure 61**). The fit parameters are listed in **Table 13**.

Table 13. Fit parameters from the SAXS patterns in Figure 61.

Sample	C ₁ (q)			C ₂ (q)				R-factor
	$\eta \cdot 10^4 / \text{nm}^{-2}$	d /nm	ξ_{TS} / nm	r /nm		$\Delta\text{SLD} / \text{nm}^{-2}$		
				core	shell	core	shell	
CoCo-1 ^{a)}	2.60	1.87	0.66	122.67	1.47	0.0012	0.00079	0.0463
Sample	$\eta \cdot 10^4 / \text{nm}^{-2}$	d /nm	ξ_{TS} / nm	I(0)*10 ⁻⁷ /nm ⁻¹	R _g /nm	D	R-factor	
CoCo-2 ^{b)}	2.83	2.01	0.62	9957.8	42.58	2.95	0.0534	
CoCo-3 ^{b)}	2.52	2.09	0.58	122.76	3.41	2.89	0.0460	
CoCo-4 ^{b)}	2.40	2.24	0.55	102.01	2.40	3.00	0.0366	
CoCo-5 ^{b)}	2.64	2.42	0.53	186.62	2.38	3.00	0.0307	
CoCo-Ref ^{b)}	2.75	2.68	0.47	101.9	2.02	2.95	0.0159	

^{a)} C₁(q): Teubner-Strey, C₂(q): Core-Shell, Gaussian size distribution

^{b)} C₁(q): Teubner-Strey, C₂(q): Mass fractal, Exponential cut-off

Every pattern can be fitted with two contributions. Common to all materials, the first contribution is the Teubner-Strey (T-S) model²⁷⁴. Originally developed for the scattering of microemulsions, this model is also applied to the scattering patterns of materials.^{275,276} For networks of interconnected, coagulated particles, the T-S model is proven to provide a more reasonable fit than a hard sphere model.^{275,277} The contribution of the T-S to the overall fit is plotted as dashed blue lines in **Figure 61**. For the T-S model, the two fitted structural parameters are the characteristic domain size ξ_{TS} and the characteristic periodic inter-domain distance d .²⁷⁷ From this, the correlation length l_c^{TS} is obtained using²⁷⁷

$$l_c^{TS} = \frac{d}{\pi} \arctan\left(\frac{2\pi\xi_{TS}}{d}\right) \quad (14)$$

The results of the T-S contribution are displayed in **Figure 63**.

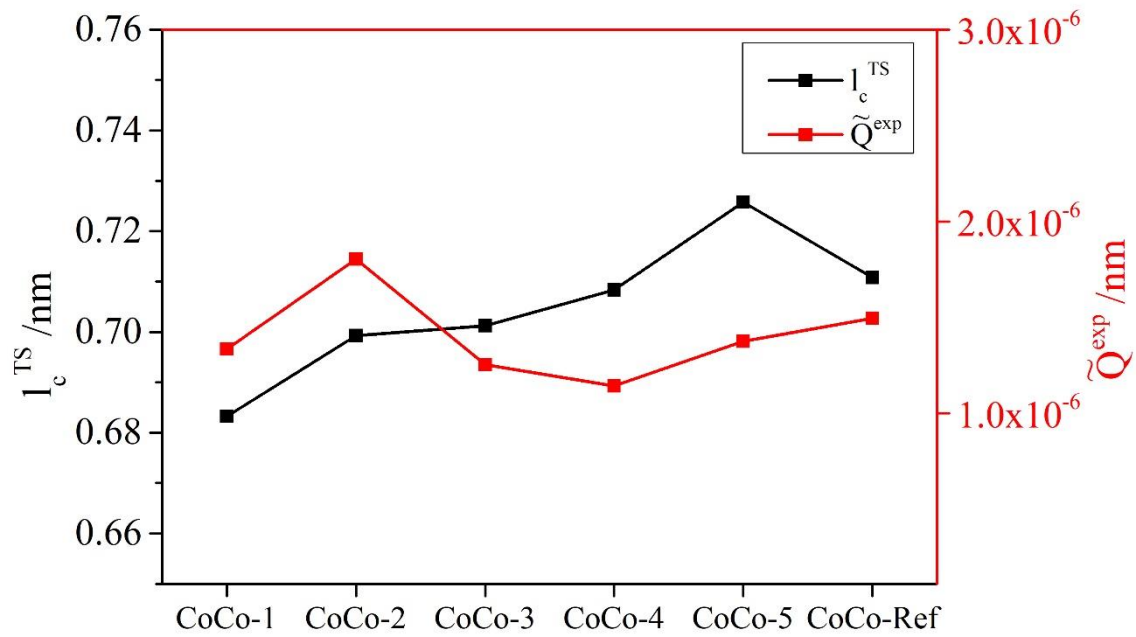


Figure 63. Correlation length l_c^{TS} and experimental scattering invariant \tilde{Q}^{exp} obtained from the SAXS patterns of the co-condensed materials (Figure 61). Only Teubner-Strey (T-S) contributions (dashed blue line in Figure 61) were intergrated for the calculation of the experimental scattering invariant.

The correlation length increases slightly in the order CoCo-1 > CoCo-5 from 0.68 nm to 0.73 nm. For the sample without **P2**, a decrease to 0.71 nm is found. These values are in the order of magnitude of the primary particle radii observed in **IV**. In the former chapter, in the case of E_{C4} , the primary particle radius was determined to be 0.28 nm. More precisely, the calculated l_c^{TS} are two times bigger than the radius and, thus, probably represent their center-to-center distance. This indicates that l_c^{TS} is closely related to the primary particle size. It is inferred that the T-S contribution describes the coagulated silica structure. The calculation of the scattering invariant \tilde{Q}^{exp} of the T-S contribution, therefore, gives information on the composition of the scattering volume of this coagulated silica structure.²⁷⁸ The calculated values are close to $1.4 \cdot 10^{-6} \text{ nm}^{-4}$ for all samples. This indicates that all materials consist of similar fundamental structures.

Using the definition of the theoretical invariant

$$\tilde{Q}^{th} = 2\pi^2\phi_a(1 - \phi_a)\Delta SLD^2 \quad (15)$$

where ϕ_a is the volume fraction of phase a and ΔSLD the scattering contrast, the volume fraction can be approximated. For the calculation, a ΔSLD of 0.0012 nm^{-2} is reasonable because the silica matrix consolidation is far from complete under acidic conditions.²⁷⁹ In this case, volume fractions ϕ_a of 0.04 to 0.08 are obtained. These volume fractions can be attributed to the bulk silica or the porosity of the material. Inspecting the TEM and SEM images, the materials were found to be highly porous. Therefore, an attribution of ϕ_a to the bulk silica appears more reasonable.

The second fit contribution is different depending on the sample. The patterns of samples CoCo-2 to CoCo-5 can be fitted with a fractal model. This sort of structure is typical for one-step HCl-catalyzed xerogels.³⁰ Here, a decreasing radius of gyration R_g with fractal dimensions close to 3 is observed in the order CoCo-2 > CoCo-Ref. (see **Table 13**). For CoCo-2 the determined radius of gyration is close to the size of the observed structures in the TEM images (see **Figure 62 d**). A decreasing radius of gyration indicates smaller coherent domains. Thus, at more delayed additions of **P2**, the materials present heterogeneities at decreasing lengths. This confirms the tendencies from the nitrogen adsorption experiments and the microscopy images where an increasing microporosity was observed.

For sample CoCo-1 a core-shell sphere structure is proposed. Using the information obtained by nitrogen sorption measurements, the microscopy images and the TGA results, the complete morphology of the sample was resolved. For the explanation, a simplified illustration drawn to scale is given in **Figure 64**.

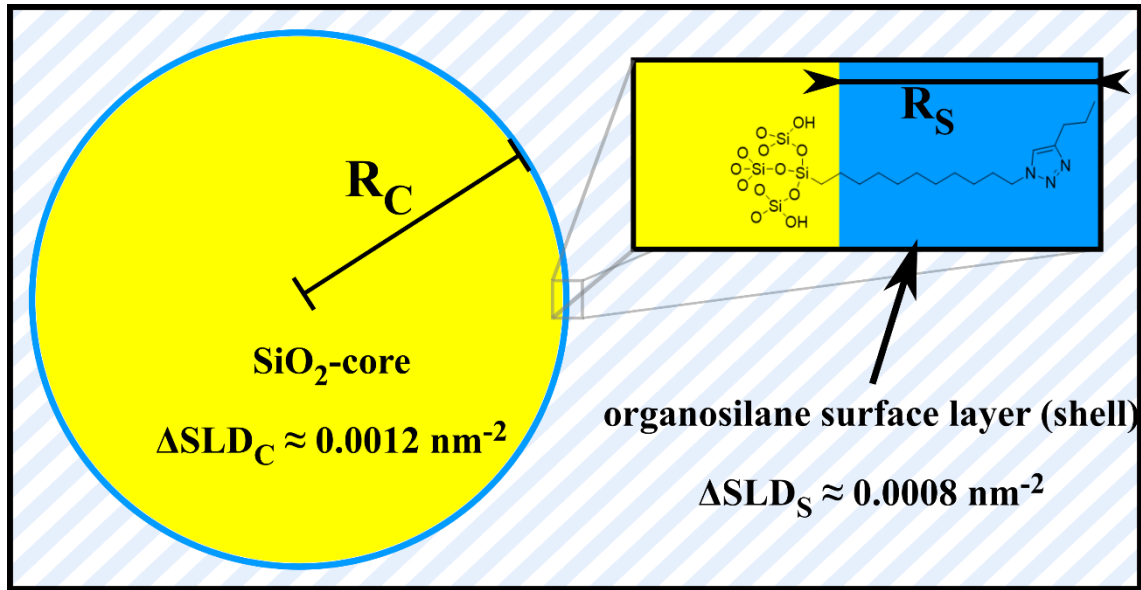


Figure 64. Simplified illustration of the fit model of CoCo-1. The illustration is drawn to scale.

The core radius (R_C) is given with a gaussian distribution of radii around 122.67 nm with a FWHM of 14.71 nm while the shell radius (R_S) is fixed to 1.47 nm. In this way, R_C corresponds to the polydisperse objects observed in the TEM images (see **Figure 62 a)** and **b)**) and R_S to the length of an extended **P2**. The scattering length density of the core (ΔSLD_C) is that of the incompletely condensed silica matrix that was used earlier. (see **Eq. (15)**) The coagulated silica network discussed earlier is considered homogeneous at this scale. The SLD of the shell (ΔSLD_S) is assumed to be that of a typical hydrocarbon chain. The model is verified by the experimental results from the TGA and nitrogen sorption experiments.

First, the volume fraction of the modeled spheres in the sample is calculated. To this end, the sphere volume is multiplied with the particle number density $N_{Spheres}$ obtained via:

$$I(0) = N_{Spheres} * \Delta\text{SLD}^2 * V_{Sphere}^2 \quad (16)$$

where ΔSLD is the scattering contrast, V_{Sphere} the volume of one sphere and $P(0)$ the applied form factor at $q = 0$ and $I(0)$ the extrapolated measured intensity at $q = 0$. The resulting volume fraction $V_{Sphere} * N_{Spheres} = 7.73 * 10^6 \text{ nm}^3 * 1.13 * 10^{-8} \text{ nm}^{-3} = 0.087$ agrees well with the volume fraction obtained from the T-S invariant. Since the microscopy images reveal that only one type of structure is present in the sample, it is concluded that the inner sphere volume is made up of the bicontinuous silica network discussed earlier. The higher volume fraction of the modeled spheres is reasonable because contained silica matrix is made up of the silica primary particles and the porosity described by the T-S model. Second, this volume fraction is multiplied by the density of

silica (2.2 g cm^{-3}) to estimate the number of spheres per sample mass Γ_{Sphere} . Taking S_{BET} of the sample into account (see **Figure 60**), the surface per sphere $A_{\text{Sphere,BET}}$ is estimated. The sphere radius $r_{\text{sphere,BET}}$ corresponding to this surface is, thus, obtained by

$$r_{\text{Sphere,BET}} = \sqrt{\frac{A_{\text{Sphere,BET}}}{4\pi}} = \sqrt{\frac{S_{\text{BET}}}{\Gamma_{\text{Sphere}}4\pi}} = 96 \text{ nm} \quad (17)$$

The obtained radius of 96 nm is in good agreement with the fitted radius (122.67 nm, see **Table 13**). This indicates that the measured specific surface area is that of the modeled core-shell spheres. The, compared to the fit result, inferior calculated radius is explained by the connections between the modeled spheres. The fit model of independent spheres neglects the lower surface-to-volume ratio in the real system that is caused by the coagulated connections between the spheres. Finally, it is possible to attribute the measured surface area to the quantity of incorporated **P2**. From TGA measurements, the weight fraction of incorporated **P2** is known (see **Figure 55**). Using Γ_{Sphere} , the number of **P2** per sphere $N_{\text{P2,Sphere}}$ is determined which is transformed to the area per **P2** A_{P2} with the help of $A_{\text{Sphere,BET}}$. Approximating the occupied area of the R-SiO_{1.5} group (A_{P2}) by that of a circle, the corresponding radius r_{P2} is calculated.

$$r_{\text{P2}} = \sqrt{\frac{A_{\text{P2}}}{\pi}} = \sqrt{\frac{A_{\text{Sphere,BET}}}{N_{\text{P2,Sphere}}\pi}} = \sqrt{\frac{A_{\text{Sphere,BET}}\Gamma_{\text{Sphere}}}{\Gamma_{\text{P2}}\pi}} = 0.67 \text{ nm} \quad (18)$$

Here, Γ_{P2} is the number of molecules **P2** per gram of material. The calculated radius of 0.67 nm is in good agreement with the midsphere radius of a regular SiO₂ tetrahedron $r_{\text{midsphere}} = 0.91 \text{ nm}$ ($d_{\text{Si-O}} = 1.6 \text{ \AA}$).²⁸⁰ Therefore, it is valid to assume that determined quantity of **P2** in the material is distributed over the measured S_{BET} . The S_{BET} , in turn, was found to be the exterior of the observed spherical objects (see **Figure 62 a and b**).

5 Discussion

The obtained results allow for a hypothesis concerning the formation of the material. The structure and the **P2** content of the material are a result of chemical and physicochemical factors in the sol. Chemically the incorporation of the organosilane precursor into the material is limited by reaction rate. From the TGA results, it can be concluded that the condensation is not completed at the moment of drying. This can be

inferred from the composition of CoCo-1 (see **Figure 55**). Despite the longest reaction time, the share of incorporated **P2** is below the share in the starting sol. The FTIR results confirm this observation. Furthermore, by examining the completion of the silica network *via* FTIR (**Figure 58**), it was possible to predict three different types of morphology depending on the degree of condensation. The reason of this difference is of physicochemical origin. The organosilane and TEOS have two different spontaneous outcoming structures in the present system. More precisely, like examined in **IV**, the acid catalyzed polymerization of pure TEOS leads to a fibrillar, fractal network that ultimately percolates. On the other hand, the organosilane precursor is unable to polymerize in three dimensions due to its molecular structure. At the same time, the long hydrocarbon chain gives the molecule surfactant-like properties that allow the formation of emulsions. The emulsion formed upon the addition of **P2** is that of a silica-rich and a solvent rich phase. It is most likely that the silica-rich phase has a large water content at the beginning of the reaction which decreases during the network consolidation. Between the two different spontaneous arrangements, that of **P2** appears to be the directing one. This is visible for the sample CoCo-1 which exhibits an emulsion-like structure with few pores and covered by the organosilane. It is the first type of morphology predicted from the FTIR spectra. When later addition times of **P2** are chosen, TEOS has the time to develop its spontaneous structure. However, the addition of **P2** still redirects the structuring upon addition. The influence is, nonetheless, attenuated. For example, the TEM images of the sample CoCo-2 still show the formation of larger (ca. 50 nm) aggregates. At later addition times, this kind of morphology is not observable anymore. It can be said that **P2** becomes unable to direct the morphology by emulsion formation but still impacts the obtained structure. This leads to the second type of morphology as predicted from the FTIR spectra. Finally, when no **P2** is added at all, the resulting microporous xerogel is the third type of morphology. In any case, in absence of the organosilane or at different addition delays, the coagulated silica structure is very similar. This was shown by fitting the scattering patterns of all samples using the Teubner-Strey model. All the samples consist of a coagulated network of primary particles like they were found in **IV**. Thus, it is concluded that the condensation processes of TEOS and **P2** occur separated and heterogeneously. The addition of **P2** is confining the space where the condensation of primary particles takes place. When the primary particle network formation is too advanced (later addition delays than CoCo-2), the organosilane grafts onto the surface.

6 Conclusion

In this study, it was possible to explore the effect of the delayed addition of an amphiphile-like organotrialkoxysilane to a sol composed of a non-ideal solvent and a tetraalkoxysilane on the properties of the resulting material. The precursor **P2** (see **Figure 53**) was selected as organotrialkoxysilane for this study because of its inability to interact

strongly *via* hydrogen bonding or ionic forces with the other components. Upon hydrolysis, **P2** develops an amphiphilic character with an ionic silicate headgroup. The emulsion-forming properties lead to a macroscale morphology where the hydrolyzed **P2** is located at the interphase between a silica-rich and a solvent-rich domain. In this case **P2** drives the obtained morphology where the silica headgroup is grafted on the surface and the triazole group is turned towards the pores. When the addition of **P2** is delayed, the gel-forming mechanism of TEOS determines the material morphology. In this case, the obtained materials become increasingly microporous. For the samples with delayed addition, the morphology is more complex and the exact localization of the organosilane could not be determined. In any case, the co-condensation was found to be heterogeneous. The primary particles originating from TEOS react with each other while the organosilane is grafted on the available surfaces. Other organosilane precursor may impact the material formation differently due to interactions that are specific to their organic functions or a change of their solubility.

VI EXTRACTION CAPACITIES OF THE SILSESQUIOXANES

1 System selection

Like stated earlier, nowadays, the recycling of REEs is a major challenge. Many possible recovery routes are available. REEs can be retrieved by the recycling of manufacturing scraps, industrial waste (phosphogypsum, red mud) or the urban mining of EOL products.⁸ To date, the high in-use stocks of REE in NdFeB magnets indicate a promising resource for urban mining.²⁸¹ However, for large magnets, metallurgical routes are already highly effective.²⁸² Concerning smaller magnets, the REE extraction from NdFeB magnets used in hard-disk drives has potential. Unfortunately, high contents of iron in the leachate of typical scraps can hinder extraction.²⁸³ Thus, the employed material for separation must be highly selective towards REEs and mechanically resistant. In literature, dyglycolamic acid derivatives embedded in silica materials or organic polymers meet these criteria in solid-liquid extraction.^{284–288}

The materials synthesized in **III** fulfill the requirements for an application in solid-liquid extraction. To investigate their affinity towards REE, extraction experiments were performed using the materials that were synthesized in sufficient quantity. Namely, **H/T-MP1-A/B-C**, **H-MP2-A-C**, **H-MP3-B-C-H**, **T-MP3-A-C-H**, **H-MP4-B-C** and **H-MP5-B-C** were tested. The structural formula of the corresponding functional groups are shown in **Figure 65**.

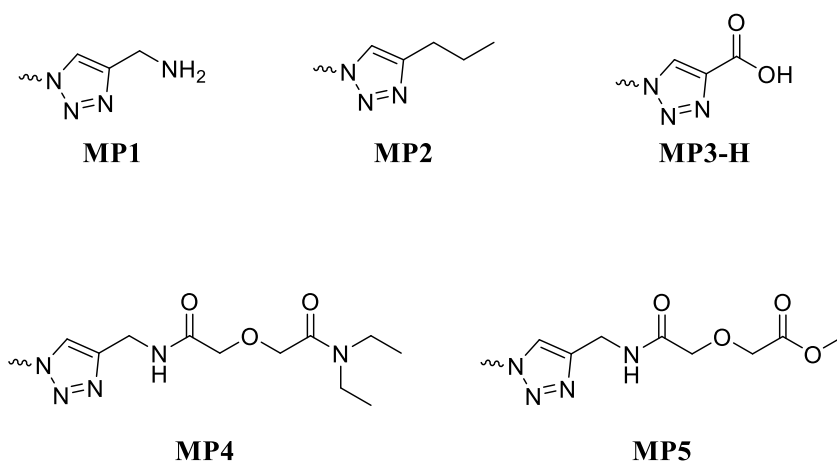


Figure 65. Extracting groups of the materials used in VI.

In the following, the obtained results are presented and discussed.

2 Extraction experiments

The metal containing aqueous solutions engaged in sorption experiments were prepared by the dilution of ICP standard solutions obtained from SCP Science. Nd stock solutions (from 1 to 250 ppm) were prepared at the desired acidity ($[\text{HNO}_3] = 1.10^{-4} - 1.10^{-1} \text{ M}$) from 1000 or 10000 mg/L ICP standard solutions (aqueous solution with 4% of nitric acid).

A simulated leachate of NdFeB magnets was prepared from B (1.1 w%; 10 ppm), Co (1.6 w%; 15 ppm), Dy (1.3 w%; 12 ppm), Fe (67.2 w%; 630 ppm), Nd (24.5 w%; 230 ppm), Ni (0.6 w%; 6 ppm), Pr (3.7 w%; 35 ppm) from 10000 mg/L and 1000 mg/L ICP standard solutions. The desired concentrations were attained by dilution with ultrapure water (Milli-Q, Millipore, 18 M Ω /cm) and the acidity was adjusted to pH 1 with 1 M nitric acid solution.

Batch contacts were performed for 24 h under rotary agitation (1 rotation/s) at 25°C. Various volume to solid ratio (V/m) have been used from 5000 (0.2 g/L) to 100 (10 g/L). After the contact, the mixtures were centrifuged and then filtered through a 0.2- μm cellulose acetate membrane. The initial and the remaining metal ion concentrations in the liquid phase were determined by ICP/AES or ICP/MS.

Metal concentrations were measured before and after extraction by inductively coupled plasma/atomic emission spectroscopy (ICP/AES) using a SPECTRO ARCOS spectrometer or Inductively Coupled Plasma Mass Spectrometry (ICP/MS) using a Thermo Scientific iCAP RQ instrument.

For the ICP/AES, the wavelengths were chosen to avoid any spectral interference between the elements: B (249.773, 249.677, 182.641 nm); Co (228.616, 238.892, 230.786 nm); Dy (353.170, 394.468, 340.780 nm); Fe (259.941, 238.204, 239.562 nm); Nd (401.225, 430.358, 406.109 nm); Ni (231.604, 221.648, 232.003 nm); Pr (411.846, 422.535, 414.311 nm).

For the ICP/MS standard mode, no gas (STD) and He mode with kinetic energy discrimination (KED) were used for the following elements: ^{10}B (KED); ^{58}Ni (KED); ^{59}Co (STD); ^{141}Pr (KED); ^{162}Dy (KED).

The cation uptake capacity Q_e (mg/g or mmol/g) and adsorption efficiency E (%) were calculated respectively using the Eq. $Q_e = (C_i - C_f) \times V/m$ and $E = ((C_i - C_f)/C_i) \times 100$. C_i refers to the initial concentration of the metal ion in solution while C_f is the residual metal ion concentration after the batch contact, V/m is the ratio of the volume of the solution to the mass of the solid (V = volume of the treated solution and m = mass of the material used). The separation factor $SF(M_1/M_2)$ between two metals (M_1 and M_2) was determined according to the eq. $SF(M_1/M_2) = Q_{M1}/Q_{M2}$.

Langmuir or Freundlich isotherm was estimated using the equation:

$Q_e = Q_{max} \frac{L C_e}{1 + L C_e}$ or $Q_e = K_F C_e^{1/n}$ where Q_e is the amount of adsorbed metal ions at equilibrium, L is the Langmuir constant, which is related to adsorption energy, Q_m is the adsorption capacity of the adsorbent, and C_e is the equilibrium concentration of rare earth metal ions in the solution, K_F is the Freundlich adsorption capacity constant.

3 Metal separation using silsesquioxanes

1.1 Screening of the extraction properties at different pH

The extraction behavior of the materials was first evaluated using batch extractions on pure Nd solutions at pH 1, 2 and 4 with a ligand-to-metal ratio (L/M) of 10. The molar masses were used as determined in TGA experiments (see **III**). The efficiencies are described by the capacity or adsorption ability Q_e (mmol g^{-1} or mg g^{-1}) of the material to extract the Nd. The equilibrium was considered to be reached after 24 h of contact at 25 °C since no exact data of the kinetics is present at the moment. The results are shown in **Figure 66**.

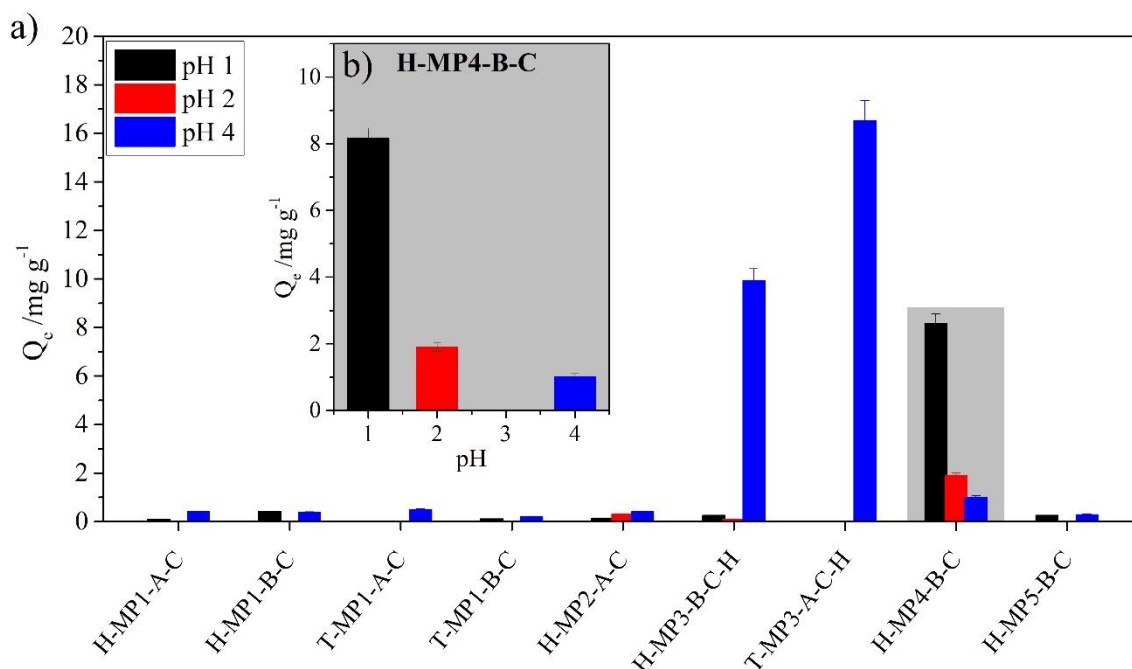


Figure 66. Q_e of the Neodymium extraction of the tested materials at pH 1 to pH 4 (a) and a zoom on the results for H-MP4-B-C (b).

Figure 66 a) shows that a considerable extraction of Nd is only observed for the materials containing the carboxylic acid (H-MP3-B-C-H, T-MP3-A-C-H) and the diglycolic diamide (H-MP4-B-C) headgroup. The absence of extraction for material H-MP2-A-C indicates, that the triazole group does not participate in the extraction which is in agreement with the literature.²⁸⁹ The pH has a significant impact on the extraction behavior. For the carboxylic acid function, extraction was only observed at pH 4. This suggests that the extraction is driven by the ion exchange between the proton and the Nd-ion. The extraction by simple carboxylic acids *via* the described mechanism is known but unspecific towards REE.²⁹⁰ For H-MP4-B-C (see **Figure 66 b**), the tendency is inverted and a higher nitric acid concentration leads to better extraction performance. The results

are in good agreement with the behavior observed in liquid-liquid extraction systems using neutral ligands (solvating agents). Generally, an increase in the nitric acid concentration leads to an increase in the distribution ratio values.^{291,292} Regarding these observations, the Nd could be desorbed by adjusting the pH.

To confirm this hypothesis, after the adsorption of Nd from a solution at pH 1 on H-MP4-B-C, the material was submitted to a stripping step with Milli-Q water (pH 6.5) with a similar volume to solid ratio as the extraction step (typically $V = 10$ mL, $m = 7$ mg). The data show that approximately up to 80% of extracted REEs could be recovered from the material (see **Table 14**)

Table 14. Results of the extraction and stripping experiments performed on H-MP4-B-C

	[C] /g L ⁻¹	V/m	C _i /ppm	C _f /ppm	%efficiency
Extraction	0.7	1350	14.53	8.49	42%
Stripping			6.04	4.98	82%

1.2 Mechanism of the Nd extraction by H-MP4-B-C

To evaluate the maximum extraction capacity Q_{max} of H-MP4-B-C concerning Nd, an isotherm at 298 K was recorded. To this end, the initial concentration of Nd was varied from 1 to 250 mg/L, while other parameters were kept constant ($V/m = 10$, 1 M HNO₃). The results are presented in **Figure 67**.

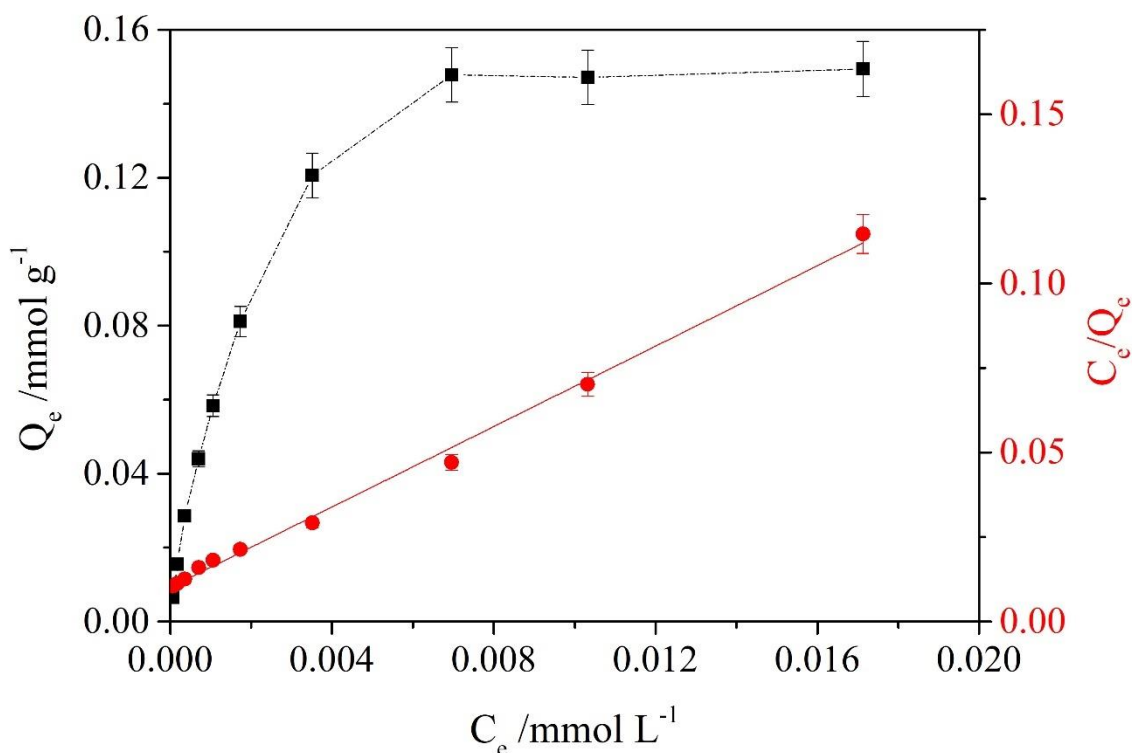


Figure 67. Uptake capacity Q_e (black) as a function of the equilibrium concentration of Nd (1 M HNO_3) after 24 h of contact with H-MP4-B-C. The red graph is the linear regression of the Langmuir model ($C_e/Q_e = 5.95(\pm 0.13) \cdot x + 0.1001(\pm 0.0009)$ with $R^2 = 0.996$).

The R^2 value (0.9962) of the Langmuir isotherms confirms the validity of the model for our system. From this it is concluded that all sites where Nd is adsorbed are similar in energy and a monolayer is formed. The adsorption isotherm based on the Freundlich equation $Q_e = K_F C_e^{1/n}$ was also investigated from the plot $\ln(Q_e) = f(\ln(C_e))$ but the obtained R^2 value of 0.94 disqualifies the Freundlich model.

The maximum extraction capacity Q_{max} for the Nd was calculated to $0.168 \text{ mmol g}^{-1}$ (24.25 mg g^{-1}). In comparison to the literature, this value is higher than the value proposed by Juère *et al.*²⁸⁸ ($200 \mu\text{g g}^{-1}$) using a diethyl diglycolamide-functionalized mesoporous silica and of the same order of magnitude as the materials used by Ogata *et al.*²⁸⁵ with diglycol amic acid functional groups with $Q_{max} = 16 \text{ mg g}^{-1}$.

To obtain further information on the Nd uptake in material H-MP4-B-C SEM images were recorded. In addition Energy-dispersive X-ray spectroscopy (EDX) was performed. The results are shown in **Figure 68**.

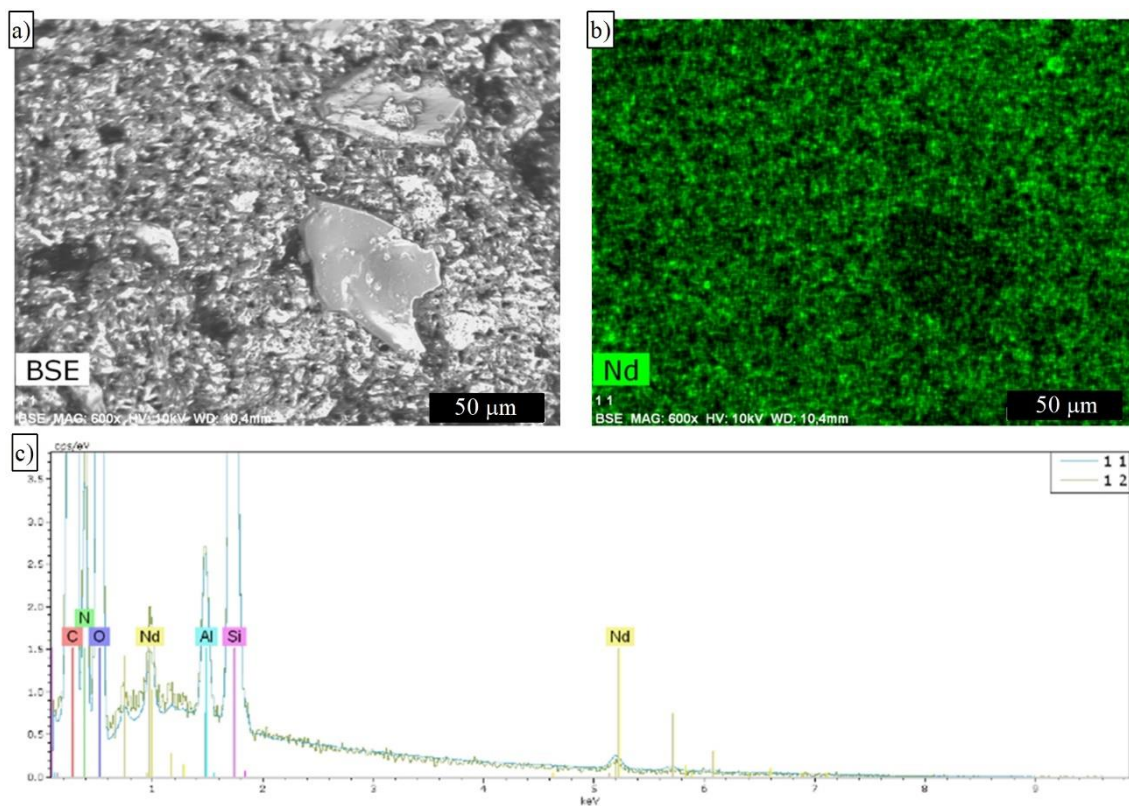


Figure 68. SEM images of H-MP4-B-C after the contact with a Nd containing solution. A) shows the morphology of the materials while b) visualizes the spatial distribution of Nd. In c) the corresponding EDX spectrum is shown.

At the observed scale, the images suggest a homogenous distribution of Nd in the H-MP4-B-C after the extraction (see **Figure 68 b**). This indicates that the solution diffused entirely into the materials and the equilibrium is effectively reached after 24 h of contact. Furthermore, by analyzing the EDX spectrum, a molar ratio of Nd/Si of 0.103 was determined. Considering the molecular weight of H-MP4-B-C ($481 \pm 30 \text{ g mol}^{-1}$, see **Figure 37**), this is slightly superior to the ratio determined from Q_{max} (0.080 ± 0.005). Mathematically, this implies that 10 to 13 headgroups participate in the extraction mechanism. For steric reasons, it is improbable that all of them participate in the coordination of one ion. It is more probable that this is due to the electrostatic repulsion between the adsorbed species that limits the ion uptake.

1.3 Competitive extraction in a simulated NdFeB magnet leachate

Considering the performance of H-MP4-B-C in the adsorption of Nd, the uptake of REE such as Nd, Pr and Dy compared to B, Co, Ni and Fe which are the major components in permanent magnets, was investigated. A new set of experiments was performed at pH 1 using a simulated leaching solution of permanent magnets with the composition provided in **Table 15**.

Table 15. Simulated leachate of a NdFeB magnet.

Elements	B	Co	Dy	Fe	Nd	Ni	Pr
w%	1.1	1.6	1.3	67.2	24.5	0.6	3.7
Concentration /ppm	11.32	15.45	12.35	641.6	218.7	3.05	34.34

A metal/material ratio was fixed between 125 to 3500 ($8 - 0.3 \text{ g L}^{-1}$, $V=1 - 25 \text{ mL}$, $m = 7 \text{ mg}$). The results are shown in **Figure 69**.

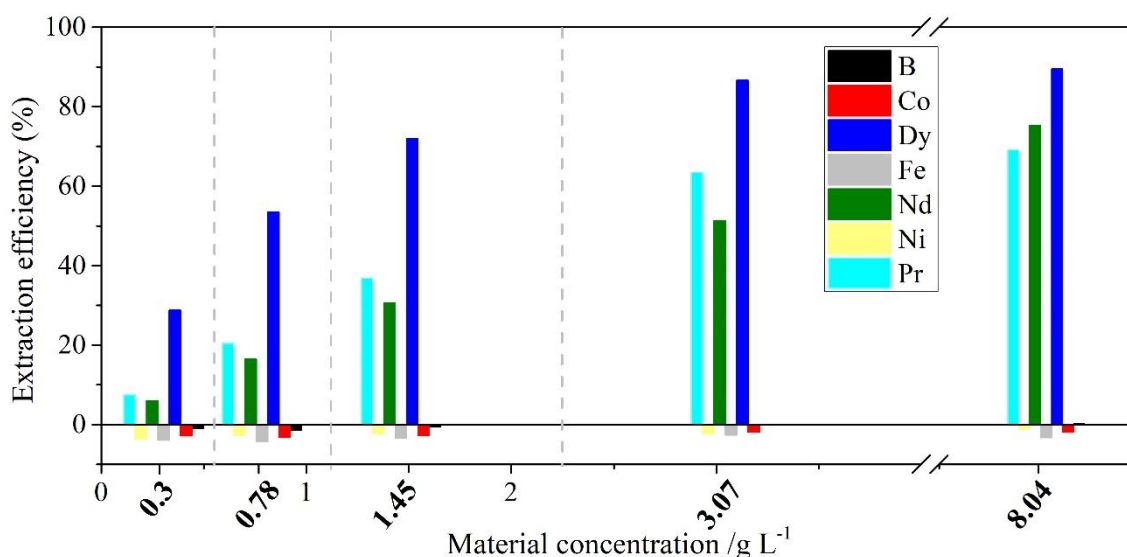


Figure 69. The extraction efficiency of various metals from a simulated NdFeB leachate as a function of the quantity of H-MP4-B-C.

Whatever the conditions, no extraction of B, Co, Fe and Ni by the material was observed. The results show that the material selectively extracts the REEs with regards to the other cations. These results demonstrate the potential use of H-MP4-B-C concerning the selective extraction of REE in the presence of competitive ions, especially iron which is the main competing ion in the NdFeB leaching solution.

4 Conclusion and outlook

The extraction experiments show the potential application of H-MP4-B-C for the selective extraction of REEs from NdFeB magnet leachates. The results show that the diethyl diglycolamide headgroup is the only effective and selective extraction function. The triazole group that is present in all materials, does not participate in the extraction. H-MP4-B-C appears to extract Nd using a non-ionic mechanism. The high number of headgroups involved in the extraction indicates a limitation of the ion uptake due to electrostatic repulsions.

However it will be interesting to perform a kinetic study in order to establish the exact time to reach the equilibrium and to investigate the controlling mechanism of the sorption process thanks to kinetics parameters determined from kinetic models such as pseudo first-order, pseudo-second-order models.²⁹³

Also, further experiments must be considered in order to evaluate the reusability of the material in consecutive extraction/stripping step and the extraction at higher concentration of competitive ions.

CONCLUSION

In the context of the implementation of a methodology for sorbent synthesis applicable to solid-liquid extraction, new SHMs were elaborated following a multi-step strategy. First, new organosilane precursors with amphiphilic characteristics were obtained in more than satisfactory yields from commercially available starting materials. This includes the synthesis of alkyne-modified diglycolamic acid derivatives and a triethoxy silane azide that were combined using Click-chemistry.

Second, these newly synthesized organosilane precursors were used for the elaboration of SHMs *via* an all-in-one approach. Characterizing the silica network and the various morphologies of the SHMs, several parameters such as the solvent (water or THF) and the catalysis (acidic or basic) were identified and pinpointed as major factors that influence the structuring of the silsesquioxane precursors. The local connectivity and the mesoscale structures were related to the specific headgroup interactions of the organosilane precursors during polymerization. It was highlighted that both depend simultaneously on the precursor organization during polymerization and the chemically directed connectivity of the growing siloxane network. This last result allows the prediction of the material morphology and structure which may help to control the mechanical, optical, insulating and extracting properties. Supplementary work on the same type of organosilane precursors still has to be done such as the modification of the chain length or the introduction of *e.g.* cyclic species in order to increase the stability of the head group.

In order to increase the surface of such non-porous materials which may improve their extraction properties, an innovative approach using structured binary TBA/water mixtures as solvent was used.

The first step was to investigate the structuring of materials formed from TEOS. The specific interactions of the initially formed silica nanoparticles with non-structuring ethanol or structuring *tert*-butanol and water were proposed to be responsible for an acceleration of the polymerization kinetics and an increased specific surface area. This result can be used to gain further understanding of the stabilization, polymerization and dissolution kinetics of metaloxides. Indeed, the affinity of nanoparticles to one solvent in a solvent mixture has the potential to be a subtle controlling parameter for the behavior of colloidal suspensions. For further studies, variations of the pH, the solvents, the precursor and the temperature should be investigated. An exhaustive SANS study with matched contrasts of TBA and silica can clarify the exact mechanism. In this case, contrast matching should be done by the deuteration of the alkyl positions of TBA in order to avoid the perturbation of the H-bonding interactions.

Conclusion

In a second step, a newly synthesized, non-functionalized organosilane precursor was added during the silica polymerization in structured solvents in order to elaborate porous SHMs in an all-in-one approach. The mechanism was investigated by relating the obtained material morphology to the addition delay of the non-functionalized organosilane precursor. The surfactant characteristics of the organosilane precursor and the advancement of the polymerization before the precursor addition were identified as the property defining parameters. For continuing studies, many parameters should be examined like the chain length in order to influence the surfactant characteristics of the precursor. This might enhance the effect of the solvent structuring on the material morphology. The variation of the headgroup might be used to further tailor the material morphology to, finally, obtain the desired properties. These materials should also be investigated concerning their extracting properties. Furthermore, the potential microporosity enables the diffusion of gases like CO₂ which allows the application for depollution.

During this work, only the non-porous SHMs were tested for REE extraction. The diethyl diglycolamide headgroup showed promising results for the selective and efficient extraction of REEs in the presence of competitive ions from a simulated NdFeB magnet leachate. Futures studies should now be focused on the extraction of REEs using the porous SHMs synthesized in chapter V. Supplementary studies should also include the variation of the material morphology to tailor the surface density of the headgroups which might allow the increase of the extraction efficiency. Moreover, the modification of the headgroup by varying the length of the alkyl chains or the amount of diglycolamide functions per molecule is possible to optimize the extraction efficiency. All modifications should be done keeping the mechanisms that govern the structuring proposed in the chapter III in mind. Finally, the reusability after several cycles and the stability of the materials regarding the solution is important for extraction and have to be explored.

Overall, this work offers promising perspectives for the all-in-one synthesis of SHMs with direct applications. The knowledge for the mechanistic comprehension is at hand but their concrete application to design the synthesis in order to obtain the desired properties still requires a large amount of investigations. For industrial application, the study of the scalability of the developed synthesis routes is important and will have to be tested.

VII RÉSUMÉ EN FRANÇAIS

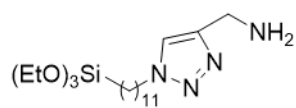
Selon l'IUPAC¹, les terres rares sont un groupe de 17 éléments chimiques du tableau périodique. Ce sont des éléments dit critiques car utilisés dans beaucoup de dispositifs technologiques comme les moteurs électriques, les technologies de l'information, les aimants, l'optique...² Leur extraction minière présentent plusieurs problèmes économiques et environnementaux, leur recyclage est très attractif⁸ et permet notamment de passer à une économie circulaire.

Un des moyens de recycler ces éléments est l'extraction solide-liquide qui peut être réalisée à l'aide de matériaux hybrides à base de silice (SHM pour "silica hybrid materials") possédant des groupes fonctionnels spécifiques. La synthèse de SHM est généralement réalisée en plusieurs phases. La première de ces phases, consiste à former un réseau siloxane afin d'obtenir une structure inorganique *via* le procédé sol-gel. C'est durant cette première phase, que le réglage d'une majorité de paramètres et l'addition d'additifs est possible afin de contrôler les propriétés désirées (morphologie, structure...). La deuxième phase correspond à l'enlèvement du solvant et la dernière à la fonctionnalisation post-synthétique du matériau avec des fonctions organiques. Une telle méthodologie peut présenter plusieurs inconvénients comme la nécessité de retirer l'additif après le procédé sol-gel et l'inhomogénéité du greffage des molécules fonctionnelles à la surface du matériau.

Une approche "tout-en-un" pour la synthèse de SHM permet d'éliminer une partie de ces inconvénients. En modifiant le précurseur siloxane, c'est-à-dire en y ajoutant directement la fonction organique, et en optimisant les conditions de synthèse du matériau, il est possible d'obtenir un SHM présentant des propriétés d'intérêt. Cette approche a déjà fait ses preuves dans des travaux précédents.^{10,11} En suivant cette même approche "tout-en-un", ce travail de thèse s'est focalisé sur la synthèse de nouveaux précurseurs organosilanes possédant un caractère amphiphile et leur utilisation pour l'élaboration de SHM dense et poreux par le développement de nouvelles voies de synthèse.

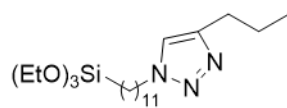
Cinq précurseurs organosilanes présentés ci-dessous (**Figure R.1**) ont été synthétisés à partir de molécules commerciales avec de bonnes valeurs de rendement. Citons, les dérivés de l'acide diglycolamique modifié par une fonction alkyne et un triéthoxysilane avec une fonction azide qui sont ensuite combinés par l'utilisation de la chimie « click ».

a)



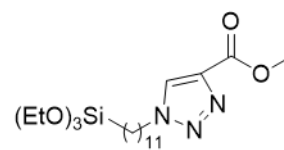
P1

b)



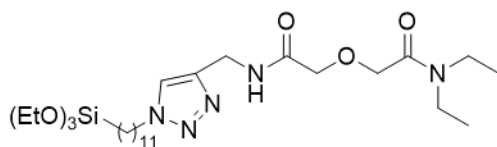
P2

c)



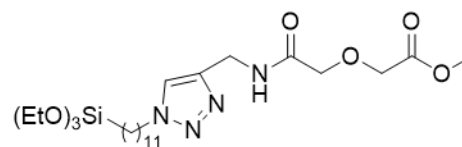
P3

d)



P4

e)



P5

Figure R.1. Précurseurs organosilanes utilisés dans cette étude.

Afin d'utiliser ces précurseurs de manière cohérente pour l'élaboration de SHM, il a tout d'abord été nécessaire de comprendre les interactions entre les différents éléments présents dans le système réactionnel, soit l'eau, l'organosilane, le co-solvant et le TEOS. C'est dans ce but, que la stratégie de l'étude en trois phases présentée ci-dessous (**Figure R.2**) a été mise en place.

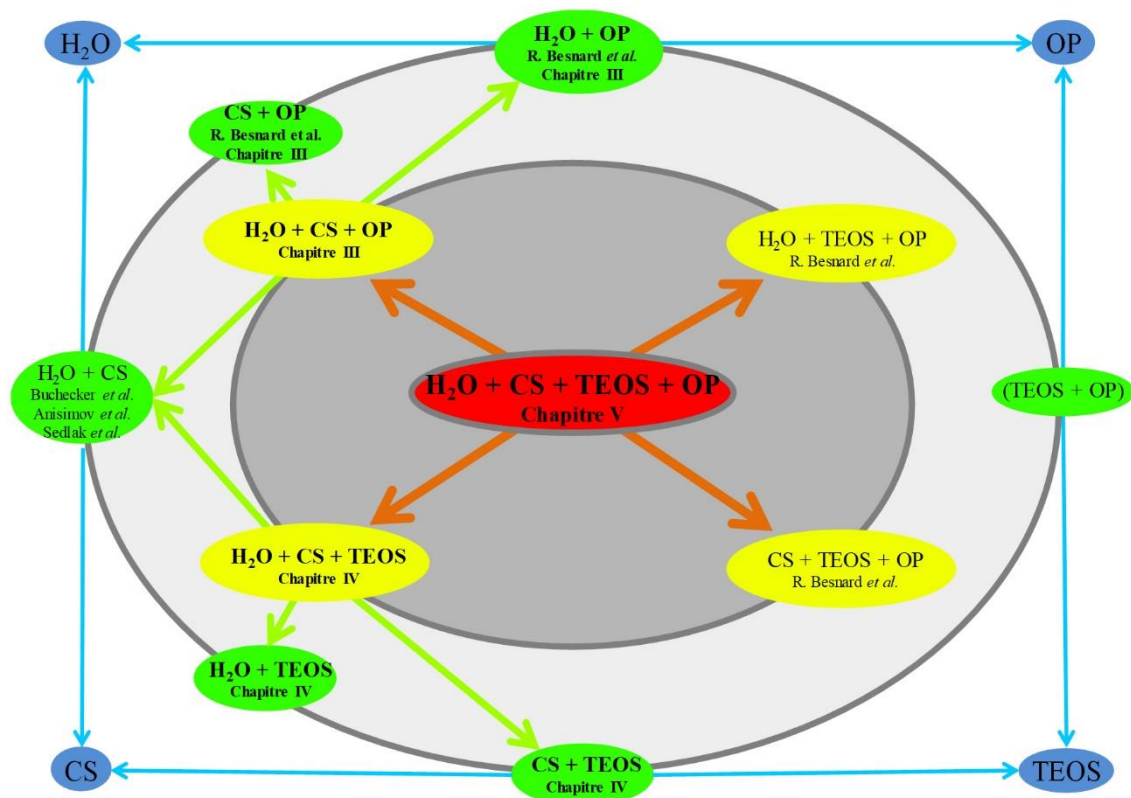


Figure R.2: Stratégie employée durant ce travail de thèse.

Durant la première phase de ce travail, des SHM ont été élaborés par polymérisation des cinq nouveaux organosilanes. Avec l'objectif de contrôler l'organisation de la structure à l'échelle mesoscopique des organosilanes dans les SHM, plusieurs voies de synthèse ont été testées : voie aqueuse et solvant (THF), ainsi que la nature de la catalyse acide et basique du procédé sol-gel. La caractérisation des matériaux au cours de leur élaboration par spectroscopie infrarouge à Transformée de Fourier (FTIR), par Analyse Thermique Gravimétrique (ATG) et par diffusion des rayons X aux petits angles (SAXS) a permis de mettre en évidence les résultats présentés sur la **Figure R.3**.

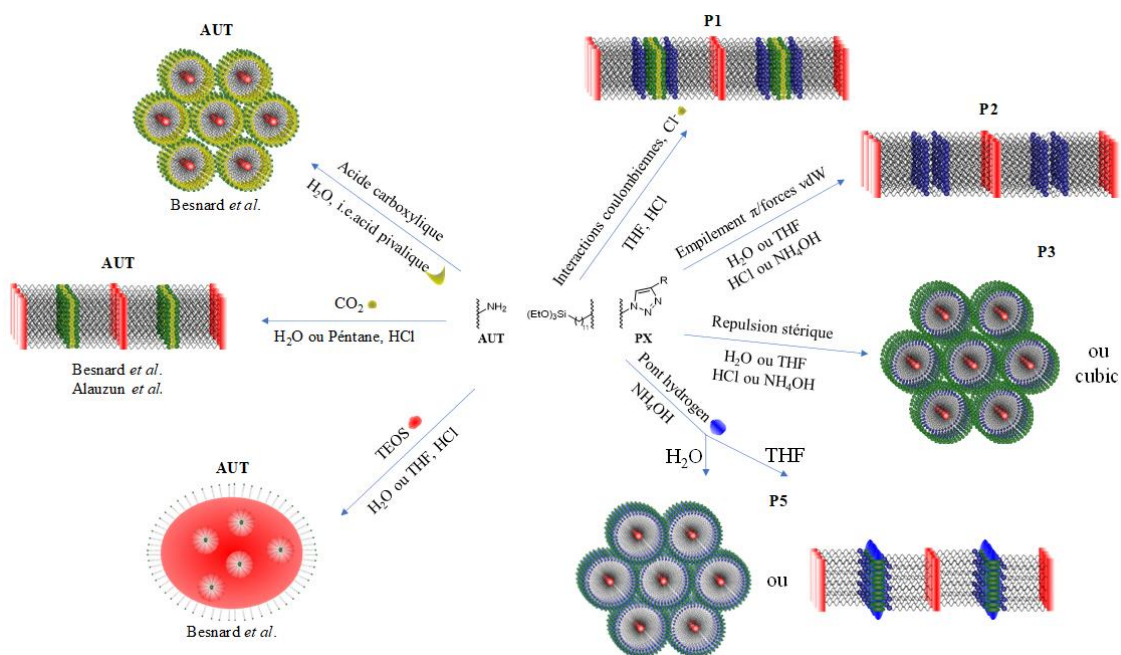


Figure R.3. Vue d'ensemble des résultats obtenus lors de l'élaboration de SHM à partir des précurseurs organosilane. Les paramètres influençant la structure à l'échelle mésoscopique sont indiqués. A titre indicatif, les résultats obtenus par Besnard et al et Alauzun et al (AUT¹⁰) sont aussi inclus.

L'étude de la polymérisation des précurseurs organosilanes a permis de mettre en évidence l'importance des interactions physico-chimiques pour contrôler la mesostructure des SHM. Tandis que ce sont des interactions coulombiennes qui conduisent à la formation d'une structure lamellaire lors de la synthèse de SHM avec P1, c'est une combinaison d'interactions π et de Van der Waals qui entraînent la formation de cette même phase avec P2. Lors de l'utilisation de P3, l'encombrement stérique du groupe de tête ester rigide est responsable de la formation de mesophases inversées avec une courbure vers la silice. Finalement, pour P5, la formation d'une pseudo-phase riche en liaisons hydrogène entre les groupes fonctionnels permet la formation d'une phase hexagonale 2D en voie aqueuse ou bien d'une phase lamellaire en voie THF. De plus, il a pu être mis en évidence par ce travail que ce sont les interactions spécifiques des groupes fonctionnels de têtes des précurseurs et l'affinité chimique entre groupes silanols qui pilotent la connectivité locale du réseau de silice et la mesostructure dans le SHM final.

La deuxième phase de ce travail de thèse a consisté à étudier une nouvelle voie de synthèse utilisant des systèmes binaires non-structurants (eau/éthanol) et structurants (eau/*tert*-butanol) pour augmenter la surface spécifique des SHM, propriété d'intérêt pour l'extraction.^{205,206,269,270} Afin de comprendre les processus de base, la cinétique de polymérisation du réseau de silice a été étudiée avec du tétraéthyl orthosilicate (TEOS). L'influence de la nature du solvant et de la fraction $[\text{H}_2\text{O}]/[\text{solvant}]$ sur le temps de gélification et la morphologie du matériau final a été étudiée par FTIR, diffusion de la lumière dynamique (DLS), SAXS et microscopie électronique à transmission (TEM). Les résultats ont permis de mettre en évidence, qu'avant la condensation, le système

eau/alcool/TEOS formait une microémulsion et ce, sans tensioactif. Cette structuration disparaît dès lors que le TEOS s'hydrolyse et forme des nanoparticules dont la taille de 0.2 à 0.5 nm de rayon, conditionnée par la fraction $[H_2O]/[solvant]$, condensent pour former un réseau fractal. Les aérogels obtenus séchés par CO_2 supercritique présentent des caractéristiques morphologiques et des surfaces spécifiques remarquables, certaines supérieures à $1400 \text{ m}^2 \cdot \text{g}^{-1}$, lorsqu'ils résultent de solvants structurés. Ces résultats ont permis de montrer que la structuration du solvant dans l'environnement immédiat des particules de silice est responsable du comportement observé. Une hypothèse de l'influence de la structuration du solvant sur le mécanisme de polymérisation est proposée dans laquelle les particules de silice s'agrègent de manière différente en fonction de la composition du solvant dans leur environnement immédiat. Dans les solvants structurés, les domaines riches en eau recouvrent les particules de silice (**Figure R.4**). Cela conduit à des conditions réactionnelles similaires à celles de l'eau pure, alors que les domaines riches en *tert*-butanol forment des régions où la polymérisation n'a pas lieu. Cette étude a fait l'objet d'un article.¹⁹⁹

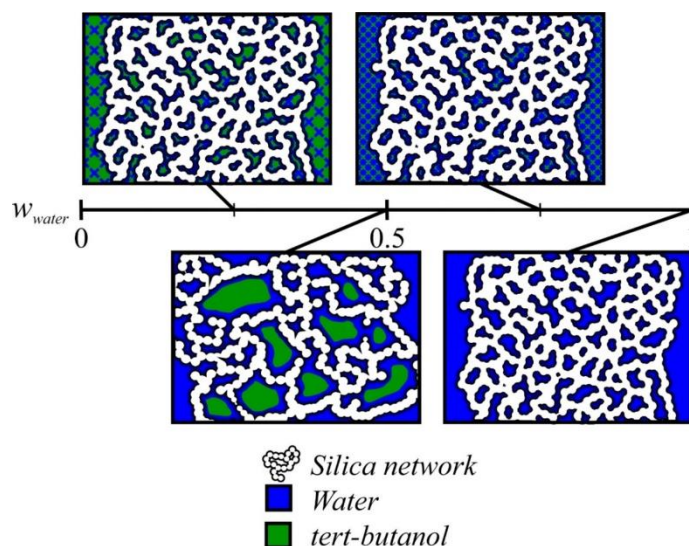


Figure R.4. Illustration simplifiée de la structuration mesoscopique du gel de silice en fonction de la fraction $[H_2O]/[tert\text{-butanol}]$.

Durant la troisième phase de ce travail, l'organotrialkoxysilane P2 a été intégré dans les systèmes eau/*tert*-butanol/TEOS en étudiant l'effet de son retard à son addition lors du processus sol-gel. P2 a été sélectionné car son groupe fonctionnel de tête ne permet pas de former de liaison hydrogène ou de liaison ionique. Ajouté initialement au système, le P2 hydrolysé développe un caractère amphiphile avec son groupe de la partie silicate ionique conduisant à la formation d'une émulsion. P2 hydrolysé est alors situé à l'interphase entre un domaine riche en silice et un domaine riche en solvant. Dans ce cas-là, c'est P2 qui dirige la morphologie du matériau final et la fonction de tête se situe à la surface des macropores. Lorsque l'ajout de P2 est retardé, c'est la formation de gel de TEOS qui pilote la morphologie du matériau. Dans ce dernier cas, les SHM obtenus deviennent de plus en plus microporeux avec la durée du retard à l'ajout de P2. Pour ces

SHM, la morphologie est plus complexe et la situation exacte de l'organosilane n'a pas pu être déterminée. Dans tous les cas, la co-condensation s'est avérée hétérogène. Les particules primaires provenant de TEOS réagissent les unes avec les autres pendant que l'organosilane est greffé sur les surfaces disponibles.

La dernière partie de ce travail a consisté à tester les propriétés d'extraction des SHM synthétisés à partir des précurseurs d'organosilane purs. Les premières expériences montrent l'application potentielle du SHM réalisé à partir de P4 par voie aqueuse et basique pour l'extraction sélective des terres rares des modèles lixiviats à aimants NdFeB. Ce dernier matériau semble extraire le Nd par un mécanisme non ionique. Le nombre élevé de groupes fonctionnels impliqués dans l'extraction indique une limitation de l'absorption d'ions due aux répulsions électrostatiques. De plus, les résultats montrent que le groupe de tête diéthyl diglycolamide est la seule fonction d'extraction efficace et sélective. Le groupe triazole, présent dans tous les matériaux, ne participe pas à l'extraction.

Dans l'ensemble, ces travaux offrent des perspectives prometteuses pour la synthèse « tout-en-un » de SHM à applications directes. Les connaissances en matière de compréhension mécanistique sont à portée de main, mais leur application concrète pour concevoir la synthèse en vue d'obtenir les propriétés souhaitées nécessite encore de nombreuses recherches. Citons par exemple, l'utilisation des précurseurs possédant des groupements fonctionnels susceptibles de générer des interactions physico-chimiques pour l'élaboration des matériaux par la voie des systèmes binaires structurants qui n'ont pu être étudiés durant ce travail.

Pour des applications industrielles potentielles, l'étude de l'évolutivité des voies de synthèse développées devra être testée.

VIII REFERENCES

- (1) Zepf, V. Rare Earth Elements: What and Where They Are. In *pringer Theses (Recognizing Outstanding Ph.D. Research)*; Berlin, 2013; pp 11–39. https://doi.org/10.1007/978-3-642-35458-8_2.
- (2) Balaram, V. Rare Earth Elements: A Review of Applications, Occurrence, Exploration, Analysis, Recycling, and Environmental Impact. *Geosci. Front.* **2019**, *10* (4), 1285–1303. <https://doi.org/10.1016/j.gsf.2018.12.005>.
- (3) Goodenough, K. M.; Wall, F.; Merriman, D. The Rare Earth Elements: Demand, Global Resources, and Challenges for Resourcing Future Generations. *Nat. Resour. Res.* **2018**, *27* (2), 201–216. <https://doi.org/10.1007/s11053-017-9336-5>.
- (4) 2011 Critical Materials Strategy Summary. 2011, p 196.
- (5) Kumari, A.; Panda, R.; Jha, M. K.; Kumar, J. R.; Lee, J. Y. Process Development to Recover Rare Earth Metals from Monazite Mineral: A Review. *Minerals Engineering*. Pergamon August 1, 2015, pp 102–115. <https://doi.org/10.1016/j.mineng.2015.05.003>.
- (6) Sengupta, M. *Environmental Impacts of Mining: Monitoring, Restoration, and Control*; Routledge, 2018. <https://doi.org/10.1201/9780203757062>.
- (7) Li, X. Y.; Ge, J. P.; Chen, W. Q.; Wang, P. Scenarios of Rare Earth Elements Demand Driven by Automotive Electrification in China: 2018–2030. *Resour. Conserv. Recycl.* **2019**, *145*, 322–331. <https://doi.org/10.1016/j.resconrec.2019.02.003>.
- (8) Yoon, H.-S.; Kim, C.-J.; Chung, K.-W.; Kim, S.-D.; Lee, J.-Y.; Kumar, J. R. Solvent Extraction, Separation and Recovery of Dysprosium (Dy) and Neodymium (Nd) from Aqueous Solutions: Waste Recycling Strategies for Permanent Magnet Processing. *Hydrometallurgy* **2016**, *165*, 27–43. <https://doi.org/10.1016/J.HYDROMET.2016.01.028>.
- (9) Yang, Y.; Walton, A.; Sheridan, R.; Güth, K.; Gauß, R.; Gutfleisch, O.; Buchert, M.; Steenari, B.-M.; Van Gerven, T.; Jones, P. T.; et al. REE Recovery from End-of-Life NdFeB Permanent Magnet Scrap: A Critical Review. *J. Sustain. Metall.* **2017**, *3* (1), 122–149. <https://doi.org/10.1007/s40831-016-0090-4>.
- (10) Besnard, R. Développement d’une Méthodologie de Synthèse de Silices Hybrides à Haute Capacité Extractante, Université de Montpellier, 2015.
- (11) Alauzun, J.; Mehdi, A.; Mouawia, R.; Reyé, C.; Corriu, R. J. P. Synthesis of New Lamellar Materials by Self-Assembly and Coordination Chemistry in the Solids. In *Journal of Sol-Gel Science and Technology*; Springer US, 2008; Vol. 46, pp 383–392. <https://doi.org/10.1007/s10971-008-1710-7>.
- (12) Mammeri, F.; Bourhis, E. Le; Rozes, L.; Sanchez, C. Mechanical Properties of

References

- Hybrid Organic–Inorganic Materials. *J. Mater. Chem.* **2005**, *15* (35–36), 3787. <https://doi.org/10.1039/b507309j>.
- (13) 3600 Google scholar search results “silica hybrid materials” scholar.google.com (accessed Mar 28, 2019).
- (14) 6600 SciFinder search results “silica hybrid materials” <https://scifinder.cas.org/> (accessed Mar 28, 2019).
- (15) 13100 Web of knowledge search results “silica hybrid materials” <https://apps.webofknowledge.com> (accessed Mar 29, 2019).
- (16) Yoo, D.-Y.; Banthia, N. Mechanical Properties of Ultra-High-Performance Fiber-Reinforced Concrete: A Review. *Cem. Concr. Compos.* **2016**, *73*, 267–280. <https://doi.org/10.1016/J.CEMCONCOMP.2016.08.001>.
- (17) Norhasri, M. S. M.; Hamidah, M. S.; Fadzil, A. M. Applications of Using Nano Material in Concrete: A Review. *Constr. Build. Mater.* **2017**, *133*, 91–97. <https://doi.org/10.1016/J.CONBUILDMAT.2016.12.005>.
- (18) Robertson, C. G.; Roland, C. M. Glass Transition and Interfacial Segmental Dynamics in Polymer-Particle Composites. *Rubber Chem. Technol.* **2008**, *81* (3), 506–522. <https://doi.org/10.5254/1.3548217>.
- (19) ten Brinke, J. W.; Debnath, S. C.; Reuvekamp, L. A. E. M.; Noordermeer, J. W. M. Mechanistic Aspects of the Role of Coupling Agents in Silica-Rubber Composites. *Compos. Sci. Technol.* **2003**, *63* (8), 1165–1174. [https://doi.org/10.1016/S0266-3538\(03\)00077-0](https://doi.org/10.1016/S0266-3538(03)00077-0).
- (20) Bao, Y.; Ma, J.; Zhang, X.; Shi, C. Recent Advances in the Modification of Polyacrylate Latexes. *J. Mater. Sci.* **2015**, *50* (21), 6839–6863. <https://doi.org/10.1007/s10853-015-9311-7>.
- (21) Peng, L.; Guo, R.; Lan, J.; Jiang, S.; Lin, S. Microwave-Assisted Deposition of Silver Nanoparticles on Bamboo Pulp Fabric through Dopamine Functionalization. *Appl. Surf. Sci.* **2016**, *386*, 151–159. <https://doi.org/10.1016/J.APSUSC.2016.05.170>.
- (22) Wu, M.; Ma, B.; Pan, T.; Chen, S.; Sun, J. Silver-Nanoparticle-Colored Cotton Fabrics with Tunable Colors and Durable Antibacterial and Self-Healing Superhydrophobic Properties. *Adv. Funct. Mater.* **2016**, *26* (4), 569–576. <https://doi.org/10.1002/adfm.201504197>.
- (23) Sanchez, C.; Julián, B.; Belleville, P.; Popall, M. Applications of Hybrid Organic–Inorganic Nanocomposites. *J. Mater. Chem.* **2005**, *15* (35–36), 3559. <https://doi.org/10.1039/b509097k>.
- (24) Wang, H.; Zhu, Q.-L.; Zou, R.; Xu, Q. Metal-Organic Frameworks for Energy Applications. *Chem* **2017**, *2* (1), 52–80. <https://doi.org/10.1016/J.CHEMPR.2016.12.002>.
- (25) Jandera, P.; Janás, P. Recent Advances in Stationary Phases and Understanding of Retention in Hydrophilic Interaction Chromatography. A Review. *Anal. Chim. Acta* **2017**, *967*, 12–32. <https://doi.org/10.1016/J.ACA.2017.01.060>.

- (26) Bharti, C.; Nagaich, U.; Pal, A. K.; Gulati, N. Mesoporous Silica Nanoparticles in Target Drug Delivery System: A Review. *Int. J. Pharm. Investig.* **2015**, *5* (3), 124–133. <https://doi.org/10.4103/2230-973X.160844>.
- (27) Faustini, M.; Nicole, L.; Boissière, C.; Innocenzi, P.; Sanchez, C.; Grosso, D. Hydrophobic, Antireflective, Self-Cleaning, and Antifogging Sol-Gel Coatings: An Example of Multifunctional Nanostructured Materials for Photovoltaic Cells. *Chem. Mater.* **2010**, *22* (15), 4406–4413. <https://doi.org/10.1021/cm100937e>.
- (28) Judeinstein, P.; Sanchez, C. Hybrid Organic-Inorganic Materials: A Land of Multidisciplinary. *J. Mater. Chem.* **1996**, *6* (4), 511–525. <https://doi.org/10.1039/JM9960600511>.
- (29) Evans, D. F.; Wennerström, H. *The Colloidal Domain*, 2nd ed.; John Wiley & Sons Inc: New York, 1999.
- (30) Brinker, C. J.; Scherer, G. W. *Sol-Gel Science: The Physics and Chemistry of Sol-Gel Processing*; Academic Press: Cambridge, 1990.
- (31) Ralph K., I. *The Chemistry of Silica: Solubility, Polymerization, Colloid and Surface Properties and Biochemistry of Silica*; Wiley: New York, 1979.
- (32) Leung, K.; Nielsen, I. M. B.; Criscenti, L. J. Elucidating the Bimodal Acid–Base Behavior of the Water–Silica Interface from First Principles. *J. Am. Chem. Soc.* **2009**, *131* (51), 18358–18365. <https://doi.org/10.1021/ja906190t>.
- (33) Vioux, A. Nonhydrolytic Sol-Gel Routes to Oxides. *Chemistry of Materials*. American Chemical Society November 1997, pp 2292–2299. <https://doi.org/10.1021/cm970322a>.
- (34) Niederberger, M.; Garnweitner, G. Organic Reaction Pathways in the Nonaqueous Synthesis of Metal Oxide Nanoparticles. *Chem. - A Eur. J.* **2006**, *12* (28), 7282–7302. <https://doi.org/10.1002/chem.200600313>.
- (35) Ayral, A.; Julbe, A.; Roualdes, S.; Rouessac, V.; Durand, J.; Sala, B. Silica Membranes - Basic Principles. In *Periodica Polytechnica Chemical Engineering*; 2006; Vol. 50, pp 67–79.
- (36) Belton, D. J.; Deschaume, O.; Perry, C. C. An Overview of the Fundamentals of the Chemistry of Silica with Relevance to Biosilicification and Technological Advances. *FEBS J.* **2012**, *279* (10), 1710–1720. <https://doi.org/10.1111/j.1742-4658.2012.08531.x>.
- (37) Cushing, B. L.; Kolesnichenko, V. L.; O'Connor, C. J. Recent Advances in the Liquid-Phase Syntheses of Inorganic Nanoparticles. *Chem. Rev.* **2004**, *104* (9), 3893–3946. <https://doi.org/10.1021/cr030027b>.
- (38) Adnan, M. M.; Dalod, A. R. M.; Balci, M. H.; Glaum, J.; Einarsrud, M. A. In Situ Synthesis of Hybrid Inorganic-Polymer Nanocomposites. *Polymers (Basel)*. **2018**, *10* (10), 1129. <https://doi.org/10.3390/polym10101129>.
- (39) Stöber, W.; Fink, A.; Bohn, E. Controlled Growth of Monodisperse Silica Spheres in the Micron Size Range. *J. Colloid Interface Sci.* **1968**, *26* (1), 62–69. [https://doi.org/10.1016/0021-9797\(68\)90272-5](https://doi.org/10.1016/0021-9797(68)90272-5).

References

- (40) Kelts, L. W.; Effinger, N. J.; Melpolder, S. M. Sol-Gel Chemistry Studied by ^1H and ^{29}Si Nuclear Magnetic Resonance. *J. Non. Cryst. Solids* **1986**, *83* (3), 353–374. [https://doi.org/10.1016/0022-3093\(86\)90248-6](https://doi.org/10.1016/0022-3093(86)90248-6).
- (41) Devreux, F.; Boilot, J. P.; Chaput, F.; Lecomte, A. Sol-Gel Condensation of Rapidly Hydrolyzed Silicon Alkoxides: A Joint ^{29}Si NMR and Small-Angle x-Ray Scattering Study. *Phys. Rev. A* **1990**, *41* (12), 6901–6909. <https://doi.org/10.1103/PhysRevA.41.6901>.
- (42) Winter, R.; Chan, J.-B.; Frattini, R.; Jonas, J. The Effect of Fluoride on the Sol-Gel Process. *J. Non. Cryst. Solids* **1988**, *105* (3), 214–222. [https://doi.org/10.1016/0022-3093\(88\)90310-9](https://doi.org/10.1016/0022-3093(88)90310-9).
- (43) Tilgner, I. C.; Fischer, P.; Bohnen, F. M.; Rehage, H.; Maier, W. F. Effect of Acidic, Basic and Fluoride-Catalyzed Sol-Gel Transitions on the Preparation of Sub-Nanostructured Silica. *Microporous Mater.* **1995**, *5* (1–2), 77–90. [https://doi.org/10.1016/0927-6513\(95\)00045-B](https://doi.org/10.1016/0927-6513(95)00045-B).
- (44) Corriu, R. J. P.; Young, J. C. Hypervalent Silicon Compounds. In *Silicon-Heteroatom Bond: Updates from the Chemistry of Functional Groups*; John Wiley & Sons, Ltd: Chichester, UK, 2010; pp 1–48. <https://doi.org/10.1002/9780470772447.ch1>.
- (45) Corriu, R.; Nguyễn, T. A. *Chimie Moléculaire, Sol-Gel et Nanomatériaux*; Éditions de l'École polytechnique, 2008.
- (46) Deshmukh, R.; Niederberger, M. Mechanistic Aspects in the Formation, Growth and Surface Functionalization of Metal Oxide Nanoparticles in Organic Solvents. *Chem. - A Eur. J.* **2017**, *23* (36), 8542–8570. <https://doi.org/10.1002/chem.201605957>.
- (47) Sharp, K. G. *A Two-Component, Non-Aqueous Route to Silica Gel Code: A7*; 1994; Vol. 2.
- (48) Orel, B.; Ješe, R.; Lavrenčič Štanger, U.; Grdadolnik, J.; Puchberger, M. Infrared Attenuated Total Reflection Spectroscopy Studies of Aprotic Condensation of $(\text{EtO})_3\text{SiRSi}(\text{OEt})_3$ and $\text{RSi}(\text{OEt})_3$ Systems with Carboxylic Acids. *J. Non. Cryst. Solids* **2005**, *351* (6–7), 530–549. <https://doi.org/10.1016/J.JNONCRY SOL.2005.01.007>.
- (49) Ionic Strength, I. In *IUPAC Compendium of Chemical Terminology*; IUPAC: Research Triangle Park, NC. <https://doi.org/10.1351/goldbook.I03180>.
- (50) Murakata, T.; Sato, S.; Ohgawara, T.; Watanabe, T.; Suzuki, T. *Control of Pore Size Distribution of Silica Gel through Sol-Gel Process Using Inorganic Salts and Surfactants as Additives*; 1992; Vol. 27.
- (51) Pope, E. J. A.; Mackenzie, J. D. Sol-Gel Processing of Silica: II. The Role of the Catalyst. *J. Non. Cryst. Solids* **1986**, *87* (1–2), 185–198. [https://doi.org/10.1016/S0022-3093\(86\)80078-3](https://doi.org/10.1016/S0022-3093(86)80078-3).
- (52) Soler-Illia, G. J. de A. A.; Sanchez, C.; Lebeau, B.; Patarin, J. Chemical Strategies To Design Textured Materials: From Microporous and Mesoporous Oxides to Nanonetworks and Hierarchical Structures. *Chem. Rev.* **2002**, *102* (11), 4093–

4138. <https://doi.org/10.1021/cr0200062>.
- (53) Hamley, I. W. *Introduction to Soft Matter— Revised Edition*; John Wiley & Sons, Ltd: Chichester, UK, 2007. <https://doi.org/10.1002/9780470517338>.
- (54) Russel, W. B.; Saville, D. A.; Schowalter, W. R. *Colloidal Dispersions*; Cambridge University Press, 1989.
- (55) Zemb, T. N.; Klossek, M.; Lopian, T.; Marcus, J.; Schöetl, S.; Horinek, D.; Prevost, S. F.; Touraud, D.; Diat, O.; Marčelja, S.; et al. How to Explain Microemulsions Formed by Solvent Mixtures without Conventional Surfactants. *Proc. Natl. Acad. Sci.* **2016**, *113* (16), 4260–4265. <https://doi.org/10.1073/pnas.1515708113>.
- (56) Schwierz, N.; Horinek, D.; Sivan, U.; Netz, R. R. Reversed Hofmeister Series— The Rule Rather than the Exception. *Curr. Opin. Colloid Interface Sci.* **2016**, *23*, 10–18. <https://doi.org/10.1016/j.cocis.2016.04.003>.
- (57) Kunz, W. Specific Ion Effects, Theory. In *Encyclopedia of Applied Electrochemistry*; Springer New York: New York, NY, 2014; pp 2050–2053. https://doi.org/10.1007/978-1-4419-6996-5_27.
- (58) Grahame, D. C. The Electrical Double Layer and the Theory of Electrocapillarity. *Chem. Rev.* **1947**, *41* (3), 441–501. <https://doi.org/10.1021/cr60130a002>.
- (59) Parsegian, V. A.; Zemb, T. Hydration Forces: Observations, Explanations, Expectations, Questions. *Curr. Opin. Colloid Interface Sci.* **2011**, *16* (6), 618–624. <https://doi.org/10.1016/J.COCIS.2011.06.010>.
- (60) Kunz, W.; Holmberg, K.; Zemb, T. Hydrotropes. *Curr. Opin. Colloid Interface Sci.* **2016**, *22*, 99–107. <https://doi.org/10.1016/j.cocis.2016.03.005>.
- (61) Srinivas, V.; Balasubramanian, D. When Does the Switch from Hydrotrophy to Micellar Behavior Occur? *Langmuir* **1998**, *14* (23), 6658–6661. <https://doi.org/10.1021/la980598c>.
- (62) Schöttl, S.; Lopian, T.; Prévost, S.; Touraud, D.; Grillo, I.; Diat, O.; Zemb, T.; Horinek, D. Combined Molecular Dynamics (MD) and Small Angle Scattering (SAS) Analysis of Organization on a Nanometer-Scale in Ternary Solvent Solutions Containing a Hydrotrope. *J. Colloid Interface Sci.* **2019**, *540*, 623–633. <https://doi.org/10.1016/j.jcis.2019.01.037>.
- (63) Buchecker, T.; Krickl, S.; Winkler, R.; Grillo, I.; Bauduin, P.; Touraud, D.; Pfitzner, A.; Kunz, W. The Impact of the Structuring of Hydrotropes in Water on the Mesoscale Solubilisation of a Third Hydrophobic Component. *Phys. Chem. Chem. Phys.* **2017**, *19* (3), 1806–1816. <https://doi.org/10.1039/C6CP06696H>.
- (64) Israelachvili, J. N.; Mitchell, D. J.; Ninham, B. W. Theory of Self-Assembly of Hydrocarbon Amphiphiles into Micelles and Bilayers. *J. Chem. Soc. Faraday Trans. 2* **1976**, *72* (0), 1525. <https://doi.org/10.1039/f29767201525>.
- (65) Finnie, K. S.; Bartlett, J. R.; Barbé, C. J. A.; Kong, L. Formation of Silica Nanoparticles in Microemulsions. *Langmuir* **2007**, *23* (6), 3017–3024. <https://doi.org/10.1021/la0624283>.

References

- (66) Sun, B.; Chai, J.; Chai, Z.; Zhang, X.; Cui, X.; Lu, J. A Surfactant-Free Microemulsion Consisting of Water, Ethanol, and Dichloromethane and Its Template Effect for Silica Synthesis. *J. Colloid Interface Sci.* **2018**, *526*, 9–17. <https://doi.org/10.1016/j.jcis.2018.04.072>.
- (67) Rouquerol, J.; Avnir, D.; Fairbridge, C. W.; Everett, D. H.; Haynes, J. M.; Pernicone, N.; Ramsay, J. D. F.; Sing, K. S. W.; Unger, K. K. Recommendations for the Characterization of Porous Solids (Technical Report). *Pure Appl. Chem.* **1994**, *66* (8), 1739–1758. <https://doi.org/10.1351/pac199466081739>.
- (68) Chang, F.; Zhou, J.; Chen, P.; Chen, Y.; Jia, H.; Saad, S. M. I.; Gao, Y.; Cao, X.; Zheng, T. Microporous and Mesoporous Materials for Gas Storage and Separation: A Review. *Asia-Pacific J. Chem. Eng.* **2013**, *8* (4), 618–626. <https://doi.org/10.1002/apj.1717>.
- (69) Doonan, C. J.; Sumbly, C. J. Metal–Organic Framework Catalysis. *CrystEngComm* **2017**, *19* (29), 4044–4048. <https://doi.org/10.1039/C7CE90106B>.
- (70) Ron, R.; Haleva, E.; Salomon, A. Nanoporous Metallic Networks: Fabrication, Optical Properties, and Applications. *Adv. Mater.* **2018**, *30* (41), 1706755. <https://doi.org/10.1002/adma.201706755>.
- (71) Wang, B.; Prinsen, P.; Wang, H.; Bai, Z.; Wang, H.; Luque, R.; Xuan, J. Macroporous Materials: Microfluidic Fabrication, Functionalization and Applications. *Chem. Soc. Rev.* **2017**, *46* (3), 855–914. <https://doi.org/10.1039/c5cs00065c>.
- (72) Yuan, Z.-Y.; Su, B.-L. Insights into Hierarchically Meso–Macroporous Structured Materials. *J. Mater. Chem.* **2006**, *16* (7), 663–677. <https://doi.org/10.1039/B512304F>.
- (73) Sen, T.; Tiddy, G. J. T.; Casci, J. L.; Anderson, M. W. One-Pot Synthesis of Hierarchically Ordered Porous-Silica Materials with Three Orders of Length Scale. *Angew. Chemie Int. Ed.* **2003**, *42* (38), 4649–4653. <https://doi.org/10.1002/anie.200351479>.
- (74) Bharti, C.; Nagaich, U.; Pal, A. K.; Gulati, N. Mesoporous Silica Nanoparticles in Target Drug Delivery System: A Review. *Int. J. Pharm. Investig.* **2015**, *5* (3), 124–133. <https://doi.org/10.4103/2230-973X.160844>.
- (75) Giraldo, L. F.; López, B. L.; Pérez, L.; Urrego, S.; Sierra, L.; Mesa, M. Mesoporous Silica Applications. *Macromol. Symp.* **2007**, *258* (1), 129–141. <https://doi.org/10.1002/masy.200751215>.
- (76) Alothman, Z. A. A Review: Fundamental Aspects of Silicate Mesoporous Materials. *Materials*. Multidisciplinary Digital Publishing Institute December 17, 2012, pp 2874–2902. <https://doi.org/10.3390/ma5122874>.
- (77) Di Renzo, F.; Cambon, H.; Dutartre, R. A 28-Year-Old Synthesis of Micelle-Templated Mesoporous Silica. *Microporous Mater.* **1997**, *10* (4–6), 283–286. [https://doi.org/10.1016/S0927-6513\(97\)00028-X](https://doi.org/10.1016/S0927-6513(97)00028-X).
- (78) Kresge, C. T.; Leonowicz, M. E.; Roth, W. J.; Vartuli, J. C.; Beck, J. S. Ordered Mesoporous Molecular Sieves Synthesized by a Liquid-Crystal Template

- Mechanism. *Nature* **1992**, 359 (6397), 710–712. <https://doi.org/10.1038/359710a0>.
- (79) Beck, J. S.; Vartuli, J. C.; Roth, W. J.; Leonowicz, M. E.; Kresge, C. T.; Schmitt, K. D.; Chu, C. T. W.; Olson, D. H.; Sheppard, E. W.; McCullen, S. B.; et al. A New Family of Mesoporous Molecular Sieves Prepared with Liquid Crystal Templates. *J. Am. Chem. Soc.* **1992**, 114 (27), 10834–10843. <https://doi.org/10.1021/ja00053a020>.
- (80) Croissant, J. G.; Cattoën, X.; Wong Chi Man, M.; Durand, J. O.; Khashab, N. M. Syntheses and Applications of Periodic Mesoporous Organosilica Nanoparticles. *Nanoscale*. The Royal Society of Chemistry December 3, 2015, pp 20318–20334. <https://doi.org/10.1039/c5nr05649g>.
- (81) Suteewong, T.; Sai, H.; Cohen, R.; Wang, S.; Bradbury, M.; Baird, B.; Gruner, S. M.; Wiesner, U. Highly Aminated Mesoporous Silica Nanoparticles with Cubic Pore Structure. *J. Am. Chem. Soc.* **2011**, 133 (2), 172–175. <https://doi.org/10.1021/ja1061664>.
- (82) Xuan, M.; Shao, J.; Lin, X.; Dai, L.; He, Q. Self-Propelled Janus Mesoporous Silica Nanomotors with Sub-100 Nm Diameters for Drug Encapsulation and Delivery. *ChemPhysChem* **2014**, 15 (11), 2255–2260. <https://doi.org/10.1002/cphc.201402111>.
- (83) Lee, J.; Kim, J.; Hyeon, T. Recent Progress in the Synthesis of Porous Carbon Materials. *Adv. Mater.* **2006**, 18 (16), 2073–2094. <https://doi.org/10.1002/adma.200501576>.
- (84) Lee, J. S.; Joo, S. H.; Ryoo, R. Synthesis of Mesoporous Silicas of Controlled Pore Wall Thickness and Their Replication to Ordered Nanoporous Carbons with Various Pore Diameters. *J. Am. Chem. Soc.* **2002**, 124 (7), 1156–1157. <https://doi.org/10.1021/ja012333h>.
- (85) Kim, T.-W.; Solovyov, L. A. Synthesis and Characterization of Large-Pore Ordered Mesoporous Carbons Using Gyroidal Silica Template. *J. Mater. Chem.* **2006**, 16 (15), 1445. <https://doi.org/10.1039/b516945c>.
- (86) Baum, M.; Rébiscoul, D.; Juranyi, F.; Rieutord, F. Structural and Dynamical Properties of Water Confined in Highly Ordered Mesoporous Silica in the Presence of Electrolytes. *J. Phys. Chem. C* **2018**, 122 (34), 19857–19868. <https://doi.org/10.1021/acs.jpcc.8b02182>.
- (87) Sananes Israel, S.; Rébiscoul, D.; Odorico, M.; Flaud, V.; Ayral, A. Surface Properties of Alkoxysilane Layers Grafted in Supercritical Carbon Dioxide. *Langmuir* **2019**, 35 (7), 2792–2800. <https://doi.org/10.1021/acs.langmuir.8b03826>.
- (88) Juère, E.; Kleitz, F. On the Nanopore Confinement of Therapeutic Drugs into Mesoporous Silica Materials and Its Implications. *Microporous Mesoporous Mater.* **2018**, 270, 109–119. <https://doi.org/10.1016/J.MICROMESO.2018.04.031>.
- (89) Knight, A. W.; Tigges, A. B.; Ilgen, A. G. Adsorption of Copper (II) on

References

- Mesoporous Silica: The Effect of Nano-Scale Confinement. *Geochem. Trans.* **2018**, *19* (1), 13. <https://doi.org/10.1186/s12932-018-0057-4>.
- (90) Hazelbaker, E. D.; Guillet-Nicolas, R.; Thommes, M.; Kleitz, F.; Vasenkov, S. Influence of Confinement in Mesoporous Silica on Diffusion of a Mixture of Carbon Dioxide and an Imidazolium-Based Ionic Liquid by High Field Diffusion NMR. *Microporous Mesoporous Mater.* **2015**, *206*, 177–183. <https://doi.org/10.1016/J.MICROMESO.2014.12.005>.
- (91) Janicke, M.; Maxwell, R. S.; Krishnamurty, M.; Kumar, D.; Huo, Q.; Stucky, G. D.; Margolese, D.; Schuth, F.; Monnier, A.; Firouzi, A.; et al. Cooperative Formation of Inorganic-Organic Interfaces in the Synthesis of Silicate Mesostructures. *Science (80-.)*. **2006**, *261* (5126), 1299–1303. <https://doi.org/10.1126/science.261.5126.1299>.
- (92) Stucky, G. D.; Monnier, A.; Schiith, F.; Huo, Q.; Margolese, D.; Kumar, D.; Krishnamurty, M.; Petroff, P.; Firouzi, A.; Janicke, M.; et al. Molecular and Atomic Arrays in Nano-and Mesoporous Materials Synthesis. *Mol. Cryst. Liq. Cryst. Sci. Technol. Sect. A. Mol. Cryst. Liq. Cryst.* **1994**, *240* (1), 187–200. <https://doi.org/10.1080/10587259408029730>.
- (93) Kresge, C. T.; Roth, W. J. The Discovery of Mesoporous Molecular Sieves from the Twenty Year Perspective. *Chem. Soc. Rev.* **2013**, *42* (9), 3663. <https://doi.org/10.1039/c3cs60016e>.
- (94) Vartuli, J. C.; Schmitt, K. D.; Kresge, C. T.; Roth, W. J.; Leonowicz, M. E.; McCullen, S. B.; Hellring, S. D.; Beck, J. S.; Schlenker, J. L.; Olson, D. H.; et al. Effect of Surfactant/Silica Molar Ratios on the Formation of Mesoporous Molecular Sieves: Inorganic Mimicry of Surfactant Liquid-Crystal Phases and Mechanistic Implications. *Chem. Mater.* **1994**, *6* (12), 2317–2326. <https://doi.org/10.1021/cm00048a018>.
- (95) Backov, R. Combining Soft Matter and Soft Chemistry: Integrative Chemistry towards Designing Novel and Complex Multiscale Architectures. *Soft Matter* **2006**, *2* (6), 452–464. <https://doi.org/10.1039/b602579j>.
- (96) Brun, N.; Ungureanu, S.; Deleuze, H.; Backov, R. Hybrid Foams, Colloids and beyond: From Design to Applications. *Chem. Soc. Rev.* **2011**, *40* (2), 771–788. <https://doi.org/10.1039/B920518G>.
- (97) Blanford, C. F.; Yan, H.; Schroden, R. C.; Al-Daous, M.; Stein, A. Gems of Chemistry and Physics: Macroporous Metal Oxides with 3D Order. *Adv. Mater.* **2001**, *13* (6), 401–407. [https://doi.org/10.1002/1521-4095\(200103\)13:6<401::AID-ADMA401>3.0.CO;2-7](https://doi.org/10.1002/1521-4095(200103)13:6<401::AID-ADMA401>3.0.CO;2-7).
- (98) Templin, M.; Franck, A.; Du Chesne, A.; Leist, H.; Zhang, Y.; Ulrich, R.; Schädler, V.; Wiesner, U. Organically Modified Aluminosilicate Mesostructures from Block Copolymer Phases. *Science (80-.)*. **1997**, *278* (5344), 1795–1798. <https://doi.org/10.1126/science.278.5344.1795>.
- (99) Van Der Voort, P.; Esquivel, D.; De Canck, E.; Goethals, F.; Van Driessche, I.; Romero-Salguero, F. J. Periodic Mesoporous Organosilicas: From Simple to Complex Bridges; a Comprehensive Overview of Functions, Morphologies and

- Applications. *Chem. Soc. Rev.* **2013**, *42* (9), 3913–3955. <https://doi.org/10.1039/C2CS35222B>.
- (100) Asefa, T.; MacLachlan, M. J.; Coombs, N.; Ozin, G. A. Periodic Mesoporous Organosilicas with Organic Groups inside the Channel Walls. *Nature* **1999**, *402* (6764), 867–871. <https://doi.org/10.1038/47229>.
- (101) Corriu, R. J. P.; Moreau, J. J. E.; Thepot, P.; Man, M. W. C. New Mixed Organic-Inorganic Polymers: Hydrolysis and Polycondensation of Bis(Trimethoxysilyl)Organometallic Precursors. *Chem. Mater.* **1992**, *4* (6), 1217–1224. <https://doi.org/10.1021/cm00024a020>.
- (102) Inagaki, S.; Guan, S.; Fukushima, Y.; Ohsuna, T.; Terasaki, O. Novel Mesoporous Materials with a Uniform Distribution of Organic Groups and Inorganic Oxide in Their Frameworks. *J. Am. Chem. Soc.* **1999**, *121* (41), 9611–9614. <https://doi.org/10.1021/ja9916658>.
- (103) Zhai, S.-R.; Kim, I.; Ha, C.-S. Synthesis and Characterization of Periodic Mesoporous Organosilicas from Bridged Organosilanes in the Presence of Mixed Salts. *J. Solid State Chem.* **2008**, *181* (1), 67–74. <https://doi.org/10.1016/J.JSSC.2007.11.011>.
- (104) Nunes, S. C.; Toquer, G.; Cardoso, M. A.; Mayoral, A.; Ferreira, R. A. S.; Carlos, L. D.; Ferreira, P.; Almeida, P.; Cattoën, X.; Wong Chi Man, M.; et al. Structuring of Alkyl-Triazole Bridged Silsesquioxanes. *ChemistrySelect* **2017**, *2* (1), 432–442. <https://doi.org/10.1002/slct.201601806>.
- (105) Shea, K. J.; Loy, D. A. Bridged Polysilsesquioxanes. Molecular-Engineered Hybrid Organic-Inorganic Materials. *Chem. Mater.* **2001**, *13* (10), 3306–3319. <https://doi.org/10.1021/cm011074s>.
- (106) Hoffmann, F.; Cornelius, M.; Morell, J.; Fröba, M. Silica-Based Mesoporous Organic-Inorganic Hybrid Materials. *Angewandte Chemie - International Edition*. John Wiley & Sons, Ltd May 12, 2006, pp 3216–3251. <https://doi.org/10.1002/anie.200503075>.
- (107) Mehdi, A.; Reye, C.; Corriu, R. From Molecular Chemistry to Hybrid Nanomaterials. Design and Functionalization. *Chem. Soc. Rev.* **2011**, *40* (2), 563–574. <https://doi.org/10.1039/b920516k>.
- (108) Ulman, A. Formation and Structure of Self-Assembled Monolayers. *Chem. Rev.* **1996**, *96* (4), 1533–1554. <https://doi.org/10.1021/cr9502357>.
- (109) Alauzun, J.; Mehdi, A.; Reyé, C.; Corriu, R. J. P. Hydrophilic Conditions: A New Way for Self-Assembly of Hybrid Silica Containing Long Alkylene Chains. *J. Mater. Chem.* **2005**, *15* (8), 841–843. <https://doi.org/10.1039/b416157b>.
- (110) Shimojima, A.; Kuroda, K. Structural Control of Multilayered Inorganic-Organic Hybrids Derived from Mixtures of Alkyltriethoxysilane and Tetraethoxysilane. *Langmuir* **2002**, *18* (4), 1144–1149. <https://doi.org/10.1021/la011016l>.
- (111) Boury, B.; Corriu, R. J. P.; Muramatsu, H. Organisation and Reactivity of Silicon-Based Hybrid Materials with Various Cross-Linking Levels. *New J. Chem.* **2002**, *26* (8), 981–988. <https://doi.org/10.1039/b110776n>.

References

- (112) Huo, Q.; Margolese, D. I.; Stucky, G. D. Surfactant Control of Phases in the Synthesis of Mesoporous Silica-Based Materials. *Chem. Mater.* **1996**, *8* (5), 1147–1160. <https://doi.org/10.1021/cm960137h>.
- (113) Ruiz-Hitzky, E.; Letaïef, S.; Prévot, V. Novel Organic-Inorganic Mesophases: Self-Templating Synthesis and Intratubular Swelling. *Adv. Mater.* **2002**, *14* (6), 439–443. [https://doi.org/10.1002/1521-4095\(20020318\)14:6<439::AID-ADMA439>3.0.CO;2-8](https://doi.org/10.1002/1521-4095(20020318)14:6<439::AID-ADMA439>3.0.CO;2-8).
- (114) Zhang, Q.; Ariga, K.; Okabe, A.; Aida, T. A Condensable Amphiphile with a Cleavable Tail as a “Lizard” Template for the Sol-Gel Synthesis of Functionalized Mesoporous Silica. *J. Am. Chem. Soc.* **2004**, *126* (4), 988–989. <https://doi.org/10.1021/ja039515r>.
- (115) Katagiri, K.; Hashizume, M.; Ariga, K.; Terashima, T.; Kikuchi, J. I. Preparation and Characterization of a Novel Organic-Inorganic Nanohybrid “Cerasome” Formed with a Liposomal Membrane and Silicate Surface. *Chem. - A Eur. J.* **2007**, *13* (18), 5272–5281. <https://doi.org/10.1002/chem.200700175>.
- (116) Voss, R.; Thomas, A.; Antonietti, M.; Ozin, G. A. Synthesis and Characterization of Highly Amine Functionalized Mesoporous Organosilicas by an “All-in-One” Approach. *J. Mater. Chem.* **2005**, *15* (37), 4010–4014. <https://doi.org/10.1039/b507084h>.
- (117) Moreau, J. J. E.; Vellutini, L.; Bied, C.; Man, M. W. C. New Approach for the Organisation and the Shaping of Organo-Bridged Silicas: An Overview. *J. Sol-Gel Sci. Technol.* **2004**, *31* (1–3), 151–156. <https://doi.org/10.1023/B:JSST.0000047977.44966.53>.
- (118) Moreau, J. J. E.; Pichon, B. P.; Arrachart, G.; Wong Chi Man, M.; Bied, C. Nanostructuring Organo-Silicas: Combination of Intermolecular Interactions and Molecular Recognition Properties to Generate Self-Assembled Hybrids with Phenylene or Adenine···thymine Bridging Units. *New J. Chem.* **2005**, *29* (5), 653. <https://doi.org/10.1039/b419376h>.
- (119) Besnard, R.; Arrachart, G.; Cambedouzou, J.; Pellet-Rostaing, S. Structural Study of Hybrid Silica Bilayers from “Bola-Amphiphile” Organosilane Precursors: Catalytic and Thermal Effects. *RSC Adv.* **2015**, *5* (71), 57521–57531. <https://doi.org/10.1039/C5RA06944K>.
- (120) Besnard, R.; Arrachart, G.; Cambedouzou, J.; Pellet-Rostaing, S. Tuning the Nanostructure of Highly Functionalized Silica Using Amphiphilic Organosilanes: Curvature Agent Effects. *Langmuir* **2016**, *32* (18), 4624–4634. <https://doi.org/10.1021/acs.langmuir.6b00589>.
- (121) Besnard, R.; Cambedouzou, J.; Arrachart, G.; Diat, O.; Pellet-Rostaing, S. Self-Assembly of Condensable “Bola-Amphiphiles” in Water/Tetraethoxysilane Mixtures for the Elaboration of Mesostructured Hybrid Materials. *Langmuir* **2013**, *29* (33), 10368–10375. <https://doi.org/10.1021/la401885t>.
- (122) Besnard, R.; Arrachart, G.; Cambedouzou, J.; Pellet-Rostaing, S. Tuning the Morphology of Functionalized Silica Using Amphiphilic Organosilanes. *J. Sol-Gel Sci. Technol.* **2017**, *81* (2), 452–467. <https://doi.org/10.1007/s10971-016-4202-1>.

- (123) Besnard, R.; Cambedouzou, J.; Arrachart, G.; Le Goff, X. F.; Pellet-Rostaing, S. Organosilica-Metallic Sandwich Materials as Precursors for Palladium and Platinum Nanoparticle Synthesis. *RSC Adv.* **2015**, *5* (95), 77619–77628. <https://doi.org/10.1039/c5ra15871k>.
- (124) Besnard, R.; Winkler, R.; Arrachart, G.; Cambedouzou, J.; Pellet-Rostaing, S. Ion Extraction Applications of Bilayer-Structured Hybrid Silicas. *Mater. Chem. Front.* **2018**, *2* (5), 1031–1039. <https://doi.org/10.1039/c8qm00022k>.
- (125) Colvin, E. W. Silicon in Organic Synthesis. *Chemical Society Reviews*. Elsevier S. Amsterdam 1978, pp 15–64. <https://doi.org/10.1039/CS9780700015>.
- (126) Rauter, G. Ueber Das Siliciumtetrachlorid. *Justus Liebig's Ann. der Chemie* **1892**, *270* (1–2), 235–266. <https://doi.org/10.1002/jlac.18922700114>.
- (127) Friedel, C.; Crafts, J. M. Ueber Einige Neue Organische Verbindungen Des Siliciums Und Das Atomgewicht Dieses Elementes. *Ann. der Chemie und Pharm.* **1863**, *127* (1), 28–32. <https://doi.org/10.1002/jlac.18631270103>.
- (128) Hurd, D. T.; Rochow, E. G. On the Mechanism of the Reaction between Methyl Chloride and Silicon-Copper. *J. Am. Chem. Soc.* **1945**, *67* (7), 1057–1059. <https://doi.org/10.1021/ja01223a007>.
- (129) Whitmore, F. C.; Sommer, L. H.; Giorgio, P. A. Di; Strong, W. A.; Strien, R. E. van; Bailey, D. L.; Hall, H. K.; Pietrusza, E. W.; Kerr, G. T. Organo-Silicon Compounds. I. Synthesis and Properties of n-Alkyltrimethyl- and n-Alkyltriethyl-Silanes. *J. Am. Chem. Soc.* **1946**, *68* (3), 475–481. <https://doi.org/10.1021/ja01207a035>.
- (130) Speier, J. L.; Webster, J. A.; Barnes, G. H. The Addition of Silicon Hydrides to Olefinic Double Bonds. Part II. The Use of Group VIII Metal Catalysts. *J. Am. Chem. Soc.* **1957**, *79* (4), 974–979. <https://doi.org/10.1021/ja01561a054>.
- (131) Karstedt, B. Platinum Complexes of Unsaturated Siloxanes and Platinum Containing Organopolysiloxanes. US 3775452 A, 1973.
- (132) Eaborn, C. Comprehensive Handbook on Hydrosilylation. *J. Organomet. Chem.* **1993**, *454* (1–2). [https://doi.org/10.1016/0022-328x\(93\)83260-3](https://doi.org/10.1016/0022-328x(93)83260-3).
- (133) Stein, J.; Lewis, L. N.; Gao, Y.; Scott, R. A. In Situ Determination of the Active Catalyst in Hydrosilylation Reactions Using Highly Reactive Pt(0) Catalyst Precursors. *J. Am. Chem. Soc.* **1999**, *121* (15), 3693–3703. <https://doi.org/10.1021/ja9825377>.
- (134) Lewis, L.; Stein, J.; Gao, Y.; Colborn, R.; Hutchins, G. Platinum Catalysts Used in the Silicones Industry. *Platin. Met. Rev* **1997**, *41* (2), 66–75.
- (135) Troegel, D.; Stohrer, J. Recent Advances and Actual Challenges in Late Transition Metal Catalyzed Hydrosilylation of Olefins from an Industrial Point of View. *Coord. Chem. Rev.* **2011**, *255* (13–14), 1440–1459. <https://doi.org/10.1016/j.ccr.2010.12.025>.
- (136) Marciniak, B. *Hydrosilylation: A Comprehensive Review on Recent Advances*; Springer, 2009.

References

- (137) Hofmann, R.; Vlatković, M.; Wiesbrock, F. Fifty Years of Hydrosilylation in Polymer Science: A Review of Current Trends of Low-Cost Transition-Metal and Metal-Free Catalysts, Non-Thermally Triggered Hydrosilylation Reactions, and Industrial Applications. *Polymers (Basel)*. **2017**, *9* (12), 534. <https://doi.org/10.3390/polym9100534>.
- (138) Witala, M.; Lages, S.; Nygård, K. Mesoscale Ordering in Binary Aqueous Solvents Induced by Ion Size Asymmetry. / *Soft Matter Soft Matter* **2016**, *12* (12), 4778–4782. <https://doi.org/10.1039/c6sm00580b>.
- (139) Pan, Z.; Liu, M.; Zheng, C.; Gao, D.; Huang, W. Study of Karstedt's Catalyst for Hydrosilylation of a Wide Variety of Functionalized Alkenes with Triethoxysilane and Trimethoxysilane. *Chinese J. Chem.* **2017**, *35* (8), 1227–1230. <https://doi.org/10.1002/cjoc.201700024>.
- (140) Kolb, H. C.; Finn, M. G.; Sharpless, K. B. Click Chemistry: Diverse Chemical Function from a Few Good Reactions. *Angew. Chemie Int. Ed.* **2001**, *40* (11), 2004–2021. [https://doi.org/10.1002/1521-3773\(20010601\)40:11<2004::AID-ANIE2004>3.0.CO;2-5](https://doi.org/10.1002/1521-3773(20010601)40:11<2004::AID-ANIE2004>3.0.CO;2-5).
- (141) Huisgen, R.; Szeimies, G.; Möbius, L. 1,3-Dipolare Cycloadditionen, XXXII. Kinetik Der Additionen Organischer Azide an CC-Mehrfachbindungen. *Chem. Ber.* **1967**, *100* (8), 2494–2507. <https://doi.org/10.1002/cber.19671000806>.
- (142) Amblard, F.; Cho, J. H.; Schinazi, R. F. Cu(I)-Catalyzed Huisgen Azide–Alkyne 1,3-Dipolar Cycloaddition Reaction in Nucleoside, Nucleotide, and Oligonucleotide Chemistry. *Chem. Rev.* **2009**, *109* (9), 4207–4220. <https://doi.org/10.1021/cr9001462>.
- (143) Jewett, J. C.; Bertozzi, C. R. Cu-Free Click Cycloaddition Reactions in Chemical Biology. *Chem. Soc. Rev.* **2010**, *39* (4), 1272. <https://doi.org/10.1039/b901970g>.
- (144) Boren, B. C.; Narayan, S.; Rasmussen, L. K.; Zhang, L.; Zhao, H.; Lin, Z.; Jia, G.; Fokin, V. V. Ruthenium-Catalyzed Azide–Alkyne Cycloaddition: Scope and Mechanism. *J. Am. Chem. Soc.* **2008**, *130* (28), 8923–8930. <https://doi.org/10.1021/ja0749993>.
- (145) Zhang, L.; Chen, X.; Xue, P.; Sun, H. H. Y.; Williams, I. D.; Sharpless, K. B.; Fokin, V. V.; Jia, G. Ruthenium-Catalyzed Cycloaddition of Alkynes and Organic Azides. *J. Am. Chem. Soc.* **2005**, *127* (46), 15998–15999. <https://doi.org/10.1021/ja054114s>.
- (146) McNulty, J.; Keskar, K.; Vemula, R. The First Well-Defined Silver(I)-Complex-Catalyzed Cycloaddition of Azides onto Terminal Alkynes at Room Temperature. *Chem. - A Eur. J.* **2011**, *17* (52), 14727–14730. <https://doi.org/10.1002/chem.201103244>.
- (147) Tornøe, C. W.; Meldal, M. Peptidotriazoles: Copper(I)-Catalyzed 1,3-Dipolar Cycloadditions on Solid-Phase. In *Peptides: The Wave of the Future*; Springer Netherlands: Dordrecht, 2001; pp 263–264. https://doi.org/10.1007/978-94-010-0464-0_119.
- (148) Rostovtsev, V. V.; Green, L. G.; Fokin, V. V.; Sharpless, K. B. A Stepwise

- Huisgen Cycloaddition Process: Copper(I)-Catalyzed Regioselective “Ligation” of Azides and Terminal Alkynes. *Angew. Chemie Int. Ed.* **2002**, *41* (14), 2596–2599. [https://doi.org/10.1002/1521-3773\(20020715\)41:14<2596::AID-ANIE2596>3.0.CO;2-4](https://doi.org/10.1002/1521-3773(20020715)41:14<2596::AID-ANIE2596>3.0.CO;2-4).
- (149) Tornøe, C. W.; Christensen, C.; Meldal, M. Peptidotriazoles on Solid Phase: [1,2,3]-Triazoles by Regiospecific Copper(I)-Catalyzed 1,3-Dipolar Cycloadditions of Terminal Alkynes to Azides. *J. Org. Chem.* **2002**, *67* (9), 3057–3064. <https://doi.org/10.1021/jo011148j>.
- (150) Kolb, H. C.; Sharpless, K. B. The Growing Impact of Click Chemistry on Drug Discovery. *Drug Discov. Today* **2003**, *8* (24), 1128–1137. [https://doi.org/10.1016/S1359-6446\(03\)02933-7](https://doi.org/10.1016/S1359-6446(03)02933-7).
- (151) Moorhouse, A. D.; Moses, J. E. Click Chemistry and Medicinal Chemistry: A Case of “Cyclo-Addiction.” *ChemMedChem* **2008**, *3* (5), 715–723. <https://doi.org/10.1002/cmdc.200700334>.
- (152) Marmuse, L.; Nepogodiev, S. A.; Field, R. A. “Click Chemistry” En Route to Pseudo-Starch. *Org. Biomol. Chem.* **2005**, *3* (12), 2225. <https://doi.org/10.1039/b504293c>.
- (153) Moitra, N.; Moreau, J. J. E.; Cattoën, X.; Wong Chi Man, M. Convenient Route to Water-Sensitive Sol–Gel Precursors Using Click Chemistry. *Chem. Commun.* **2010**, *46* (44), 8416. <https://doi.org/10.1039/c0cc03417g>.
- (154) Meldal, M.; Tornøe, C. W. Cu-Catalyzed Azide–Alkyne Cycloaddition. *Chem. Rev.* **2008**, *108* (8), 2952–3015. <https://doi.org/10.1021/cr0783479>.
- (155) Wang, C.; Ikhlef, D.; Kahlal, S.; Saillard, J.-Y.; Astruc, D. Metal-Catalyzed Azide–Alkyne “Click” Reactions: Mechanistic Overview and Recent Trends. *Coord. Chem. Rev.* **2016**, *316*, 1–20. <https://doi.org/10.1016/j.ccr.2016.02.010>.
- (156) Worrell, B. T.; Malik, J. A.; Fokin, V. V. Direct Evidence of a Dinuclear Copper Intermediate in Cu(I)-Catalyzed Azide–Alkyne Cycloadditions. *Science (80-.)*. **2013**, *340* (6131), 457–460. <https://doi.org/10.1126/science.1229506>.
- (157) Ahlquist, M.; Fokin, V. V. Enhanced Reactivity of Dinuclear Copper(I) Acetylides in Dipolar Cycloadditions. *Organometallics* **2007**, *26* (18), 4389–4391. <https://doi.org/10.1021/om700669v>.
- (158) Alonso, F.; Moglie, Y.; Radivoy, G.; Yus, M. Unsupported Copper Nanoparticles in the 1,3-Dipolar Cycloaddition of Terminal Alkynes and Azides. *European J. Org. Chem.* **2010**, *2010* (10), 1875–1884. <https://doi.org/10.1002/ejoc.200901446>.
- (159) Zhu, L.; Brassard, C. J.; Zhang, X.; Guha, P. M.; Clark, R. J. On the Mechanism of Copper(I)-Catalyzed Azide–Alkyne Cycloaddition. *Chem. Rec.* **2016**, *16* (3), 1501–1517. <https://doi.org/10.1002/tcr.201600002>.
- (160) Deraedt, C.; Pinaud, N.; Astruc, D. Recyclable Catalytic Dendrimer Nanoreactor for Part-Per-Million Cu I Catalysis of “Click” Chemistry in Water. *J. Am. Chem. Soc.* **2014**, *136* (34), 12092–12098. <https://doi.org/10.1021/ja5061388>.
- (161) Ikhlef, D.; Wang, C.; Kahlal, S.; Maouche, B.; Astruc, D.; Saillard, J.-Y. Reaction

References

- Mechanisms of Transition-Metal-Catalyzed Azide–Alkyne Cycloaddition “Click” Reactions: A DFT Investigation. *Comput. Theor. Chem.* **2015**, *1073*, 131–138. <https://doi.org/10.1016/j.comptc.2015.09.020>.
- (162) Candelon, N.; Lastécouères, D.; Diallo, A. K.; Ruiz Aranzaes, J.; Astruc, D.; Vincent, J.-M. A Highly Active and Reusable Copper-Tren Catalyst for the “Click” 1,3-Dipolar Cycloaddition of Azides and Alkynes. *Chem. Commun.* **2008**, No. 6, 741–743. <https://doi.org/10.1039/B716306A>.
- (163) Kato, M.; Sakai-Kato, K.; Toyo’oka, T. Silica Sol-Gel Monolithic Materials and Their Use in a Variety of Applications. *J. Sep. Sci.* **2005**, *28* (15), 1893–1908. <https://doi.org/10.1002/jssc.200500225>.
- (164) Cattoën, X.; Noureddine, A.; Croissant, J.; Moitra, N.; Bürglová, K.; Hodačová, J.; de los Cobos, O.; Lejeune, M.; Rossignol, F.; Toulemon, D.; et al. Click Approaches in Sol–Gel Chemistry. *J. Sol-Gel Sci. Technol.* **2013**, *70* (2), 245–253. <https://doi.org/10.1007/s10971-013-3155-x>.
- (165) Bürglová, K.; Moitra, N.; Hodačová, J.; Cattoën, X.; Wong Chi Man, M. Click Approaches to Functional Water-Sensitive Organotriethoxysilanes. *J. Org. Chem.* **2011**, *76* (18), 7326–7333. <https://doi.org/10.1021/jo201484n>.
- (166) Pichon, B. P.; Wong Chi Man, M.; Bied, C.; Moreau, J. J. E. A Simple Access to ω -Aminoalkyltrialkoxysilanes: Tunable Linkers for Self-Organised Organosilicas. *J. Organomet. Chem.* **2006**, *691* (6), 1126–1130. <https://doi.org/10.1016/j.jorganchem.2005.11.036>.
- (167) Sweetman, M. J.; Harding, F. J.; Graney, S. D.; Voelcker, N. H. Effect of Oligoethylene Glycol Moieties in Porous Silicon Surface Functionalisation on Protein Adsorption and Cell Attachment. *Appl. Surf. Sci.* **2011**, *257* (15), 6768–6774. <https://doi.org/10.1016/j.apsusc.2011.02.122>.
- (168) Lepore, S. D.; Mondal, D. Recent Advances in Heterolytic Nucleofugal Leaving Groups. *Tetrahedron* **2007**, *63* (24), 5103–5122. <https://doi.org/10.1016/j.tet.2007.03.049>.
- (169) Harmand, L.; Lescure, M.-H.; Candelon, N.; Duttine, M.; Lastécouères, D.; Vincent, J.-M. Huisgen Click Cycloadditions from a Copper(II)-Tren Precatalyst without External Sacrificial Reductant. *Tetrahedron Lett.* **2012**, *53* (11), 1417–1420. <https://doi.org/10.1016/j.tetlet.2012.01.035>.
- (170) Stewart, B.; Harriman, A.; Higham, L. J. Predicting the Air Stability of Phosphines. *Organometallics* **2011**, *30* (20), 5338–5343. <https://doi.org/10.1021/om200070a>.
- (171) Soler-Illia, G. J. A. A.; Azzaroni, O. Multifunctional Hybrids by Combining Ordered Mesoporous Materials and Macromolecular Building Blocks. *Chem. Soc. Rev.* **2011**, *40* (2), 1107. <https://doi.org/10.1016/j.jcis.2006.03.044>.
- (172) Kickelbick, G. Silsesquioxanes. *Struct. Bond.* **2014**, *155* (5), 1–28. https://doi.org/10.1007/430_2013_108.
- (173) Lee, A. S.; Choi, S. S.; Lee, H. S.; Baek, K. Y.; Hwang, S. S. A New, Higher Yielding Synthetic Route towards Dodecaphenyl Cage Silsesquioxanes: Synthesis and Mechanistic Insights. *Dalt. Trans.* **2012**, *41* (35), 10585–10588.

- <https://doi.org/10.1039/c2dt30659j>.
- (174) Cordes, D. B.; Lickiss, P. D.; Rataboul, F. Recent Developments in the Chemistry of Cubic Polyhedral Oligosilsesquioxanes. *Chem. Rev.* **2010**, *110* (4), 2081–2173. <https://doi.org/10.1021/cr900201r>.
- (175) Mattsson, S.; Dahlström, M.; Karlsson, S. A Mild Hydrolysis of Esters Mediated by Lithium Salts. *Tetrahedron Lett.* **2007**, *48* (14), 2497–2499. <https://doi.org/10.1016/j.tetlet.2007.02.029>.
- (176) Al-Oweini, R.; El-Rassy, H. Synthesis and Characterization by FTIR Spectroscopy of Silica Aerogels Prepared Using Several Si(OR)₄ and R''Si(OR')₃ Precursors. *J. Mol. Struct.* **2009**, *919* (1–3), 140–145. <https://doi.org/10.1016/j.molstruc.2008.08.025>.
- (177) Arkles, B.; Larson, G. *Silicon Compounds: Silanes & Silicones*, Dr. Gupta.; Morrisville, PA, USA, 2013.
- (178) Murugavel, S.; Ravikumar, C.; Jaabil, G.; Alagusundaram, P. Synthesis, Crystal Structure Analysis, Spectral Investigations (NMR, FT-IR, UV), DFT Calculations, ADMET Studies, Molecular Docking and Anticancer Activity of 2-(1-Benzyl-5-Methyl-1H-1,2,3-Triazol-4-Yl)-4-(2-Chlorophenyl)-6-Methoxypyridine – A Novel Poten. *J. Mol. Struct.* **2019**, *1176*, 729–742. <https://doi.org/10.1016/j.molstruc.2018.09.010>.
- (179) Wong, P. T. T.; Mantsch, H. H. Pressure Effects on the Infrared Spectrum of 1,2-dipalmitoyl Phosphatidylcholine Bilayers in Water. *J. Chem. Phys.* **1985**, *83* (7), 3268–3274. <https://doi.org/10.1063/1.449185>.
- (180) Vaia, R. A.; Teukolsky, R. K.; Giannelis, E. P. Interlayer Structure and Molecular Environment of Alkylammonium Layered Silicates. *Chem. Mater.* **1994**, *6* (7), 1017–1022. <https://doi.org/10.1021/cm00043a025>.
- (181) Bantignies, J. L.; Vellutini, L.; Maurin, D.; Hermet, P.; Dieudonné, P.; Man, M. W. C.; Bartlett, J. R.; Bied, C.; Sauvajol, J. L.; Moreau, J. J. E. Insights into the Self-Directed Structuring of Hybrid Organic - Inorganic Silicas through Infrared Studies. *J. Phys. Chem. B* **2006**, *110* (32), 15797–15802. <https://doi.org/10.1021/jp060975r>.
- (182) Singh, S.; Wegmann, J.; Albert, K.; Müller, K. Variable Temperature FT-IR Studies of n-Alkyl Modified Silica Gels. *J. Phys. Chem. B* **2002**, *106* (4), 878–888. <https://doi.org/10.1021/jp012979w>.
- (183) Orel, B.; Ješe, R.; Vilčnik, A.; Štangar, U. L. Hydrolysis and Solvolysis of Methyltriethoxysilane Catalyzed with HCl or Trifluoroacetic Acid: IR Spectroscopic and Surface Energy Studies. *J. Sol-Gel Sci. Technol.* **2005**, *34* (3), 251–265. <https://doi.org/10.1007/s10971-005-2522-7>.
- (184) Lee, A. S.; Choi, S. S.; Baek, K. Y.; Hwang, S. S. Hydrolysis Kinetics of a Sol-Gel Equilibrium Yielding Ladder-like Polysilsesquioxanes. *Inorg. Chem. Commun.* **2016**, *73*, 7–11. <https://doi.org/10.1016/j.inoche.2016.09.004>.
- (185) Issa, A. A.; Luyt, A. S. Kinetics of Alkoxysilanes and Organoalkoxysilanes Polymerization: A Review. *Polymers*. Multidisciplinary Digital Publishing

References

- Institute March 21, 2019, p 537. <https://doi.org/10.3390/polym11030537>.
- (186) Katritzky, A. R.; Wang, Z.; Tsikolia, M.; Hall, C. D.; Carman, M. Benzotriazole Is Thermally More Stable than 1,2,3-Triazole. *Tetrahedron Lett.* **2006**, *47* (43), 7653–7654. <https://doi.org/10.1016/J.TETLET.2006.08.021>.
- (187) Hyde, S. Identification of Lyotropic Liquid Crystalline Mesophases. In *Handbook of Applied Surface and Colloid Chemistry*; Holmberg, K., Ed.; Wiley, 2001; pp 300–334.
- (188) Dourdain, S. Caractérisation Structurale Poreuse Mécanique de Films Minces de Silice Mésoporeuse. Influence de La Fonctionnalisation, Académie de Nantes, 2006.
- (189) Skoulios, A. Organisation et Problèmes Structuraux de Copolymères Séquencés. *Informations Chim.* **1973**, 41–46.
- (190) Besnard, R.; Arrachart, G.; Cambedouzou, J.; Pellet-Rostaing, S. Tuning the Morphology of Functionalized Silica Using Amphiphilic Organosilanes. *J. Sol-Gel Sci. Technol.* **2017**, *81* (2), 452–467. <https://doi.org/10.1007/s10971-016-4202-1>.
- (191) Glatter, O. *Scattering Methods and Their Application in Colloid and Interface Science*, Elsevier.; Elsevier: Amsterdam, Netherlands, 2018. <https://doi.org/10.1016/C2016-0-04640-5>.
- (192) Alauzun, J.; Besson, E.; Mehdi, A.; Reyé, C.; Corriu, R. J. P. Reversible Covalent Chemistry of CO₂: An Opportunity for Nano-Structured Hybrid Organic-Inorganic Materials. *Chem. Mater.* **2008**, *20* (2), 503–513. <https://doi.org/10.1021/cm701946w>.
- (193) Aleese, L. Mac; Simon, A.; McMahon, T. B.; Ortega, J.-M.; Scuderi, D.; Lemaire, J.; Maître, P. Mid-IR Spectroscopy of Protonated Leucine Methyl Ester Performed with an FTICR or a Paul Type Ion-Trap. *Int. J. Mass Spectrom.* **2006**, *249–250*, 14–20. <https://doi.org/10.1016/J.IJMS.2006.01.008>.
- (194) Coblenz Society Inc. Evaluated Infrared Reference Spectra <https://webbook.nist.gov/cgi/cbook.cgi?ID=B6000448&Mask=80#IR-Spec>.
- (195) Athokpam, B.; Ramesh, S. G.; McKenzie, R. H. Effect of Hydrogen Bonding on the Infrared Absorption Intensity of OH Stretch Vibrations. *Chem. Phys.* **2017**, *488–489*, 43–54. <https://doi.org/10.1016/j.chemphys.2017.03.006>.
- (196) Philippe, L.; Sammon, C.; Lyon, S. B.; Yarwood, J. An FTIR/ATR in Situ Study of Sorption and Transport in Corrosion Protective Organic Coatings: 1. Water Sorption and the Role of Inhibitor Anions. *Prog. Org. Coatings* **2004**, *49* (4), 302–314. <https://doi.org/10.1016/J.PORGCOAT.2003.07.002>.
- (197) Crupi, V.; Longo, F.; Majolino, D.; Venuti, V. Vibrational Properties of Water Molecules Adsorbed in Different Zeolitic Frameworks. *J. Phys. Condens. Matter* **2006**, *18* (15), 3563–3580. <https://doi.org/10.1088/0953-8984/18/15/004>.
- (198) Kubelka, J.; Keiderling, T. A. Ab Initio Calculation of Amide Carbonyl Stretch Vibrational Frequencies in Solution with Modified Basis Sets. 1. JV-Methyl Acetamide. *J. Phys. Chem. A* **2001**, *105* (48), 10922–10928.

- <https://doi.org/10.1021/JP013203Y>.
- (199) Winkler, R.; Ré, E.; Arrachart, G.; Pellet-Rostaing, S. Impact of Solvent Structuring in Water/Tert-Butanol Mixtures on the Assembly of Silica Nanoparticles to Aerogels. *Langmuir* **2019**, *35* (24), 7905–7915. <https://doi.org/10.1021/acs.langmuir.9b00655>.
- (200) Riffat, S. B.; Qiu, G. A Review of State-of-the-Art Aerogel Applications in Buildings. *Int. J. Low-Carbon Technol.* **2013**, *8* (1), 1–6. <https://doi.org/10.1093/ijlct/cts001>.
- (201) Plata, D. L.; Briones, Y. J.; Wolfe, R. L.; Carroll, M. K.; Bakrania, S. D.; Mandel, S. G.; Anderson, A. M. Aerogel-Platform Optical Sensors for Oxygen Gas. *J. Non. Cryst. Solids* **2004**, *350*, 326–335. <https://doi.org/10.1016/j.jnoncrysol.2004.06.046>.
- (202) Danilyuk, A. ; Kirillov, V. ; Savelieva, M. ; Bobrovnikov, V. ; Buzykaev, A. ; Kravchenko, E. ; Lavrov, A. ; Onuchin, A. . Recent Results on Aerogel Development for Use in Cherenkov Counters. *Nucl. Instruments Methods Phys. Res. Sect. A Accel. Spectrometers, Detect. Assoc. Equip.* **2002**, *494* (1–3), 491–494. [https://doi.org/10.1016/S0168-9002\(02\)01537-1](https://doi.org/10.1016/S0168-9002(02)01537-1).
- (203) Gnade, B.; Cho, C.-C.; Levine, J. D. Low Density, High Porosity Material as Gate Dielectric for Field Emission Device. US5569058A, 1996.
- (204) Gurav, J. L.; Jung, I.-K.; Park, H.-H.; Kang, E. S.; Nadargi, D. Y. Silica Aerogel: Synthesis and Applications. *J. Nanomater.* **2010**, *2010*, 1–11. <https://doi.org/10.1155/2010/409310>.
- (205) Hu, F.; Wu, S.; Sun, Y. Hollow-Structured Materials for Thermal Insulation. *Adv. Mater.* **2018**, 1801001. <https://doi.org/10.1002/adma.201801001>.
- (206) Shi, M.; Tang, C.; Yang, X.; Zhou, J.; Jia, F.; Han, Y.; Li, Z. Superhydrophobic Silica Aerogels Reinforced with Polyacrylonitrile Fibers for Adsorbing Oil from Water and Oil Mixtures. *RSC Adv.* **2017**, *7* (7), 4039–4045. <https://doi.org/10.1039/C6RA26831E>.
- (207) Kim, C.; Baek, S.; Ryu, Y.; Kim, Y.; Shin, D.; Lee, C.-W.; Park, W.; Urbas, A. M.; Kang, G.; Kim, K. Large-Scale Nanoporous Metal-Coated Silica Aerogels for High SERS Effect Improvement. *Sci. Rep.* **2018**, *8* (1), 15144. <https://doi.org/10.1038/s41598-018-33539-z>.
- (208) Perdigoto, M. L. N.; Martins, R. C.; Rocha, N.; Quina, M. J.; Gando-Ferreira, L.; Patrício, R.; Durães, L. Application of Hydrophobic Silica Based Aerogels and Xerogels for Removal of Toxic Organic Compounds from Aqueous Solutions. *J. Colloid Interface Sci.* **2012**, *380* (1), 134–140. <https://doi.org/10.1016/j.jcis.2012.04.062>.
- (209) Huo, Q.; Margolese, D. I.; Ciesla, U.; Feng, P.; Gier, T. E.; Sieger, P.; Leon, R.; Petroff, P. M.; Schüth, F.; Stucky, G. D. Generalized Synthesis of Periodic Surfactant/Inorganic Composite Materials. *Nature* **1994**, *368* (6469), 317–321. <https://doi.org/10.1038/368317a0>.
- (210) Mihaly, M.; Lacatusu, I.; Olteanu, N.-L.; Meghea, A. A Systematic Methodology

References

- to Design Silica Templates: Silica Microemulsion Formulation and Nanodroplet Type and Size Estimation. *Comptes Rendus Chim.* **2014**, *17* (4), 342–351. <https://doi.org/10.1016/j.crci.2013.09.018>.
- (211) Schmidt-Winkel, P.; Glinka, C. J.; Stucky, G. D. Microemulsion Templates for Mesoporous Silica. *Langmuir* **2000**, *16* (2), 356–361. <https://doi.org/10.1021/la9906774>.
- (212) Narayan, R.; Nayak, U.; Raichur, A.; Garg, S. Mesoporous Silica Nanoparticles: A Comprehensive Review on Synthesis and Recent Advances. *Pharmaceutics* **2018**, *10* (3), 118. <https://doi.org/10.3390/pharmaceutics10030118>.
- (213) Kunz, W.; Holmberg, K.; Zemb, T. Hydrotropes. *Curr. Opin. Colloid Interface Sci.* **2016**, *22*, 99–107. <https://doi.org/10.1016/j.cocis.2016.03.005>.
- (214) Esquera, J.; Solans, C. No Title Found. *Surf. Sci. Ser.* **2006**, *132*, 245–261.
- (215) Hayashi, H.; Nishikawa, K.; Iijima, T. Small-Angle X-Ray Scattering Study of Fluctuations in 1-Propanol-Water and 2-Propanol-Water Systems. *J. Phys. Chem.* **1990**, *94* (21), 8334–8338. <https://doi.org/10.1021/j100384a062>.
- (216) Takamuku, T.; Maruyama, H.; Watanabe, K.; Yamaguchi, T. Structure of 1-Propanol–Water Mixtures Investigated by Large-Angle X-Ray Scattering Technique. *J. Solution Chem.* **2004**, *33* (6/7), 641–660. <https://doi.org/10.1023/B:JOSL.0000043631.21673.8b>.
- (217) Nishikawa, K.; Iijima, T. Small-Angle X-Ray Scattering Study of Fluctuations in Ethanol and Water Mixtures. *J. Phys. Chem.* **1993**, *97* (41), 10824–10828. <https://doi.org/10.1021/j100143a049>.
- (218) Nishikawa, K.; Hayashi, H.; Iijima, T. Temperature Dependence of the Concentration Fluctuation, the Kirkwood-Buff Parameters, and the Correlation Length of Tert-Butyl Alcohol and Water Mixtures Studied by Small-Angle x-Ray Scattering. *J. Phys. Chem.* **1989**, *93* (17), 6559–6565. <https://doi.org/10.1021/j100354a054>.
- (219) Misawa, M. Mesoscale Structure and Fractal Nature of 1-Propanol Aqueous Solution: A Reverse Monte Carlo Analysis of Small Angle Neutron Scattering Intensity. *J. Chem. Phys.* **2002**, *116* (19), 8463. <https://doi.org/10.1063/1.1471903>.
- (220) Kežić, B.; Perera, A. Aqueous Tert -Butanol Mixtures: A Model for Molecular-Emulsions. *J. Chem. Phys.* **2012**, *137* (1), 014501. <https://doi.org/10.1063/1.4730524>.
- (221) Schöttl, S.; Marcus, J.; Diat, O.; Touraud, D.; Kunz, W.; Zemb, T.; Horinek, D. Emergence of Surfactant-Free Micelles from Ternary Solutions. *Chem. Sci.* **2014**, *5* (8), 2949–2954. <https://doi.org/10.1039/C4SC00153B>.
- (222) Klossek, M. L.; Touraud, D.; Kunz, W. Eco-Solvents--Cluster-Formation, Surfactantless Microemulsions and Facilitated Hydrotropy. *Phys. Chem. Chem. Phys.* **2013**, *15* (26), 10971–10977. <https://doi.org/10.1039/c3cp50636c>.
- (223) Sedlák, M.; Rak, D. On the Origin of Mesoscale Structures in Aqueous Solutions of Tertiary Butyl Alcohol: The Mystery Resolved. *J. Phys. Chem. B* **2014**, *118*

- (10), 2726–2737. <https://doi.org/10.1021/jp500953m>.
- (224) Shimizu, S.; Matubayasi, N. Statistical Thermodynamic Foundation for Mesoscale Aggregation in Ternary Mixtures. *Phys. Chem. Chem. Phys.* **2018**, *20* (20), 13777–13784. <https://doi.org/10.1039/C8CP01207E>.
- (225) Shimizu, S.; Matubayasi, N. Unifying Hydrotropy under Gibbs Phase Rule. *Phys. Chem. Chem. Phys.* **2017**, *19* (35), 23597–23605. <https://doi.org/10.1039/C7CP02132A>.
- (226) Kononov, L. O. Chemical Reactivity and Solution Structure: On the Way to a Paradigm Shift? *RSC Adv.* **2015**, *5* (58), 46718–46734. <https://doi.org/10.1039/C4RA17257D>.
- (227) Krickl, S.; Buchecker, T.; Meyer, A. U.; Grillo, I.; Touraud, D.; Bauduin, P.; König, B.; Pfitzner, A.; Kunz, W. A Systematic Study of the Influence of Mesoscale Structuring on the Kinetics of a Chemical Reaction. *Phys. Chem. Chem. Phys.* **2017**, *19* (35), 23773–23780. <https://doi.org/10.1039/C7CP02134H>.
- (228) Krickl, S.; Touraud, D.; Bauduin, P.; Zinn, T.; Kunz, W. Enzyme Activity of Horseradish Peroxidase in Surfactant-Free Microemulsions. *J. Colloid Interface Sci.* **2018**, *516*, 466–475. <https://doi.org/10.1016/j.jcis.2018.01.077>.
- (229) Hou, W.; Xu, J. Surfactant-Free Microemulsions. *Curr. Opin. Colloid Interface Sci.* **2016**, *25*, 67–74. <https://doi.org/10.1016/j.cocis.2016.06.013>.
- (230) Yan, X.; Alcouffe, P.; Sudre, G.; David, L.; Bernard, J.; Ganachaud, F. Modular Construction of Single-Component Polymer Nanocapsules through a One-Step Surfactant-Free Microemulsion Templated Synthesis. *Chem. Commun.* **2017**, *53* (8), 1401–1404. <https://doi.org/10.1039/C6CC09701D>.
- (231) Lee, D.-W.; Jin, M.-H.; Park, J.-H.; Lee, Y.-J.; Choi, Y.-C.; Chan Park, J.; Chun, D. H. Alcohol and Water Free Synthesis of Mesoporous Silica Using Deep Eutectic Solvent as a Template and Solvent and Its Application as a Catalyst Support for Formic Acid Dehydrogenation. *ACS Sustain. Chem. Eng.* **2018**, *6* (9), 12241–12250. <https://doi.org/10.1021/acssuschemeng.8b02606>.
- (232) Wang, X.; Xu, J.; Wang, Q.; Xu, A.; Zhai, Y.; Luo, J.; Jiang, Y.; He, N.; Wang, Z. Wet Chemical Synthesis of Silica Nanosheets via Ethyl Acetate-Mediated Hydrolysis of Silica Precursors and Their Applications. *Small* **2017**, *13* (13), 1603369. <https://doi.org/10.1002/smll.201603369>.
- (233) Klossek, M. L.; Touraud, D.; Kunz, W. Eco-Solvents – Cluster-Formation, Surfactantless Microemulsions and Facilitated Hydrotropy. *Phys. Chem. Chem. Phys.* **2013**, *15* (26), 10971. <https://doi.org/10.1039/c3cp50636c>.
- (234) Shimizu, S.; Matubayasi, N. Hydrotropy: Monomer-Micelle Equilibrium and Minimum Hydrotrope Concentration. *J. Phys. Chem. B* **2014**, *118* (35), 10515–10524. <https://doi.org/10.1021/jp505869m>.
- (235) Euliss, G. W.; Sorensen, C. M. Dynamic Light Scattering Studies of Concentration Fluctuations in Aqueous t-butyl Alcohol Solutions. *J. Chem. Phys.* **1984**, *80* (10), 4767–4773. <https://doi.org/10.1063/1.446549>.

References

- (236) Clark, G. N. I.; Cappa, C. D.; Smith, J. D.; Saykally, R. J.; Head-Gordon, T. The Structure of Ambient Water. *Mol. Phys.* **2010**, *108* (11), 1415–1433. <https://doi.org/10.1080/00268971003762134>.
- (237) Tomšič, M.; Jamnik, A.; Fritz-Popovski, G.; Glatter, O.; Vlček, L. Structural Properties of Pure Simple Alcohols from Ethanol, Propanol, Butanol, Pentanol, to Hexanol: Comparing Monte Carlo Simulations with Experimental SAXS Data. *J. Phys. Chem. B* **2007**, *111* (7), 1738–1751. <https://doi.org/10.1021/jp066139z>.
- (238) IUPAC Goldbook <https://goldbook.iupac.org/html/M/M03853.html> (accessed Nov 30, 2018).
- (239) Pelster, S. A.; Schrader, W.; Schüth, F. Monitoring Temporal Evolution of Silicate Species during Hydrolysis and Condensation of Silicates Using Mass Spectrometry. *J. Am. Chem. Soc.* **2006**, *128* (13), 4310–4317. <https://doi.org/10.1021/ja057423r>.
- (240) Diat, O.; Klossek, M. L.; Touraud, D.; Deme, B.; Grillo, I.; Kunz, W.; Zemb, T. Octanol-Rich and Water-Rich Domains in Dynamic Equilibrium in the Pre-Ouzo Region of Ternary Systems Containing a Hydrotrope. *J. Appl. Crystallogr.* **2013**, *46* (6), 1665–1669. <https://doi.org/10.1107/S002188981302606X>.
- (241) Lopian, T.; Schöttl, S.; Prévost, S.; Pellet-Rostaing, S.; Horinek, D.; Kunz, W.; Zemb, T. Morphologies Observed in Ultraflexible Microemulsions with and without the Presence of a Strong Acid. *ACS Cent. Sci.* **2016**, *2* (7), 467–475. <https://doi.org/10.1021/acscentsci.6b00116>.
- (242) Klossek, M. L.; Touraud, D.; Zemb, T.; Kunz, W. Structure and Solubility in Surfactant-Free Microemulsions. *ChemPhysChem* **2012**, *13* (18), 4116–4119. <https://doi.org/10.1002/cphc.201200667>.
- (243) Fischer, V.; Marcus, J.; Touraud, D.; Diat, O.; Kunz, W. Toward Surfactant-Free and Water-Free Microemulsions. *J. Colloid Interface Sci.* **2015**, *453*, 186–193. <https://doi.org/10.1016/j.jcis.2015.04.069>.
- (244) Matsunaga, T.; Shibayama, M. Gel Point Determination of Gelatin Hydrogels by Dynamic Light Scattering and Rheological Measurements. *Phys. Rev. E* **2007**, *76* (3), 030401. <https://doi.org/10.1103/PhysRevE.76.030401>.
- (245) Meakin, P.; Jullien, R. The Effects of Restructuring on the Geometry of Clusters Formed by Diffusion-limited, Ballistic, and Reaction-limited Cluster–Cluster Aggregation. *J. Chem. Phys.* **1988**, *89* (1), 246–250. <https://doi.org/10.1063/1.455517>.
- (246) Aubert, C.; Cannell, D. S. Restructuring of Colloidal Silica Aggregates. *Phys. Rev. Lett.* **1986**, *56* (7), 738–741. <https://doi.org/10.1103/PhysRevLett.56.738>.
- (247) Lim, J.-H.; Ha, S.-W.; Lee, J.-K. Precise Size-Control of Silica Nanoparticles via Alkoxy Exchange Equilibrium of Tetraethyl Orthosilicate (TEOS) in the Mixed Alcohol Solution. *Bull. Korean Chem. Soc.* **2012**, *33* (3), 1067–1070. <https://doi.org/10.5012/bkcs.2012.33.3.1067>.
- (248) Chen, K. C.; Tsuchiya, T.; Mackenzie, J. D. Sol-Gel Processing of Silica. *J. Non-Cryst. Solids* **1986**, *81* (1–2), 227–237. [180](https://doi.org/10.1016/0022-</p></div><div data-bbox=)

- 3093(86)90272-3.
- (249) Kryven, I.; Lazzari, S.; Storti, G. Population Balance Modeling of Aggregation and Coalescence in Colloidal Systems. *Macromol. Theory Simulations* **2014**, *23* (3), 170–181. <https://doi.org/10.1002/mats.201300140>.
- (250) Sun, W.; Zeng, Q.; Yu, A.; Kendall, K. Calculation of Normal Contact Forces between Silica Nanospheres. *Langmuir* **2013**, *29* (25), 7825–7837. <https://doi.org/10.1021/la401087j>.
- (251) Reerink, H.; Overbeek, J. T. G. The Rate of Coagulation as a Measure of the Stability of Silver Iodide Sols. *Discuss. Faraday Soc.* **1954**, *18*, 74. <https://doi.org/10.1039/df9541800074>.
- (252) Du, Q.; Freysz, E.; Shen, Y. R. Vibrational Spectra of Water Molecules at Quartz/Water Interfaces. *Phys. Rev. Lett.* **1994**, *72* (2), 238–241. <https://doi.org/10.1103/PhysRevLett.72.238>.
- (253) Valle-Delgado, J. J.; Molina-Bolívar, J. A.; Galisteo-González, F.; Gálvez-Ruiz, M. J.; Feiler, A.; Rutland, M. W. Hydration Forces between Silica Surfaces: Experimental Data and Predictions from Different Theories. *J. Chem. Phys.* **2005**, *123* (3), 034708. <https://doi.org/10.1063/1.1954747>.
- (254) Kipkemboi, P. K.; Eastal, A. J. Densities and Viscosities of Binary Aqueous Mixtures of Nonelectrolytes: Tert -Butyl Alcohol and Tert -Butylamine. *Can. J. Chem.* **1994**, *72* (9), 1937–1945. <https://doi.org/10.1139/v94-247>.
- (255) Khattab, I. S.; Bandarkar, F.; Fakhree, M. A. A.; Jouyban, A. Density, Viscosity, and Surface Tension of Water+ethanol Mixtures from 293 to 323K. *Korean J. Chem. Eng.* **2012**, *29* (6), 812–817. <https://doi.org/10.1007/s11814-011-0239-6>.
- (256) Kaatze, U.; Schumacher, A.; Pottel, R. The Dielectric Properties of Tert.-Butanol/Water Mixtures as a Function of Composition. *Berichte der Bunsengesellschaft für Phys. Chemie* **1991**, *95* (5), 585–592. <https://doi.org/10.1002/bbpc.19910950508>.
- (257) Wyman, J. The Dielectric Constant of Mixtures of Ethyl Alcohol and Water from -5 to 40°. *J. Am. Chem. Soc.* **1931**, *53* (9), 3292–3301. <https://doi.org/10.1021/ja01360a012>.
- (258) Duval, Y.; Mielczarski, J. A.; Pokrovsky, O. S.; Mielczarski, E.; Ehrhardt, J. J. Evidence of the Existence of Three Types of Species at the Quartz-Aqueous Solution Interface at PH 0-10: XPS Surface Group Quantification and Surface Complexation Modeling. *J. Phys. Chem. B* **2002**, *106* (11), 2937–2945. <https://doi.org/10.1021/jp012818s>.
- (259) Lagström, T.; Gmür, T. A.; Quaroni, L.; Goel, A.; Brown, M. A. Surface Vibrational Structure of Colloidal Silica and Its Direct Correlation with Surface Charge Density. *Langmuir* **2015**, *31* (12), 3621–3626. <https://doi.org/10.1021/acs.langmuir.5b00418>.
- (260) Lowe, B. M.; Skylaris, C. K.; Green, N. G.; Shibuta, Y.; Sakata, T. Calculation of Surface Potentials at the Silica-Water Interface Using Molecular Dynamics: Challenges and Opportunities. In *Japanese Journal of Applied Physics*; IOP

References

- Publishing, 2018; Vol. 57, p 04FM02. <https://doi.org/10.7567/JJAP.57.04FM02>.
- (261) He, F.; Zhao, H.; Qu, X.; Zhang, C.; Qiu, W. Modified Aging Process for Silica Aerogel. *J. Mater. Process. Technol.* **2009**, *209* (3), 1621–1626. <https://doi.org/10.1016/j.jmatprotec.2008.04.009>.
- (262) Chou, K.; Lee, B. I. Solvent Effect on Ageing of Silica Gels. *J. Mater. Sci.* **1994**, *29* (13), 3565–3571. <https://doi.org/10.1007/BF00352064>.
- (263) Sorensen, C. M.; Wang, G. M. Size Distribution Effect on the Power Law Regime of the Structure Factor of Fractal Aggregates. *Phys. Rev. E* **1999**, *60* (6), 7143–7148. <https://doi.org/10.1103/PhysRevE.60.7143>.
- (264) Marlière, C.; Woignier, T.; Dieudonné, P.; Primera, J.; Lamy, M.; Phalippou, J. Two Fractal Structures in Aerogel. *J. Non. Cryst. Solids* **2001**, *285* (1–3), 175–180. [https://doi.org/10.1016/S0022-3093\(01\)00450-1](https://doi.org/10.1016/S0022-3093(01)00450-1).
- (265) Schaefer, D. W.; Keefer, K. D. Fractal Aspects of Ceramic Synthesis. *MRS Proc.* **1986**, *73*, 277. <https://doi.org/10.1557/PROC-73-277>.
- (266) Duval, Y.; Mielczarski, J. A.; Pokrovsky, O. S.; Mielczarski, E.; Ehrhardt, J. J. Evidence of the Existence of Three Types of Species at the Quartz–Aqueous Solution Interface at PH 0–10: XPS Surface Group Quantification and Surface Complexation Modeling. *J. Phys. Chem. B* **2002**, *106* (11), 2937–2945. <https://doi.org/10.1021/jp012818s>.
- (267) Pileni, M.-P. The Role of Soft Colloidal Templates in Controlling the Size and Shape of Inorganic Nanocrystals. *Nat. Mater.* **2003**, *2* (3), 145–150. <https://doi.org/10.1038/nmat817>.
- (268) Richard, B.; Lemyre, J.-L.; Ritcey, A. M. Nanoparticle Size Control in Microemulsion Synthesis. *Langmuir* **2017**, *33* (19), 4748–4757. <https://doi.org/10.1021/acs.langmuir.7b00773>.
- (269) Kim, C.; Baek, S.; Ryu, Y.; Kim, Y.; Shin, D.; Lee, C.-W.; Park, W.; Urbas, A. M.; Kang, G.; Kim, K. Large-Scale Nanoporous Metal-Coated Silica Aerogels for High SERS Effect Improvement. *Sci. Rep.* **2018**, *8* (1), 15144. <https://doi.org/10.1038/s41598-018-33539-z>.
- (270) Perdigoto, M. L. N.; Martins, R. C.; Rocha, N.; Quina, M. J.; Gando-Ferreira, L.; Patrício, R.; Durães, L. Application of Hydrophobic Silica Based Aerogels and Xerogels for Removal of Toxic Organic Compounds from Aqueous Solutions. *J. Colloid Interface Sci.* **2012**, *380* (1), 134–140. <https://doi.org/10.1016/j.jcis.2012.04.062>.
- (271) Huh, S.; Wiench, J. W.; Yoo, J. C.; Pruski, M.; Lin, V. S.-Y. Organic Functionalization and Morphology Control of Mesoporous Silicas via a Co-Condensation Synthesis Method. *Chem. Mater.* **2003**, *15* (22), 4247–4256. <https://doi.org/10.1021/cm0210041>.
- (272) Asefa, T.; Kruk, M.; MacLachlan, M. J.; Coombs, N.; Grondy, H.; Jaroniec, M.; Ozin, G. A. Novel Bifunctional Periodic Mesoporous Organosilicas, BPMOs: Synthesis, Characterization, Properties and in-Situ Selective Hydroboration - Alcoholysis Reactions of Functional Groups. *J. Am. Chem. Soc.* **2001**, *123* (35),

- 8520–8530. <https://doi.org/10.1021/ja0037320>.
- (273) Thommes, M.; Kaneko, K.; Neimark, A. V.; Olivier, J. P.; Rodriguez-Reinoso, F.; Rouquerol, J.; Sing, K. S. W. Physisorption of Gases, with Special Reference to the Evaluation of Surface Area and Pore Size Distribution (IUPAC Technical Report). *Pure Appl. Chem.* **2015**, *87* (9–10), 1051–1069. <https://doi.org/10.1515/pac-2014-1117>.
- (274) Teubner, M.; Strey, R. Origin of the Scattering Peak in Microemulsions. *J. Chem. Phys.* **1987**, *87* (5), 3195–3200. <https://doi.org/10.1063/1.453006>.
- (275) D'hollander, S.; Gommès, C. J.; Mens, R.; Adriaensens, P.; Goderis, B.; Du Prez, F. Modeling the Morphology and Mechanical Behavior of Shape Memory Polyurethanes Based on Solid-State NMR and Synchrotron SAXS/WAXD. *J. Mater. Chem.* **2010**, *20* (17), 3475. <https://doi.org/10.1039/b923734h>.
- (276) Besselink, R.; Stawski, T. M.; Castricum, H. L.; Ten Elshof, J. E. Evolution of Microstructure in Mixed Niobia-Hybrid Silica Thin Films from Sol-Gel Precursors. *J. Colloid Interface Sci.* **2013**, *404*, 24–35. <https://doi.org/10.1016/j.jcis.2013.04.031>.
- (277) Prévost, S.; Gradzielski, M.; Zemb, T. Self-Assembly, Phase Behaviour and Structural Behaviour as Observed by Scattering for Classical and Non-Classical Microemulsions. *Adv. Colloid Interface Sci.* **2017**, *247*, 374–396. <https://doi.org/10.1016/J.CIS.2017.07.022>.
- (278) Boldon, L.; Laliberte, F.; Liu, L. Review of the Fundamental Theories behind Small Angle X-Ray Scattering, Molecular Dynamics Simulations, and Relevant Integrated Application. *Nano Rev.* **2015**, *6* (1), 25661. <https://doi.org/10.3402/nano.v6.25661>.
- (279) Framery, E.; Mutin, P. H. ²⁹Si MAS-NMR Study of Silica Gels and Xerogels: Influence of the Catalyst. *J. Sol-Gel Sci. Technol.* **2002**, *24* (3), 191–195. <https://doi.org/10.1023/A:1015391922572>.
- (280) Helms, C. R.; Poindexter, E. H. The Silicon-Silicon Dioxide System: Its Microstructure and Imperfections. *Reports Prog. Phys.* **1994**, *57* (8), 791–852. <https://doi.org/10.1088/0034-4885/57/8/002>.
- (281) Du, X.; Graedel, T. E. Global Rare Earth In-Use Stocks in NdFeB Permanent Magnets. *J. Ind. Ecol.* **2011**, *15* (6), 836–843. <https://doi.org/10.1111/j.1530-9290.2011.00362.x>.
- (282) Lixandru, A.; Poenaru, I.; Güth, K.; Gauß, R.; Gutfleisch, O. A Systematic Study of HDDR Processing Conditions for the Recycling of End-of-Life Nd-Fe-B Magnets. *J. Alloys Compd.* **2017**, *724*, 51–61. <https://doi.org/10.1016/j.jallcom.2017.06.319>.
- (283) Wang, L.; Long, Z.; Huang, X.; Yu, Y.; Cui, D.; Zhang, G. Recovery of Rare Earths from Wet-Process Phosphoric Acid. *Hydrometallurgy* **2010**, *101* (1–2), 41–47. <https://doi.org/10.1016/j.hydromet.2009.11.017>.
- (284) Ogata, T.; Narita, H.; Tanaka, M. Immobilization of Diglycol Amic Acid on Silica Gel for Selective Recovery of Rare Earth Elements. *Chem. Lett.* **2014**, *43* (9),

References

- 1414–1416. <https://doi.org/10.1246/cl.140446>.
- (285) Ogata, T.; Narita, H.; Tanaka, M. Adsorption Behavior of Rare Earth Elements on Silica Gel Modified with Diglycol Amic Acid. *Hydrometallurgy* **2015**, *152*, 178–182. <https://doi.org/10.1016/j.hydromet.2015.01.005>.
- (286) Ogata, T.; Narita, H.; Tanaka, M. Adsorption Mechanism of Rare Earth Elements by Adsorbents with Diglycolamic Acid Ligands. *Hydrometallurgy* **2016**, *163*, 156–160. <https://doi.org/10.1016/J.HYDROMET.2016.04.002>.
- (287) Shinozaki, T.; Ogata, T.; Kakinuma, R.; Narita, H.; Tokoro, C.; Tanaka, M. Preparation of Polymeric Adsorbents Bearing Diglycolamic Acid Ligands for Rare Earth Elements. *Ind. Eng. Chem. Res.* **2018**, *57* (33), 11424–11430. <https://doi.org/10.1021/acs.iecr.8b01797>.
- (288) Juère, E.; Florek, J.; Larivière, D.; Kim, K.; Kleitz, F. Support Effects in Rare Earth Element Separation Using Diglycolamide-Functionalized Mesoporous Silica. *New J. Chem.* **2016**, *40* (5), 4325–4334. <https://doi.org/10.1039/c5nj03147h>.
- (289) Wehbie, M.; Arrachart, G.; Arrambide Cruz, C.; Karamé, I.; Ghannam, L.; Pellet-Rostaing, S. Organization of Diglycolamides on Resorcinarene Cavitand and Its Effect on the Selective Extraction and Separation of HREEs. *Sep. Purif. Technol.* **2017**, *187*, 311–318. <https://doi.org/10.1016/J.SEPPUR.2017.06.062>.
- (290) Preston, J. S. Solvent Extraction of Metals by Carboxylic Acids. *Hydrometallurgy* **1985**, *14* (2), 171–188. [https://doi.org/10.1016/0304-386X\(85\)90032-5](https://doi.org/10.1016/0304-386X(85)90032-5).
- (291) Mokili, B.; Poitrenaud, C. Medium Effect on the Separation Factor in Liquid-Liquid Extraction. Application to the Separation of Trivalent Lanthanide Nitrates by Tri-n-Butylphosphate. *Solvent Extr. Ion Exch.* **1997**, *15* (3), 455–481. <https://doi.org/10.1080/07366299708934488>.
- (292) Wehbie, M.; Arrachart, G.; Karamé, I.; Ghannam, L.; Pellet-Rostaing, S. Triazole Diglycolamide Cavitand for Lanthanide Extraction. *Sep. Purif. Technol.* **2016**, *169*, 17–24. <https://doi.org/10.1016/j.seppur.2016.06.003>.
- (293) Chiron, N.; Guilet, R.; Deydier, E. Adsorption of Cu(II) and Pb(II) onto a Grafted Silica: Isotherms and Kinetic Models. *Water Res.* **2003**, *37* (13), 3079–3086. [https://doi.org/10.1016/S0043-1354\(03\)00156-8](https://doi.org/10.1016/S0043-1354(03)00156-8).
- (294) Gujadhur, R.; Venkataraman, D.; Kintigh, J. T. Formation of Arylnitrogen Bonds Using a Soluble Copper(I) Catalyst. *Tetrahedron Lett.* **2001**, *42* (29), 4791–4793. [https://doi.org/10.1016/S0040-4039\(01\)00888-7](https://doi.org/10.1016/S0040-4039(01)00888-7).
- (295) Edwards, H. G. M.; Lewis, I. R.; Turner, P. H. Raman and Infrared Spectroscopic Studies of Tris Triphenyl Phosphine Chloride Complexes of Transition Metals. *Inorganica Chim. Acta* **1994**, *216* (1–2), 191–199. [https://doi.org/10.1016/0020-1693\(93\)03713-K](https://doi.org/10.1016/0020-1693(93)03713-K).
- (296) Barré, G.; Taton, D.; Lastécouères, D.; Vincent, J. M. Closer to the “Ideal Recoverable Catalyst” for Atom Transfer Radical Polymerization Using a Molecular Non-Fluorous Thermomorphic System. *J. Am. Chem. Soc.* **2004**, *126* (25), 7764–7765. <https://doi.org/10.1021/ja048096a>.

- (297) Hussein, G. A. M.; Khedr, M. H.; Farghali, A. A. Gadolinium Oxide from Gadolinium Oxalate Hydrate Physicochemical Characterization. *Colloids Surfaces A Physicochem. Eng. Asp.* **2002**, *203* (1–3), 137–142. [https://doi.org/10.1016/S0927-7757\(01\)01091-3](https://doi.org/10.1016/S0927-7757(01)01091-3).
- (298) Kobayashi, S.; Manabe, K. Green Lewis Acid Catalysis in Organic Synthesis. *Pure Appl. Chem.* **2007**, *72* (7), 1373–1380. <https://doi.org/10.1351/pac200072071373>.
- (299) Kobayashi, S.; Sugiura, M.; Kitagawa, H.; Lam, W. W.-L. Rare-Earth Metal Triflates in Organic Synthesis. *Chem. Rev.* **2002**, *102* (6), 2227–2302. <https://doi.org/10.1021/cr010289i>.
- (300) Rouquerol, F.; Rouquerol, J.; Llewellyn, P.; Denoyel, R. Texture Des Matériaux Divisés Aire Spécifique Des Matériaux Pulvérulents Ou Nanoporeux. *Tech. l'ingénieur Surfaces Struct. Fonct.* **2017**, *1*, 50–54.

List of Figures

Figure 1. Medium-term (2015-2025) criticality matrix as developed in 2011. ⁴	1
Figure 2. Spectrum of organic-inorganic hybrid materials as a function of the inorganic part.	5
Figure 3. Fundamental reactions of the sol-gel process using TEOS as example. Hydrolysis and condensation take place under acidic or basic conditions.	7
Figure 4. Influence of the sol pH and the ionic strength on the morphology of the obtained silica polymer. The Figure is redrawn from literature. ³⁰	9
Figure 5. General chemical formula of silanes.	12
Figure 6. Classical sol-gel solvents plotted as a function of their relative dielectric constant and the relative charges on the oxygen atom and the labile proton (if present).	14
Figure 7. Decomposition of the Gibbs free energy of a typical colloidal system. The Gibbs free energy is given in units of $k_B T$ and plotted against the distance.	17
Figure 8. Packing parameter of surfactant molecules and the resulting morphologies of the self-assembled structures.	22
Figure 9: Porosity in different scales as recommended by IUPAC. ⁶⁷	24
Figure 10. Molecular structure of 11-aminoundecyltriethoxysilane.	26
Figure 11. Material morphologies obtained by Romain Besnard <i>et al.</i> The curvature of the self-assemblies of the investigated molecule 11-aminoundecyltriethoxysilane was tailored using TEOS or counter-ions. ¹⁰	27
Figure 12. Impact of co-solvent or TEOS addition on the angle between two connected organosilane precursor molecules.	29
Figure 13. Splitting of the quaternary system water/co-solvent(CS)/TEOS/organosilane precursor(OP) into the ternary and binary subsystems. The relations are indicated by the arrows. The description of the ellipses indicates the literature or chapter number where the corresponding results can be found.	30
Figure 14: The two catalysts used for CuAAC: tris-triphenylphosphane copper bromide ($[Cu(PPh_3)_3]Br$, C1) and tris(2-dioctadecylaminoethyl)amine copper bromide ($[Cu(C_{18}tren)]Br$, C2).	40
Figure 15: The monitoring of the normalized content of starting material 4 as determined by the internal standard method applied to GC-MS analysis. The inset shows the reaction conditions.	41
Figure 16. Typical structures of cage- (a) and ladder-like (b) silsesquioxanes.	45
Figure 17. The strategy outline as developed earlier. The indicated area shows the systems that will be investigated in Chapter III.	46
Figure 18. Structural formula of the organosilane precursors used for silsesquioxane synthesis.	46
Figure 19. Overview of the experimental procedure for the synthesis of the SHMs from the precursor molecules (see II for details).	47

Figure 20. FTIR spectra of the fresh and thermally treated materials obtained from the precursor P2 using a) water or b) THF as solvent in the synthesis.	49
Figure 21. TGA weight loss curves in percent of the original mass during heating to 1000 °C. The dashed grey line indicates the residual mass percentage at 700 °C.	51
Figure 22. SAXS patterns of the silsesquioxanes elaborated from the precursor P2 in water (a) and THF (b). The indicated slopes serve as visual guide. The labels q_{n00} indicate the Bragg peak positions.	53
Figure 23. Scheme of the supramolecular arrangement of the MP2 materials when looking at two repeat units (a, Red = SiO _{1.5} , Blue = triazole) or a stack of several repeat units (b) with height H and length L	54
Figure 24 FTIR spectra of the fresh and thermally treated materials obtained from the precursor P1 using a) water or b) THF as solvent in the synthesis.	57
Figure 25. ²⁹ Si(HPDEC)-NMR spectra of the materials H/T-MP1-A/B-C. The two contributions coming from different silanol species (T ² and T ³) were fitted. Open circles represent the measured data. The blue line represents the cumulative fit obtained by the addition of the two contributions (red and green lines). The determined percentage of each contribution to the total area is indicated. It is used to calculate the degree of polycondensation (τ_{Cond}).	59
Figure 26. TGA weight loss curves of the P1 materials in percent of the original mass during heating to 1000 °C. The dashed grey line indicates the residual mass percentage at 700 °C.	60
Figure 27. SAXS patterns of the materials produced from the precursor P1 in water (a) and THF (b). The indicated slopes serve as visual guide. The labels q indicate the Bragg peak positions.	62
Figure 28. TEM images of the samples T-MP1-A-C (a) and T-MP1-B-C (b).	64
Figure 29. FTIR spectra of the fresh and thermally treated materials obtained from the precursor P3 using a) water or b) THF as solvent in the synthesis.	66
Figure 30. TGA weight loss curves of the P3 materials in percent of the original mass during heating to 1000 °C. The dashed grey line indicates the residual mass percentage at 700 °C.	68
Figure 31. SAXS patterns of the materials produced from the precursor P3 in water (a) and THF (b). The indicated slopes serve as visual guide. The labels q indicate the Bragg peak positions.	70
Figure 32. FTIR spectra of the P3 materials before (dashed lines) and after (solid lines) the hydrolysis reaction.	74
Figure 33. TGA weight loss curves of the hydrolyzed materials in percent of the original mass during heating to 1000 °C. The dashed grey line indicates the residual mass percentage at 700 °C.	75
Figure 34. SAXS patterns of the hydrolyzed P3 materials. The labels q indicate the Bragg peak positions.	77
Figure 35. FTIR spectra of the fresh and thermally treated materials obtained from the precursors P4 (a) or P5 (b).	79

References

- Figure 36. Zoom of the FTIR spectra of the P5 materials. The assigned modes illustrated above..... 80
- Figure 37. TGA weight loss curves of H-MP4-B-C (a) and H/T-MP5-B-C (b) in percent of the original mass during heating to 1000 °C. The dashed grey line indicates the residual mass percentage at 700 °C. 81
- Figure 38. SAXS patterns of the materials synthesized from P4 (a), and P5 in water (b) or THF (c). The labels q indicate the Bragg peak positions..... 83
- Figure 39. Scheme of the structural evolution of the material T-MP5-B during thermal treatment. The inset graph shows the SLD model used for the SAXS fits in Figure 38 c). 85
- Figure 40. Overview of the identified methods to influence the mesoscale structure of the linear silsesquioxane precursors AUT¹⁰ and PX (this work)..... 88
- Figure 41. Illustration of the physical interaction hierarchy in systems containing water, co-solvent (CS), TEOS and a surfactant-like organosilane precursor (OP). A detailed explanation is given with Figure 13. The black circle marks the system discussed in Materials from TEOS in mixed solventsIV..... 91
- Figure 42. Ternary phase diagrams of the systems water/TBA/TEOS and water/EtOH/TEOS in weight fractions determined at $25 \pm 0.5^\circ\text{C}$. The mono- and biphasic regions are indicated in the respective areas. The selected sols are referred A to H (see Table 9 for compositions). “A” to “G” denote both A_{C2} and A_{C4} to G_{C2} and G_{C4} . For presentability, the water and the HCl weight fraction in the prepared samples (see Table 9 for compositions) were added to give “ w_{water} ” in the diagram. 96
- Figure 43. a) and c) SWAXS patterns of binary alcohol/water mixtures. b) and d) SWAXS spectra of ternary TEOS/alcohol/water mixtures at neutral pH just after the 7.5 w% TEOS addition. Data for c) was already published earlier.⁶³ Sample compositions of ternary mixtures are given in Table 10..... 98
- Figure 44. Gel times of the samples as a function of the molar fraction of water x_{water} as determined by observation and by DLS..... 101
- Figure 45. a) Evolution of the SAXS patterns of the sols C_{C4} and C_{C2} during the sol-gel transition. The symbol color intensifies with sample ageing. b) evolutions of the scattering intensity at $q=0.3 \text{ nm}^{-1}$ of the SAXS patterns as a function of time. 102
- Figure 46. Reaction constants for the different sols estimated considering the electrostatic repulsion between primary particles. 106
- Figure 47. Specific surface areas (S_{BET}) of aerogels obtained by the BET method as a function of the molar fraction of water x_{water} in the corresponding sol. 107
- Figure 48. SAXS patterns of the aerogels with their corresponding fits. Data was multiplied by a factor of 10^x for better visibility. a) shows the SAXS patterns for aerogels obtained from ethanol containing samples and b) from TBA containing samples. 108
- Figure 49. TEM images of aerogels produced from different sols: a) B_{C2} , b) E_{C2} , c) G_{C2} , d) H_{REF} , e) A_{C4} , f) D_{C4} , g) E_{C4} , h) F_{C4} . Scale bar = 100 nm..... 111
- Figure 50. Simplified illustration of the structuring at the mesoscale during the sol-gel process according to the proposed mechanism..... 114

- Figure 51. Mixing entropy gain per molecule alcohol when adding one molecule of alcohol into the solution. 116
- Figure 52. The strategy outline as developed in the introduction. The subject of the present chapter is highlighted by the black rectangle..... 119
- Figure 53. Molecular structure of 4-propyl-1-(11-(triethoxysilyl)undecyl)-1H-1,2,3-triazole (P2). 120
- Figure 54. TGA weight loss curves for the different materials obtained by the co-condensation approach. The weight loss curve of sample H-MP2-B-C from chapter III is plotted for clarity. The lines (a) and (b) mark important features as discussed in the text. 122
- Figure 55. Molar percentage of the incorporated organosilane P2 in the material as a function of its time of addition a) after TEOS or b) before drying. The red line marks the initial percentage in the starting sol. The dashed blue line is a linear fit of the samples CoCo-1 to CoCo-4 (a) or CoCo-1 to CoCo-5 (b). 124
- Figure 56. FTIR spectra of the materials obtained by the co-condensation approach. The spectrum of H-MP2-B-C from Chapter III is plotted for clarity. Points (a)-(d) designate important signals are discussed in the text. 125
- Figure 57. Intensity ratio (R_{xy}) of the CH₂ signals to the silica matrix signal in Figure 56 as a function of the time of P2 addition a) after TEOS or b) before drying. 127
- Figure 58. Intensity ratio (R_{cd}) of the signals attributed to the free Si-OH and the siloxane bridges in the silica matrix in Figure 56 as a function of the time of P2 addition after TEOS for sample CoCo-1 to CoCo-5. The sample CoCo-Ref is plotted for comparison. The dashed lines indicate characteristic y-values as discussed in the text. Error bars of 5% are plotted. 128
- Figure 59. Nitrogen adsorption isotherms of the samples CoCo-1, CoCo-2, CoCo-3 and CoCo-Ref. 130
- Figure 60. Results from N₂ sorption experiments for the materials obtained by co-condensation. The specific surface obtained by the BET method S_{BET} is plotted on a log-scale. The external specific surface area fraction of S_{BET} is obtained from the Harkins and Jura t-plot. The microporous volume fraction of the total pore volume is obtained from the linear transformed BET equation. 132
- Figure 61. SAXS patterns of the materials produced by co-condensation. The measured patterns are represented by the open symbols. The corresponding fits are superimposed as red lines. The Teubner-Strey (T-S) contribution ($C_I(q)$) is added as a blue dashed line) For better presentability, the patterns were shifted by a factor of ten. Important features are indicated by (i) and (ii) and are described in the text..... 133
- Figure 62. SEM and TEM images of the co-condensed materials: a) SEM CoCo-1 with zoomed inset, b) TEM CoCo-1, c) SEM CoCo-2, d) TEM CoCo-2, e) SEM CoCo-5, f) TEM CoCo-3, g) SEM CoCo-Ref, h) TEM CoCo-Ref. Scale bars are displayed in the images. 134
- Figure 63. Correlation length l_c^{TS} and experimental scattering invariant Q_{exp} obtained from the SAXS patterns of the co-condensed materials (Figure 61). Only Teubner-Strey

References

(T-S) contributions (dashed blue line in Figure 61) were intergrated for the calculation of the experimental scattering invariant.....	137
Figure 64. Simplified illustration of the fit model of CoCo-1. The illustration is drawn to scale.....	139
Figure 65. Extracting groups of the materials used in VI.....	143
Figure 66. Q_e of the Neodymium extraction of the tested materials at pH 1 to pH 4 (a) and a zoom on the results for H-MP4-B-C (b).	146
Figure 67. Uptake capacity Q_e (black) as a function of the equilibrium concentration of Nd (1 M HNO ₃) after 24 h of contact with H-MP4-B-C. The red graph is the Langmuir isotherm of this data.	148
Figure 68. SEM images of H-MP4-B-C after the contact with a Nd containing solution. A) shows the morphology of the materials while b) visualizes the spacial distirbution of Nd. In c) the corresponding EDX spectrum is shown.	149
Figure 69. The extraction efficiency of various metals from a simulated NdFeB leachate as a function of the quantity of H-MP4-B-C.....	150

IX EXPERIMENTAL

1 Chemicals

All chemicals were used without further purification. LiBr ($\geq 99\%$), MgSO_4 ($\geq 99.5\%$), CuBr_2 ($\geq 99\%$), Palladium on charcoal (10w%) and 11-undecen-1-ol ($\geq 99\%$) were obtained from Alfa Aesar (Kandel, Germany). Triethoxysilane ($\geq 97\%$), and Karstedt's catalyst (2.1-2.4w% Pt) were obtained from abcr GMBH (Karlsruhe, Germany). 1-Iodoctane ($\geq 98\%$), dicyclohexylcarbodiimide (DCC, $\geq 99\%$), tetraethoxy orthosilicate (TEOS, $\geq 98\%$), DMF anhydrous ($\geq 99.8\%$), propargylamine ($\geq 99\%$), diglycolic anhydride (DGA, $\geq 97\%$), acetonitrile anhydrous ($\geq 99.9\%$), 1,4-dioxane anhydrous (≥ 99.8), and THF anhydrous (≥ 99.5) were purchased from Acros Organics (Geel, Belgium). Hydrogen (H_2), Argon (Ar), and Nitrogen (N_2) were purchased from Air Liquide France Industrie (Jay, France). Ethanol absolute anhydrous (p.a), Acetone (tech), dichloromethane (DCM, $\geq 99.8\%$), chloroform ($\geq 99.95\%$), ethylacetate ($\geq 99.8\%$), cyclohexane ($\geq 99.8\%$), toluene ($\geq 99.8\%$), pentane ($\geq 95\%$), diethylether ($\geq 99.8\%$), methanol ($\geq 99.9\%$), and 37% (w/w) HCl were obtained from Carlo Erba (Val-de-Reuil, France). Animal charcoal, gadolinium (III) nitrate ($\text{Gd}(\text{NO}_3)_3$, $\geq 99.9\%$), and Sodium Oxalate ($\geq 99.5\%$) were obtained from Fisher Scientific SAS (Illkirch, France). 1-hydroxybenzotriazole (HOBt, $\geq 98\%$) was purchased from Honeywell (New Jersey, USA). Methyl propiolate ($\geq 98\%$) was purchased from TCI EUROPE N.V. (Zwijndrecht, Belgium). *Tert*-butanol (TBA, $\geq 98\%$), 28-30% (w/w) NH_4OH solution, triethylamine (NEt_3 , $\geq 99\%$), methanesulfonyl chloride ($\geq 99.7\%$), NaCl ($\geq 99\%$), Celite® S, Silica Powder (60 Å, 40-63 μm), diethylamine ($\geq 99.5\%$), triphenylphosphine (≥ 99), copper(II) bromide ($\geq 99.999\%$), tris(2-aminoethyl)amine ($\geq 96\%$), 1-iodooctadecane ($\geq 95\%$), 1-pentyne (≥ 99), 4-bromo-1-butyne ($\geq 97\%$), phenylacetylene ($\geq 98\%$), trifluoromethanesulfonic acid (TfOH, $\geq 99\%$), and sodium azide (NaN_3 , $\geq 99\%$) were obtained from Sigma-Aldrich (Lyon, France).

2 Methods

1.1 Dynamic Light Scattering (DLS)

Dynamic light scattering was used for the determination of the gel times in **IV**. To this end, DLS was done at 50°C on a Zetasizer Nano ZS (Malvern Panalytical Ltd., United Kingdom) with automatic attenuation in silicone glue sealed 10 mm polystyrene cuvettes. Acquisition was performed at 173° for 5 runs of 20 s each every hour and data were treated using a method adapted from literature.²⁴⁴ The time of the last correlation function consisting of a single monomodal exponential function was chosen as gel-time.

1.2 Gas Chromatography-Mass Spectrometry (GC-MS)

Gas Chromatography analysis was performed with a gas chromatograph mass spectrometer Shimadzu GCMS-QP2010 Ultra with a SLB®-5ms Supelco capillary GC column (L × I.D. 30 m × 0.25 mm, df 0.25 μm). Sample split injection (2 μL) was used with a split of 120 and an injector temperature of 250°C, Helium (115 kPa) was used as the carrier gas. The following time–temperature program was used for the analysis: 50°C (1 min); 50–270 °C at 25°C/min, 275°C (10 min).

1.3 Electrospray Ionization Mass Spectrometry (ESI-MS)

ESI-MS was performed on a Flexar SQ 300 MS instrument.

1.4 Fourier Transformed Infrared Spectroscopy/Attenuated Total Reflection (FTIR/ATR)

Fourier Transformed Infrared spectroscopy (FTIR) was performed with a Perkin Elmer Spectrum 100 spectrometer in Attenuated Total Reflection (ATR) mode equipped with a DTGS/KBR detector. Liquid samples were placed at the surface of the diamond in a PTFE set-up to avoid solvent evaporation. Solid samples were pressed on the diamond. The spectra were recorded from 380 to 4000 cm⁻¹ adding 4 scans with a 4 cm⁻¹ of resolution correcting from the background spectrum for each substrate. Baseline adjustments and peak decomposition were performed using the Origin software.

1.5 Nitrogen adsorption-desorption

Nitrogen adsorption-desorption analyses were carried out using a Micromeritics apparatus (ASAP 2020). Before analysis, all samples were outgassed at 60 °C during 24 h under high vacuum (10^{-5} Pa). Specific surface area was obtained using the Brunauer–Emmett–Teller (BET) model.

1.6 Nuclear Magnetic Resonance spectroscopy (NMR)

NMR analyses were performed on a Bruker 400 ultrashield VS spectrometer.

1.7 Small/Wide-Angle X-ray Scattering (SWAXS)

Small and Wide Angle X-ray Scattering (SWAXS) analysis were carried out in transmission geometry with a Xenocs setup equipped with a Mo anode ($\lambda = 0.71 \text{ \AA}$) using a MAR345 2D imaging plate detector. Such short wavelength allows to cover a scattering range for standard SWAXS that extends to large wave vectors in order to obtain information at a small scale down to few angstroms typically a wavenumber q ranged from 0.2 nm^{-1} to 30 nm^{-1} . The collimation was ensured by a Fox2D multilayer mirror and by a set of scatterless slits that delimited the beam to a square section (0.8 mm side length at the sample position). The distance from the sample to the detector was about 750 mm and was calibrated using silver behenate powder. The samples were analyzed in glass capillaries of 2 mm of diameter. Azimuthal averaging of 2D-data recorded by a MAR345 imaging plate detector was performed using the FIT2D software taking into account the electronic background of the detector, the empty cell subtraction and an intensity calibration. The scattered intensity in absolute scale (in cm^{-1}) was expressed versus the magnitude of the scattering vector $q = (4\pi\sin\theta)/\lambda$, where θ was the scattering angle. Experimental resolution was $\Delta q/q = 0.02$. Data was fitted using the SASfit software. The respective fitting procedure is added in the appropriate position in **X**.

1.8 Scanning Electron Microscopy (SEM)

SEM was performed on a FEI QUANTA 200 ESEM FEG operating at 15 kV equipped with a Everhart-Thornley detector.

1.9 Transmission electron microscopy (TEM)

For transmission electron microscopy (TEM) and high-resolution transmission electron microscopy (HRTEM) measurements, one or more drops of the dilute solution of dried sample in ethanol are deposited on the amorphous carbon film. High-resolution transmission electron microscopic measurements were carried out using a JEOL 2200FS microscope that operates at 200 kV. Transmission electron microscopy observations were then carried out using a FEI Tecnai G2 TEM microscope equipped with a LaB6 filament that operates at 200 kV.

1.10 Ternary phase diagrams

Ternary phase diagrams in **IV** were determined at room temperature using a static and dynamic process as described in literature.⁶³ For this purpose, binary mixtures of water/alcohol and alcohol/TEOS were prepared. The third component was added dropwise and the tube was stirred after every addition. The composition at the moment of demixing was noted as the phase boundary. After every addition, the tube was closed and then stirred. To limit the TEOS hydrolysis, ultrapure water was used.

1.11 ThermoGravimetric Analysis (TGA)

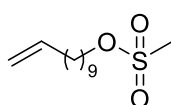
Thermal analysis (TGA) was performed with a Mettler Toledo Instrument with a Type-S thermocouple under air flow with a heating rate of 5 °C/min from 25 to 1000 °C.

X APPENDIX/NMR SPECTRA

1 Chapter II

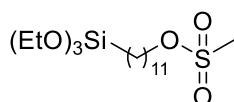
Protocols and Analysis

Methanesulfonic acid undec-10-enyl ester 2



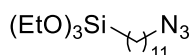
10-undecen-1-ol (34.058 g, 0.2 mol, 1 eq) and NEt_3 (25.5 g, 0.252 mol, 1.26 eq) were added to 700 mL CHCl_3 . Over the course of 90 min MsCl (27.494 g, 0.24 mol, 1.2 eq) dissolved in 100 mL of CHCl_3 were added dropwise to the stirred solution at room temperature. The temperature was controlled by a water bath. Addition of MsCl produced HCl which was removed by frequent venting. After 20 h the solution has turned slightly yellow. Half of the reaction mixture was washed with 450 mL water. The aqueous phase was extracted with CHCl_3 (2x100 mL). The same procedure was repeated for the second half. All the united aqueous phases were again extracted with CHCl_3 (100 mL). The organic phases were reduced to 200 mL and washed with brine (100 mL). CHCl_3 was evaporated and the residue was distilled at 80 °C and 0.5 mbar to remove volatile impurities. The resulting dark oil was again distilled at 160 °C and 0.3 mbar to afford the product **2** as translucent brown oil (45.12 g, 0.18 mol, 91%) in the distillate.

$^1\text{H-NMR}$ (400 MHz, CDCl_3): δ = 5.78 (m, 1H), 4.93 (m, 2H), 4.2 (t, J = 6.61 Hz, 2H), 2.98 (s, 3H), 2 (q, J = 6.97 Hz, 2H), 1.72 (quint, J = 6.85 Hz, 2H), 1.4-1.15 (m, 13H). **$^{13}\text{C-NMR}$** (100 MHz, CDCl_3): δ = 139.36, 114.36, 70.4, 37.56, 33.98, 29.54, 29.32, 29.25, 29.2, 29.08, 25.61. **HRMS** (ESI) exact mass calc. for $\text{C}_{12}\text{H}_{24}\text{O}_3\text{S}$: m/z 248.14, found: m/z 248.17 $[\text{M}+\text{H}]^+$

11-methanesulfonic acid undecyl ester triethoxysilane 3

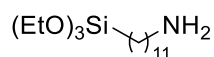
Under N₂-atmosphere Karstedt's catalyst (2.1-2.4 wt% Pt, 0.462 g, 0.02 mmol, 3x10⁻⁴ eq) was added to a stirred mixture of **2** (15 g, 60.05 mmol, 1 eq) and triethoxysilane (22.99 g, 139.94 mmol, 2.33 eq) at room temperature. The temperature was kept constant using a water bath. After 20 h activated charcoal (2 g) was added and the mixture was stirred at 40 °C for 1 h. The mixture was filtered and the filtrate distilled at 170 °C (0.3 mbar) to remove more volatile impurities. The product **3** was obtained as brown oil (21.87 g, 53.06 mmol, 88%).

¹H-NMR (400 MHz, CDCl₃): δ = 4.18 (t, *J* = 6.6 Hz, 2H), 3.77 (q, *J* = 7.09 Hz, 6H), 2.96 (s, 3H), 1.7 (quint, *J* = 7.46 Hz, 2H), 1.4-1.15 (m, 25H), 0.58 (t, *J* = 8.68 Hz, 2H). **¹³C-NMR** (100 MHz, CDCl₃): δ = 70.5, 58.49, 37.55, 33.38, 29.7 (d, *J* = 3.67 Hz), 29.62, 29.35 (t, *J* = 9.9 Hz), 25.64, 22.97, 18.52, 10.6

11-azidoundecyl triethoxysilane 4

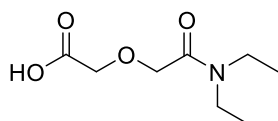
Under N₂-atmosphere, NaN₃ (7.09 g, 109.14 mmol, 3 eq) suspended in dry CH₃CN (100 mL) was heated to 85 °C. **3** (15 g, 36.4 mmol, 1 eq) in dry CH₃CN (50 mL) was added dropwise to the heated mixture. After 48 h the mixture was cooled to 0 °C filtered, washing the residue with cold dry CH₃CN (2x20 mL). After evaporation of dry CH₃CN more volatile compounds were removed by distillation at 110 °C (0.6 mbar) for 2 h. The residue was distilled 200 °C (0.6 mbar) to afford the product **4** as clear, colorless oil (11.94 g, 31.75 mmol, 87%) in the distillate.

¹H-NMR (400 MHz, CDCl₃): δ = 3.79 (q, *J* = 6.97 Hz, 6H), 3.23 (t, *J* = 6.97, 2H), 1.57 (quint, *J* = 8.07 Hz, 2H), 1.4-1.15 (m, 27H), 0.58 (t, *J* = 8.68 Hz, 2H). **¹³C-NMR** (100 MHz, CDCl₃): δ = 58.26, 51.48, 33.2, 29.6, 29.55, 29.27 (d, *J* = 7.34 Hz), 28.92, 26.79, 22.82, 18.32, 10.46. **HRMS** (ESI) exact mass calc. for C₁₈H₄₁N₃O₃Si: *m/z* 375.29, found: *m/z* 375.1 [M+H]⁺

11-aminoundecyl triethoxysilane 5

Under Ar-atmosphere, EtOH anhydr. (500 mL) was added to Palladium supported on carbon (Pd/C, 10 w%) (0.2 g, 0.19 mmol, 0.01 eq) and 4 balloons filled with H₂ were bubbled through. A solution of **4** (7.9 g, 21 mmol, 1 eq) dissolved in EtOH (250 mL) was infused by bubbling through one balloon of H₂. The solution containing **4** was then added dropwise under H₂-atmosphere over the course of 1 h. After 2 h of stirring at room temperature the solution was filtered over celite® and the solvent of the filtrate was evaporated. The residue was dissolved in pentane and the resulting solution containing a white precipitate was again filtered over celite®. The pentane was evaporated and the product **5** was obtained as a slightly yellow liquid (5.5 g, 16.4 mmol, 78 %) after fractionated distillation at 200 °C (0.7 mbar).

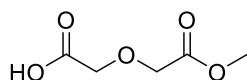
¹H-NMR (400 MHz, CDCl₃): δ = 3.78 (q, *J* = 7.09 Hz, 6H), 2.66 (t, *J* = 6.84 Hz, 2H), 2.41 (m, 2H), 1.4-1.15 (m, 29H), 0.59 (t, *J* = 8.31 Hz, 2H). ¹³C-NMR (100 MHz, CDCl₃): δ = 58.48, 42.15, 33.42, 29.83, 29.75, 29.69, 29.48, 27.1, 22.97, 18.51, 10.6

2-(2-(diethylamino)-2-oxoethoxy)acetic acid ADEA

To 2.19 g (30 mmol, 1 eq) of diethyl amine in 40 mL THF, 3.5 g (30 mmol, 1 eq) diglycolic anhydride (**DGA**) were added in portions. The solution was stirred overnight and, then, washed with 80 mL of 1 M HCl (2x40 mL). The organic phase was evaporated and the yellowish crude product was purified using flash column chromatography (EA/CH increasing gradient). The desired product was obtained as a colorless oil (4.3 g, 22.8 mmol, 76 %).

¹H-NMR (400 MHz, CDCl₃): δ = 4.35 (s, 2H), 4.14 (s, 2H), 3.43 (q, *J* = 7.45 Hz, 2H), 3.21 (q, *J* = 7.45 Hz, 2H), 1.21 (t, *J* = 7.16 Hz, 3H), 1.16 (t, *J* = 7.16 Hz, 3H). ¹³C-NMR (100 MHz, CDCl₃): δ = 171.97, 170.22, 72.59, 71.03, 41.07, 40.92, 13.72, 12.61. **R_f** (EA-CH, 5/5) = 0.1. **HRMS** (ESI) exact mass calc. for C₈H₁₅NO₄: *m/z* 190.1, found: *m/z* 190.1 [M+H]⁺

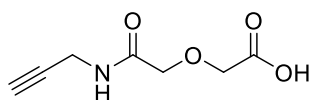
2-(2-methoxy-2-oxoethoxy)acetic acid **AE**



To 3.5 g (30 mmol, 1 eq) diglycolic anhydride (**DGA**) in 10 mL DCM, 1.22 mL (30 mmol, 1.1 eq) of methanol were added. The solution was refluxed for 2 hours and, then, evaporated and the yellowish crude product was purified using flash column chromatography (EA/CH increasing gradient). The desired product was obtained as a colorless oil (3.67 g, 25 mmol, 83 %).

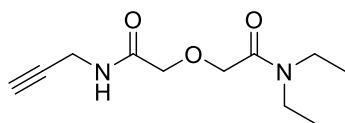
¹H-NMR (400 MHz, CDCl₃): δ = 4.24 (s, 2H), 4.2 (s, 2H), 3.74 (s, 3H). **¹³C-NMR** (100 MHz, CDCl₃): δ = 173.38, 172.25, 68.64, 68.6, 52.29. **R_f** (EA-CH, 8/2) = 0.55. **HRMS** (ESI) exact mass calc. for C₅H₈O₅: m/z 149.04, found: m/z 149 [M+H]⁺

2-(2-oxo-2-(prop-2-yn-1-ylamino)ethoxy)acetic acid **APA**



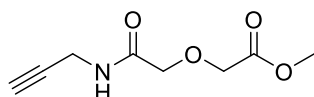
To 3.48 g (30 mmol, 1 eq) diglycolic anhydride (**DGA**) in 90 mL THF, 1.65 g (30 mmol, 1.1 eq) of propargylamine were added in portions. The mixture was evaporated and the yellowish crude product was purified using flash column chromatography (EA/CH, increasing gradient). The desired product was obtained as a colorless oil (3.9 g, 22.8 mmol, 76 %).

¹H-NMR (400 MHz, MeOD): δ = 4.2 (s, 2H), 4.09 (s, 2H), 4.03 (d, J = 2.83 Hz, 2H), 2.58 (t, J = 2.28 Hz, 1H) **¹³C-NMR** (100 MHz, MeOD): δ = 172.28, 170.34, 70.7, 70.74, 69.9, 67.63, 27.55. **HRMS** (ESI) exact mass calc. for C₇H₉NO₄: m/z 172.06, found: m/z 172.1 [M+H]⁺

N,N-diethyl-2-(2-oxo-2-(prop-2-yn-1-ylamino)ethoxy)acetamide **A4**

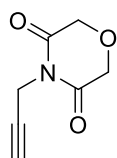
A solution of 4.3 g **ADEA** (23 mmol, 1 eq), 1.84 mL SOCl_2 (25.3 mmol, 1.1 eq) and 3 drops of DMF in 80 mL DCM was stirred for 3 hours at r.t. Then, the volatile components were removed by vacuum distillation and the residue was dissolved in 40 mL DCM. In second flask, a solution of 1.62 mL propargylamine (25.3 mmol, 1.1 eq) and 2.53 g triethylamine (25.3 mmol, 1.1 eq) in 40 mL was prepared. To this solution, the distillation residue was added dropwise over 1 hour. The now turbid solution was stirred for 2 hours at r.t. and, then, washed with 80 mL 1 M HCl (2x40 mL). The organic phase was evaporated and the resulting crude product was purified by flash column chromatography. (EA/DCM, increasing gradient). The desired product was isolated as colorless oil (2.75 g, 0.12 mmol, 53 %)

$^1\text{H-NMR}$ (400 MHz, CDCl_3): δ = 7.99 (s, 1H), 4.2 (s, 2H), 4.03 (dd, J = 5.5, 2.5 Hz, 2H), 3.32 (q, J = 7.1 Hz, 2H), 3.13 (q, J = 7.1 Hz, 2H), 2.15 (t, J = 2.5 Hz, 1H), 1.11 (t, J = 7 Hz, 3H), 1.07 (t, J = 7.27 Hz, 3H). $^{13}\text{C-NMR}$ (100 MHz, CDCl_3): δ = 169.29, 167.67, 79.34, 71.65, 71.02, 69.52, 40.7, 40.31, 28.28, 14, 12.74. **HRMS** (ESI) exact mass calc. for $\text{C}_{11}\text{H}_{18}\text{N}_2\text{O}_3$: m/z 227.14, found: m/z 227.1 $[\text{M}+\text{H}]^+$

Methyl 2-(2-oxo-2-(prop-2-yn-1-ylamino)ethoxy)acetate **A5**

A solution of 2.96 g **AE** (20 mmol, 1 eq), 1.6 mL SOCl_2 (22 mmol, 1.1 eq) and 3 drops of DMF in 80 mL DCM was stirred for 3 hours at r.t. Then, the volatile components were removed by vacuum distillation and the residue was dissolved in 40 mL DCM. In second flask, a solution of 1.4 mL propargylamine (22 mmol, 1.1 eq) and 2.8 mL triethylamine (22 mmol, 1.1 eq) in 40 mL was prepared. To this solution the distillation residue was added dropwise over 1 hour. The now turbid solution was stirred for 2 hours at r.t. and, then, washed with 80 mL 1 M HCl (2x40 mL). The organic phase was evaporated and the resulting crude product was purified by flash column chromatography. (EA/CH, increasing gradient). The desired product was isolated as colorless oil (1.96 g, 10.6 mmol, 53 %)

$^1\text{H-NMR}$ (400 MHz, CDCl_3): δ = 7.1 (s, 1H), 4.13 (s, 2H), 4.04 (d, J = 7.7 Hz, 2H), 4.04 (s, 2H), 3.72 (s, 3H), 2.11 (t, J = 2.6 Hz, 1H) **$^{13}\text{C-NMR}$** (100 MHz, CDCl_3): δ = 170.05, 168.49, 79.1, 71.44 (d, J = 2.3 Hz), 70.93 (t, J = 3.6 Hz), 68.46 (t, J = 3.4 Hz), 52 (q, J = 3.8 Hz), 28.38 (t, J = 2.9 Hz). **R_f** (EA-CH, 5/5) = 0.25. **HRMS** (ESI) exact mass calc. for $\text{C}_8\text{H}_{11}\text{NO}_4$: m/z 186.07, found: m/z 186 $[\text{M}+\text{H}]^+$

4-(prop-2-yn-1-yl)morpholine-3,5-dione **AP**

This product was obtained following the synthesis for **A4** or **A5** on **APA**. After flash column chromatography (EA/CH, increasing gradient), the product was isolated as colorless solid.

$^1\text{H-NMR}$ (400 MHz, CDCl_3): δ = 4.5 (d, J = 2.6 Hz, 2H), 4.41 (s, 4H), 2.56 (t, J = 2.5 Hz, 1H) **$^{13}\text{C-NMR}$** (100 MHz, CDCl_3): δ = 169, 77.47, 70.63, 67.09, 26.82. **R_f** (EA-CH, 6/4) = 0.76. **HRMS** (ESI) exact mass calc. for $\text{C}_7\text{H}_7\text{NO}_3$: m/z 154.05, found: m/z 154.1 $[\text{M}+\text{H}]^+$

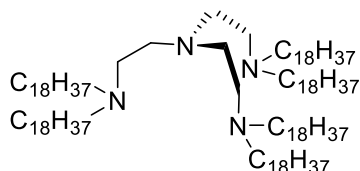
[Cu(PPh₃)₃]Br C1

C1 was synthesized as described in literature.²⁹⁴ PPh₃ (6 g, 22.9 mmol, 4 eq) was dissolved in hot (85°C) methanol (100 mL). To this solution, CuBr₂ (1.24 g, 5.6 mmol, 1 eq) was added in portions leading to a white precipitate. Afterwards, the suspension was left to cool to r.t. and filtered. After washing with ethanol and diethyl ether and subsequent drying in vacuum, **C1** was obtained as a white solid (5.22 g, 77%). The presence of the desired product was verified by FTIR.²⁹⁵

IR (neat, cm⁻¹): 3047, 3028, 3006, 1968, 1896, 1826, 1773, 1671, 1605, 1586, 1576, 1479, 1434, 1335, 1315, 1286, 1187, 1153, 1091, 1070, 1029, 1000, 842, 741, 691, 618, 517, 506, 480, 437, 427, 412, 401

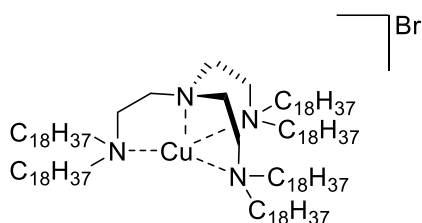
Synthesis of [Cu(C₁₈tren)]Br C2

Synthesis was adapted from literature.²⁹⁶

Tris(2(dioctadecylamino)ethyl)amine C₁₈tren

To acetonitrile (50 mL) Tris(2-aminoethyl)amine (0.5 g, 3.42 mmol, 1 eq) and K₂CO₃ (5.25 g, 37.5 mmol, 11 eq) were added. After the addition of Iodoctadecan (8 g, 20.9 mmol, 6 eq) the solution was refluxed under agitation. After 48 h the suspension was cooled to 0 °C and filtrated. The solid residue was washed with ice-cooled acetonitrile (3 x 30 mL). The filtrate was washed with cold water (3 x 20 mL) and methanol (2 x 40 mL). The filtrate was dried over MgSO₄ and recrystallized in 1,4-dioxane. After column chromatography on silica gel (DCM/EtOAc (1/1)), the product was isolated as white solid (1.79 g, 1.1 mmol, 32%)

¹H-NMR (400 MHz, CDCl₃): δ = 2.8-2.36 (m, 24H), 1.73 (m, 12H), 1.47-1.23 (m, 192H), 0.88 (t, *J* = 6.79 Hz, 18H). **¹³C-NMR** (100 MHz, CDCl₃): δ = 54.86, 53.34, 52.3, 31.95, 29.75, 29.39, 27.67, 27.11, 22.71, 14.13. **HRMS** (ESI) exact mass calc. for C₁₁₄H₂₃₄N₄: *m/z* 1659.18, found: *m/z* 1661.8 [M+2H]²⁺. **IR** (neat, cm⁻¹): 2916, 2849, 1467, 1377, 1297, 1283, 1094, 1074, 1034, 890, 719

[Cu(C₁₈tren)]Br C2

C₁₈tren and CuBr were added to degassed 1,4-Dioxane under Ar atmosphere and the solution was stirred at 60 °C during 3 h. Afterwards, the solution was left to cool to r.t. and filtrated. The product was obtained as greenish solid after drying under dynamic vacuum.

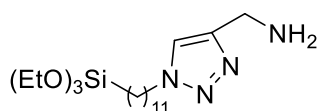
¹H-NMR (400 MHz, CDCl₃): δ = 1.8-1.1 (m, 192H), 0.88 (t, *J* = 5.77 Hz, 18H). **¹³C-NMR** (100 MHz, CDCl₃): δ = 31.95, 29.7, 29.4, 28.26, 22.72, 14.13. **IR** (neat, cm⁻¹): 2916, 2849, 1467, 1377, 1289, 1254, 1123, 1084, 888, 875, 720. **HRMS** (ESI) exact mass calc. for C₁₁₄H₂₃₄N₄BrCu: *m/z* 1803.5, found: *m/z* 1803.7 [M+H]⁺

General procedure of CuAAC using [Cu(PPh₃)₃]Br C1

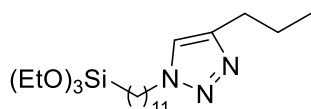
Under Ar atmosphere, azido precursor **4** (1.88 g, 5 mmol, 1 eq) and the alkyne precursor (7.5 mmol, 1.5 eq) were added to THF/NEt₃ (1:1) (10 mL). **C1** (0.047 g, 0.05 mmol, 0.01 eq) was added and mixture was stirred at 40 °C during 24 h. The solution was evaporated at 10 mbar and 50 °C and the residue was dissolved in pentane (10 mL). The suspension was filtered over 20 mL compacted celite® using approximately 200 mL pentane and the solvent evaporated to obtain the desired product as viscous oil in the yields reported in **Table 3**.

General procedure of CuAAC using $[Cu(C_{18}stren)]Br$ **C2**

Under Ar atmosphere, **C2** (0.036 g, 0.02 mmol, 0.01 eq) was dissolved in toluene (12 mL). azido precursor **4** (0.752 g, 2 mmol, 1 eq) and the alkyne precursor (3 mmol, 1.5 eq) were added and the solution was stirred at 40 °C for 5 h. The solution was evaporated at 10 mbar and 50 °C and the residue was dissolved in anhydrous ethanol (10 mL). The suspension was left to precipitate at -4 °C overnight and filtered using 0.2 μ m syringe filters. After the evaporation of ethanol the desired product was obtained as viscous oil in the yields reported in **Table 3**.

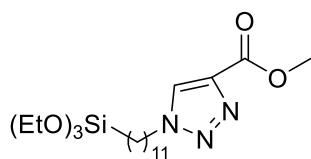
(1-(11-(triethoxysilyl)undecyl)-1H-1,2,3-triazol-4-yl)methanamine **P1**

¹H-NMR (400 MHz, CDCl₃): δ = 7.46 (s, 1H), 4.28 (t, J = 6.72 Hz, 2H), 3.77 (q, J = 6.96 Hz, 6H), 1.85 (t, J = 6.72 Hz, 2H), 1.4-1.15 (m, 27H), 0.58 (t, J = 8.06 Hz, 2H). **¹³C-NMR** (100 MHz, CDCl₃): δ = 58.26, 58.23, 58.19, 50.54, 33.12, 31.87, 30.1, 29.65, 29.41, 29.28, 29.16, 28.97, 26.47, 26.35, 22.7, 18.25, 10.33. **HRMS** (ESI) exact mass calc. for C₂₀H₄₂N₄O₃Si: m/z 415.3, found: m/z 415.3 [M+H]⁺

4-propyl-1-(11-(triethoxysilyl)undecyl)-1H-1,2,3-triazole **P2**

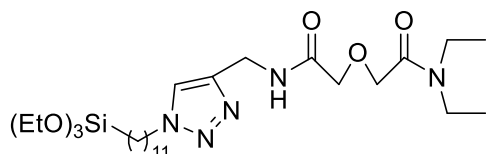
¹H-NMR (400 MHz, CDCl₃): δ = 7.24 (s, 1H), 4.29 (t, J = 7.28 Hz, 2H), 3.8 (q, J = 7 Hz, 6H), 2.68 (t, J = 7.58 Hz, 2H), 1.86 (t, J = 7 Hz, 2H), 1.68 (sex, J = 7.46 Hz, 2H), 1.4-1.15 (m, 27H), 0.61 (t, J = 8.14 Hz, 2H). **¹³C-NMR** (100 MHz, CDCl₃): δ = 148.13, 120.37, 58.22, 50.1, 33.11, 30.3, 29.44, 29.4, 29.31, 29.15, 28.95, 27.65, 26.44, 22.69, 18.24, 13.72, 10.32. **HRMS** (ESI) exact mass calc. for C₂₂H₄₅N₃O₃Si: m/z 428.33, found: m/z 428.33 [M+H]⁺

Methyl 1-(11-(triethoxysilyl)undecyl)-1H-1,2,3-triazole-4-carboxylate P3



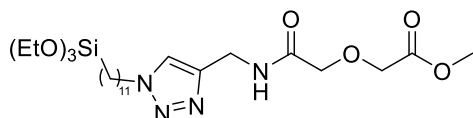
¹H-NMR (400 MHz, CDCl₃): δ = 8.07 (s, 1H), 4.39 (t, *J* = 7.22 Hz, 2H), 3.94 (s, 3H), 3.8 (q, *J* = 7 Hz, 6H), 1.91 (t, *J* = 7.06 Hz, 2H), 1.4-1.15 (m, 27H), 0.61 (t, *J* = 8.16 Hz, 2H). **¹³C-NMR** (100 MHz, CDCl₃): δ = 161.24, 127.25, 58.26, 52.16, 50.71, 33.14, 30.12, 29.45, 29.41, 29.3, 29.18, 28.9, 26.34, 22.72, 18.27, 10.35.

N,N-diethyl-2-(2-oxo-2-(((1-(11-(triethoxysilyl)undecyl)-1H-1,2,3-triazol-4-yl)methyl)amino)ethoxy)acetamide P4



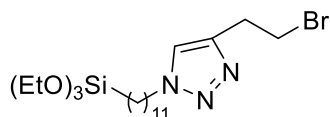
¹H-NMR (400 MHz, CDCl₃): δ = 8.01 (s, 1H), 7.54 (s, 1H), 4.56 (d, *J* = 5.8 Hz, 2H), 4.27 (t, *J* = 7.3 Hz, 2H), 4.21 (s, 2H), 4.08 (s, 2H), 3.78 (q, *J* = 7 Hz, 6H), 3.34 (q, *J* = 7.15 Hz, 2H), 3.17 (q, *J* = 7.15 Hz, 2H), 1.85 (t, *J* = 6.82 Hz, 2H), 1.4-1.15 (m, 25H), 0.61 (t, *J* = 8.14 Hz, 2H). **¹³C-NMR** (100 MHz, CDCl₃): δ = 169.42, 167.51, 71.26, 69.31, 57.92, 50.25, 40.62, 40.08, 32.81, 29.34, 29.18, 29.12, 29.03, 28.88, 28.68, 22.4, 17.97, 13.85, 13.78, 12.58, 10.03. **HRMS** (ESI) exact mass calc. for C₂₈H₅₅N₅O₆Si: *m/z* 586.4, found: *m/z* 586.4 [M+H]⁺

Methyl 2-(2-oxo-2-(((1-(11-(triethoxysilyl)undecyl)-1H-1,2,3-triazol-4-yl)methyl)amino)ethoxy)acetate P5



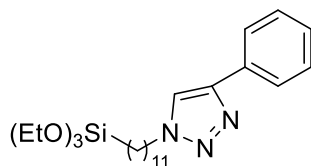
¹H-NMR (400 MHz, CDCl₃): δ = 7.35 (s, 1H), 7.35 (s, 1H), 4.58 (d, *J* = 5.9 Hz, 2H), 4.31 (t, *J* = 7.1 Hz, 2H), 4.15 (s, 2H), 4.09 (s, 2H), 3.81 (q, *J* = 7 Hz, 6H), 3.75 (s, 3H), 1.88 (t, *J* = 7.5 Hz, 2H), 1.45-1.15 (m, 25H), 0.62 (t, *J* = 8.2 Hz, 2H). **¹³C-NMR** (100 MHz, CDCl₃): δ = 170.05, 168.93, 71.07, 68.54, 58.27 (t, 3.3 Hz), 52.11, 52.07, 50.42, 34.43, 33.17, 30.25, 29.68, 29.51, 29.46, 29.36, 29.21, 28.99, 26.5, 22.74, 18.29, 10.37. **HRMS** (ESI) exact mass calc. for C₂₅H₄₈N₄O₇Si: *m/z* 545.33, found: *m/z* 545.3 [M+H]⁺

4-(bromoethyl)-1-(11-(triethoxysilyl)undecyl)-1H-1,2,3-triazole P7

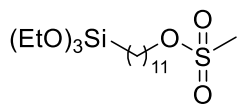


¹H-NMR (400 MHz, CDCl₃): δ = 7.39 (s, 1H), 4.28 (t, *J* = 7.2, 2H), 3.76 (q, *J* = 6.9 Hz, 6H), 3.6 (t, *J* = 6.8 Hz, 2H), 3.24 (t, *J* = 7 Hz, 2H), 1.84 (quin, *J* = 6.8 Hz, 2H), 1.4-1.15 (m, 27H), 0.57 (t, *J* = 8.1 Hz, 2H).

4-phenyl-1-(11-(triethoxysilyl)undecyl)-1H-1,2,3-triazole P8

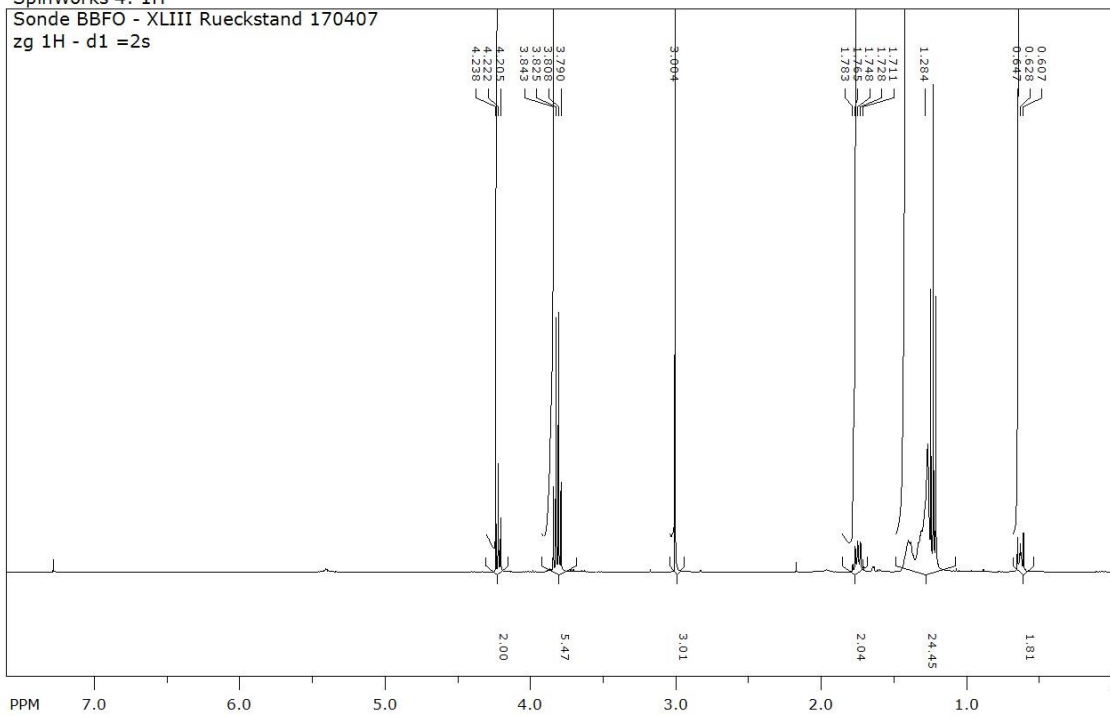


¹H-NMR (400 MHz, CDCl₃): δ = 7.82 (d, *J* = 7.28 Hz, 2H), 7.73 (s, 1H), 7.41 (t, *J* = 7.52 Hz, 2H), 7.31 (t, *J* = 7.36 Hz, 2H), 4.37 (t, *J* = 7.22 Hz, 2H), 3.8 (q, *J* = 6.99 Hz, 6H), 1.93 (t, *J* = 4.56 Hz, 2H), 1.4-1.15 (m, 27H), 0.61 (t, *J* = 5.41 Hz, 2H). **¹³C-NMR** (100 MHz, CDCl₃): δ = 147.66, 130.71, 128.76, 128, 125.63, 119.34, 58.24, 50.39, 33.13, 30.31, 29.47, 29.42, 29.33, 29.17, 28.98, 26.46, 22.71, 18.26, 10.34.



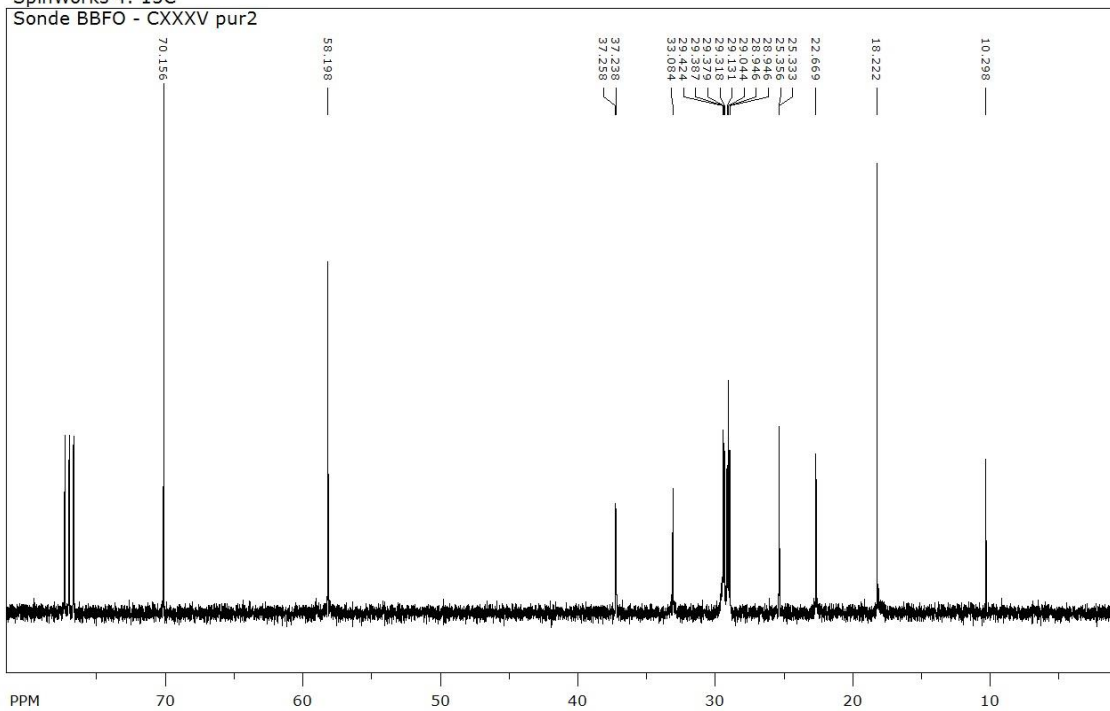
SpinWorks 4: 1H

Sonde BBFO - XLIII Rueckstand 170407
zg 1H - d1 =2s

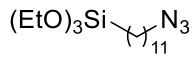


SpinWorks 4: 13C

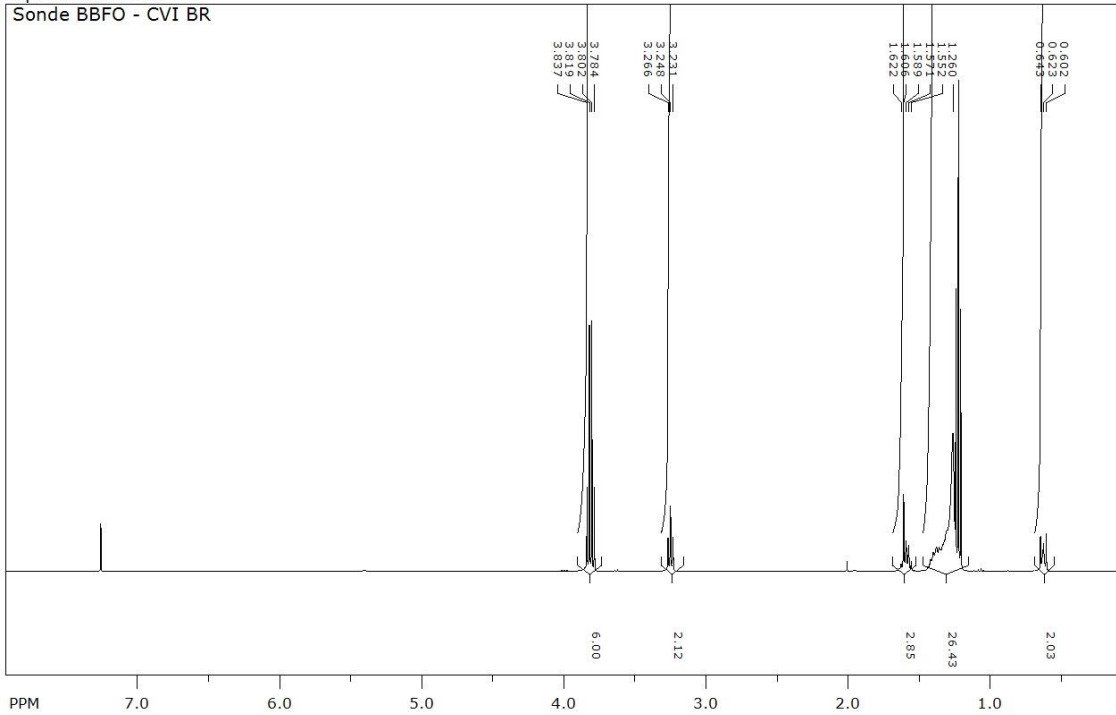
Sonde BBFO - CXXXV pur2



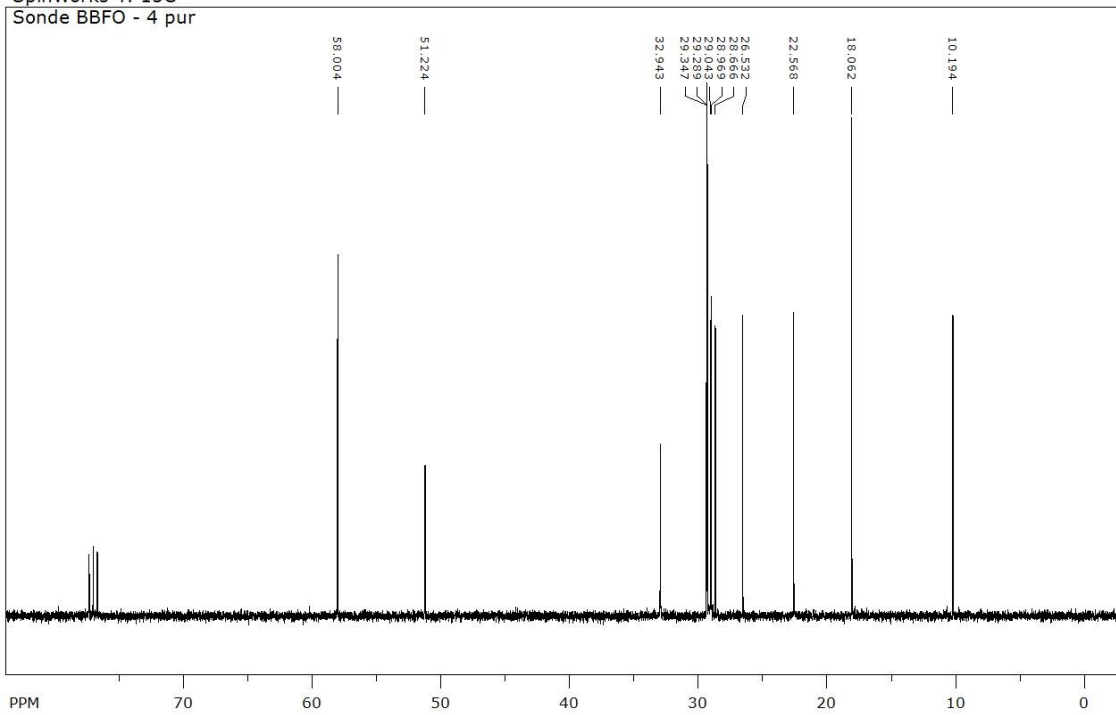
Appendix/NMR Spectra

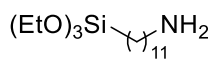


SpinWorks 4: 1H
Sonde BBFO - CVI BR

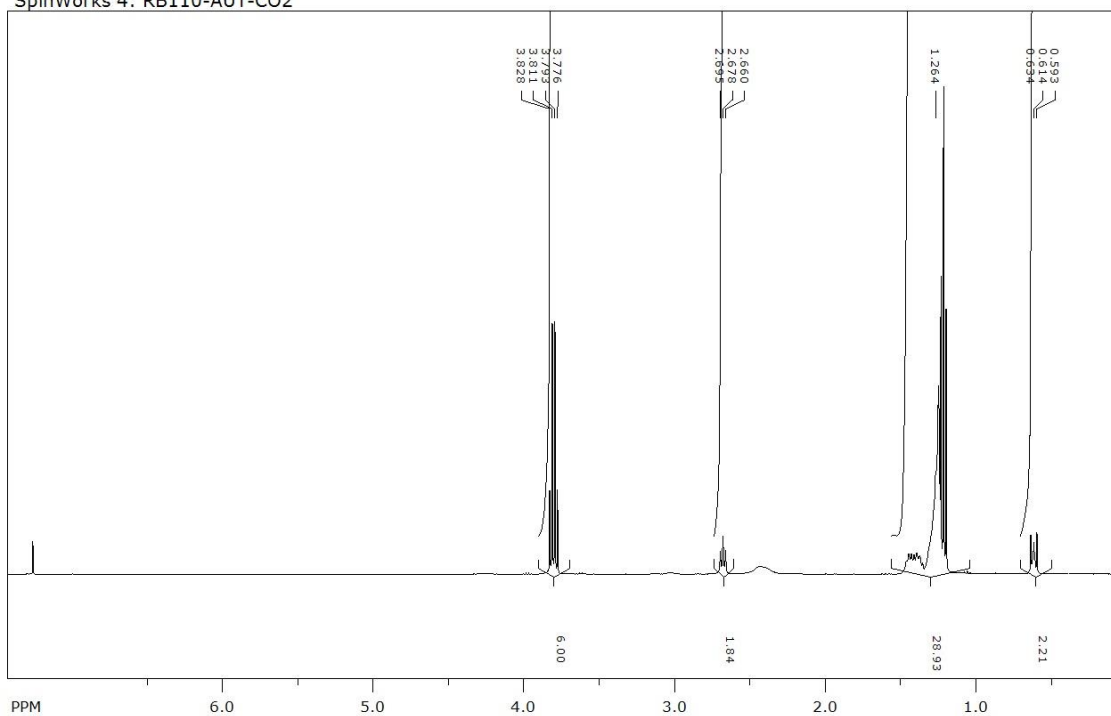


SpinWorks 4: 13C
Sonde BBFO - 4 pur

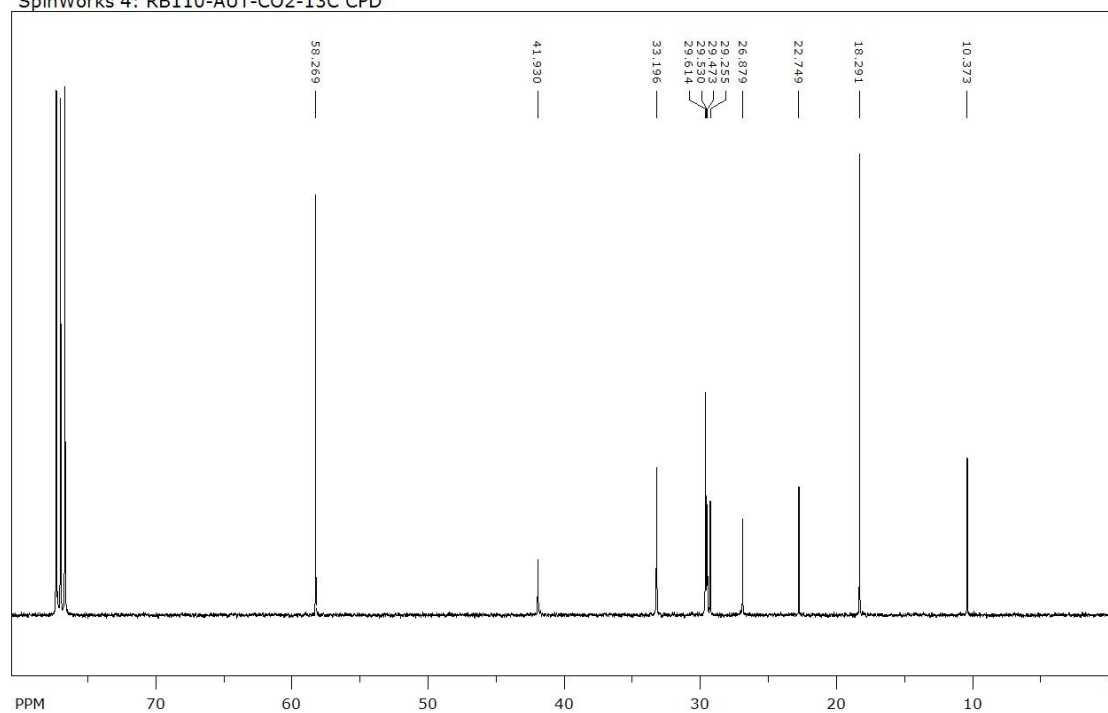




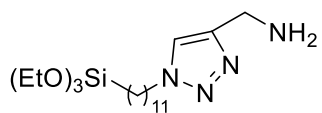
SpinWorks 4: RB110-AUT-CO2



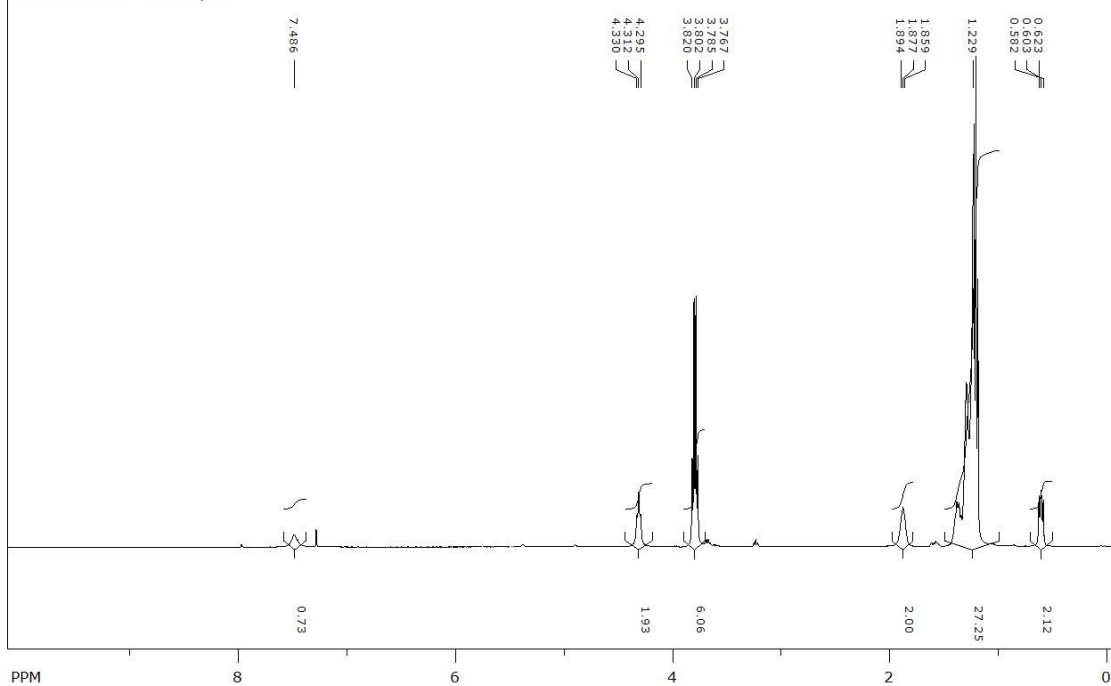
SpinWorks 4: RB110-AUT-CO2-13C CPD



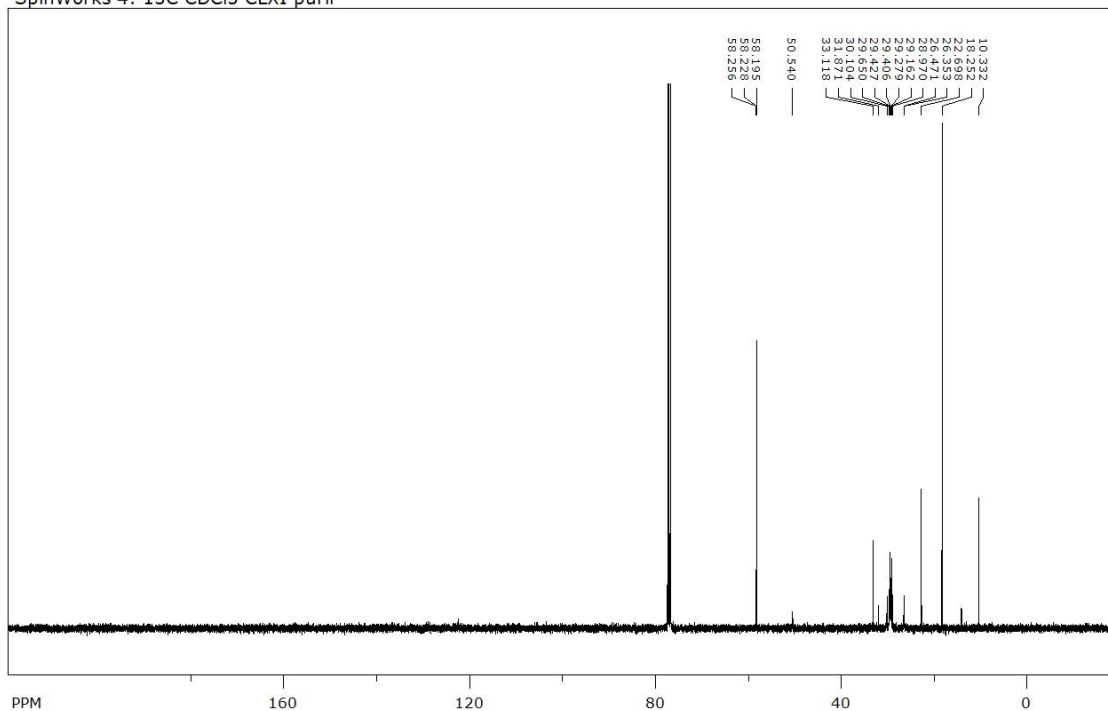
Appendix/NMR Spectra

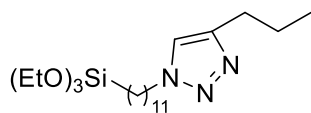


SpinWorks 4: 1H
Sonde BBFO - CXIV purif

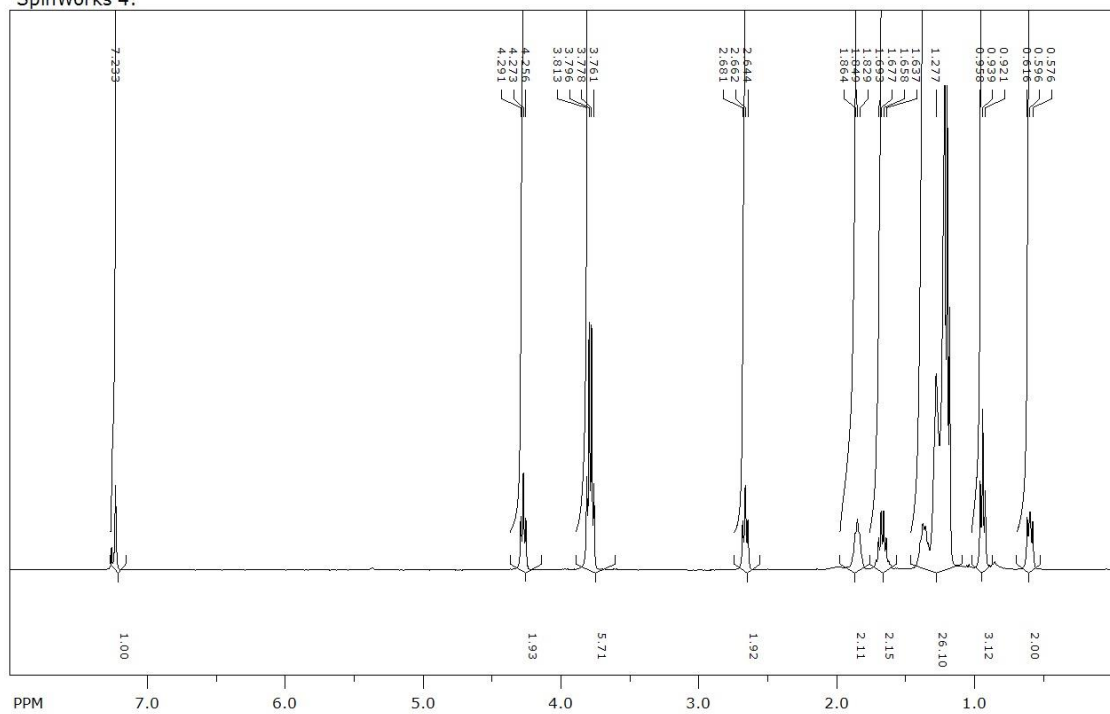


SpinWorks 4: 13C CDCl3 CLXI purif

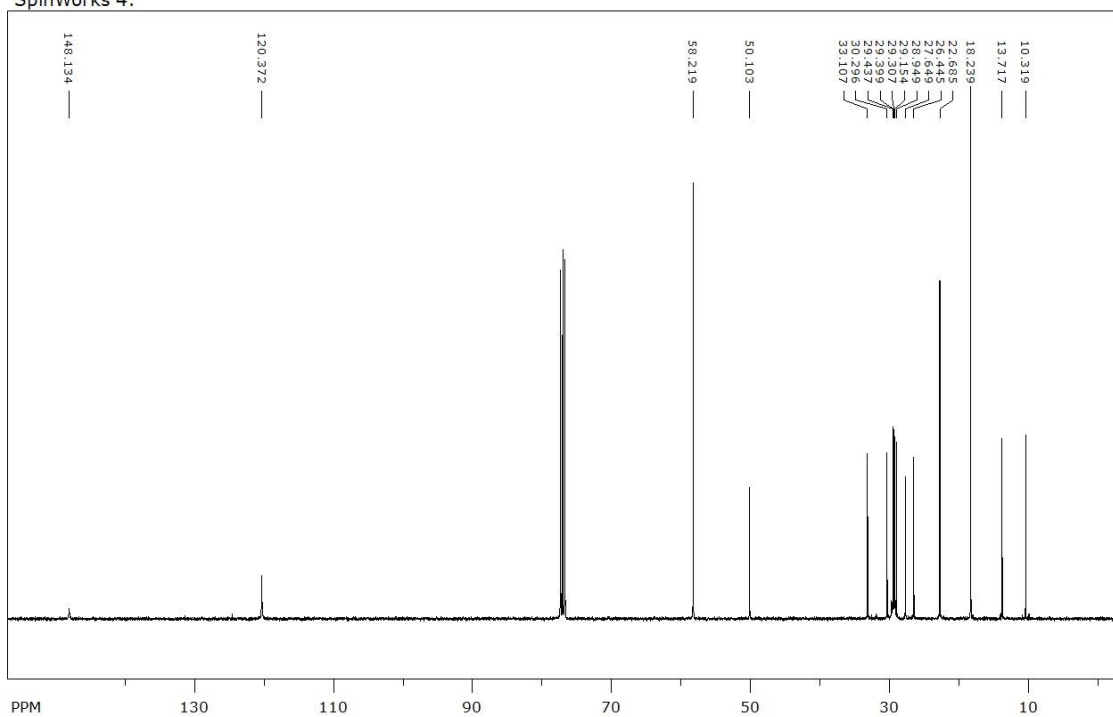




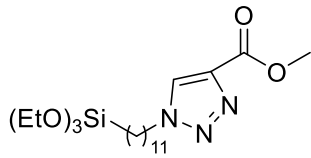
SpinWorks 4:



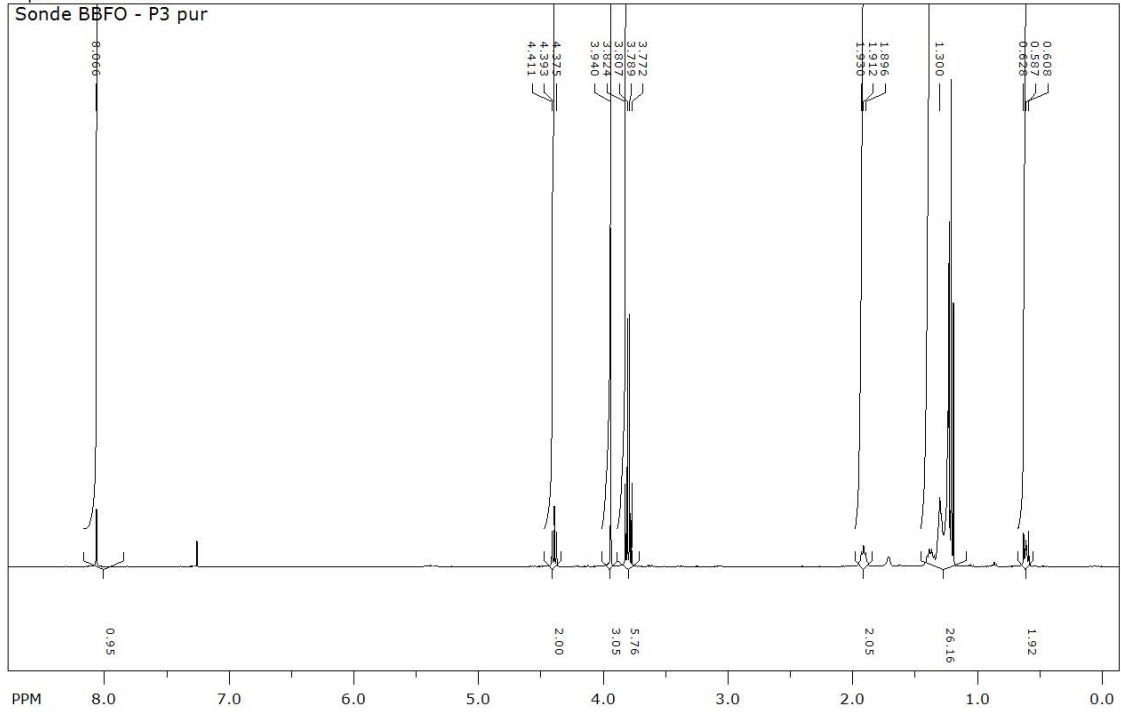
SpinWorks 4:



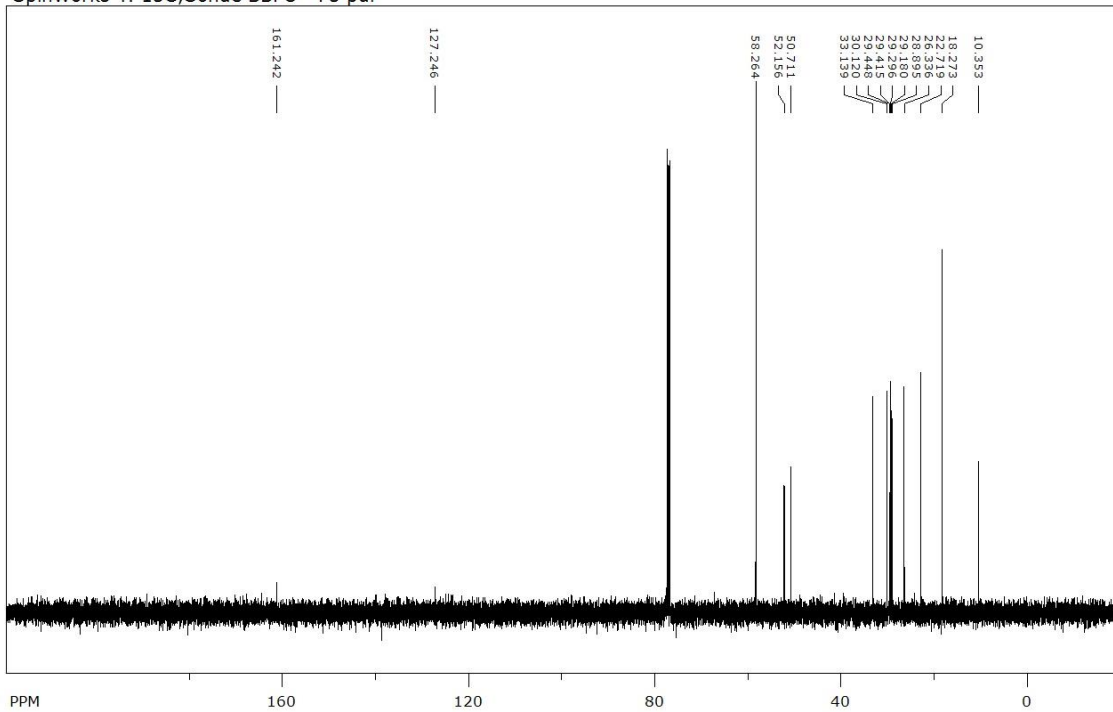
Appendix/NMR Spectra

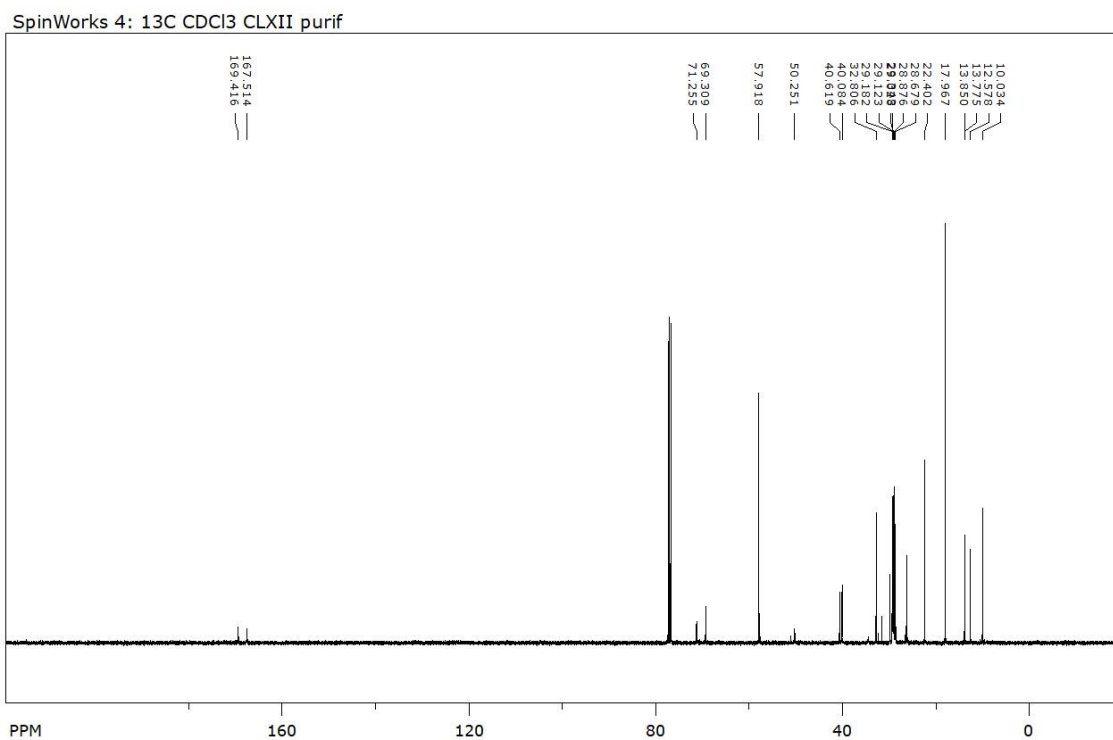
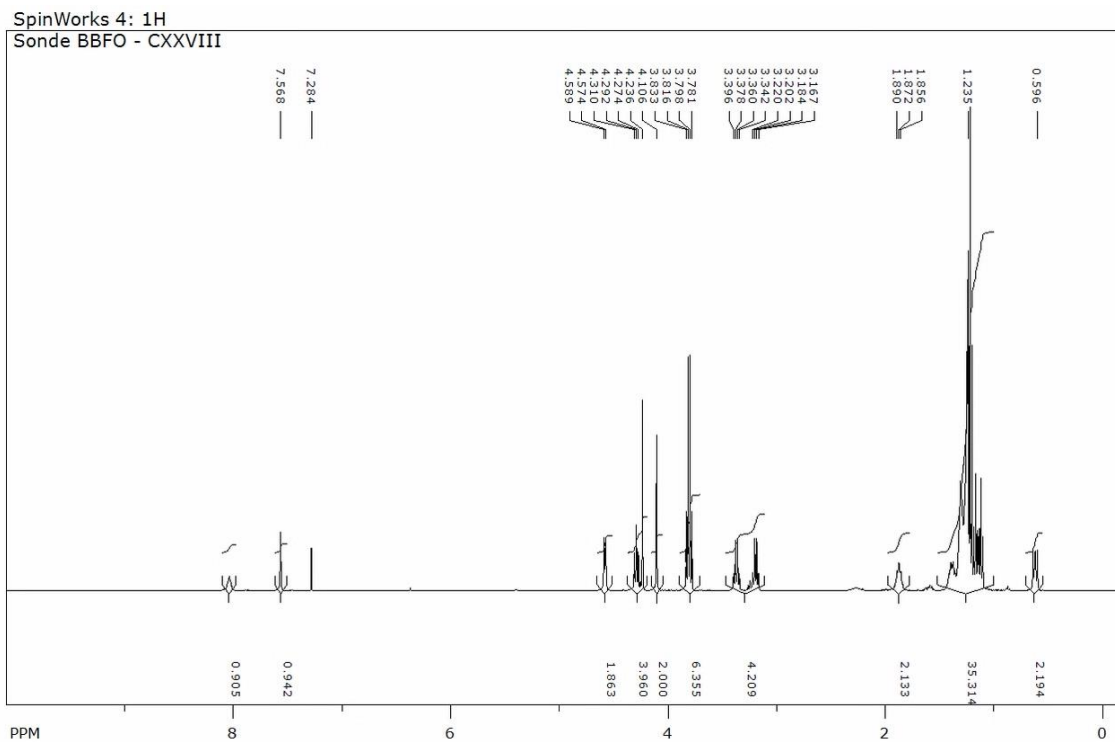
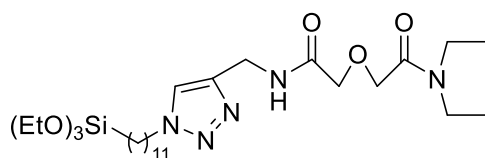


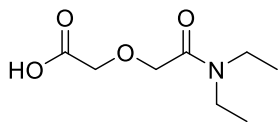
SpinWorks 4: 1H
Sonde BBFO - P3 pur



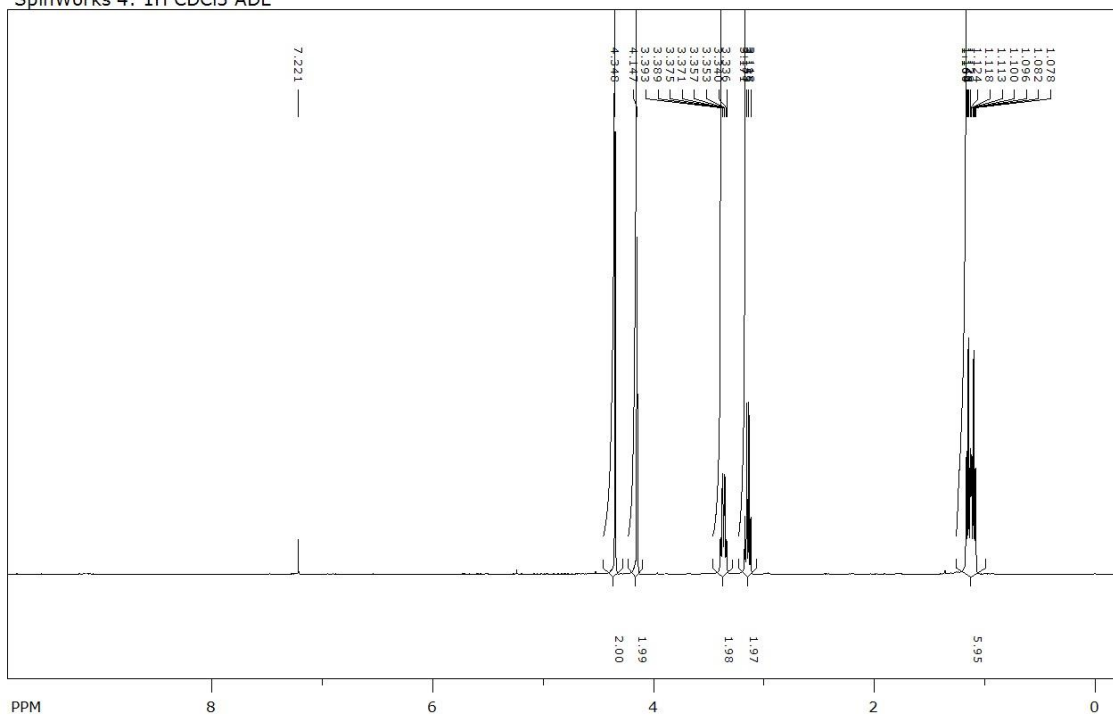
SpinWorks 4: 13C;Sonde BBFO - P3 pur



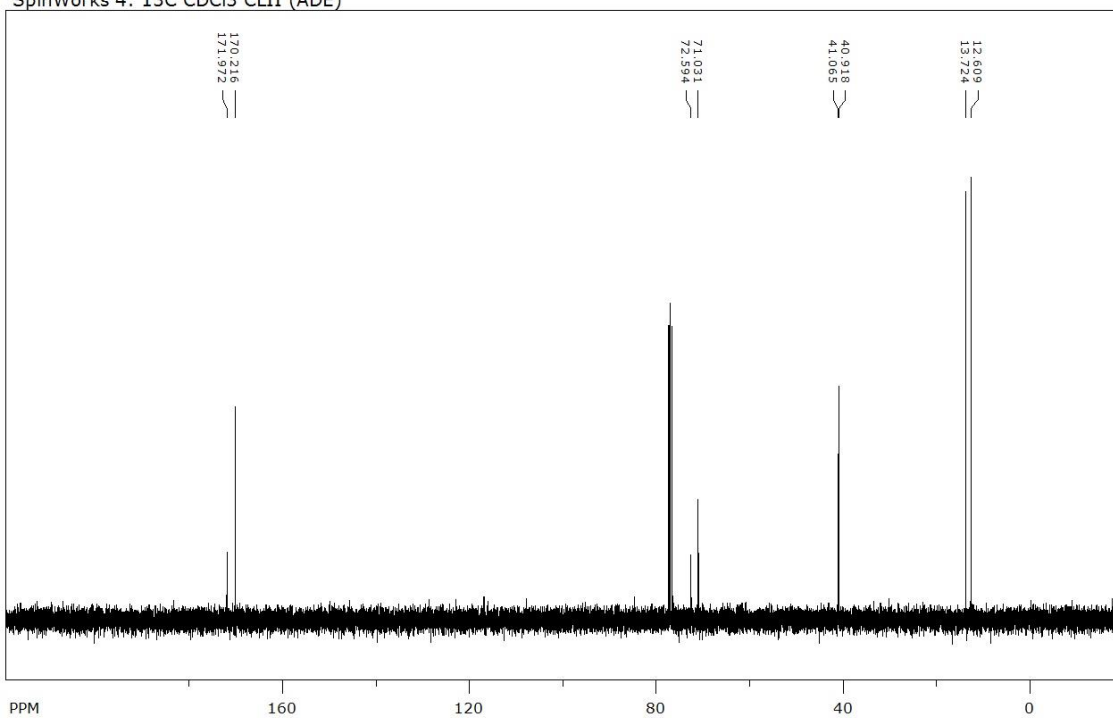




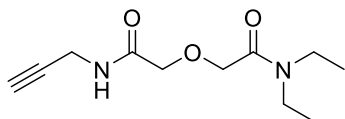
SpinWorks 4: 1H CDCl3 ADE



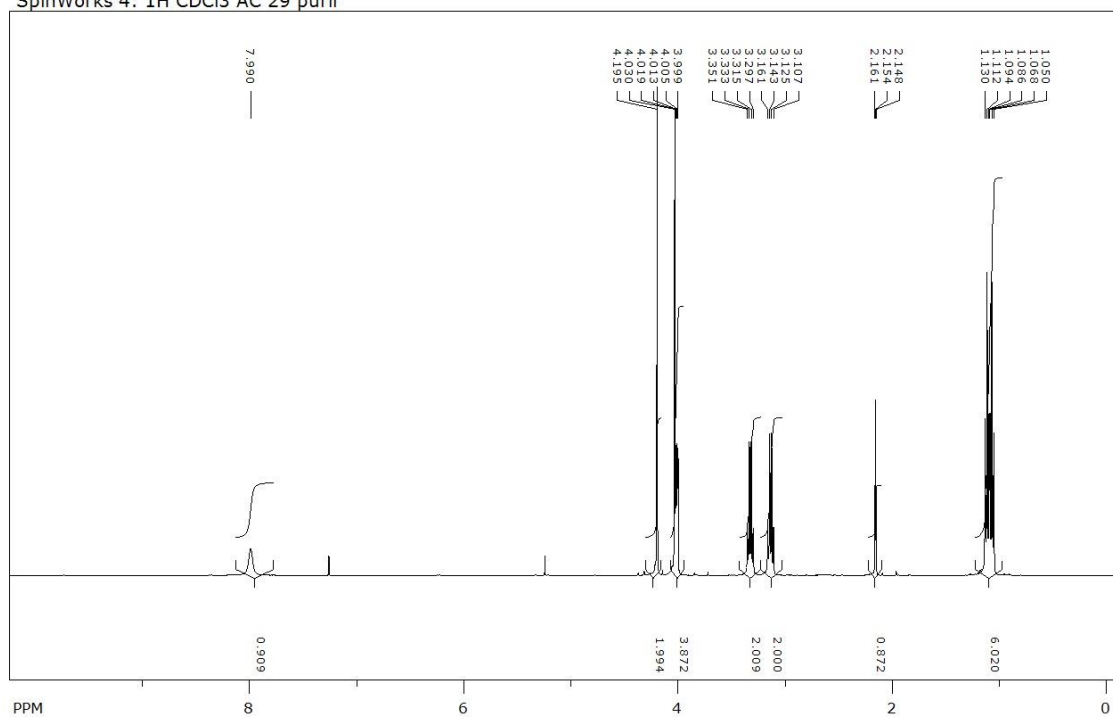
SpinWorks 4: 13C CDCl3 CLII (ADE)



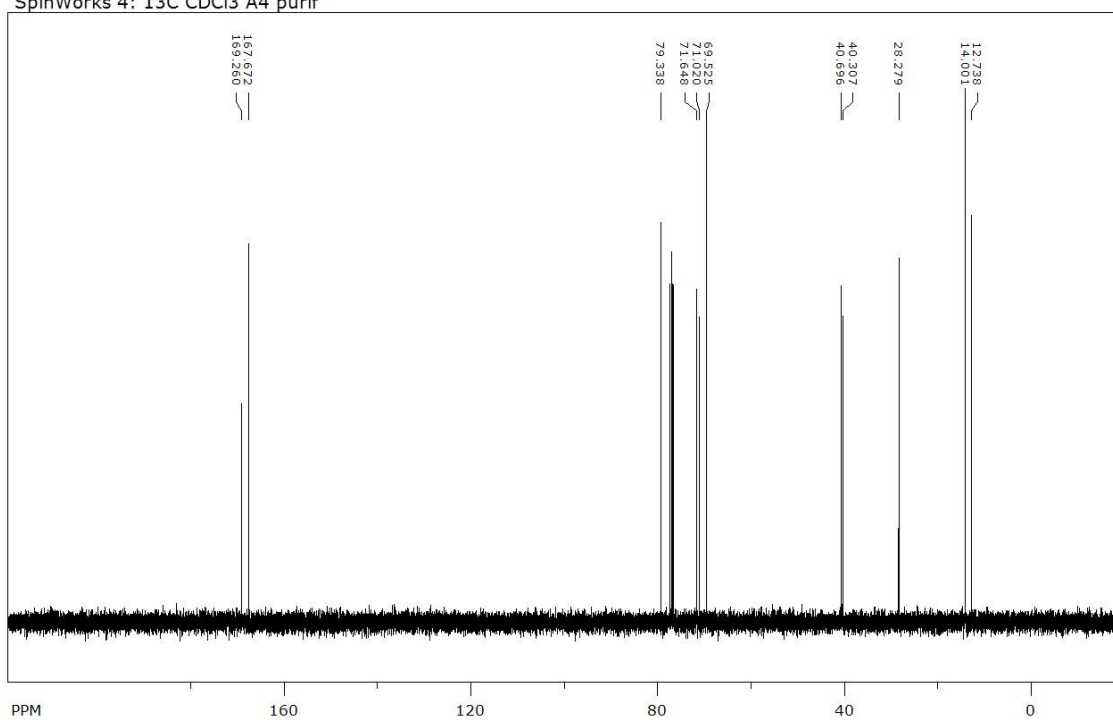
Appendix/NMR Spectra

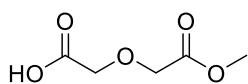


SpinWorks 4: 1H CDCl3 AC 29 purif

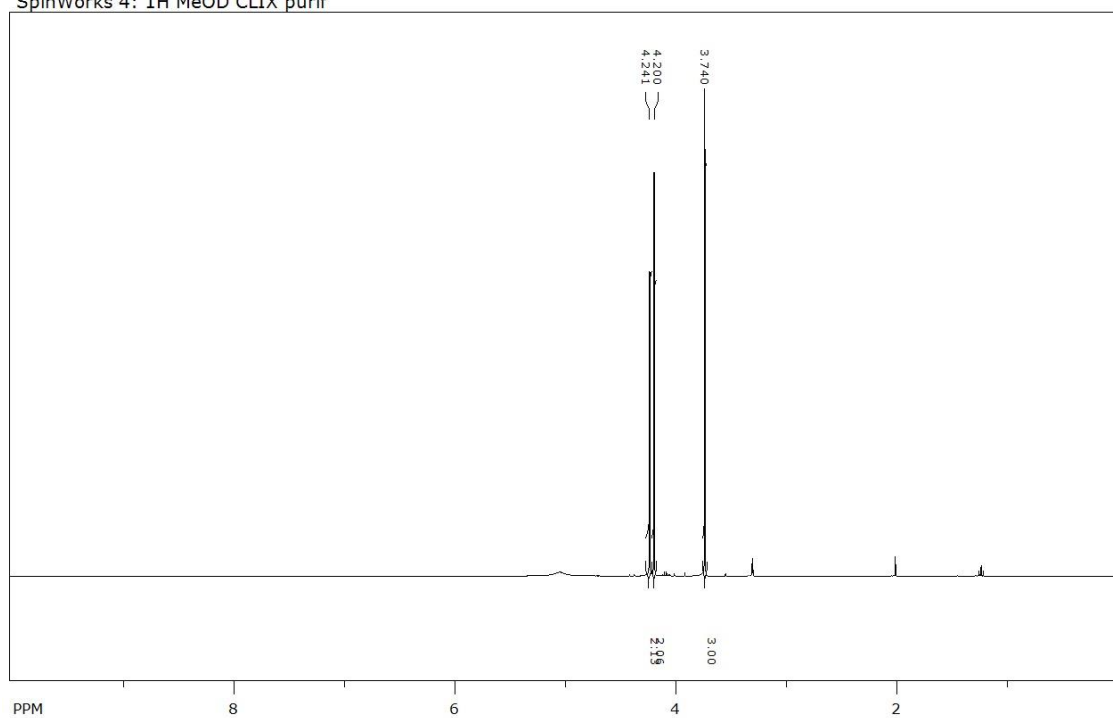


SpinWorks 4: 13C CDCl3 A4 purif

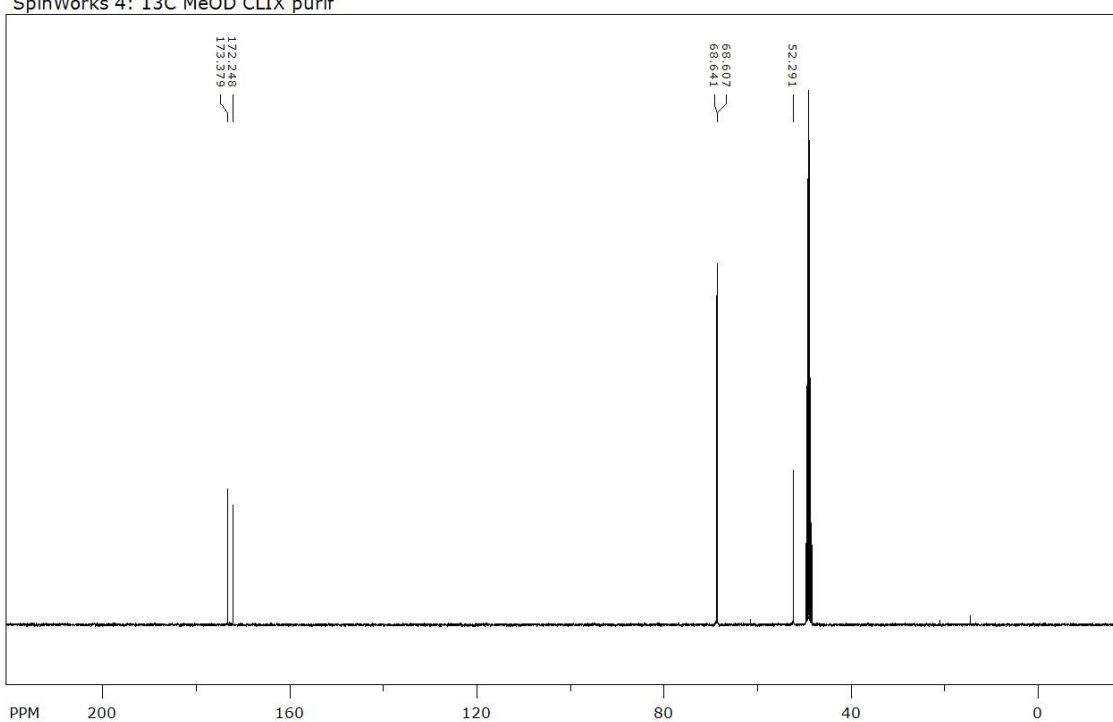




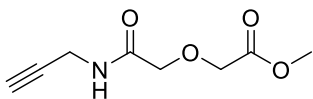
SpinWorks 4: 1H MeOD CLIX purif



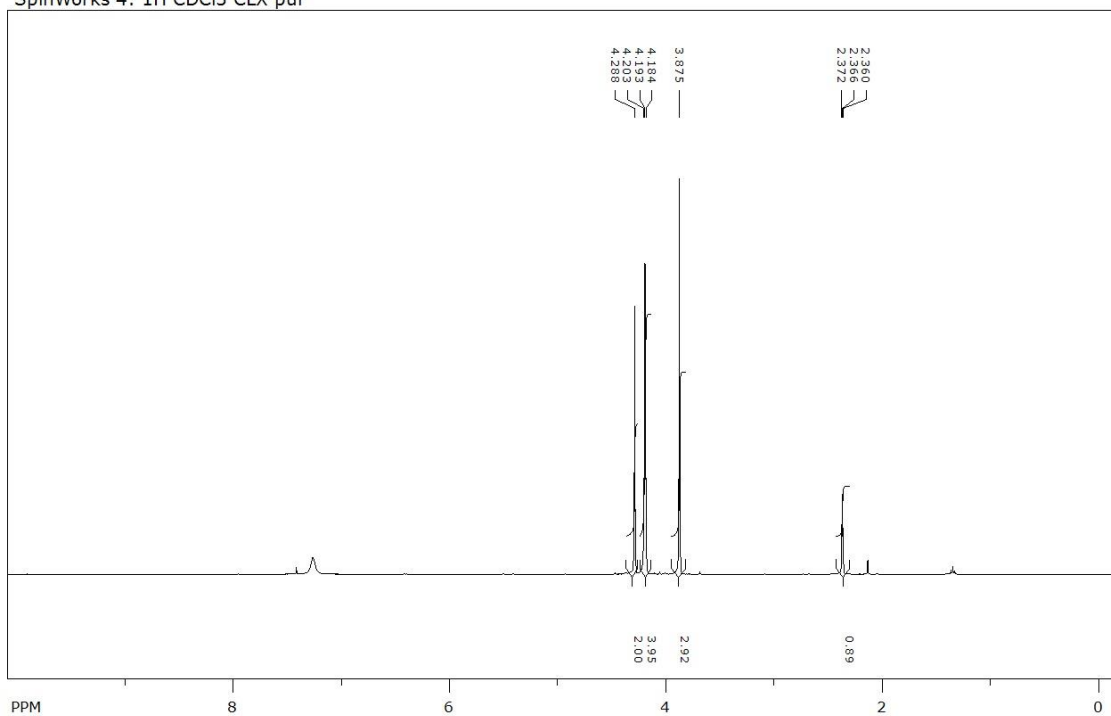
SpinWorks 4: 13C MeOD CLIX purif



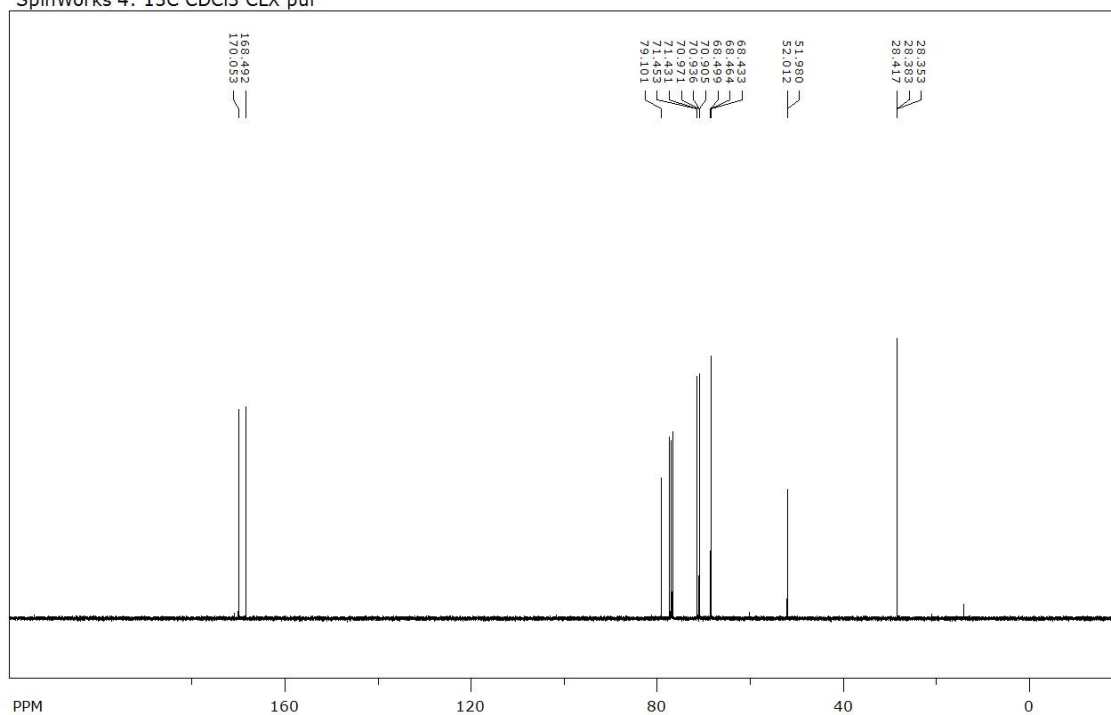
Appendix/NMR Spectra

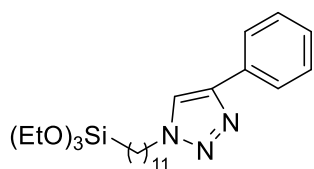


SpinWorks 4: 1H CDCl3 CLX pur

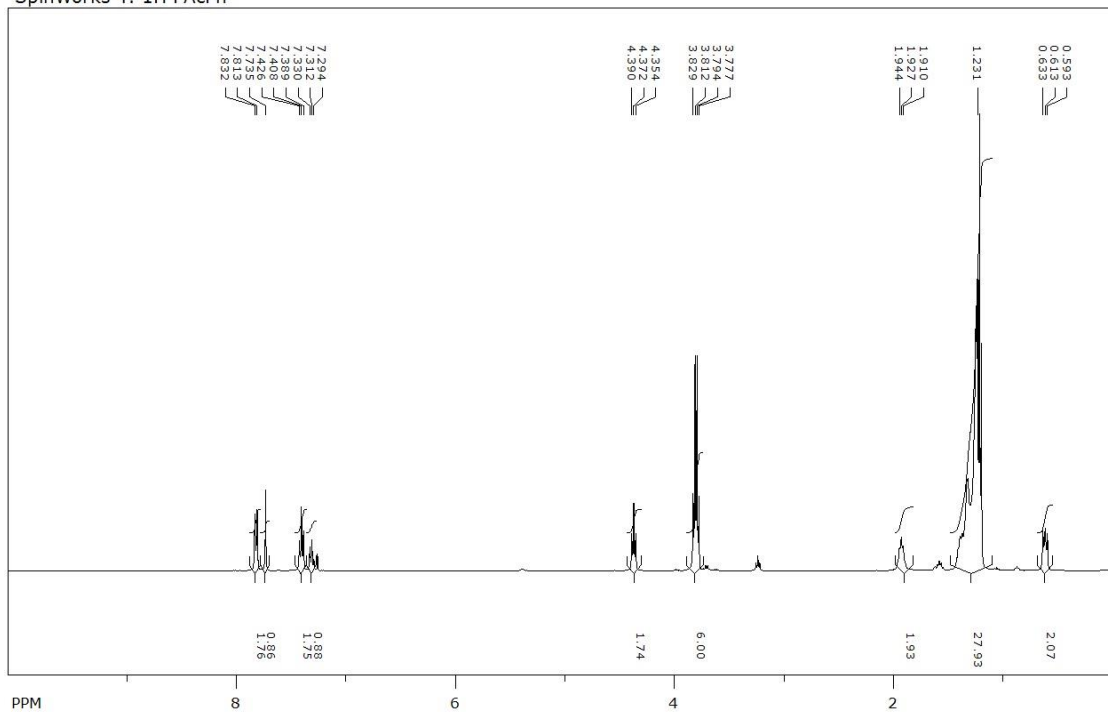


SpinWorks 4: 13C CDCl3 CLX pur

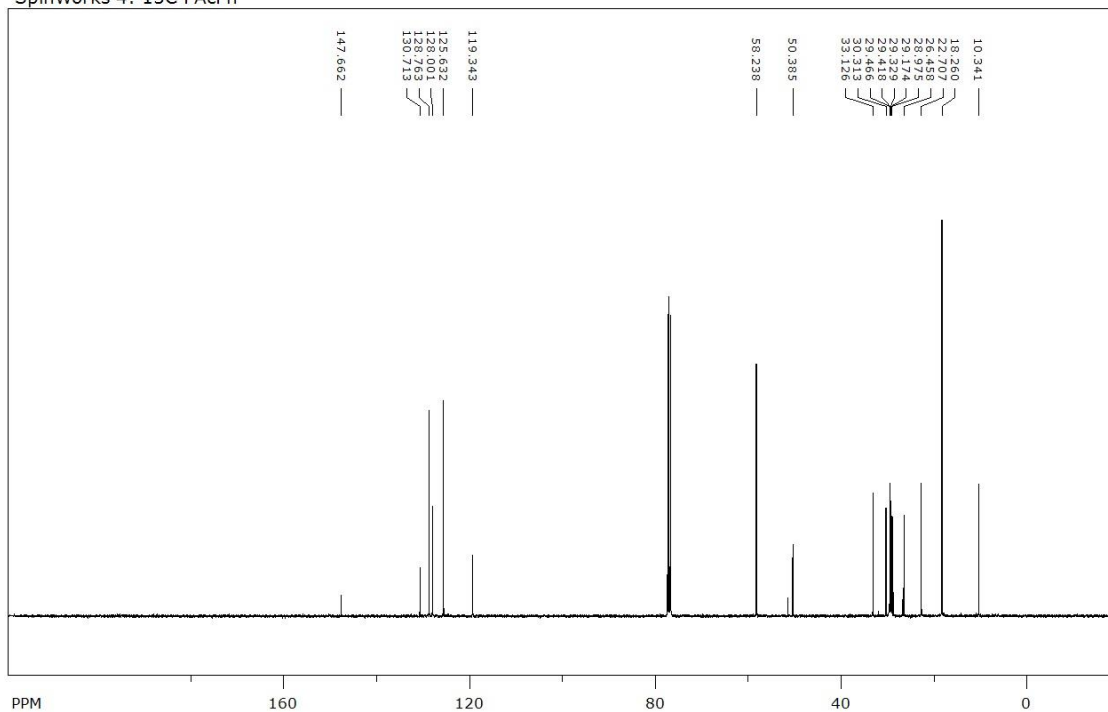




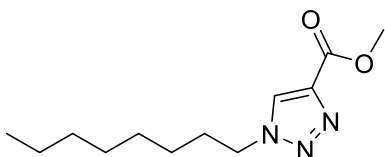
SpinWorks 4: 1H PACPh



SpinWorks 4: 13C PACPh

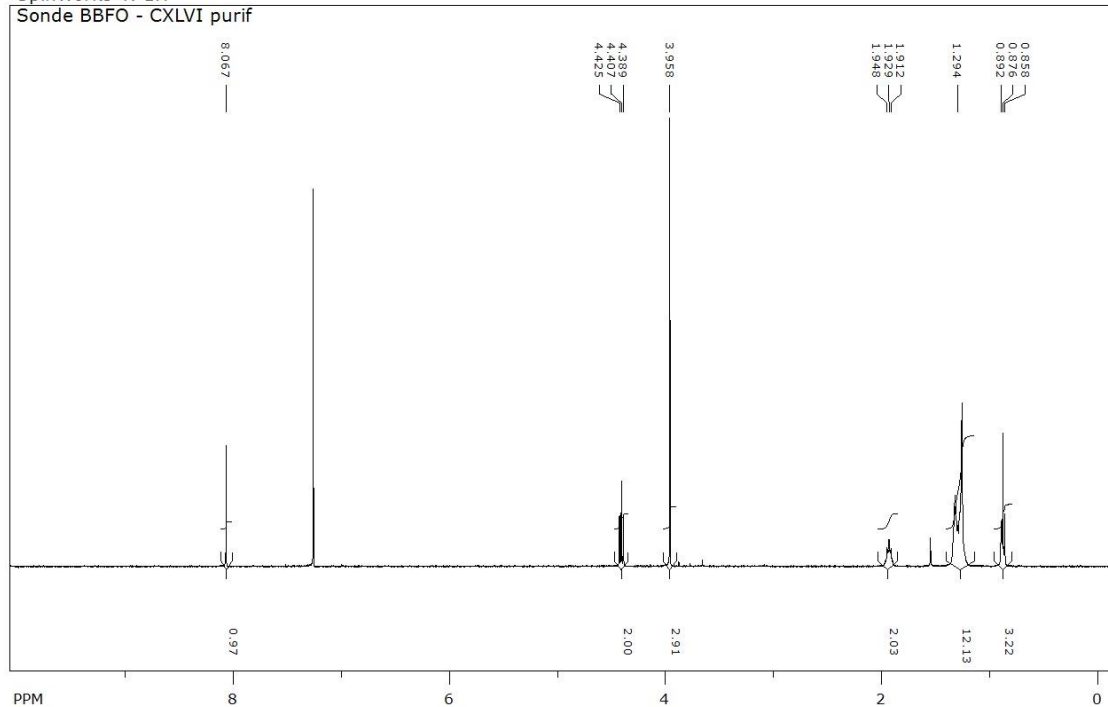


Appendix/NMR Spectra



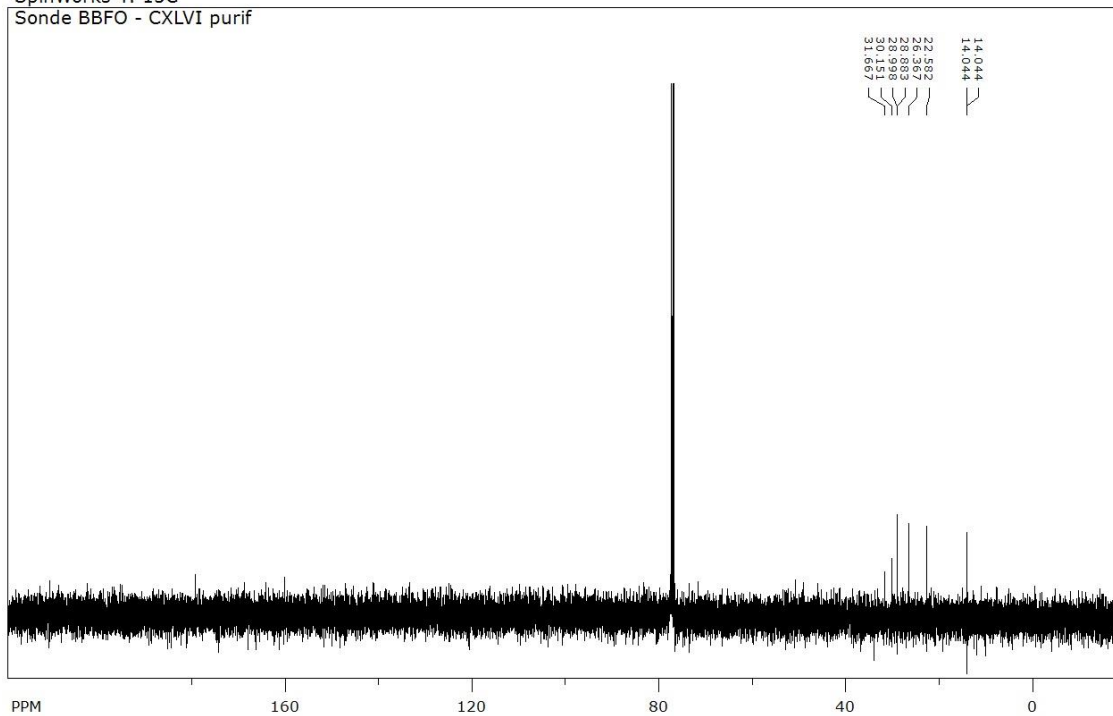
SpinWorks 4: 1H

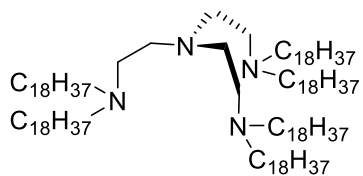
Sonde BBFO - CXLVI purif



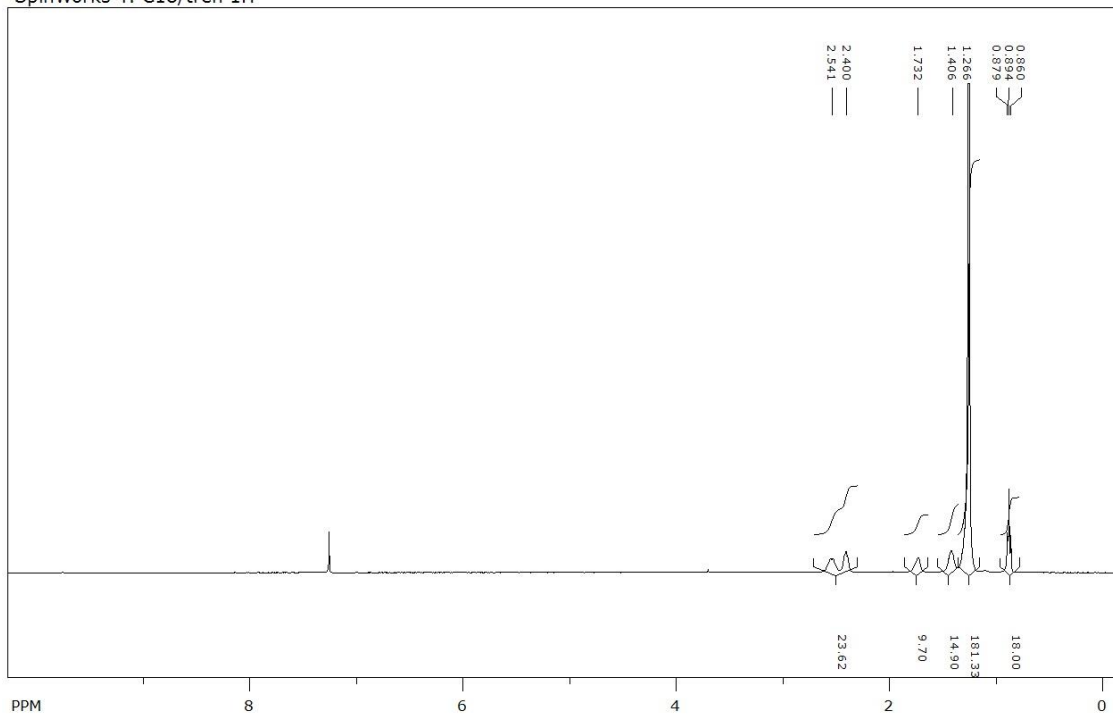
SpinWorks 4: 13C

Sonde BBFO - CXLVI purif

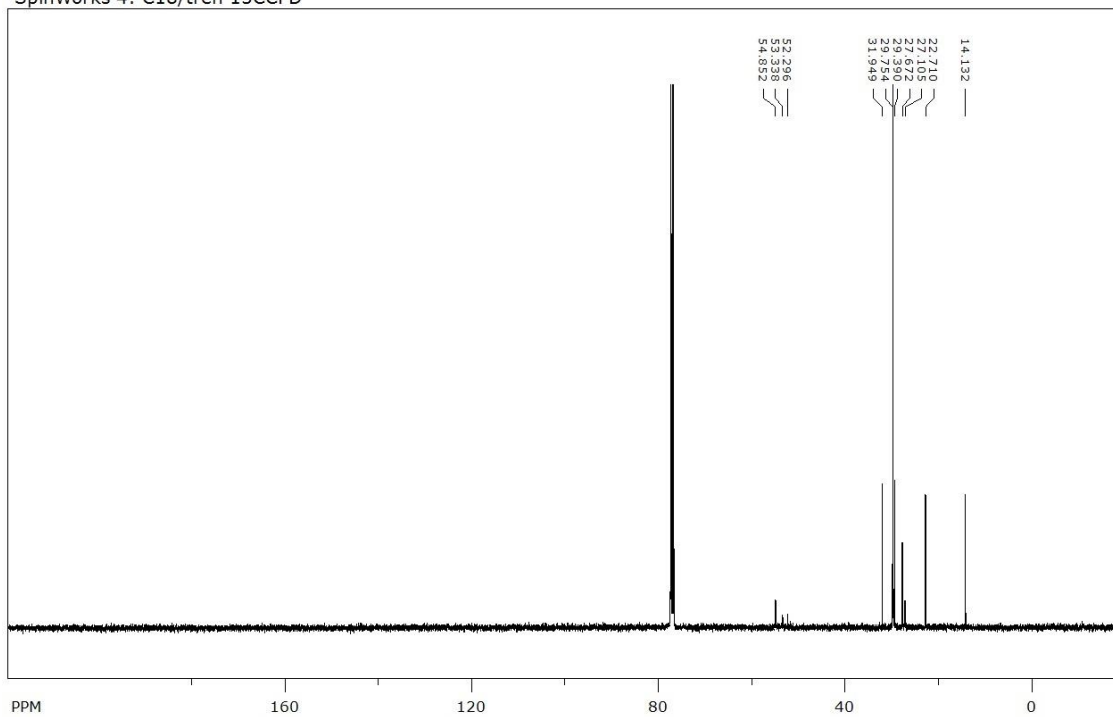




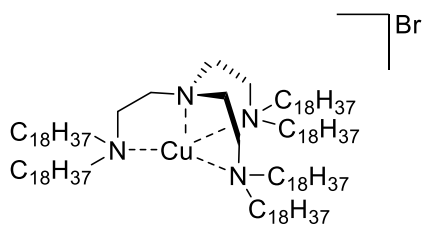
SpinWorks 4: C18/tren 1H



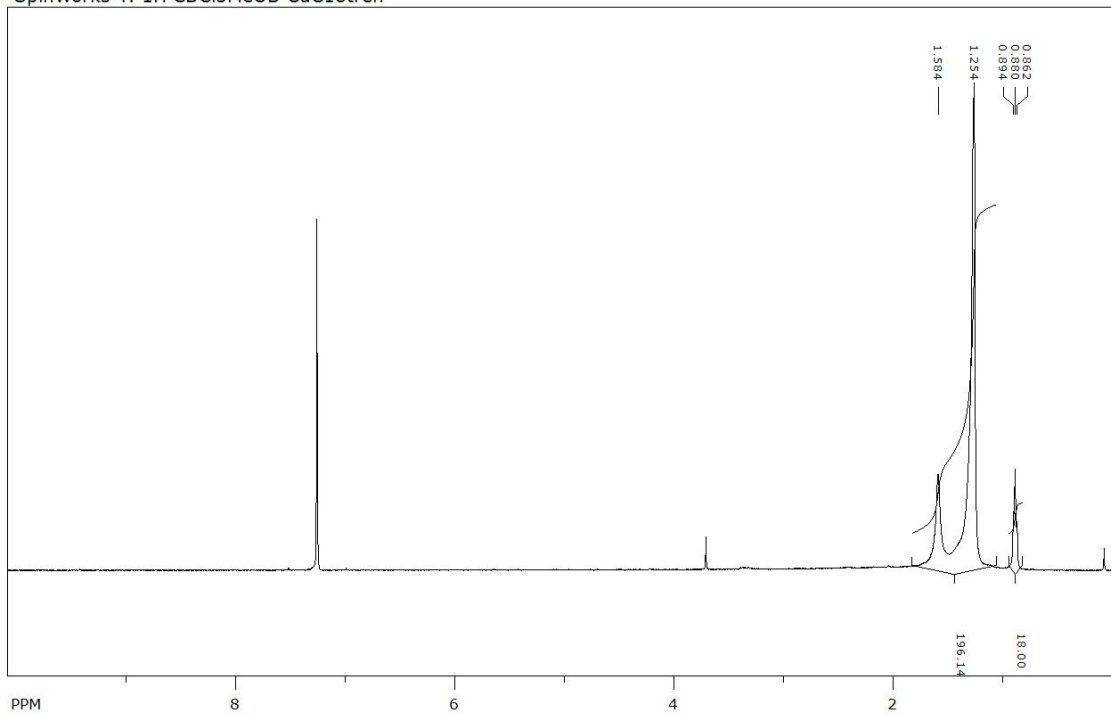
SpinWorks 4: C18/tren 13CCPD



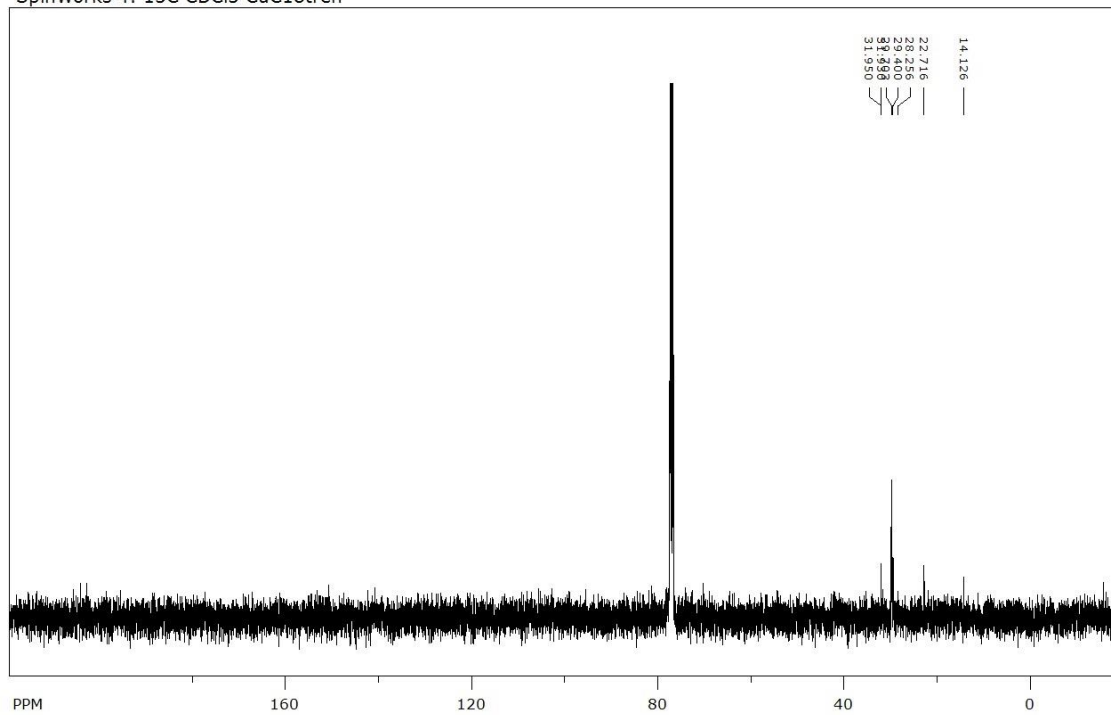
Appendix/NMR Spectra

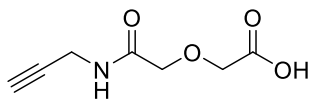


SpinWorks 4: 1H CDCl3MeOD CuC18tren

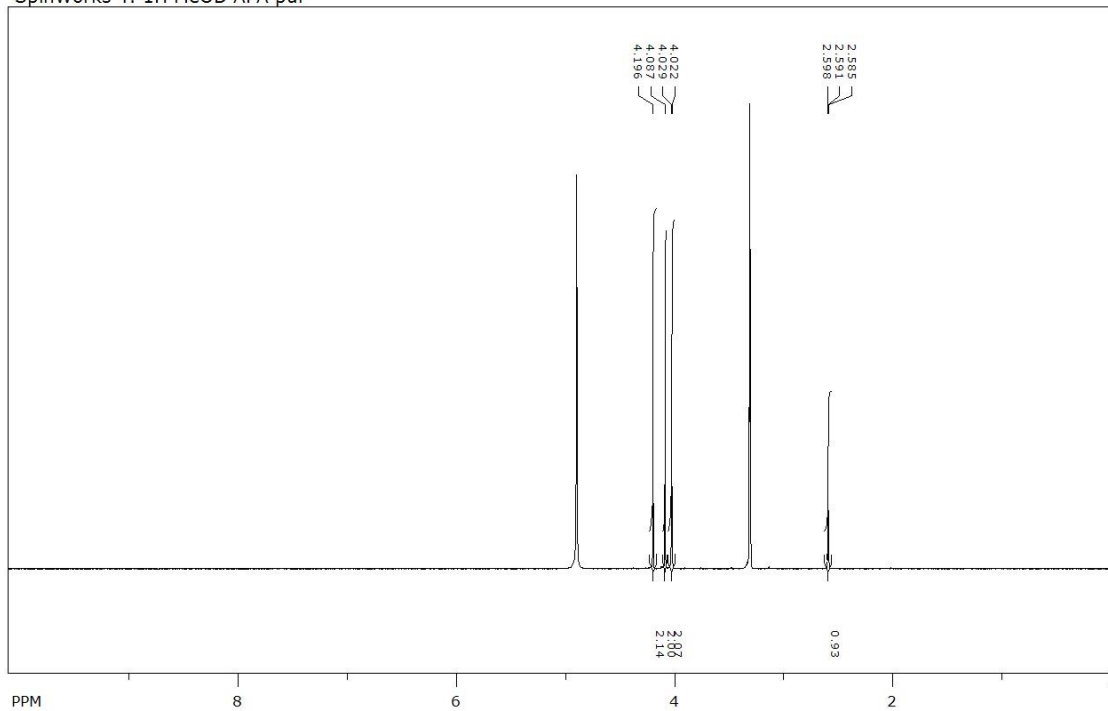


SpinWorks 4: 13C CDCl3 CuC18tren

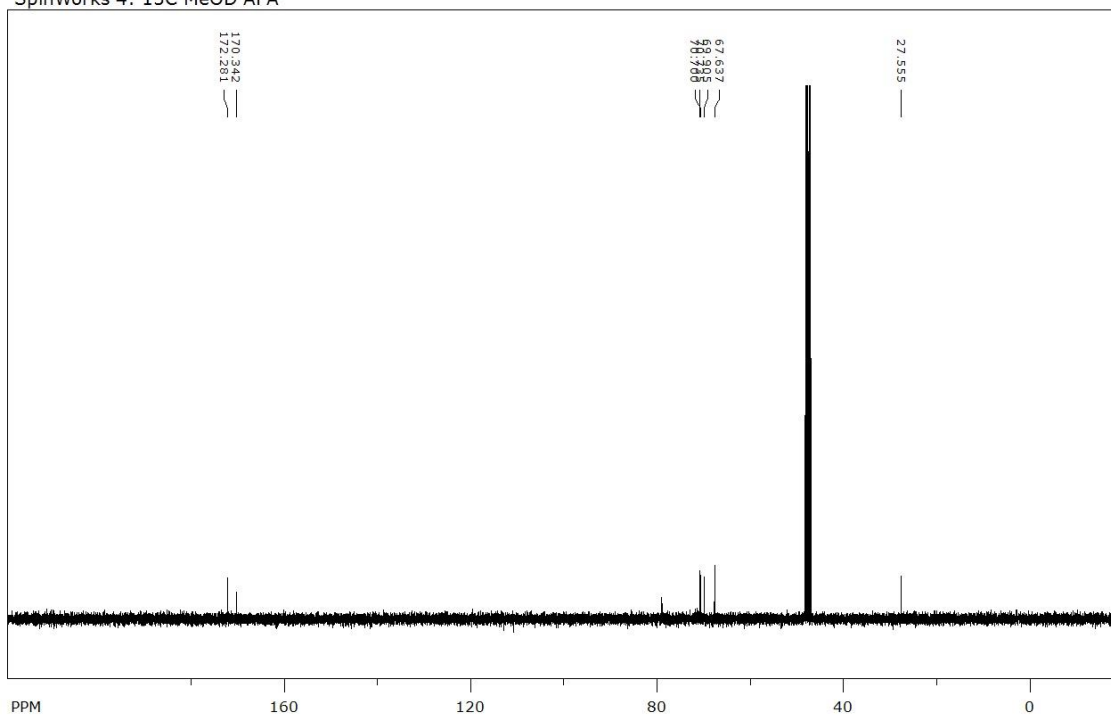




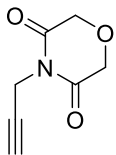
SpinWorks 4: 1H MeOD APA pur



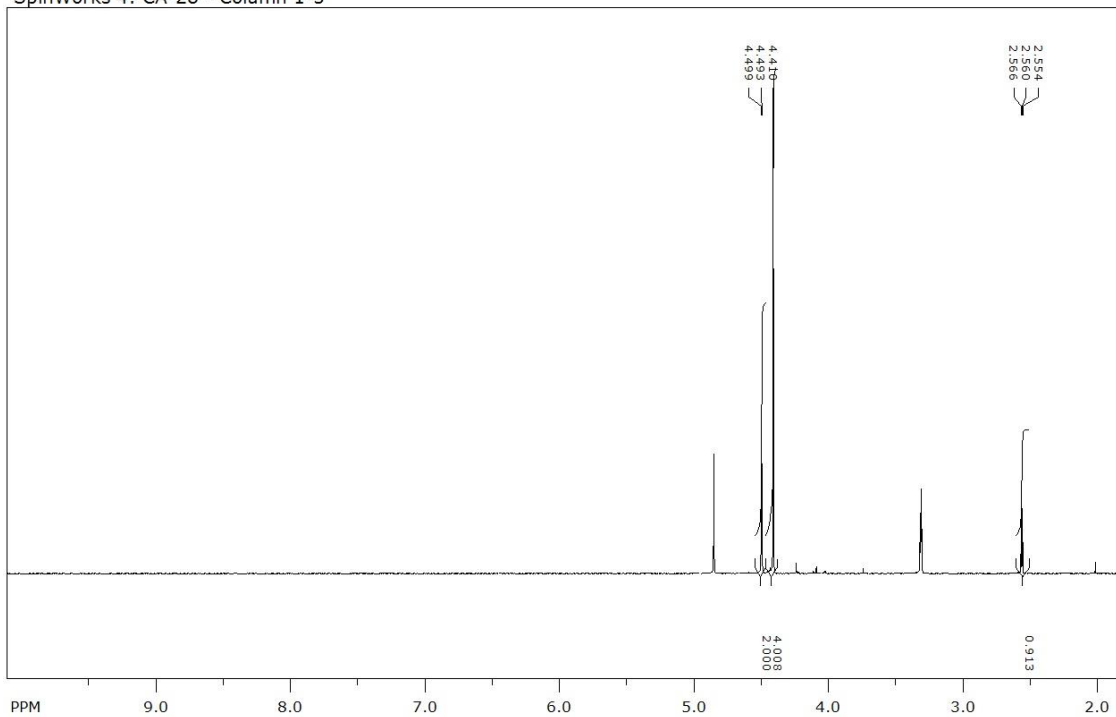
SpinWorks 4: 13C MeOD APA



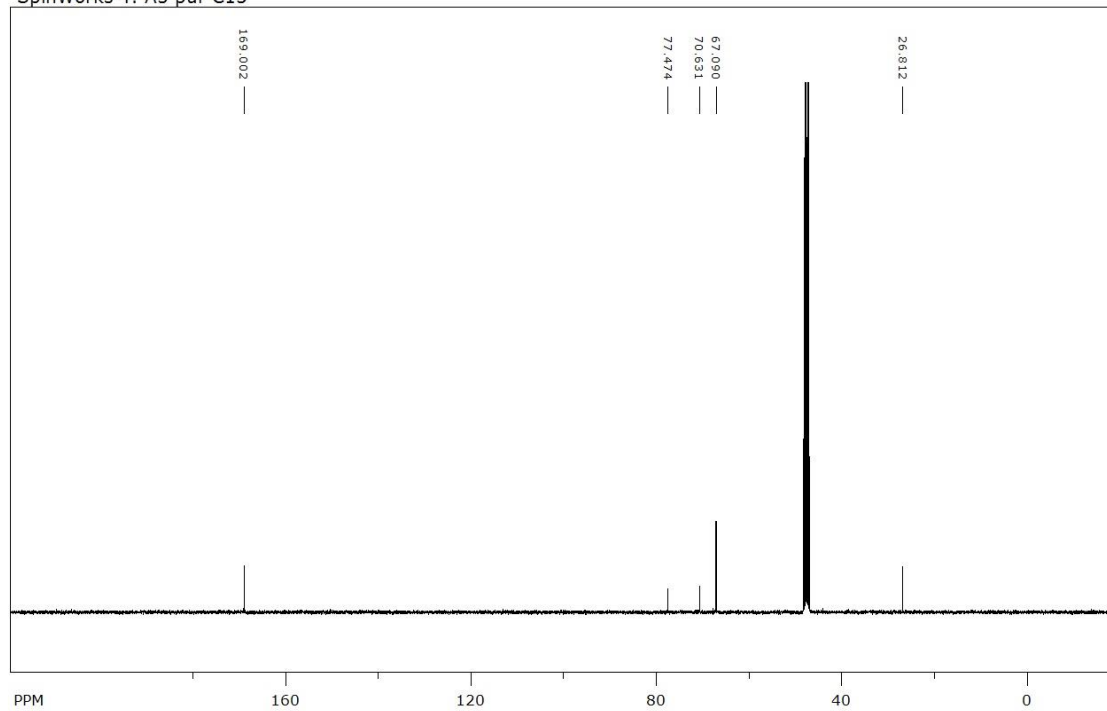
Appendix/NMR Spectra



SpinWorks 4: CA-28 - Column 1-5



SpinWorks 4: A5 pur C13



2 Chapter III

Residue after the TGA experiments

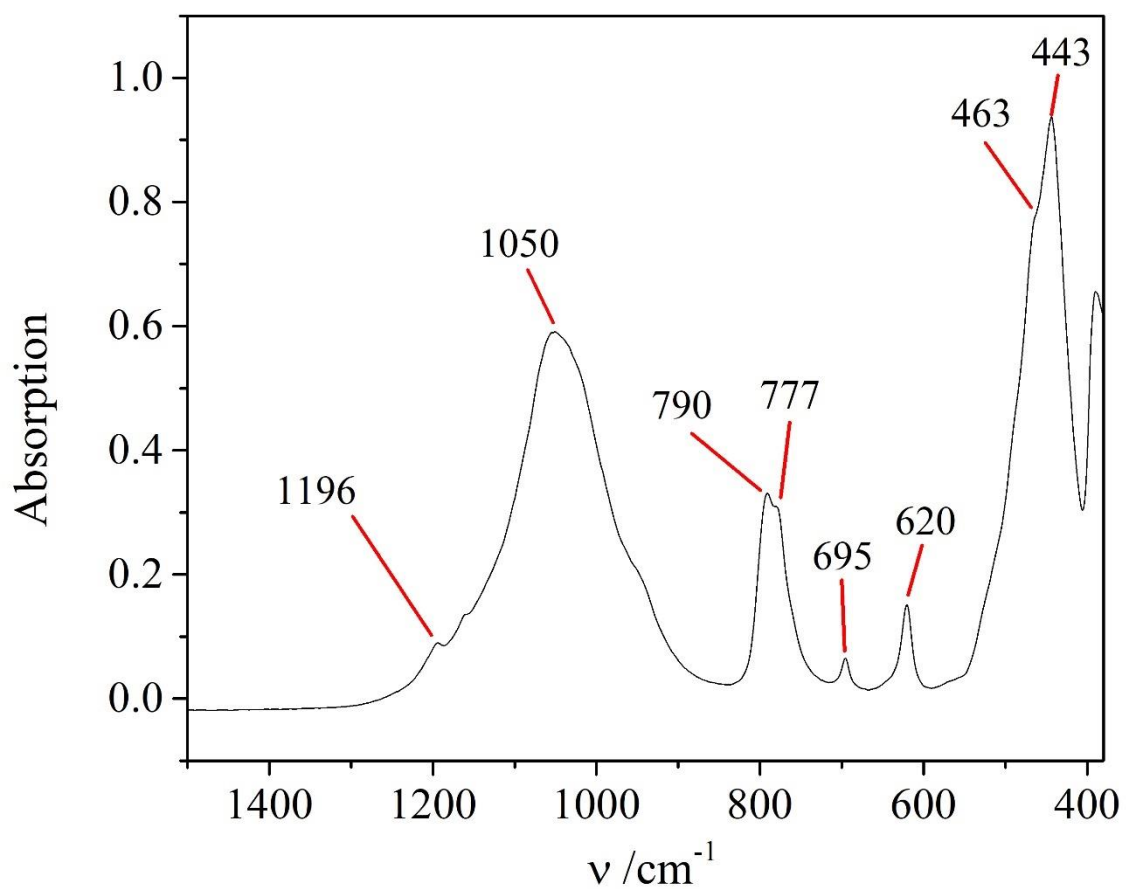


Figure A.1. FTIR spectrum of the residue after the TGA experiment.

The FTIR spectrum of the residue show peaks that can be attributed to a mixture of amorphous silica and cristoballite.¹⁷⁷

MP2

Table A.1. Peak positions and the ratios $R_{alkyl} = \frac{I(\nu_2)}{I(\nu_3)}$ and $R_{silica} = \frac{I(P_T)}{I(P_L)}$ in the FTIR spectra of the P2 materials.

Material	Pos. (ν_2)	Pos (ν_3)	$I(\nu_2)/I(\nu_3)$	Pos (P_T)	Pos (P_L)	$I(P_T)/I(P_L)$
H-MP2-A-C	2920	2851	1.34	1113	1008	0.74
H-MP2-B-C	2920	2851	1.4	1114	1028	0.98
T-MP2-A-C	2919	2850	1.37	1120	1006	0.44
T-MP2-B-C	2919	2850	1.35	1120	1007	0.43

MP1

Table A.2. Peak positions and the ratios $R_{alkyl} = \frac{I(\nu_2)}{I(\nu_3)}$ and $R_{silica} = \frac{I(P_T)}{I(P_L)}$ in the FTIR spectra of the P1 materials.

Material	Pos. (ν_2)	Pos (ν_3)	$I(\nu_2)/I(\nu_3)$	Pos (P_T)	Pos (P_L)	$I(P_T)/I(P_L)$
H-MP1-A-C	2921	2851	1.27	1106	1012	0.77
H-MP1-B-C	2921	2852	1.30	1111	1016	0.81
T-MP1-A-C	2921	2851	1.25	1100	1021	0.90
T-MP1-B-C	2921	2852	1.26	1103	1034	1.18

MP3

Table A.3. Peak positions and the ratios $R_{alkyl} = \frac{I(\nu_2)}{I(\nu_3)}$ and $R_{silica} = \frac{I(P_T)}{I(P_L)}$ in the FTIR spectra of the P3 materials.

Material	Pos. (ν_2)	Pos (ν_3)	$I(\nu_2)/I(\nu_3)$	Pos (P_T)	Pos (P_L)	$I(P_T)/I(P_L)$
H-MP3-A-C	2920	2852	1.34	1109	1009	0.75
H-MP3-B-C	2920	2851	1.36	1107	1000	0.71
T-MP3-A-C	2921	2851	1.35	1111	1003	0.79
T-MP3-B-C	2920	2851	1.31	1109	1007	0.94

First order peak extinction in lamellar structures

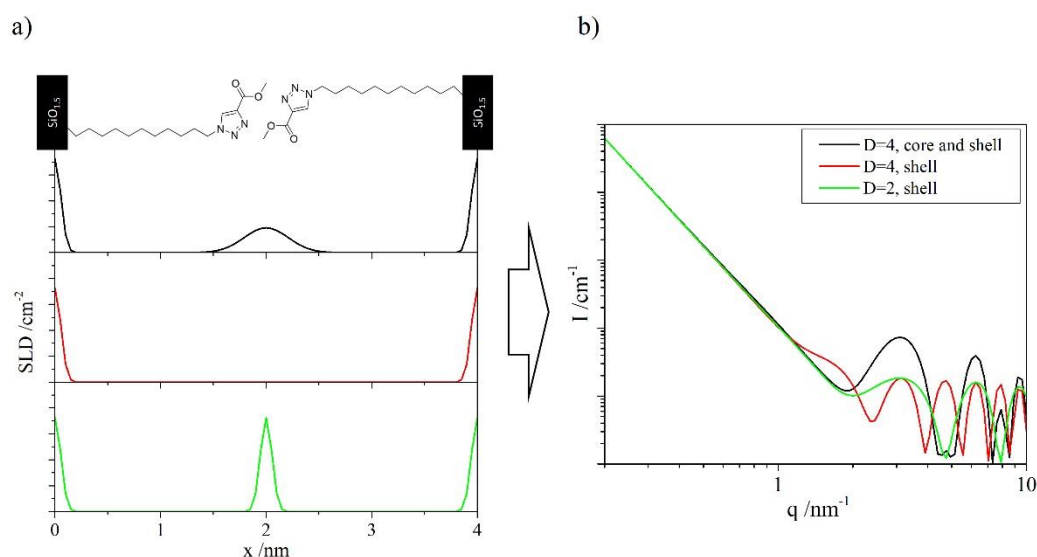


Figure A.2. Different repeat unit arrangements for the lamellar structure of P3 materials (a) and the corresponding simulated SAXS patterns (b).

Figure A.2 b) shows three simulated form factors of a bilayer with gaussian SLD distribution. The SAXS patterns were simulated using the SLDs for dodecane ($7.3E10 \text{ cm}^{-2}$) $\text{SiO}_{1.5}$ ($1.2E11 \text{ cm}^{-2}$) and 1,2,3-triazole ($1.06E11 \text{ cm}^{-2}$) When the total bilayer thickness (D) is set to 4, two cases can be distinguished. First, one SLD is attributed to the silica shell and one SLD is attributed to the hydrocarbon interphase (red line). In this case, the SAXS pattern shows the typical Bragg peaks with the first visible order at $q = 1.57 \text{ nm}^{-1}$. Second, an additional SLD is attributed to the core of the interphase simulating the headgroup (black line). This must not be confused with the case where the repeat unit length is cut in half (green line). Both show the first visible Bragg peak at $q = 3.14 \text{ nm}^{-1}$. However, in the latter this is the first order peak which is extinct in the former case. The distinction can be made using higher order peaks.

In-situ hydrolysis tests

For the following experiments, Methyl 1-octyl-1H-1,2,3-triazole-4-carboxylate (**T1**) was employed.

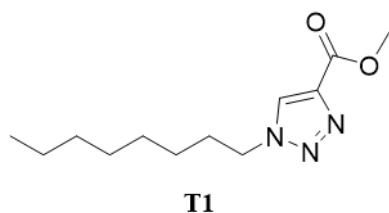


Figure A.3. Structural formula Methyl 1-octyl-1H-1,2,3-triazole-4-carboxylate (T1)

The first test reaction was inspired by literature.¹⁷⁵ Six samples with a 0.03 M solution of **T1** in acetonitrile were prepared and separated into two series of three. The first series also contained 0.09 M HCl whereas the second contained 0.09 NH₄OH. In each series, one sample contained 2, 5 and 10 equiv of LiBr as a Lewis catalyst. After 3 days, 10 mL were taken from each suspension. After the addition of 10 mL 1 M HCl, the aqueous phase was extracted using 20 mL ethyl acetate. After the evaporation of the organic phase NMR was performed. The results are shown in **Figure A.4**.

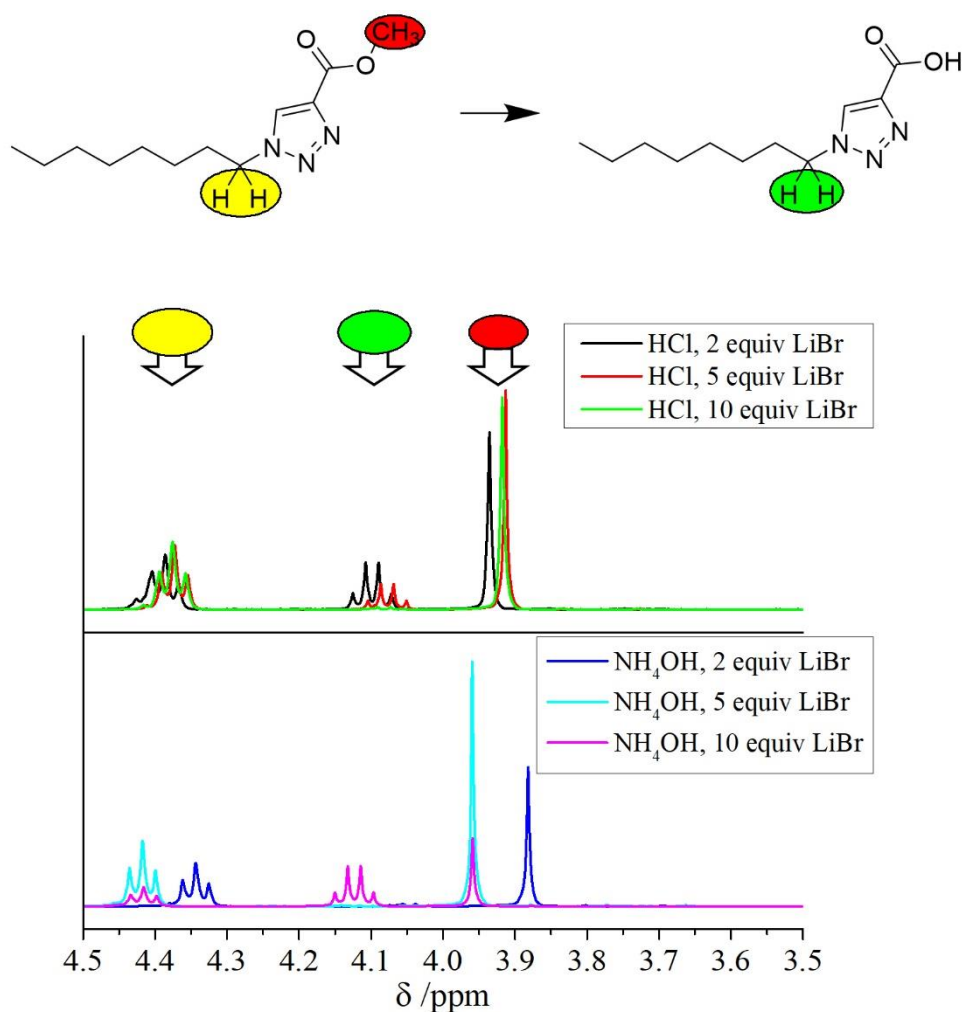


Figure A.4. NMR spectra of the reaction products from the hydrolysis test using LiBr.

None of the sample showed complete conversion. This can be seen from the presence of the methyl group (red circle). However, some progress is seen for 2 and 5 equiv LiBr under acidic conditions and 10 equiv LiBr under basic conditions. Under acidic conditions, the protonation of the future leaving group is required for the reaction. This is unfavorable when Li^+ withdraws electron density from the carbonyl function. Therefore, the reaction proceeds more slowly when more LiBr is present. Under basic conditions, the situation is inverted. The attacking nucleophile OH^- prefers the electron depleted carbonyl function that is coordinated to Li^+ . Hence a reaction is observed at the highest LiBr concentration. It is concluded, that in close to anhydrous conditions, the catalysis using LiBr might be considerable.

The second test was performed using the Lewis acid $\text{Gd}(\text{OTf})_3$ that was reported to be water resistant in literature.^{297,298} The reaction conditions were inspired from literature.²⁹⁹ For the test, six samples were prepared that were separated into two series. For each series, 0.03 M **T1** with 10 mol% $\text{Gd}(\text{OTf})_3$ were added to a pure aqueous phase, an aqueous phase/THF (1:1) mixture or THF with 5 equiv of water. Concerning the aqueous phases, the samples of the first series were prepared using pure water whereas in the second series a 1 M HCl solution was used. After 4 h of reaction at 60 °C, 10 mL ethyl acetate were added. After the addition of 10 mL 1 M HCl, the aqueous phase was extracted using 20 mL ethyl acetate. After the evaporation of the organic phase NMR was performed. During purification, the samples that contained no THF were accidentally mixed. The results are displayed in **Figure A.5**.

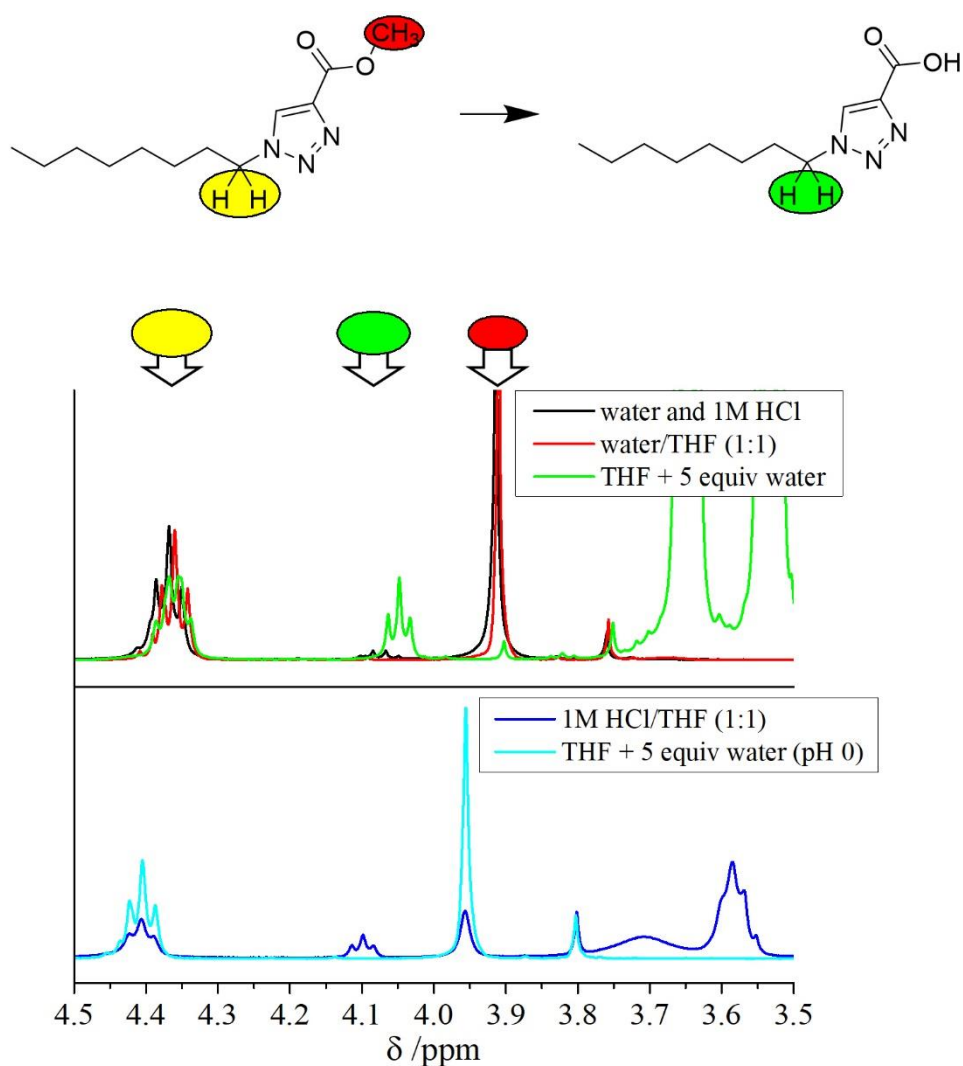


Figure A.5. NMR spectra of the reaction products of the hydrolysis test using $\text{Gd}(\text{OTf})_3$

None of the sample showed complete conversion. The reactions in pure aqueous solution showed very little conversion. The catalyst, thus, is ineffective in these conditions and useful for the desired application in the all-in-one approach. The best reaction was observed in pure THF with stoichiometric amounts of water. This, however,

is not new. In these conditions, Lewis acids are known to effectively catalyze hydrolysis reactions.

MP4 and MP5

FTIR peak assignment of the dyglycolic amide derivatives

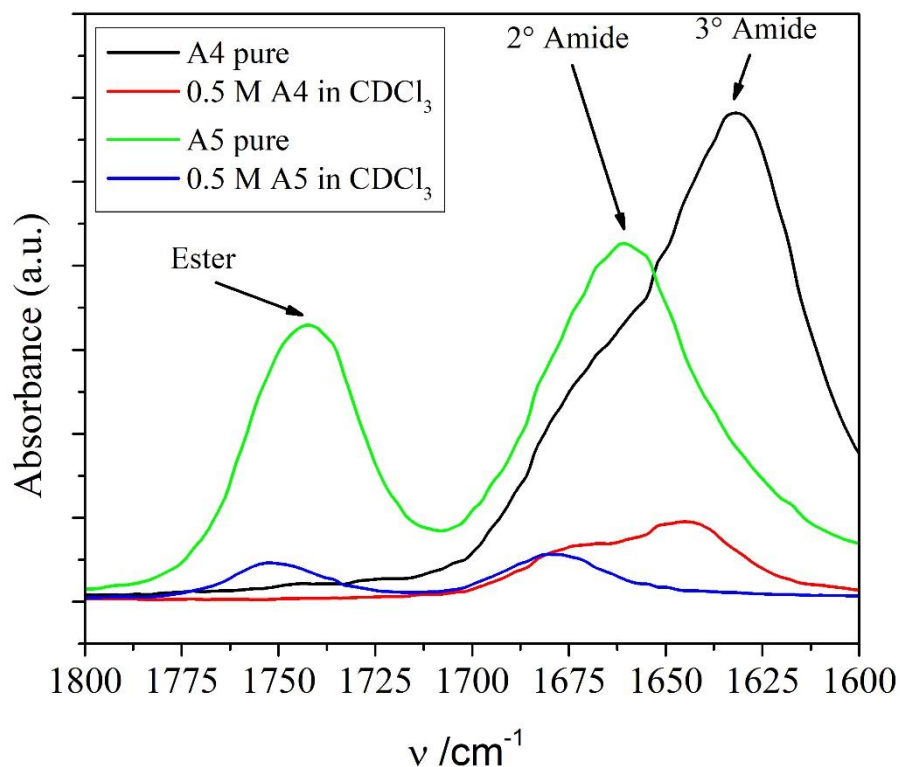


Figure A.6. FTIR spectra of A4 and A5 in the region from 1800 to 1600 cm^{-1} . The spectra were recorded in undiluted state and in 0.5 M CDCl_3 solution.

The spectra show the peaks that are attributed to the C=O stretching modes of the carbonyl functions. Upon dilution these peaks are blue shifted by $\sim 10 \text{ cm}^{-1}$ indicating the strengthening of the C=O bond. This can occur by the decrease of H-bonding of the secondary amide and the carbonyl functions.¹⁹⁸

Table A.4. Peak positions and the ratio $R_{alkyl} = \frac{I(v_2)}{I(v_3)}$ in the FTIR spectra of the P4 and P5 materials.

Material	Pos. (ν_2)	Pos (ν_3)	$I(\nu_2)/I(\nu_3)$
H-MP4-B-C	2922	2853	1.50
H-MP5-B-C	2921	2851	1.34
T-MP5-B-C	2923	2852	1.34

WAXS of H-MP5-B and T-MP5-B

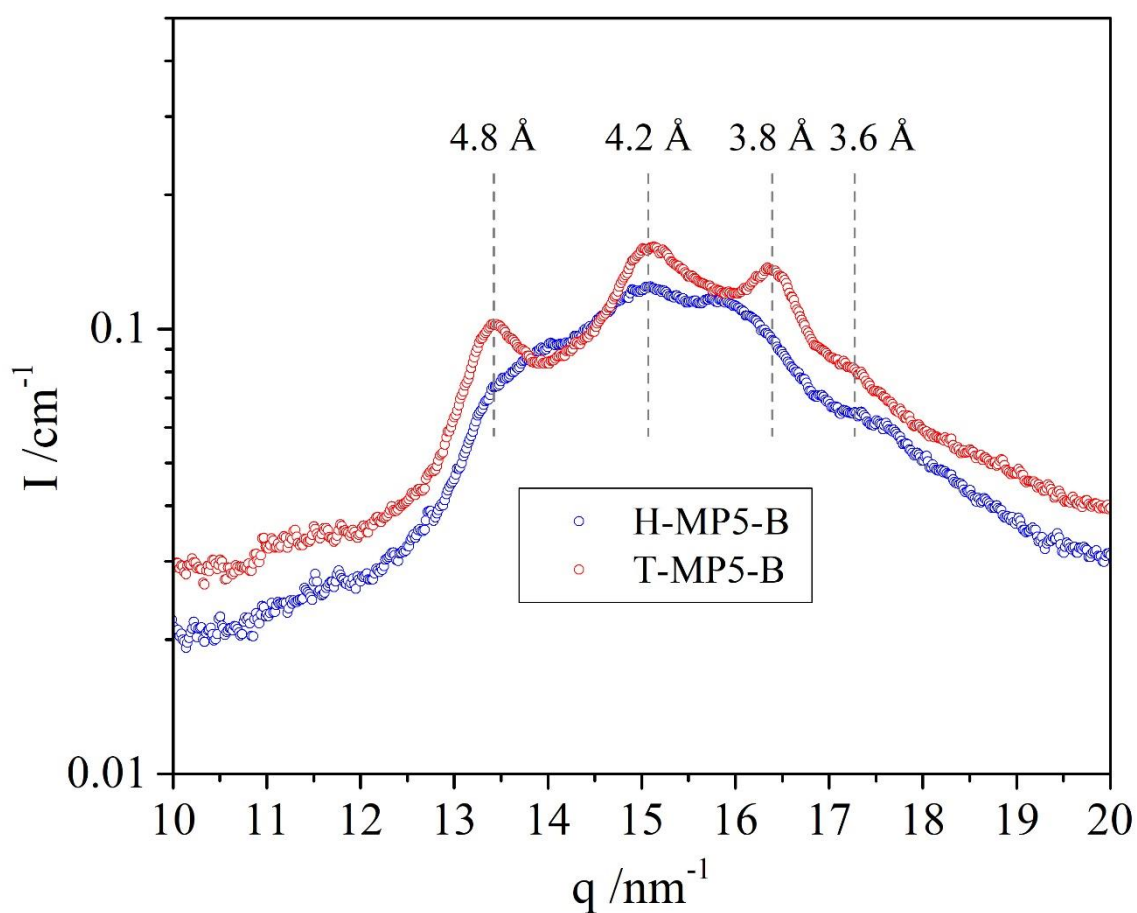


Figure A.7. WAXS pattern of the materials H-MP5-B and T-MP5-B.

3 Chapter IV

Ternary phase diagrams in molar fractions

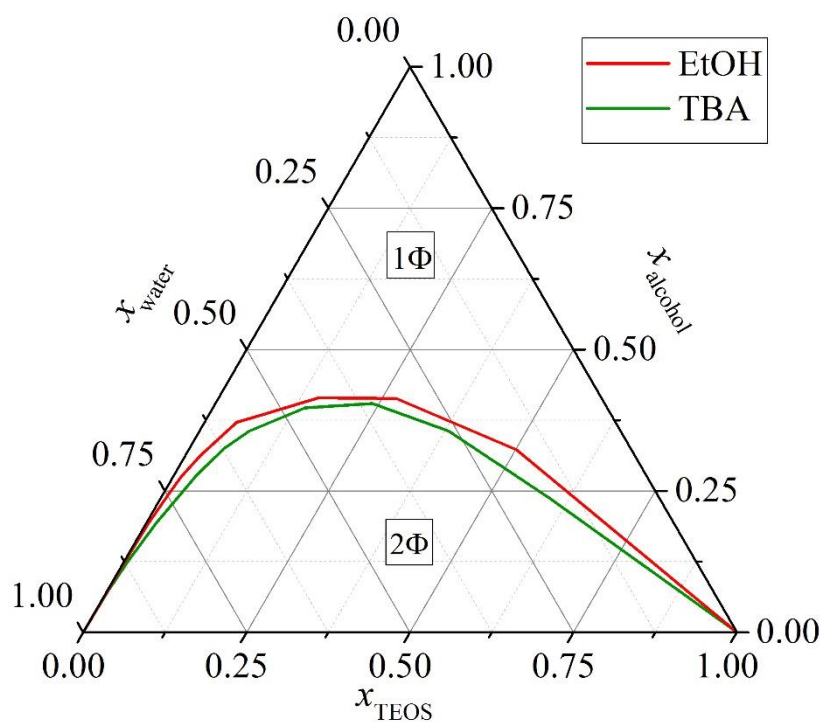


Figure A.8. Ternary phase diagrams of the systems water/TBA/TEOS and water/EtOH/TEOS in molar fractions determined at $25 \pm 0.5^\circ\text{C}$. The mono- and biphasic regions are indicated in the respective areas.

SAXS patterns of TEOS/TBA solutions at different ratios

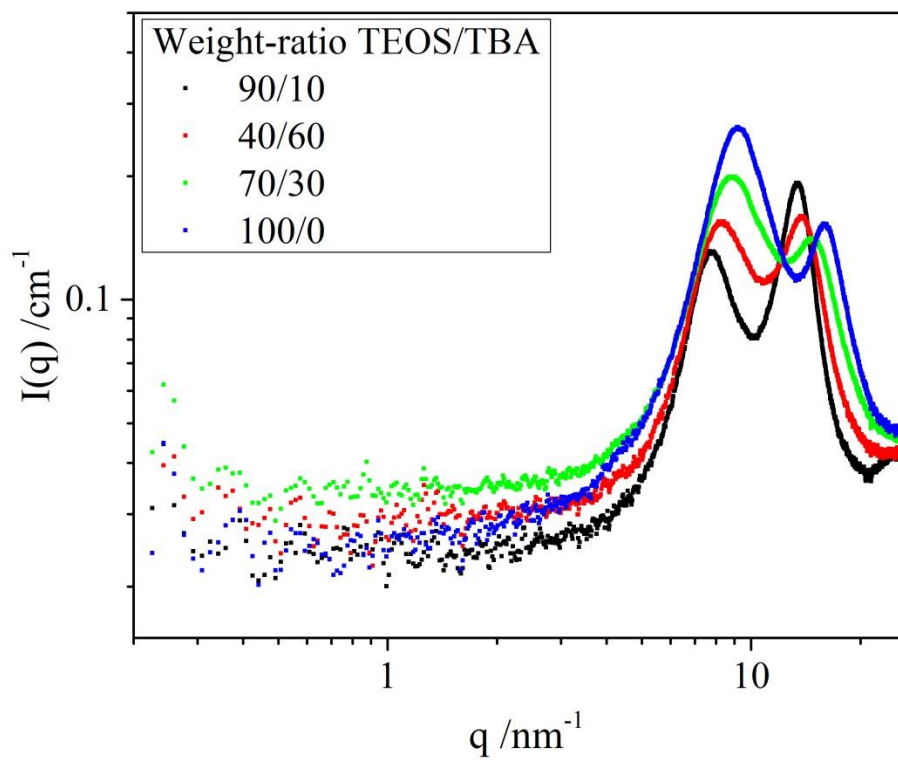


Figure A.9. SAXS patterns of binary mixtures containing TEOS and TBA at different weight ratios. The patterns were used to identify peaks in section Figure 43

Silica matrix evolution as followed by FTIR

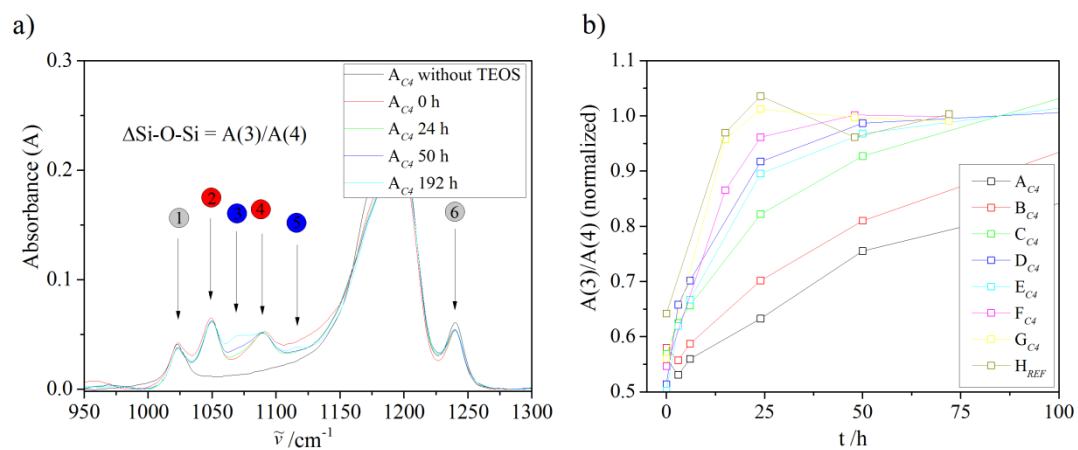


Figure A.10. a) Example to illustrate the development of the Si-O-Si peaks in the FTIR spectra. b) shows the normalized absorbance ratio of peak 3 to peak 4 for different sols as a function of their polymerization time. Illustrates the trends observed in Figure 45.

Exemplary FTIR spectrum of the water and oxonium ion bending modes

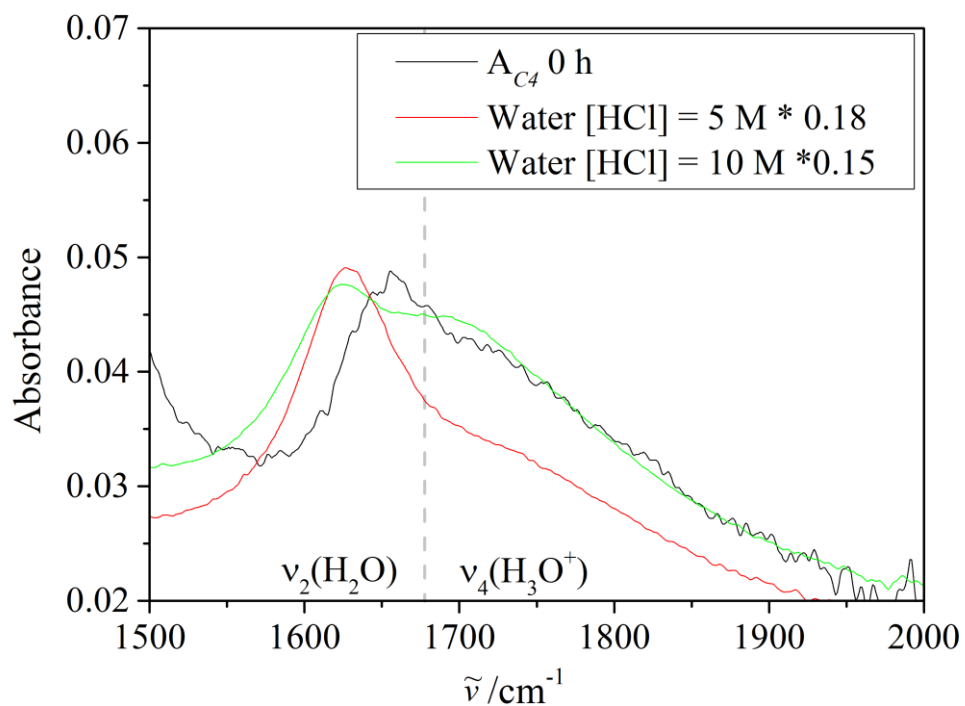


Figure A.11. Exemplary FTIR spectrum of sol A_{C4} at 0 h and the spectra of pure water at different HCl concentrations. The spectra of pure water were corrected by multiplication to match the absorbance of the sol spectrum. This way, the effective HCl concentration can be estimated by comparing the shape of the region between 1500 and 2000 cm^{-1} . Mentioned concerning Figure 44.

Viscosities of different water/alcohol mixtures

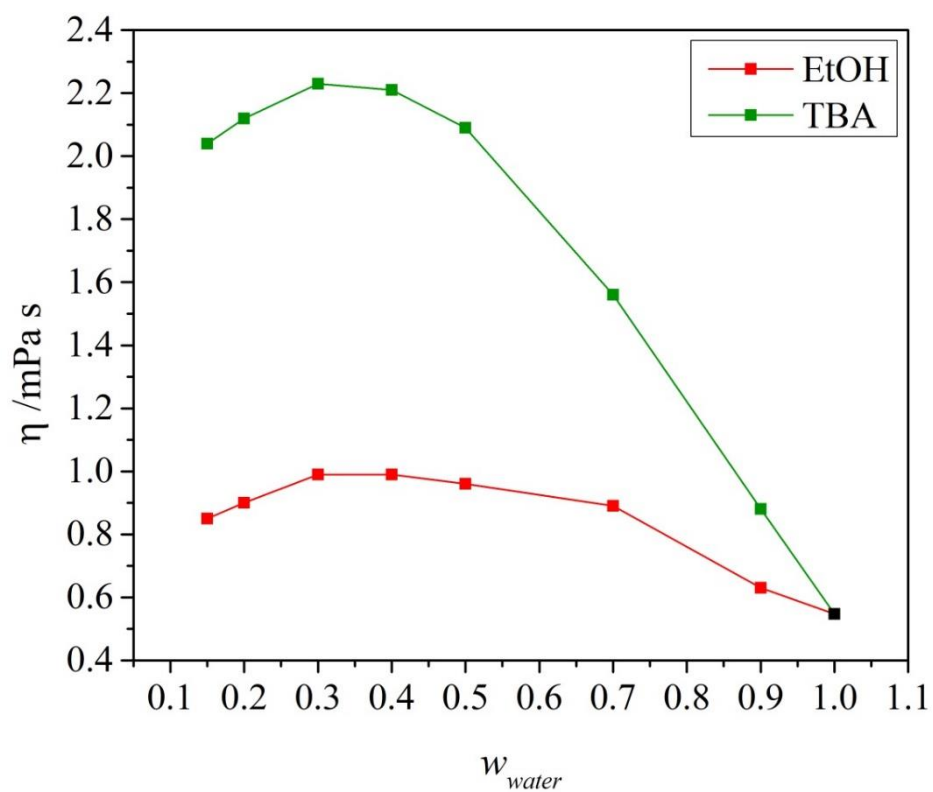


Figure A.12. Viscosities of binary water/alcohol mixtures as reported in literature.^{254,255}

Dielectric constants of different water/alcohol mixtures

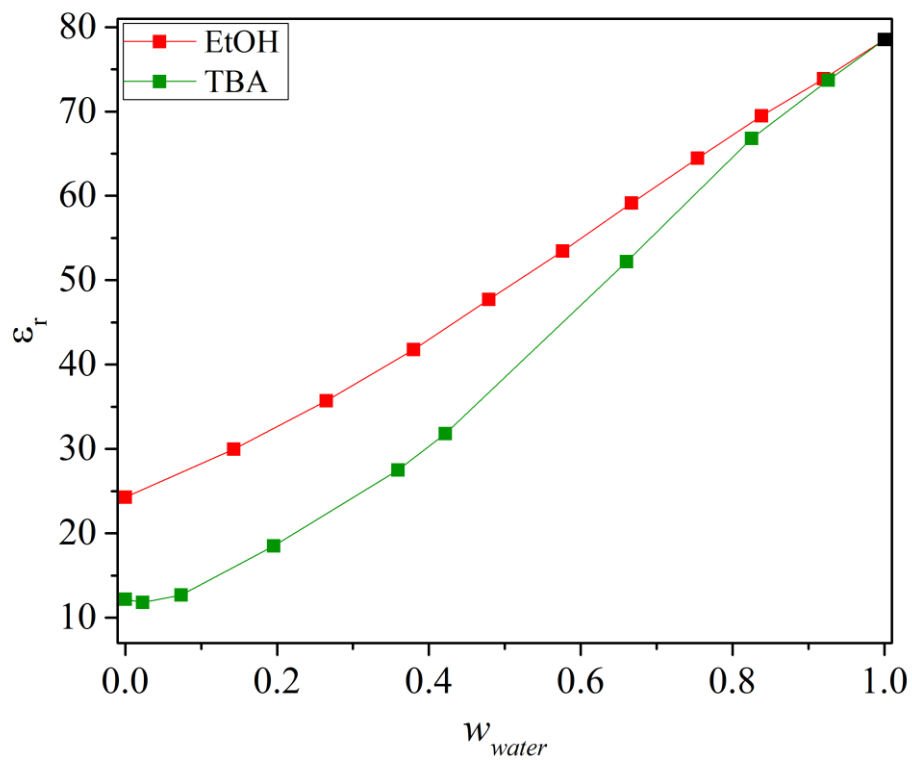


Figure A.13. Dielectric constants for binary water/alcohol mixtures as reported in literature.^{256,257} Mentioned concerning Figure 44.

4 Chapter V

Types of Adsorption/Desorption isotherms

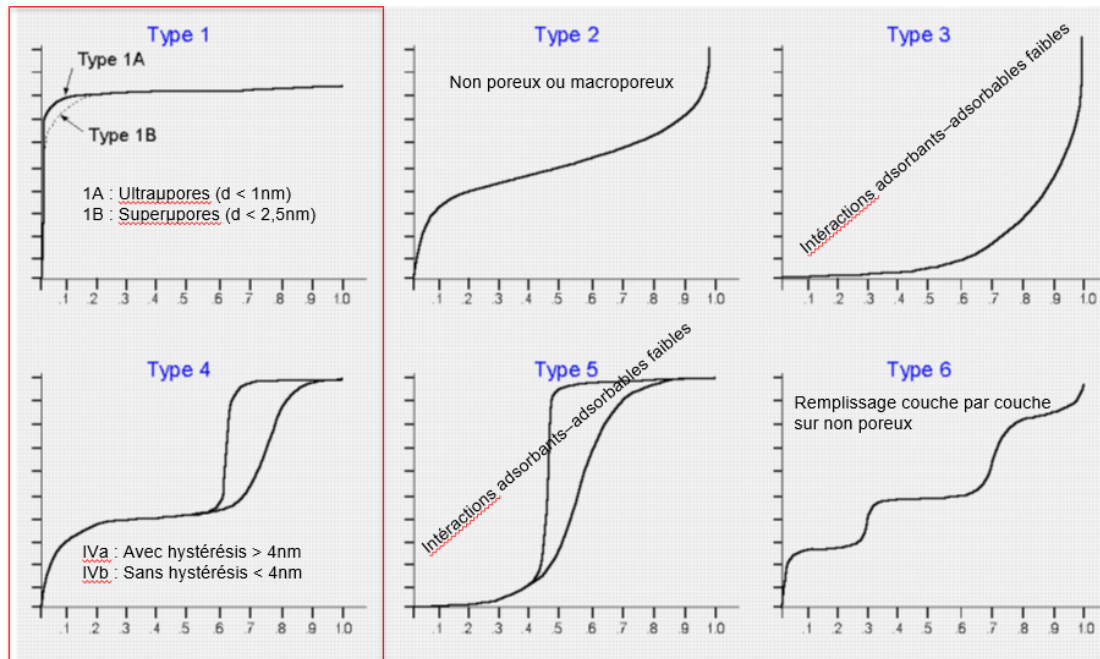


Figure A.14. Exemplary adsorption/desorption isotherms with their classification according to IUPAC.

Example Analysis of CoCo-3

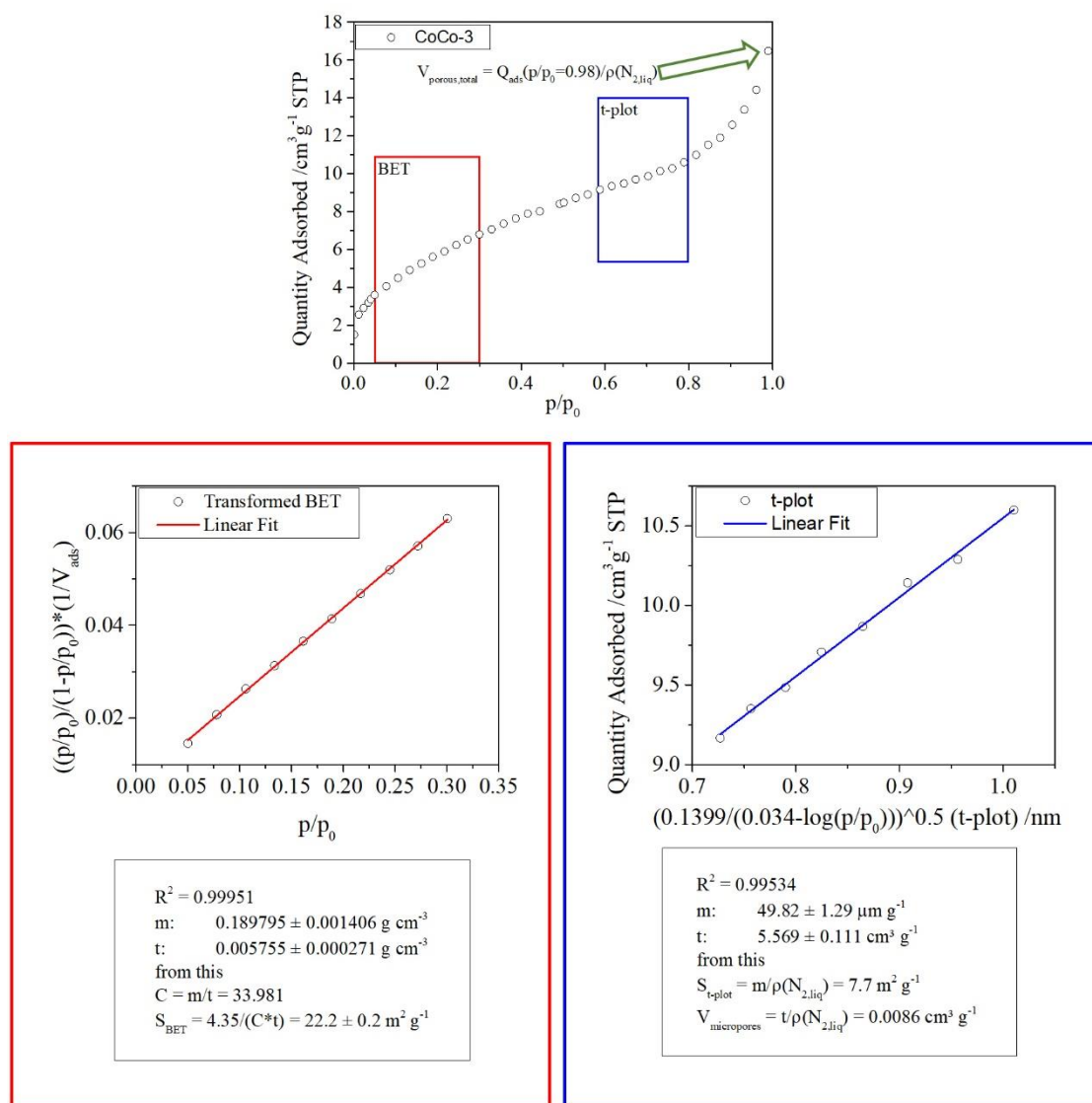


Figure A.15. Example analysis on CoCo-3. The partial pressures that are suitable for the corresponding analysis are marked by a coloured rectangle in the adsorption curve. The BET or t-plot graph was fitted with a linear equation $y = m \cdot x + t$. The green arrow indicates the point from which the total pore volume was calculated. The procedures were performed as explained in literature.³⁰⁰